Surface and Interface Effects in Nanoscopic Metallic Spin Transport Devices

A DISSERTATION
SUBMITTED TO THE FACULTY OF THE GRADUATE SCHOOL
OF THE UNIVERSITY OF MINNESOTA
BY

Michael John Erickson

IN PARTIAL FULFILLMENT OF THE REQUIREMENTS
FOR THE DEGREE OF
Doctor of Philosophy

Paul A. Crowell

January, 2013

© Michael John Erickson 2013
ALL RIGHTS RESERVED

Acknowledgements

There are many people that have earned my gratitude for their contribution to my time in graduate school. To my parents, brother, and the atomic mass unit (Ania). Further my advisors Paul Crowell and Chris Leighton, classmates, and labmates.

In the academic world I must acknowledge the contributions of the most essential individuals in my education, my advisors Professor Paul Crowell and Professor Chris Leighton. They gave me invaluable instruction and guidance throughout my tenure as a graduate student. I will be forever appreciative to them for their time, effort, and perseverance. I cannot emphasize how important these two people have been in my life, and my gratitude to them. I must also thank my high school physics teacher Steve Gabriel, my undergraduate research advisor Professor Jason Engbrecht, and my undergraduate academic advisor Professor Amy Kolan. Each of them were instrumental in my development as a scientist.

One cannot survive the education process in a vacuum. From my time as a high school student: Joe Aaker, Tim Binder, Cody Byrum, Nicholas Grey, and Jake Salcone. As an undergraduate the role of classmates, and fellow physicists were played by Katie Huber, Casey Rutherford, and Mike Bongard among a larger cast of many great friends. By the time I reached graduate school this close knit group was based around the people I shared a teaching office with: Seth Cooper, Matt Loth, and Tanner Schulz. My labmates over the years have been very important: Eric Garlid, Mike Manno, Mun Chan, Rob Compton, Manish Sharma, and Jeff Parker. All the other members of the Crowell and Leighton groups not listed must be thanked as well for our time together.

My parents and brother encouraged me throughout the years to become a curious and intellectual person. They set me on the path to becoming a scientist interested in how the world around me works and making sure I had the opportunities to satisfy that

curiosity. My parents always supported me in my endeavors as did my older brother who blazed the trail, being a great example of a student, researcher, and educator all while being a good person. My (now) wife has exemplified these same traits and was an essential support throughout my graduate school experience. I appreciate all the support and assistance from everyone in my life, with these the most notable examples.

Dedication

To those who have supported, helped, taught, and encouraged me through the years especially my parents Ed and Loretta, my brother Dave, and my wife Ania.

Abstract

This thesis describes the effects of surfaces and interfaces on spin-dependent electron transport in metallic ferromagnetic-normal metal nanostructures. Bulk spin-dependent transport properties of metals can be understood in terms of the charge transport properties for devices larger than the characteristic diffusion length for spin polarized electrons. For devices with reduced cross-sectional dimensions, approaching the electronic mean-free-path, the surfaces of the device begin to dominate the spin dependent transport. Additionally, the interplay of the transport properties of the ferromagnet and normal metal collectively determine the overall properties in concert with the effect of the surfaces.

A process to fabricate lateral metallic spin transport devices was developed using electron beam lithography to pattern two-angle shadow masks for deposition and lift-off. Ferromagnetic metals (FM), NiFe or Co, and normal metals (N), Cu or Al, were evaporated from high purity sources in ultra-high vacuum, without breaking vacuum, to minimize interfacial resistance. The temperature-dependent magnitude of the non-equilibrium spin accumulation was measured in a non-local geometry to obtain information on spin injection and relaxation. Further, the reduction in spin accumulation as the source-detector separation was increased allowed for a measurement of the effective spin diffusion length in the nanoscopic devices, measured here to be less than 600 nm. The application of experimentally-constrained analytical 1D models of spin transport returns not only information about the spin-dependent properties of the N, but also that of the FM. By measuring four different combinations of N and FM metals, the contributions from the N and FM properties can be separated from those of the interfaces. Additionally, modifying the cross-sectional geometry of the device gave information about the contributions of boundaries to spin relaxation. A complementary measurement of these properties can be attained through electrical Hanle effect measurements, although quantitative analysis is possible only by developing models that include both diffusive FM/N interfaces and surfaces. Elliot-Yafet theory (EY) predicts spin diffusion lengths greater than 1000 nm for bulk materials, much larger than measured here. EY relaxation was invoked in numerical simulations of the full lateral device in three dimensions;

the simulations were conducted to model the temperature and spatial dependence of the spin accumulation. Through these simulations we demonstrate that enhanced spin relaxation at surfaces can reproduce the general experimental observations, including the dependence on cross-sectional geometry.

Contents

Acknowledgements **i**

Dedication **iii**

Abstract **iv**

List of Tables **xii**

List of Figures **xiv**

1 Introduction **1**

1.1 Introduction to Spintronics 2

1.1.1 Brief Introduction to Spin-Dependent Transport Experiments . . 3

1.2 Spin Transport Fundamentals 6

1.2.1 Transport in Metals 6

1.2.2 Ferromagnetism and Spin Polarization 7

1.2.3 Boltzmann Equation 9

1.2.4 Spin-Dependent Boltzmann Equation 11

1.2.5 Macroscopic Equations Describing Transport in Metals 13

1.2.6 Spin Injection Across Diffusive Ferromagnetic/Non-Magnetic Interfaces 15

1.2.7 Solving for the Spin-Resolved Chemical Potential Across a Ferromagnet - Normal Metal Interface 17

1.2.8 Tunnel Barrier Interfaces 18

1.2.9 Two Diffusive FM/N Interfaces - Giant Magneto Resistance . . . 20

1.2.10 Non-Local Detection of the Non-Equilibrium Spin Accumulation 21
1.2.11 Diffusive Non-Local Spin Transport: Spin-Resistor Network Solution . . . 23
1.2.12 Characterizing Spin Relaxation: The Spin Diffusion Length . . . 26
1.2.13 Spin-Relaxation at Surfaces . . . 28
1.2.14 Spin Precession and Dephasing - the Electrical Hanle Effect . . . 29
1.3 Review of Spin Transport in Metals Experiments . . . 31
1.3.1 Vertical Devices - GMR and TMR . . . 33
1.3.2 Lateral Spin Valve Experiments . . . 36
1.4 Remarks . . . 38

2 Experimental Techniques 39
2.1 Introduction to Experimental Techniques . . . 39
2.2 Sample Patterning Techniques . . . 40
2.2.1 Lithography . . . 40
2.2.2 Multi-Angle Deposition Lithography . . . 46
2.2.3 Non-Local Spin Valve Device Design . . . 47
2.3 Deposition of Materials in Vacuum . . . 48
2.3.1 Ultra-High Vacuum Deposition System . . . 50
2.3.2 Electron Beam Evaporation . . . 50
2.3.3 Growth Control Shutters . . . 54
2.3.4 Multi-Angle Deposition . . . 55
2.4 Materials and Structural Characterization Techniques . . . 57
2.4.1 X-Ray Diffraction . . . 58
2.4.2 Grazing-Incidence X-Ray Reflectivity . . . 58
2.4.3 Polarized Neutron Reflectivity . . . 61
2.4.4 Scanning Electron Microscopy . . . 65
2.4.5 Atomic Force Microscopy . . . 69
2.5 Transport Measurements . . . 72
2.5.1 Helium-Vapor Cryostat Operation . . . 72
2.5.2 Measurement Probe Design . . . 73
2.5.3 Transport Measurement Techniques and Apparatus . . . 79

2.5.4 Data Acquisition Software 83

3 Transport Measurements and Basic Characterization 84

3.1 Four-Terminal Channel Resistance Measurement 84

3.2 Measurement of the Ferromagnet-Normal Metal Interface Resistance . . 90

3.3 Non-Local Spin Transport Measurements 93

3.4 Non-Local Spin Valve Measurement 93

3.4.1 Dependence of Spin Accumulation on Injection Current 98

3.5 Origin of the Non-Local Background 101

3.5.1 Spin-Independent Background Due to Charge Current Spreading 102

3.5.2 Non-Local Background - Thermoelectric Effects 106

3.6 Non-Local Electrical Hanle Effect Measurement 106

4 Spin Transport Results and Analysis 111

4.1 Temperature Dependence of ΔR_{NL} 111

4.2 Separation Dependence of ΔR_{NL} 115

4.3 Dependence of ΔR_{NL} on Channel Thickness 115

4.4 Non-Local Spin Valve Effect Fitting 120

4.4.1 Application of Transparent Interface Modeling to the Dependence of ΔR_{NL} on d 120

4.4.2 Interdependence of ΔR_{NL} on $\lambda_{s,FM}$ and α_{FM} 123

4.4.3 Temperature-Dependent λ_s from Spin Valve Effect Fitting 126

4.4.4 Fitting the Channel Thickness Dependence of ΔR_{NL} vs. d for Py/Cu Spin Valves. 131

4.5 Hanle Effect Results and Analysis 135

4.5.1 Hanle Effect Data for Aluminum Channels 136

4.5.2 Hanle Effect Analysis: Aluminum 138

4.5.3 Hanle Effect Analysis: Copper 143

4.5.4 Fitting Hanle Data for Devices with Copper Channels 146

5 Spin Diffusion and Relaxation Simulations 153

5.1 Spin-Transport Simulation Details 155

5.1.1 Spin-Dependent Diffusion Simulations 158

5.2 Non-Local Spin Transport Simulations: Results 162
5.2.1 Simulated Temperature Dependence of ΔR_{NL} 163
5.2.2 Simulated Temperature Dependence of the N Spin Diffusion Length in NLSVs 165
5.2.3 Simulated Thickness Dependence of the Spin Transport in Cu . . 166
5.2.4 Hanle Effect Simulation Results 168

6 Work in Progress and Future Research 172
6.1 Tunnel Barriers 172
6.2 Novel Ferromagnets for Lateral Spin Valves 174
6.2.1 Cu_xNi_{1-x} 174
6.2.2 Cobalt-Based Disulfides ($CoS_2 - Co_{1-x}Fe_xS_2$) 177
6.3 Further Increasing Spin Relaxation at Surfaces 180
6.4 Changing the Ferromagnetic - Non-magnetic Interfaces 181
6.4.1 Experimental Tests of Interdiffusion by Sample Annealing 181
6.4.2 Preliminary Polarized Neutron Reflectivity 182

7 Conclusion 186

References 190

Appendix A. Glossary and Acronyms 200
A.1 Glossary 200
A.2 Symbols 201
A.3 Acronyms 206

Appendix B. Device Fabrication Recipes and Technical Information 208
B.1 Resist and Process Information 208
B.1.1 Resists 210
B.1.2 Exposure 212
B.1.3 Developing 214
B.1.4 Deposition 215
B.1.5 Liftoff 216
B.2 Design Considerations 216

B.2.1 Pattern Design Requirements 216
B.3 Electron Beam Exposure Dosage: The Proximity Effect 218
B.4 Photolithography Recipes 219
B.4.1 Spin Resist 219
B.4.2 Expose 221
B.4.3 Develop and Ash 221
B.4.4 Metalization 221
B.5 e-Beam Lithography Recipes 222
B.5.1 Spin Resist 222
B.5.2 Expose 222
B.5.3 Develop 223
B.5.4 DeScum 223
B.5.5 Deposit 223
B.5.6 Liftoff 223

Appendix C. Vacuum Systems and Evaporation Equipment **224**
C.1 Ultra-High Vacuum Deposition System 224
C.1.1 Pumping 227
C.1.2 Vacuum Gauges 228
C.2 Electron Beam Evaporation 230
C.2.1 Depositing onto Resist Patterned Substrates 234
C.3 Thermal Evaporation 235
C.4 Quartz Crystal Thickness Monitors 239
C.4.1 Quartz Crystal Monitor Calibration 240
C.5 Multiple Source Evaporation 241
C.5.1 Growth Control Shutters 242

Appendix D. Radak Design and Installation **244**
D.1 Radak Mount Design 245

Appendix E. Probe Design and Schematics **252**
E.1 Probe Schematics 252
E.2 Sample Rotation Stage Schematic 255

E.2.1 Sample Rotation Stage in Retaining Block 257
E.3 Design of the Sample Holder 259
E.3.1 Probe Wiring 261
E.4 Probe Rotation Block Calibration 264
E.5 Helium Vapor Cryostat Operation 265

List of Tables

1.1 Experimentally-determined ferromagnetic polarizations from tunneling experiments. . . . 34
1.2 Experimentally determined ferromagnetic spin diffusion lengths. 36
1.3 Experimentally-determined non-magnetic metal diffusion lengths. 37
1.4 Experimentally-determined ferromagnetic diffusion lengths. 38
3.1 Typical values of ρ_{FM} at $T = 5\,\mathrm{K}$ and 292 K with RRR measured using films and patterned wires $w_{FM} \approx 200\,\mathrm{nm}$. . . . 87
3.2 Typical values of ρ_N measured using patterned lateral non-local devices, with both FM materials serving as contacts. . . . 90
3.3 Typical values of experimentally measured $R_{I,E}$, calculated background $R_{I,M}$, and the resulting R_I after accounting for current spreading. . . . 93
4.1 Fit parameters for the 1D spin transport model in the diffusive FM/N interface limit. . . . 123
4.2 Fitting parameters α_{FM}, $\lambda_{s,FM}$, and $\lambda_{s,N}$ along with the corresponding χ^2_r from fitting ΔR_{NL} as a function of d for Co/Cu devices with the one FM parameter held fixed shown in bold. Each line of the table represents a different fit. . . . 126
4.3 The Bloch $T^{3/2}$ law parameters: the 0 K FM polarization $P_{0,FM}$ and temperature coefficient α_B from fits of $\alpha_{FM}(T)$ determined from fitting of ΔR_{NL} vs d for non-local spin valves of various FM/N combinations. 132
5.1 The ratio of measured ρ_N from §3.1 and fitted $\lambda_{s,N}$ from §4.4.3 at $T = 5\,\mathrm{K}$ and 275 K for lateral NLSV devices with transparent interfaces. 154
6.1 Experimentally determined range of $\rho_{Cu}(T)$ and RRR for Co/Cu samples before and after vacuum annealing at $T = 250\,^\circ\mathrm{C}$ and 350 °C for 2 h. . . 183

6.2 Grazing-incidence x-ray and polarized neutron reflectometry fitting parameters. 185
7.1 The measured ρ_N, ΔR_{NL} for $d = 220\,\text{nm}$, and the fitted $\lambda_{s,N}$ for lateral NLSV devices with transparent interfaces as well as the ratio of each at $T = 5\,\text{K}$ and $275\,\text{K}$. 187
7.2 $\lambda_{s,N}$ as determined from fits of ΔR_{NL} vs. d for Py/Cu devices at $T = 5\,\text{K}$, $50\,\text{K}$, and $275\,\text{K}$. 188
A.1 Symbols 201
A.2 Acronyms 206
B.1 Deposition conditions and evaporation rates for photolithographic Ti/Au contacts. 222
E.1 Transport properties of commonly used materials for low temperature cryostat wiring. For each material the Residual Resistivity Ratio $\rho(T = 295\text{ K})/\rho(T = 5\text{ K})$, $T = 5$ K magnetoresistance $(R(H = 10\text{ T}) - R(H = 0\text{ T}))/R(H = 0\text{ T})$, and magnetic suceptabilities are shown. 264

List of Figures

1.1 Generic representation of a ferromagnetic density of states which is separately shown for the spin-up (left) and spin-down (right) bands composed of the symmetric s-band and exchange-split d-bands. 9
1.2 Representation of a ferromagnetic/normal metal interface used for spin injection. The arrows illustrate the charge and spin current directions. . 16
1.3 Spin-dependent density of states depicting spin injection from a ferromagnet to a normal metal. 16
1.4 Calculated position dependence of (a) the spin-up and -down chemical potential, (b) non-equilibrium spin polarization, and (c) polarization of the spin current. 19
1.5 (a) Representative diagram of a non-local spin valve device with arrows representing the electron and spin currents, J_e and J_s, respectively. Depiction of spin injection and detection using spin dependent DOS diagrams for the (b) parallel and (c) anti-parallel magnetization states. . . 22
1.6 Layout of the non-local resistor network. The N and FM spin resistances are labeled with $R_{s,N}$ and $R_{s,FM}$, respectively. The non-local current and voltage connections are labeled as well. 24
1.7 Modeled Hanle effect field sweeps of $R_{NL,\uparrow\uparrow}$ and $R_{NL,\uparrow\downarrow}$, normalized by the magnitude of the spin valve effect, for $D = 6\,\mu\text{m}^2\,\text{ns}^{-1}$, $\tau_{s,N} = 15\,\text{ps}$, and $d = 2000\,\text{nm}$ for (a) FM contacts with fixed magnetization, (b) for FMs that rotate out-of-plane, and (c) the difference between parallel and antiparallel magnetization configurations $(R_{NL,\uparrow\uparrow} - R_{NL,\uparrow\downarrow})/\Delta R_{NL}$ with(without) FM rotation plotted in orange(blue). 32

2.1 Graphical depiction of the generalized fabrication steps of electron beam lithography, deposition, and liftoff processes. (a) A resist bi-layer is spun onto a substrate then (b) exposed using a rastered electron beam depicted by darkened resist. (c) The top layer is developed first first followed by (d) the second layer which creates an undercut. (e) Materials are then deposited and (f) the excess material is removed by lift-off of the resist. 41
2.2 General scheme for the multi-angle shadow evaporation technique. A FM material is deposited at an angle relative to the substrate followed by an N material deposited at normal incidence so that they overlap to create a lateral spin valve. 47
2.3 Non-local spin valve pattern layout for shadow evaporation (blue) and the FM projection due to deposition at an angle (red). 49
2.4 Graphical depiction of the main components of an electron beam evaporation source. 52
2.5 Optical micrographs of metal films on resist. (a) Blistering of resist due to secondary electrons. (b) Application of a magnetic field removes the secondary electron flux. 54
2.6 (a) A photograph of the sample platen and substrate with stepped growth contours. (b) An xy-plot of the calibrated contours due to intermediate positioning of the sample shutter. 55
2.7 *In situ* photographs of the transfer arm taken from the side in the orientation used for (a) transfering platens to and from the manipulator, (b) deposition of materials at non-zero angle of incidence, and (c) deposition of materials at zero angle of incedence. 56
2.8 The chuck for adjusting inplane rotation (left) and the back of the growth platen (right). 57
2.9 Diagrammatic geometry of a grazing-incidence scattering experiment. . 59
2.10 Example of grazing-incidence x-ray reflectivity data with corresponding fit for a thin film heterostructure comprised of the following layers with nominal growth thicknesses: Si / SiN (200 nm) / Co (16 nm) / Cu (100 nm) / Al (5 nm) and fitted thicknesses: Si / SiN (196 nm) / Co (15.1 nm) / Cu (94.2 nm) / Al (3 nm). 60

2.11 Geometry of a polarized neutron reflectivity experiment with the incident angle θ_i, reflected angle θ_r, and scattering wavevector q which is out-of-plane 62
2.12 Schematic representation of the scattering length densities for R^{++} and R^{--} through the depth Z of a SiN/Co/Cu multilayer. 63
2.13 Example R^{++} and R^{--} PNR data with corresponding fits for a thin film heterostructure comprised of the following layers with nominal growth thicknesses: Si / SiN (200 nm) / Co (16 nm) / Cu (100 nm) / Al (5 nm). The fitted values are Co (15.1 nm) / Cu (94.2 nm) / Al 3 nm) with a 9 Å thick FM/N interlayer with $M_s = 260\,\mathrm{emu/cm^3}$. 64
2.14 Scanning electron micrograph of a fabricated lateral spin valve with the non-local wiring configuration labeled. 67
2.15 Energy-dispersive X-ray spectra of Cu, Al, Py, and Co thin films deposited on doped Si/SiO_x. The Lα and Kα lines of the transition metals are labeled. 69
2.16 Depiction of the components of an atomic force microscope including the piezoelectric scanner, sample, AFM tip, laser, and photodiode array. . . 70
2.17 Atomic force microscope spatial height map of a Py/Cu non-local spin valve with measured geometric parameters $t_N = 202$ nm, $w_N = 260$ nm, and $d = 1970$ nm. 71
2.18 Schematic drawings of sample stage (a) above the sample position and (b) 3D rendering of the stage with dimensions labeled in inches. (c) Picture of stage held in place at end of sample probe with electrical wiring, sample rotation wires, and tension spring in place. 73
2.19 Photographs of the sample stage, electrical socket, and retaining apparatus. (a) Overhead image shows the socket, heatsink for electrical connections, and the BeCu centering spring with (b) a closeup of the rotation stage from an oblique angle. (c) A photograph of the back side of the rotation stage showing twisted-pair wiring for the sample leads, foil resistive heater, and cryogenic Hall sensor. 75
2.20 Diagram of the operational scheme of a Hall probe as a magnetic field sensor. 78

2.21 Block diagram of the low-temperature measurement system used in this work. . . . 81
3.1 Illustration of the four-terminal measurement configuration (a) used for measuring channel resistivities with an SEM micrograph (b) of a lateral device from which w_N is measured. . . . 86
3.2 SEM micrograph of a patterned nanowire used for measuring $\rho_{FM}(T)$. . . 87
3.3 Typical temperature dependent resistivites of FM thin films and patterned nanowires of Py (permalloy) and Co. . . . 88
3.4 Typical temperature dependent resistivites of the Cu channel for several t_N. . . . 88
3.5 Typical temperature-dependent resistivites of the materials used in this thesis that have been patterned into nanowires and devices. . . . 89
3.6 (a) Diagram of the three-terminal measurement configuration for interface resistance measurements also (b) labeled on a plan view SEM micrograph. . . . 92
3.7 (a) Diagram of low-temperature measurement used in this work. (b) SEM micrograph with the current source and voltmeter connections and magnetic field orientations labeled. . . . 94
3.8 Measured non-local resistance R_{NL} vs magnetic field B showing the spin-valve effect. Measurements are shown for (a) Py/Cu, (b) Co/Cu, (c) Py/Al, and (d) Co/Al at $T = 5$, 50, 100, 150, 200, 250 K, $J_e = 1\,\mathrm{mA}$, and $d \approx 220\,\mathrm{nm}$. . . . 95
3.9 Measured non-local resistance for the parallel state $R_{NL,\uparrow\uparrow}$ and antiparallel state $R_{NL,\uparrow\uparrow}$ for both the descending field sweep ($B < 0\,\mathrm{G}$) and the ascending field sweep ($B > 0\,\mathrm{G}$) as a function of temperature for (a) Py/Cu, (b) Co/Cu, (c) Py/Al, and (d) Co/Al at $J_e = 1\,\mathrm{mA}$, and $d \approx 220\,\mathrm{nm}$. . . . 96
3.10 Measured coercive fields H_c, one for each contact for both ascending and descending field sweeps, as a function of temperature for Py/Cu, Co/Cu, Py/Al, and Co/Al non-local devices with $d \approx 220\,\mathrm{nm}$. . . . 98
3.11 Dependence of the non-local detector voltage V_{NL} on the injector bias current J_e. . . . 99

3.12 Dependence of the non-local detector voltage ΔV_{NL} and resistance ΔR_{NL} on the injector bias current J_e. 100
3.13 Comparison of non-local spin valve field sweeps either immersed or not immersed in liquid He. 101
3.14 Modeled charge transport through a non-local spin valve with (a) the spatial current density and the spatial potential shown with (b) a 2.9 mV scale and (c) a 5 µV scale. 104
3.15 Non-local resistance as a function of temperature for an all-copper device measured using each of the leads attached to the detector (V^- and V^-_{Opp}). 105
3.16 Non-local resistance as a function of temperature for a Py/Cu device measured using both of the leads attached to the detector (V^- and V^-_{Opp}). 105
3.17 Measured non-local background resistance as a function of temperature for Py/Cu non-local devices with various contact separations. 107
3.18 Measured non-local background resistance as a function of temperature for Py/Cu, Co/Cu, Py/Al, and Co/Al non-local devices with $d \approx 220$ nm. 108
3.19 (a) Raw Hanle effect data of $R_{NL,\uparrow\uparrow}$ and $R_{NL,\uparrow\downarrow}$ as well as (b) the difference between parallel and antiparallel magnetization configurations ($R_{NL,\uparrow\uparrow} - R_{NL,\uparrow\downarrow}$) for a Py/Al device. 110
4.1 Temperature dependence of the difference of the non-local resistance between the parallel and anti-parallel contact magnetization states ΔR_{NL} for Py/Cu, Co/Cu, Py/Al and Co/Al devices with a source-detector separation of $d = 220 \pm 10$ nm. 112
4.2 Temperature dependence of ΔR_{NL} for (a) Py/Cu, (b) Py/Al, (c) Co/Cu, and (d) Co/Al at FM contact separations ranging from 220 nm to 2 µm. 114
4.3 ΔR_{NL} measured for Py/Cu, Co/Cu, Py/Al, and Co/Al as a function of contact separation for $t_N = 200$ nm at $T = 5$ K. 116
4.4 Temperature dependence of ΔR_{NL} measured for Py/Cu devices with $t_N = 200$ nm, 300 nm, and 400 nm at (a) $d = 220$ nm, (b) 800 nm, and (c) 2000 nm. 118
4.5 Temperature dependence of ΔR_{NL} normalized by $\Delta R_{NL}(50\,\mathrm{K})$ for Py/Cu devices for $t_N = 200$ nm, 300 nm, and 400 nm at (a) $d = 220$ nm, (b) 800 nm, and (c) 2000 nm. 119

4.6 Plots of FM injector-detector separation dependence of ΔR_{NL}, plotted on (a) linear and (b) semi-logarithmic scales. 121
4.7 Comparison of fits to the NLSV ΔR_{NL} data as a function of contact separation d using either α_{FM} (solid black) or $\lambda_{s,FM}$ (dashed red) as the additional fixed parameter. The difference between the fits, with α_{FM} or $\lambda_{s,FM}$ fixed, is shown with short blue dashes. 124
4.8 ΔR_{NL} as a function of injector-detector separation d plotted for several temperatures between 5 K and 250 K for different combinations of FM and N (a) Py/Cu, (b) Py/Al, (c) Co/Cu, and (d) Co/Al with the accompanying transparent interface model fits. 128
4.9 Free fit parameters (a) $\lambda_{s,N}(T)$ and (b) $\lambda_{s,FM}(T)$, resulting from constrained fitting of ΔR_{NL} vs. d, using the model incorporating transparent interfaces for each materials combination with $P_{Py} = 45\,\%$ and $P_{Co} = 42\,\%$ fixed and all other parameters experimentally determined. . 129
4.10 Fit parameter $\lambda_{s,FM}(T)$, resulting from fits of ΔR_{NL} vs. d using the model incorporating transparent interfaces, for each materials combination with a temperature dependent $\alpha_{FM}(T)$ specified to be the Bloch $T^{3/2}$ form. 132
4.11 Fit parameter $\alpha_{FM}(T)$, resulting from fits of ΔR_{NL} vs. d using the model of spin transport incorporating transparent interfaces for Py/Cu, Co/Cu, Py/Al, and Co/Al material combinations with a temperature independent $\lambda_{s,FM} = 4\,\text{nm}$. 133
4.12 $\lambda_{s,N}$ vs. T for Py/Cu NLSVs with $t_N = 200\,\text{nm}$, 300 nm, and 400 nm determined by fitting of $\Delta R_{NL}(T)$ vs. d with the model for transparent FM/N interfaces. 134
4.13 (a) Raw non-local Hanle effect data for parallel ($R_{NL,\uparrow\uparrow}$) and antiparallel ($R_{NL,\uparrow\downarrow}$) FM magnetization configurations as well as (b) the difference between the two ($R_{NL,\uparrow\uparrow} - R_{NL,\uparrow\downarrow}$) for a Py/Al device with $d = 1960 \pm 20\,\text{nm}$. 137
4.14 Raw Hanle effect data: (a) $R_{NL,\uparrow\uparrow}$ (black) and $R_{NL,\uparrow\downarrow}$ (red), and (b) $R_{NL,\uparrow\uparrow} - R_{NL,\uparrow\downarrow}$ as a function of $B_{\perp}$ for a non-local Co/Al device with $d = 780 \pm 20\,\text{nm}$. 139

4.15 Non-local resistance R_{NL} measured to $\pm 9\,\mathrm{T}$ with the offset at $B = 0\,\mathrm{T}$ $R_{NL,0}$ subtracted. Data from devices with contact separations $d = 220\,\mathrm{nm}$, $400\,\mathrm{nm}$, and $600\,\mathrm{nm}$ are shown at $T = 5\,\mathrm{K}$. 140

4.16 Hanle effect data $R_{NL,\uparrow\uparrow} - R_{NL,\uparrow\downarrow}$ for (a) a Py/Al lateral non-local device and (b) a Co/Al lateral non-local device, with corresponding fits to the analytic model of diffusion and relaxation in the N channel only, which includes diffusion, relaxation, and precession. 141

4.17 $\lambda_{s,Al}$ computed from fits to Hanle effect data using the model for precession, relaxation, and diffusion within the N only (open symbols). 142

4.18 $R_{NL,\uparrow\uparrow}$ data for large applied field for Co/Cu devices with the magnetic field applied out-of-plane ($B_\perp$) for (a) $d = 400\,\mathrm{nm}$, (b) $600\,\mathrm{nm}$, and (c) $800\,\mathrm{nm}$ and in-plane ($B_\parallel$) for (d) $400\,\mathrm{nm}$, (e) $600\,\mathrm{nm}$, and (f) $800\,\mathrm{nm}$, with $R_{NL}(B = 0\,\mathrm{G})$ subtracted. 144

4.19 In-plane field sweep data of R_{NL} for (a) Co/Cu and (b) Co/Al devices with $d = 400\,\mathrm{nm}$ at various temperatures and an offset $R_{NL}(B = 0\,\mathrm{G})$. . 146

4.20 Temperature-dependent Hanle effect data $R_{NL,\uparrow\uparrow}$ for a Co/Cu device with $d = 600 \pm 20\,\mathrm{nm}$ and a background of the form shown in Figure 4.18 subtracted. 147

4.21 Hanle effect data $R_{NL,\uparrow\uparrow}$ and 1D diffusion model fits at various T for a Co/Cu device with a background subtracted. 148

4.22 $\lambda_{s,Cu}$ from the fitting of Hanle effect data $R_{NL,\uparrow\uparrow}(B_\perp)$ (open triangles) for a Co/Cu device at various T with $\lambda_{s,Cu}$ from spin valve effect fitting of measurements of the same device set (closed circles). 149

4.23 Spin lifetime $\tau_{s,N}$ found by fitting Hanle effect $R_{NL,\uparrow\uparrow}$ data and spin valve effect data for Co/Cu devices. 150

4.24 Temperature dependence of the spin lifetime $\tau_{s,N}$ found by fitting Hanle effect. $R_{NL,\uparrow\uparrow} - R_{NL,\uparrow\downarrow}$ and spin valve effect data for Al lateral non-local devices. 151

5.1 The simulation geometry of a non-local spin valve. Boundaries shaded green(red) mark the current injection(extraction) surface with spin-up and spin-down electrons shown with representative vectors depicting random steps, some of which scatter specularly from surfaces. 156

5.2 (a) Graphical representation of the three-dimensional linear FM-N-FM simulation geometry with (b) the resulting shift $\delta\mu$ due to the simulated charge current J_e. 159
5.3 Simulated spin-dependent chemical potentials $\mu_\uparrow$ and $\mu_\downarrow$ and the analytical solution for a FM-N-FM structure with the FMs in the (a) parallel ($\uparrow\uparrow$) and (b) antiparallel ($\uparrow\downarrow$) states. 161
5.4 The simulated $\lambda_{s,N}$ for various T and t_N as a function of the ratio of surface to bulk spin-flip scattering probabilities $p_{\uparrow\downarrow,Sur}/p_{\uparrow\downarrow,Bulk}$. 163
5.5 Temperature dependence of (a) the simulated and (b) measured ΔR_{NL} at a source-detector separation of $d \approx 220$ nm. 164
5.6 (a) Simulated temperature dependence of the effective $\lambda_{s,N}$ for devices with each of the material combinations Py/Cu, Co/Cu, Py/Al, and Co/Al for $t_N = 200$ nm for comparison with the measured $\lambda_{s,N}$ shown in panel (b). 165
5.7 Temperature dependence of the simulated ΔR_{NL} at source-detector separations of (a) 220, (b) 800, and (c) 2000 nm for $t_N = 200$, 300, and400 nm. The corresponding experimental data are shown in panels (d), (e), and (f).167
5.8 Temperature dependence of (a) the simulated and (b) measured $\lambda_{s,N}$ at $t_N = 200$, 300, and400 nm for Py/Cu devices and $t_N = 200$ nm for Co/Cu devices. 168
5.9 (a) $R_{NL,\uparrow\uparrow} - R_{NL,\uparrow\downarrow}$ Hanle effect data for Py/Al devices (solid symbols) with the fit without FMs or surface relaxation (red) as well as a modeled curve using $\lambda_{s,N}$ fixed from spin valve fitting (blue dashed). Panel (b) shows the data with the results of Monte Carlo simulated spin diffusion including FMs and surface relaxation. 169
5.10 Spin diffusion length for Py/Al and Co/Al devices found in three different ways: spin valve effect vs contact separation (closed symbols), Hanle effect fits using channel diffusion and precession only (open symbols), and the interpretation of data using simulated Hanle effect including surface relaxation and diffusive FMs (half-filled symbols). 171

6.1 Calculated ΔR_{NL} vs. T for the tunnel barrier model as well as the case of transparent interfaces using the measured $\rho(T)$ shown in Figure 3.5, along with $\lambda_{s,N}(5\,\mathrm{K}) = 400\,\mathrm{nm}$, $\lambda_{s,FM} = 5\,\mathrm{nm}$, and $P_{FM} = 45\%$. 173
6.2 (a) T_c and (b) M_s (red squares) as a function of Cu composition x. The blue lines are fits to values reported in the literature [128, 129]. 175
6.3 Predicted temperature dependence of ΔR_{NL} for a CuNi/Cu lateral NLSV with $d = 220\,\mathrm{nm}$. 176
6.4 Temperature dependence of ρ_{FM} of CoS_2 for $t_{FM} = 25\,\mathrm{nm}$ thin films and $w_{FM} = 200\,\mathrm{nm}$ nanowires. 178
6.5 SEM micrograph of a CoS_2/Al NLSV. The horizontal Al channel, vertical CoS_2 FM contacts, and the Ti/Al bonding pad vias, with clusters of sulfur on the surface, are labeled. 179
6.6 Four-terminal measurements of a Cu channel using Co electrodes. Curves are shown for an unannealed device and annealed at $T = 250\,^{\circ}\mathrm{C}$ and $T = 350\,^{\circ}\mathrm{C}$ for 2 hour. 182
6.7 The measured ΔR_{NL} vs. T for a Co/Cu device with $d = 220\,\mathrm{nm}$, $t_N = 200\,\mathrm{nm}$, and $t_{FM} = 60\,\mathrm{nm}$. Curves are shown for an unannealed device and after annealing at $T = 250\,^{\circ}\mathrm{C}$ and $T = 350\,^{\circ}\mathrm{C}$ for 2 hours. 183
B.1 Depiction of general steps of electron beam lithography liftoff process. . 209
B.2 Resist thickness as a function of angular spin speed for PMMA-A6 and PMGI-SF9 measured on $20\,\mathrm{mm} \times 20\,\mathrm{mm}$ substrates by profilometry. . . 211
B.3 Layout of a non-local spin valve pattern for shadow evaporation with the N channel horizontal along the x-axis and the FM contacts vertical along the y-axis each flaring out to larger regions interconnecting bonding pads. 217
B.4 Layout of a non-local spin valve for shadow evaporation including the projection of the FM deposited at an angle (red) and the area to be patterned (blue). 218
B.5 Electron exposure dose for lateral non-local spin valve structures with higher dosages shown as warm colors, lower dose as colder. 220
C.1 Photograph of the load lock attached to the system. 226
C.2 General layout of the main components of an electron beam evaporation source. 232

C.3 Photographs of the electron beam evaporator used in this thesis (a) from the side and (b) from above. Two of the four in-line source pockets in the copper hearth are indicated with arrows along with the opening allowing the high-energy electron beam originating from below the hearth to be bent by a magnetic field to be incident on the source material. 233
C.4 Optical micrographs of metal films on resist. (a) Blistering of resist due to secondary electrons. (b) Application of a magnetic field removes the secondary electron flux. 235
C.5 Cross sectional schematic of a resistively heated thermal deposition cell taken from the product manual [144]. 236
C.6 Photos of resistive heating thermal evaporators. 238
C.7 Photographs of two Quartz crystal thickness monitoring micro-balances, located (a) above the main thermal source and (b) near the sample stage. 240
C.8 Growth contours due to intermediate positioning of the sample shutter with an xy-plot of the contours. 243
D.1 Three-dimensional rendering of the design for the thermal source, mount, and feedthrough. The 2³/4" ConFlat flange (grey), stainless supports (blue), power connectors (yellow), and the Radak evaporator (red) are shown. 246
D.2 Cross sectional schematic of a resistively heated thermal deposition Radak II source taken from the product manual [144]. 247
D.3 A top-view schematic of the design for the thermal source, mount, and feedthrough. The stainless supports (blue) are shown with various dimensions labeled in inches. 249
D.4 A side-view schematic of the design for the thermal source, mount, and feedthrough. The stainless supports (blue) are shown with the thicknesses of the bridge support and rods labeled as well as the offsets from the center of the flange. 250
D.5 A side-view schematic (perpendicular to the view shown in Figure D.4) of the design for the thermal source, mount, and feedthrough. The stainless supports (blue) are shown with the lengths of each section extending from the flange face into the interior of the vacuum system. 251

E.1 Schematics of complete multi sample electrical transport probe with sample rotation stage. Three-dimensional schematics of the rotator probe shown from different viewing angles, (b) from the side and (c) front as loaded into the cryostat. The rendering in panel (d) is the same as panel (a) except that it is transparent to see internal structure of the parts. . 253
E.2 Schematics of the main stainless rod and NW-16 feedthrough attached to the top NW-40 flange which form the backbone of the rotator probe. 254
E.3 Design schematic of the five radiation baffles that are along the probe. Dimensions are given in inches. 256
E.4 Schematics of sample rotation stage. 257
E.5 Schematics of sample rotation stage retained by support block. 258
E.6 Photographs of (a) the sample rotation stage retained by the support block, the (b) front side of the rotator probe sample package mount, and (c) back views of the rotation stage foil heater and Hall sensor. 259
E.7 Photographs of packages for mounting and wirebonding samples to be loaded into the cryostat for transport measurements. 262
E.8 Sample Hall voltage from sensor on rotation probe plotted as a function of the linear feedthrough position in order to align the sample angle under various conditions. 265
E.9 Schematic diagram of cryostat. 267

Chapter 1

Introduction

The work described in this thesis aims to understand the injection, transport, and relaxation of non-equilibrium electron spins in metallic lateral devices. The focus is on the regime of diffusive transport in devices patterned on $\sim 100\,\text{nm}$ length scales. Probing this regime is accomplished via measurements of spin transport in lateral devices in a non-local configuration. The non-local configuration is used to generate and measure pure spin currents, enabling us to probe the influence of diffusive ferromagetic contacts used for the injection and detection of the non-equilibrium spin accumulation. Relaxation of non-equilibrium spins in the bulk and at surfaces of the normal metal transport channel is also examined. Experimental data, analysis, and simulations addressing these effects will be presented throughout this thesis. The chapters contained in this thesis are organized as follows:

- Chapter 1 briefly presents the history and scientific background of spintronics, focusing on the theory of spin transport in metals.
- Chapter 2 reviews the experimental techniques and methods required to conduct the experiments contained in this thesis. Appendices B, C, D, and E contain additional information and background on these topics.
- Chapter 3 reports on the charge- and spin-dependent transport data taken using lateral non-local spin valves and other nanostructures.
- Chapter 4 presents analysis of spin transport measurements of metallic non-local

spin valves with low-resistance ferromagnetic contacts.

- Chapter 5 presents numerical simulations used to model the experimental measurements of spin-dependent transport in three-dimensional lateral structures.
- Chapter 6 lays out work in progress which aims to further understand spin transport in metallic lateral spin valves.
- Chapter 7 presents a concluding discussion of the experiments and analyses presented in this thesis.

1.1 Introduction to Spintronics

Electronics have been central to the development of new technologies, infrastructure, and research during the last century. The discovery of the electron and subsequent ability to manipulate electron charges in condensed matter structures via the Coulomb (electric) and Lorentz (magnetic) forces have led to the development of a plethora of electronic devices with various functionalities. The subsequent discovery of the associated spin of the electron has provided another degree of freedom to manipulate. The research field in which the charge and spin of the electron is utilized in magneto-electronic devices has been dubbed 'spintronics'.

Spin-dependent transport in materials and at interfaces is at the heart of phenomena such as giant magnetoresistance (GMR) [1, 2], tunneling magnetoresistance (TMR) [3], electrical spin injection and detection in metals [4] and semiconductors [5], and, more recently, a new class of spin-based thermoelectric effects [6, 7]. These effects have enabled, and promise to further enhance, the development of spin-based functionality for devices such as hard disk read heads, magnetic memory and data storage [8], and other technological devices.

Magneto-transport phenomena such as anisotropic magnetoresistance (AMR), GMR, and TMR have been utilized in several consumer technologies, especially high-sensitivity magnetic field sensors. These sensors are widely used and the increasing demands of magnetic data storage technologies drive forward technological research and development efforts to shrink and improve these devices. This began with the adaptation of AMR sensors into hard disk read heads in the early 1990s, which led to increased storage

densities [9]. The adoption of GMR sensors in the years leading up to 2000, followed by the emergence of TMR-based sensors in 2005, have led to further rapid increases in storage densities [10].

New methods to reduce the dimensions of the data elements used in hard disk storage media are further pushing the requirements of read head dimensions and sensitivities. Perpendicular media, with magnetization out-of-plane rather than in-plane, has reduced magnetic element sizes. Bit-patterned media, rather than continuous magnetic media, promise to further reduce magnetic bit dimensions. As the relevant storage media dimensions are reduced, a corresponding reduction of the read sensor dimensions is required. The reduction of the dimensions of TMR read sensors leads to increased sensor resistance which can reach a critical resistance making implementation in technological devices no longer possible. Although barriers employed in TMR read sensors have been thinned to reduce the junction resistance, GMR-type read heads with low-resistance FM/N interfaces provide a possible solution to reach the required nanoscale read heads. Understanding the transport behavior of GMR structures with decreased dimensions will require understanding not only the detailed role of the interfaces but also the contribution of material surfaces and microstructure to the spin-transport properties.

1.1.1 Brief Introduction to Spin-Dependent Transport Experiments

Charge carrier transport which depends on the spin degree of freedom is referred to as spin-dependent transport. The first measurement of spin-dependent transport was the demonstration of AMR, in which the measured resistance of a ferromagnetic material depends on the orientation of the charge current $\vec{J_e}$ relative to the sample magnetization $\vec{M}$. This was first observed in 1856 by William Thomson, later known as Lord Kelvin. This effect is a manifestation of spin-dependent carrier scattering in ferromagnetic materials.

Mott was the first to describe several unique transport properties of transition metals and alloys [11, 12]. The electrons in a ferromagnet are described as either majority or minority spin, with a magnetic moment parallel or antiparallel to the magnetization. Mott expressed the charge transport through a material as the sum of two independent channels, one for each of the two spin orientations, resulting in spin-polarized current when the currents in each channel are not equal. This basic two-current model was later

updated by Fert and Campbell [13]. It was further modified by Valet and Fert to understand spin-transport and magnetoresistive phenomena in magnetic heterostructures [14]. The two-channel model for spin transport will be discussed in greater detail in §1.2.

Transport experiments conducted by Meservey and Tedrow [15] in FM / insulator / superconductor devices were used to study the polarization of the tunneling current into the superconductor. Meservey and Tedrow used a simple model based on the density of states (DOS), which depends on the polarization of the ferromagnetic material. This was similar to the model later used by Jullière to examine the change in conductance between the parallel ($\uparrow\uparrow$) and antiparallel ($\uparrow\downarrow$) magnetization states of FM / insulator / FM junctions [3]. Jullière explained the tunneling conductance in terms of the tunneling current within each spin band as determined by the spin-resolved DOS of each material.

Jullière's model describes a spin valve effect, wherein the total resistance of FM / spacer / FM junctions change as a function of the relative orientation of the magnetizations of the FM layers. The magnetoresistance ratio is often used to characterize device performance. For the case of TMR this is given by

$$\frac{R_{\uparrow\downarrow} - R_{\uparrow\uparrow}}{R_{\uparrow\uparrow}} = \frac{2P_{FM1}P_{FM2}}{1 - P_{FM1}P_{FM2}}, \tag{1.1}$$

where $R_{\uparrow\uparrow(\uparrow\downarrow)}$ the resistance of the parallel(antiparallel) magnetization states and P_{FM1} and P_{FM2} are the polarization of the FM layers. The spin-valve effect has been demonstrated in multilayer structures with both ohmic junctions, displaying giant magnetoresistance [1, 2], and tunnel junctions, exhibiting tunneling magnetoresistance [3]. These effects have been utilized extensively in magnetic field sensors in technological applications and form the basis for understanding lateral spin valves with an extended channel forming the spacer between FM electrodes. This is explained further in §1.2.10.

Two primary types of GMR structures have been used and are classified according to whether the current flows in-plane (CIP-GMR), parallel to the FM interfaces, or perpendicular to the plane (CPP-GMR), perpendicular to the interfaces. Although the CIP geometry is frequently used in technological applications, the CPP geometry is more straightforward to understand and model theoretically. Fitting CPP-GMR models, described in §1.2.9, to experimental data allows for the determination of spin-dependent parameters. The ferromagnetic spin polarization and the spin relaxation lengths of the

non-equilibrium carriers in the ferromagnetic and non-magnetic layers can be determined. There remain, however, questions about the reliability of these parameters in various device geometries, especially for structures with dimensions smaller than the corresponding spin relaxation lengths. These spin relaxation lengths are of the order 100 nm in non-magnetic metals and 10 nm in the ferromagnetic materials.

The aforementioned spin-transport phenomena depend strongly on the polarization P_{FM} of the FM materials. These effects generally rely on one factor of the polarization for the source and one for the detector. As a result, the creation of materials with large spin polarizations would enhance the performance of TMR, GMR, spin-transfer torque, and electrical spin-injection devices. Highly spin-polarized materials have been the subject of extensive research efforts. The ideal case of 100% polarization, known as a half-metallic ferromagnet, has been researched in several material systems. Some examples include: CrO_2 [16], Heusler alloys [17], Perovskite oxides [18], and $Co_xFe_{1-x}S_2$ [19]. Although high polarizations have been measured, the thermodynamic stability and Curie temperature of many of these materials are unsuitable for device applications. Despite this, they continue to be a rich research area due to fundamental science available in these systems.

The lateral device geometry, utilized extensively in this work, is a flexible experimental system for testing and measuring spin injection, detection, and relaxation in patterned metals. In this work the non-local lateral device geometry has been employed. In the non-local configuration a charge current is used to generate a spin current which is separated from the net charge current. The pure spin current is then measured useing a second FM contact. The measurement of spin transport in the non-local configuration is discussed further in §1.2.10. The electrical injection of spins from a FM was proposed in 1976 by Aronov [20] and later the detection of spins, again using a FM, by Silsbee in 1980 [21]. The first experimental demonstration of electrical injection and detection in metals was made by Johnson and Silsbee in 1985 [22]. They used permalloy ferromagnetic injectors and detectors with an aluminum transport channel which produced small voltage signals $\sim 10\,\mathrm{pV}$, requiring measurement using a SQUID. The ability to create smaller devices allowed Jedema *et al.* to fabricate sub-micron devices in the lateral geometry that produced much larger signals $\sim 1\,\mu\mathrm{V}$ with permalloy ferromagnetic contacts with a copper channel [23]. Several experiments in metallic systems have since

followed, the results of which are reviewed in §1.3.

There are, however, constraints on the materials that can be investigated in lateral spin-injection experiments. Spin injection from a ferromagnetic metal into a high-mobility semiconductor through low-resistance contacts is unachievable due to the so-called “conductivity mismatch” problem [24]. This has been overcome with the insertion of a tunnel barrier [25], allowing spin injection and detection through tunnel junctions to be studied in the lateral geometry. Diffusive interfaces, however, offer different challenges. Metals typically have shorter spin diffusion lengths than semiconductors and require device patterning on sub-micron length scales. Due to the similarity of the spin diffusion lengths and the conductivities of metallic ferromagnets and non-magnetic metals, spin injection can be achieved using low-resistance interfaces.

1.2 Spin Transport Fundamentals

1.2.1 Transport in Metals

The transport of electrons in metals has been described using a variety of models since their discovery by J. J. Thomson in 1897. As described by Drude [26, 27], the first models treated charge transport as a kinetic gas of electrons with statistical distributions describing the behavior. The theory was later updated by Boltzmann. The electrons in a metal can be affected both by external fields and by concentration gradients. The electrons also scatter, for example from phonons and defects, losing momentum and driving the system towards equilibrium. The effects of fields and concentration gradients are opposed by scattering and result in steady-state transport. This problem is generally treated using the Boltzmann equation and many texts discuss this topic, including References [28–32]. We introduce the Boltzmann equation here in the context of charge transport, then extend it to justify the macroscopic equations for spin diffusion.

The charge transport in materials is generally given by

$$\vec{j} = \sigma \vec{E} + eD\nabla\delta n, \tag{1.2}$$

where $\vec{j}$ is the current density, σ is the conductivity, $\vec{E}$ is the electric field, e is the elementary charge, D is the diffusion constant, and δn is the non-equilibrium density of carriers. The first term on the right hand side of Equation 1.2 is the well-known form

of Ohm's law $\vec{j} = \sigma\vec{E}$. The second term is the contribution that describes the diffusion of non-equilibrium carriers.

First described by Mott [11, 12, 33], the current flowing can be separated into the contributions from each of two spin sub-bands, one for spin up ($\uparrow$) and one for spin down ($\downarrow$) electrons. The total charge current J_e and spin current J_s flowing through the system in the two band model can be expressed as,

$$J_e = -\left(J_\uparrow + J_\downarrow\right), \tag{1.3}$$

$$J_s = \frac{\hbar}{2e}\left(J_\uparrow - J_\downarrow\right), \tag{1.4}$$

where $J_\uparrow$ and $J_\downarrow$ are the spin-up and -down currents, respectively. Equation 1.2 can be written for each of the spin-bands, spin up ($\uparrow$) and spin down ($\downarrow$),

$$\vec{j_\uparrow} = \sigma_\uparrow\vec{E} + eD_\uparrow\nabla\delta n_\uparrow, \tag{1.5}$$

$$\vec{j_\downarrow} = \sigma_\downarrow\vec{E} + eD_\downarrow\nabla\delta n_\downarrow, \tag{1.6}$$

where $\vec{j}_{\uparrow(\downarrow)}$ is the spin up(down) current density, $\sigma_{\uparrow(\downarrow)}$ is the spin up(down) conductivity, $D_{\uparrow(\downarrow)}$ is the spin up(down) diffusion constant, and $\delta n_{\uparrow(\downarrow)}$ is the spin up(down) non-equilibrium density of carriers. The spin-dependent transport constants $\sigma_{\uparrow(\downarrow)}$ and $D_{\uparrow(\downarrow)}$ in Equations 1.5 – 1.6 depend on the spin up(down) Density of States (DOS) $g_{\uparrow(\downarrow)}$ at the Fermi energy ε_F. For normal metals the properties of the spin-up and down bands are equal, i.e. $g_\uparrow(\varepsilon_F) = g_\downarrow(\varepsilon_F)$, $\sigma_\uparrow = \sigma_\downarrow$, and $D_\uparrow = D_\downarrow$. This is not the case in ferromagnetic metals.

1.2.2 Ferromagnetism and Spin Polarization

Thus far, we have only been concerned with non-(ferro)magnetic materials, which have been described in terms of transport properties that are independent of spin orientation. This is not the case for ferromagnetic materials, in which the symmetry of the up and down spins has been broken. Although a brief discussion of ferromagnetism follows, there are many texts on the subject, including References [34–36].

Magnetism arises from the spin of the electron. The ordering of the spins in a material is determined by several factors, and one must necessarily consider quantum mechanics. Since electrons are fermions and obey the Pauli exclusion principle, two

electrons cannot occupy the same quantum state. This requires the wave function of the system be antisymmetric under exchange of any two electrons. As a result the symmetry of the spin part of the wave function influences the spatial wavefunction and changes the Coulomb energy of the system. The difference in energy between the symmetric and antisymmetric spin part of the wavefunction is referred to as the exchange energy. For some materials, the total energy is minimized by particular configurations of the electron spins which have net spin, giving rise to ferromagnetism.

Ferromagnetism occurs in the transition metals Fe, Ni, and Co as well as some other materials. Each of these transition metals are used for their ferromagnetic properties in this work. It is noteworthy that the next element in the periodic table, Cu, is not ferromagnetic as the 3d shell is completely filled with the addition of one more electron. Cu is also used in this work as a non-magnetic transport channel.

The electrons of transition metal ferromagnets can be described in terms of bands with the 3s and 3d bands partially filled. The 3d bands for spin-up and -down split by the exchange interaction. The result of the exchange splitting of the up and down bands appears as an energy shift of the spin-resolved DOS. This is shown in Figure 1.1, with the exchange-split d-bands and a net imbalance of occupied states below ϵ_F.

Due to the broken symmetry between the spin bands resulting from the exchange splitting $g_\uparrow \neq g_\downarrow$, so the spin-dependent transport properties for each spin band are unequal: $\sigma_\uparrow \neq \sigma_\downarrow$, and $D_\uparrow \neq D_\downarrow$. Since the transport properties depend on $g_\uparrow(\epsilon_F)$ and $g_\downarrow(\epsilon_F)$ it is useful to define a polarization at the Fermi level. The polarization of the electrons is defined as,

$$P_{FM} \equiv \frac{g_\uparrow(\epsilon_F) - g_\downarrow(\epsilon_F)}{g_\uparrow(\epsilon_F) + g_\downarrow(\epsilon_F)}, \tag{1.7}$$

at $\varepsilon = \varepsilon_F$. The current polarization flowing through the FM material can be expressed in terms of the conductivities of the spin up ($\sigma_{\uparrow,FM}$) and spin down channels ($\sigma_{\downarrow,FM}$). The polarization of the current is then given by:

$$\alpha_{FM} = \frac{\sigma_{\uparrow,FM} - \sigma_{\downarrow,FM}}{\sigma_{\uparrow,FM} + \sigma_{\downarrow,FM}}. \tag{1.8}$$

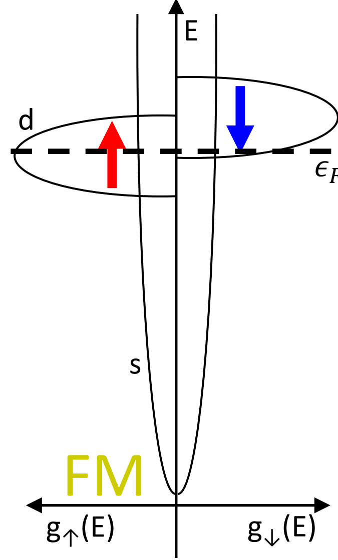

Figure 1.1: Generic representation of a ferromagnetic density of states which is separately shown for the spin-up (left) and spin-down (right) bands composed of the symmetric s-band and exchange-split d-bands.

1.2.3 Boltzmann Equation

The Boltzmann equation describes the steady state condition for the distribution function $f(\vec{r},\vec{k},t)$ which gives the probability of finding an electron at a position $\vec{r}$, momentum $\hbar\vec{k}$, and at time t. So the sum of the contributions due to diffusion, fields, and collisions total to zero:

$$\left.\frac{\partial f(\vec{r},\vec{k},t)}{\partial t}\right|_{\text{diffusion}} + \left.\frac{\partial f(\vec{r},\vec{k},t)}{\partial t}\right|_{\text{fields}} + \left.\frac{\partial f(\vec{r},\vec{k},t)}{\partial t}\right|_{\text{collisions}} = 0. \tag{1.9}$$

The diffusion process term can be rewritten as,

$$\left.\frac{\partial f(\vec{r},\vec{k},t)}{\partial t}\right|_{\text{diffusion}} = -\vec{v}(\vec{k})\frac{\partial f(\vec{r},\vec{k},t)}{\partial \vec{r}}, \tag{1.10}$$

and the term for the fields may be written as,

$$\left.\frac{\partial f(\vec{r},\vec{k},t)}{\partial t}\right|_{\text{fields}} = -\frac{\vec{k}}{t}\frac{\partial f(\vec{r},\vec{k},t)}{\partial \vec{k}}, \tag{1.11}$$

to give the Boltzmann equation:

$$\frac{\partial f(\vec{r},\vec{k},t)}{\partial t} + \vec{v}(\vec{k})\frac{\partial f(\vec{r},\vec{k},t)}{\partial \vec{r}} + \frac{\vec{k}}{t}\frac{\partial f(\vec{r},\vec{k},t)}{\partial \vec{k}} = \left.\frac{\partial f(\vec{r},\vec{k},t)}{\partial t}\right|_{\text{collisions}}. \tag{1.12}$$

To solve the general equation, two approximations are made. The first is that the equilibrium distribution f_0 is perturbed only a small amount amount away from equilibrium f_1 such that the distribution can be linearized and written as:

$$f(\vec{r},\vec{k}) = f_0 + f_1(\vec{r},\vec{k},t). \tag{1.13}$$

The second assumption is the relaxation-time approximation,

$$\left.\frac{\partial f}{\partial t}\right|_{\text{collisions}} = -\frac{f - f_0}{\tau_p} = \frac{-f_1}{\tau_p}, \tag{1.14}$$

where τ_p is the relaxation time that characterizes the time required for the distribution to return to equilibrium with no gradients or applied fields. That is, the non-equilibrium distribution would decay to zero following:

$$-\frac{\partial f_1}{\partial t} = \frac{f_1}{\tau_p}. \tag{1.15}$$

Further, the equilibrium distribution for the electrons is the Fermi-Dirac distribution with the form:

$$f_0(\varepsilon) = \frac{1}{1 + e^{(\varepsilon - \varepsilon_F)/k_B T}}, \tag{1.16}$$

where ε is the energy of a level, ε_F is the Fermi energy, k_B is the Boltzmann constant, and T is the temperature.

Quantities such as the electrical conductivity can be expressed. Starting from the current density,

$$\vec{j_e} = \int e\vec{v}f\mathrm{d}\vec{k}, \tag{1.17}$$

where $\vec{v}$ is the velocity, and $\vec{k}$ is the reciprocal wave vector. The integral of the equilibrium term f_0 is by definition zero. Using the standard form of $\vec{j_e} = \vec{\sigma} \cdot \vec{E}$ allows the conductivity to be written for an isotropic medium as:

$$\sigma = \frac{1}{4\pi^3}\frac{e^2}{3\hbar}\int_{\text{Fermi surface}} \lambda \, d^2S, \tag{1.18}$$

with the *mean free path* defined as:

$$\lambda = \tau_p v. \tag{1.19}$$

Since the number density of electrons is $n = (1/4\pi^3)(4\pi/3)k_F^3$ and the momentum can be expressed $p = mv_F = \hbar k_F$, then the conductivity can be written as

$$\sigma = \frac{ne^2\tau_p}{m} = \frac{1}{\rho}. \tag{1.20}$$

The momentum mean free path can be written in terms of ρ,

$$\lambda_p = \tau_p v_F = \frac{mv_F}{\rho ne^2}. \tag{1.21}$$

The conductivity can be written in terms of the diffusion constant D with the Einstein relation,

$$\sigma = e^2 g(\varepsilon_F)D, \tag{1.22}$$

where $g(\epsilon_F)$ is the DOS at the Fermi energy of the material. The transport theory discussed so far will be adapted to describe spin transport in §1.2.4 in terms of spin-dependent parameters.

1.2.4 Spin-Dependent Boltzmann Equation

The Boltzmann equation can also be written to describe spin transport. The following is a summary of work by Valet and Fert [14], who showed that a macroscopic spin-diffusion model arises from the Boltzmann Equation for the case where the spin diffusion length is much larger than the mean free path. The linearized Boltzmann Equation can be written for the distribution function $f_s(r, \vec{v})$,

$$\begin{aligned} v_r \frac{\partial f_s}{\partial r}(r, \vec{v}) - eE(r)v_r \frac{\partial f_0}{\partial \varepsilon}(v) = \\ \int d^3v' \delta[\varepsilon(v') - \varepsilon(v)] P_p[r, \varepsilon(v)][f_s(r, \vec{v}') - f_s(r, \vec{v})] + \\ + \int d^3v' \delta[\varepsilon(v') - \varepsilon(v)] P_s[r, \varepsilon(v)][f_{-s}(r, \vec{v}') - f_s(r, \vec{v})], \end{aligned} \tag{1.23}$$

where $\varepsilon(v)$ is the energy of the electrons, $E(r) = -\partial V(r)/\partial r$ is the local electric field, and $P_p(r, \varepsilon)$ and $P_s(r, \varepsilon)$ are the spin-conserving and spin-flip transition probabilities, respectively. These probabilities are assumed to be isotropic, so momentum is not

transfered for spin-flip scattering. The distribution function $f_s(r,\vec{v})$ is written as the sum of the Fermi-Dirac distribution, Equation 1.16, and a small perturbation,

$$f_s(r,\vec{v}) = f_0(v) + \frac{\partial f_0}{\partial \varepsilon}\left([\mu_0 - \mu_s(r)] + f_{sa}(r,\vec{v})\right), \tag{1.24}$$

where μ_0 is the equilibrium chemical potential, $\mu_s(r)$ is the local spin-dependent chemical potential for spin s, and $\partial f_0/\partial\varepsilon\ f_{s,a}$ is the anisotropic part of the perturbation to the electron distribution. Inserting Equation 1.24 into Equation 1.23 and keeping only the linear terms, it becomes,

$$v_r\frac{\partial f_{s,a}}{\partial r}(r,\vec{v}) + \left(\frac{1}{\tau_p}+\frac{1}{\tau_s}\right)f_{s,a}(r,\vec{v}) = \left(v_r\frac{\partial\bar{\mu}_s}{\partial r}(r) + \frac{\bar{\mu}_s(z)-\bar{\mu}_{-s}(z)}{\tau_s}\right), \tag{1.25}$$

where $\bar{\mu}_s(r) = \mu_s(r) - eV(r)$ is the total electrochemical potential for spin s. The probabilities P_p and P_s give rise to the lifetimes τ_p and τ_s, respectively.

Valet and Fert showed that the vertical device structure, that of CPP-GMR devices, is described by a series of differential equations. Given here are the first two equations in the series:

$$\frac{\partial f_{s,a}^{(1)}}{\partial r} = \lambda_p\frac{\bar{\mu}_s-\bar{\mu}_{-s}}{\lambda_s^2}, \tag{1.26}$$

$$\frac{2}{5}\frac{\partial f_{s,a}^{(2)}}{\partial r} - \frac{\partial\bar{\mu}_s}{\partial r} = -\frac{f_{s,a}^{(1)}}{\lambda_p}, \tag{1.27}$$

where they have used,

$$\lambda_p = v_F\left(\frac{1}{\tau_p}+\frac{1}{\tau_s}\right), \tag{1.28}$$

$$\lambda_s = \sqrt{\frac{1}{3}(v_F\lambda_p)\tau_s} = \sqrt{D_s\tau_s}. \tag{1.29}$$

Valet-Fert showed the identity, $J_s = f_{s,a}^{(1)}/\rho_s e\lambda_p$ and therefore,

$$\rho_s e\frac{\partial J_s}{\partial r} = \frac{\bar{\mu}_s-\bar{\mu}_{-s}}{\lambda_s^2}, \tag{1.30}$$

$$\frac{\partial\bar{\mu}_s}{\partial r} = e\rho_s J_s + \frac{2}{5}\frac{\partial f_{s,a}^{(2)}}{\partial r}, \tag{1.31}$$

can be written. Valet and Fert showed that the $\partial f_{s,a}^{(2)}/\partial r$ term in Equation 1.31 will be proportional to $\lambda_p(\partial J_s/\partial r)$ which is approximately $J\lambda_p/\lambda_s$. For metals $\lambda_p \ll \lambda_s$ which leads to this term going to zero. As a consequence the $\partial f_{s,a}^{(2)}/\partial r$ term does not appear in Equation 1.31 for metals. Equations 1.30 and 1.31 are the macroscopic equations used in §1.2.5 to model diffusive spin transport.

1.2.5 Macroscopic Equations Describing Transport in Metals

The macroscopic diffusion equations derived in §1.2.4 are used to describe the spin transport in materials in terms of the chemical potential μ. The equilibrium carrier densities n_0 and currents j_e through materials and heterostructures have been successfully described by solving for the position dependent μ. Here $\mu = 0$ at the Fermi energy of a material, which can be shifted by connection to an external potential V_e. By definition the energy required to add a carrier to the system is given by μ, therefore the non-equilibrium carrier density δn is related to μ by the DOS at the Fermi Level $g(\epsilon_F)$.

The non-equilibrium polarization of the spin current, which relaxes towards equilibrium, is not conserved. In the case of the two spin-band model, the carrier spins may be flipped from one spin-band to the other. The timescale associated with flipping from the spin-up to -down bands is $\tau_{\uparrow\downarrow}$, and -down to -up $\tau_{\downarrow\uparrow}$. The spin-dependent continuity equations become,

$$\frac{\partial n_\uparrow}{\partial t} = -\frac{1}{e}\nabla J_\uparrow - \frac{n_\uparrow}{\tau_{\uparrow\downarrow}} + \frac{n_\downarrow}{\tau_{\downarrow\uparrow}}, \tag{1.32}$$

$$\frac{\partial n_\downarrow}{\partial t} = -\frac{1}{e}\nabla J_\downarrow - \frac{n_\downarrow}{\tau_{\downarrow\uparrow}} + \frac{n_\uparrow}{\tau_{\uparrow\downarrow}}. \tag{1.33}$$

Detailed balance,

$$\frac{g_\uparrow(\epsilon_F)}{\tau_{\uparrow\downarrow}} = \frac{g_\downarrow(\epsilon_F)}{\tau_{\downarrow\uparrow}}, \tag{1.34}$$

must be satisfied for the spin-flip times and spin-dependent DOS at ϵ_F. In this case the diffusion time scale is τ_p, with the density of each band governed by the relevant spin-flip time, $\tau_{\uparrow\downarrow}$ or $\tau_{\downarrow\uparrow}$. In the case of non-magnetic materials, $\tau_{\uparrow\downarrow} = \tau_{\downarrow\uparrow}$, and typically $\tau_{\uparrow\downarrow} \gg \tau_p$. In contrast, for the case of FMs $\tau_{\uparrow\downarrow} \neq \tau_{\downarrow\uparrow}$. Both lifetimes can be short, similar to the momentum scattering times.

Substituting the current densities in each sub-band ,

$$j_\uparrow = \frac{\sigma_\uparrow}{e}\frac{\partial \mu_\uparrow}{\partial x}, \tag{1.35}$$

$$j_\downarrow = \frac{\sigma_\downarrow}{e}\frac{\partial \mu_\downarrow}{\partial x}, \tag{1.36}$$

into Equations 1.32 - 1.33 with the average diffusion constant,

$$D = \frac{D_\uparrow D_\downarrow \left(g_\uparrow\left(\epsilon_F\right) + g_\downarrow\left(\epsilon_F\right)\right)}{\left(g_\uparrow\left(\epsilon_F\right) D_\uparrow + g_\downarrow\left(\epsilon_F\right) D_\downarrow\right)}, \tag{1.37}$$

and the average spin-flip time,

$$\frac{1}{\tau_s} = \frac{1}{\tau_{\uparrow\downarrow}} + \frac{1}{\tau_{\downarrow\uparrow}}, \tag{1.38}$$

yields a spin-dependent diffusion equation:

$$D\frac{\partial^2 (\mu_\uparrow - \mu_\downarrow)}{\partial x^2} = \frac{\mu_\uparrow - \mu_\downarrow}{\tau_s}. \tag{1.39}$$

Similar to the mean free path λ_p that characterizes the momentum scattering length, the spin diffusion length,

$$\lambda_s = \sqrt{D\tau_s}\,, \tag{1.40}$$

characterizes spin diffusion that follows Equation 1.39. The spin diffusion length is of utmost interest in characterizing the spin transport properties of materials. Throughout the text the subscript will be modified to indicate the material being described, $\lambda_{s,N}$ and $\lambda_{s,FM}$, for the N and FM materials, respectively.

The Einstein relation, Equation 1.22, is valid for transport within each spin band with a spin-dependent conductivity, DOS, and diffusion constant:

$$\sigma_{\uparrow(\downarrow)} = e^2 g_{\uparrow(\downarrow)} D_{\uparrow(\downarrow)}. \tag{1.41}$$

The spin-dependent chemical potentials are expressed in terms of the potential to give the density of carriers $n_\uparrow$ and $n_\downarrow$ in each spin sub-band:

$$\mu_\uparrow = -eV + \frac{n_\uparrow - n_0}{g_\uparrow(\epsilon_F)} = -eV + \frac{\delta n_\uparrow}{g_\uparrow(\epsilon_F)}, \tag{1.42}$$

$$\mu_\downarrow = -eV + \frac{n_\downarrow - n_0}{g_\downarrow(\epsilon_F)} = -eV + \frac{\delta n_\downarrow}{g_\downarrow(\epsilon_F)}. \tag{1.43}$$

The spin current flowing through an FM can be described using Equation 1.4,

$$J_s = -\frac{\hbar}{2e}\alpha_{FM}\sigma_{FM}J_e, \tag{1.44}$$

in terms of the fundamental constants $\hbar$ and e, the charge current J_e, the FM conductivity σ_{FM}, and α_{FM} is the normalized difference of the spin-dependent conductivities of the spin bands, which is defined in Equation 1.8. α_{FM} is often taken as P_{FM} but it is worth noting that α_{FM} is not necessarily the same as P_{FM}.

1.2.6 Spin Injection Across Diffusive Ferromagnetic/Non-Magnetic Interfaces

The basic concepts introduced in §1.2.1 - §1.2.5 describing carrier transport within spin sub-bands, the 'Two-Channel Model', have been extended to describe diffusive spin transport across material interfaces by Van Son *et al.* [37]. FM/N interfaces, where transport is diffusive rather than by tunneling, are often referred to as diffusive or transparent interfaces. Valet and Fert (VF) developed a comprehensive theoretical description of multiple transparent FM/N interfaces based on Boltzmann theory [14]. This model has been employed to quantitatively describe CPP-GMR devices with a variety of material combinations [38, 39]. Johnson and Silsbee independently developed a theory to describe spin transport, but it is not discussed further here.

The base component of a spin-dependent transport heterostructure is a ferromagnetic (FM) - nonmagnetic (N) interface. As the polarized current passes from FM into N, it injects non-equilibrium spins into N. The FMs serve as a source of spin-polarized electrons for injection experiments. A simple graphic depicting this process is shown in Figure 1.2, with arrows representing the charge and spin currents flowing through the system. The non-equilibrium spins injected into the N diffuse until relaxation occurs and the spin polarization relaxes to equilibrium. This buildup of non-equilibrium spins is referred to as the spin accumulation. The single interface shown here is a building block of other devices, such as GMR devices consisting of two back-to-back interfaces, FM/N/FM, which will be described in §1.2.9.

The basics of spin injection can be understood by examining the energy-dependent DOS for the FM and N. The DOS for each material is illustrated for the spin-up $g_\uparrow$ and spin-down $g_\downarrow$ bands independently, with the Fermi energy ε_F in Figure 1.3. The left side of the figure shows a cartoon of the spin-resolved DOS for a FM, with exchange-split d-bands. The right hand side depicts the parabolic DOS of a paramagnet. An electron current is depicted moving across the interface from the FM to the N, with J_e composed primarily of spin-$\uparrow$ electrons. This spin-polarized current results in a (non-equilibrium) spin accumulation of spin-$\uparrow$ electrons in the N, marked by an increase in spin up chemical potential $\mu_\uparrow$ and decrease in the spin down chemical potential $\mu_\downarrow$ from the spin-independent value (dashed line). The spin independent chemical potential will vary spatially from the equilibrium value corresponding to a gradient due to a charge

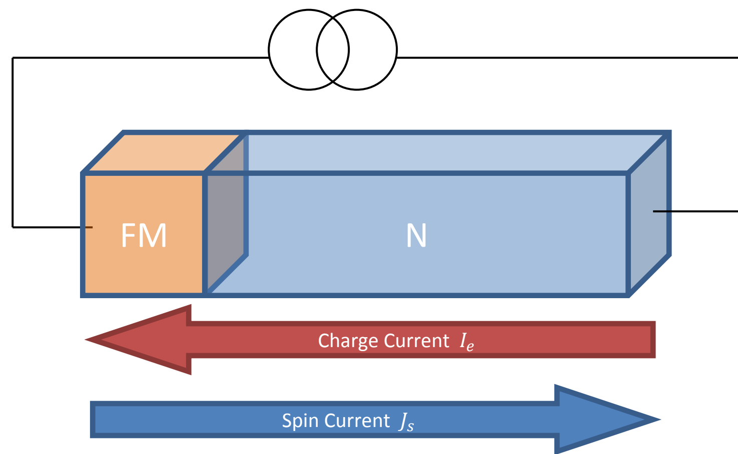

Figure 1.2: Representation of a ferromagnetic/normal metal interface used for spin injection. The arrows illustrate the charge and spin current directions.

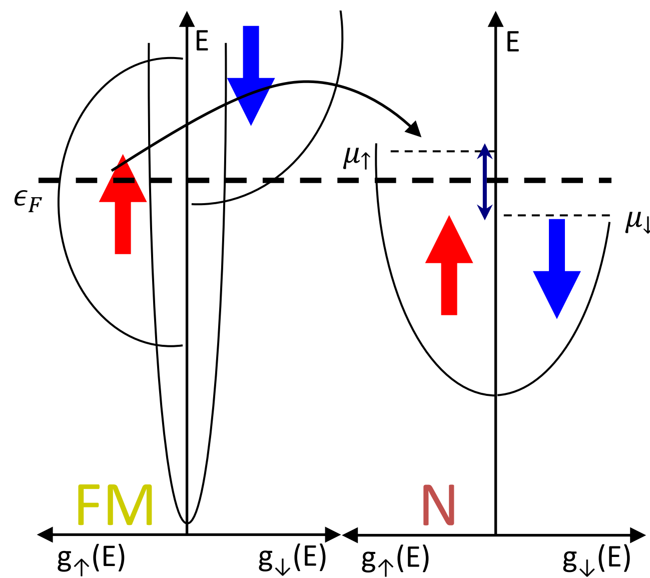

Figure 1.3: Spin-dependent density of states depicting spin injection from a ferromagnet to a normal metal.

current. The spin accumulation is defined as the difference in spin-dependent chemical potentials, $\mu_\uparrow - \mu_\downarrow$. This framework forms the basic understanding of electronic spin injection experiments.

The spin accumulation is not conserved and is subject to relaxation while scattering, as discussed further in §1.2.12. Spin injection is balanced against spin relaxation which determines the system's steady-state spin accumulation. The relaxation of spins results in a spatial decay of the accumulation away from the interface.

1.2.7 Solving for the Spin-Resolved Chemical Potential Across a Ferromagnet - Normal Metal Interface

The spin-dependent diffusion Equation 1.39 can now be applied to diffusive transport through ferromagnets, non-magnetic materials, and the interfaces between them. The one-dimensional general solution to the diffusion equation for $P_{FM} > 0$ 1.39 is given by,

$$\mu_\uparrow(x) = C_1 - j_e \rho x + C_2 \rho_\uparrow e^{-x/\lambda_s} + C_3 \rho_\uparrow e^{x/\lambda_s}, \tag{1.45}$$

$$\mu_\downarrow(x) = C_1 - j_e \rho x - C_2 \rho_\downarrow e^{-x/\lambda_s} - C_3 \rho_\downarrow e^{x/\lambda_s}, \tag{1.46}$$

where x is the spatial position and the constants C_1, C_2, C_3, and C_4 are determined by the application of boundary conditions. The following boundary conditions apply in the case of diffusive interfaces:

1. $\mu_\uparrow$ and $\mu_\downarrow$ are continuous everywhere. This boundary condition includes the ferromagnet/normal metal interface so that:

$$\mu_{\uparrow,FM}|_{\text{Interface}} = \mu_{\uparrow,N}|_{\text{Interface}}\,, \tag{1.47}$$

$$\mu_{\downarrow,FM}|_{\text{Interface}} = \mu_{\downarrow,N}|_{\text{Interface}}\,. \tag{1.48}$$

2. $J_\uparrow$ and $J_\downarrow$, defined in Equation 1.4, and the related spin-current densities in 1.35-1.36 must be conserved across the interface in the absence of spin-flip interfacial scattering:

$$J_{\uparrow,FM}|_{\text{Interface}} = J_{\uparrow,N}|_{\text{Interface}}\,, \tag{1.49}$$

$$J_{\downarrow,FM}|_{\text{Interface}} = J_{\downarrow,N}|_{\text{Interface}}\,. \tag{1.50}$$

3. The difference in chemical potential $\Delta\mu = \mu_\uparrow - \mu_\downarrow$ must go to zero far from the interface. For a FM extending to $-\infty$ and the N to ∞, the splitting of the spin-dependent chemical potentials can be written as:

$$\left.(\mu_{\uparrow,FM} - \mu_{\downarrow,FM})\right|_{x\to-\infty} = 0, \tag{1.51}$$

$$\left.(\mu_{\uparrow,N} - \mu_{\downarrow,N})\right|_{x\to\infty} = 0. \tag{1.52}$$

The spin-dependent chemical potentials can be written for the FM/N with the boundary conditions above and the interface at $x = 0$ as:

$$\mu_\uparrow(x) = \begin{cases} C_1 - j_e\rho_{FM}x + C_{3,FM}\rho_{\uparrow,FM}e^{x/\lambda_{s,FM}} & \text{if } x < 0 \\ -j_e\rho_N x + 2C_{2,N}\rho_N e^{-x/\lambda_{s,N}} & \text{if } x > 0 \end{cases} \tag{1.53}$$

$$\mu_\downarrow(x) = \begin{cases} C_1 - j_e\rho_{FM}x - C_{3,FM}\rho_{\downarrow,FM}e^{x/\lambda_{s,FM}} & \text{if } x < 0 \\ -j_e\rho_N x - 2C_{2,N}\rho_N e^{-x/\lambda_{s,N}} & \text{if } x > 0 \end{cases} \tag{1.54}$$

where $\rho^{-1} = \rho_\uparrow^{-1} + \rho_\downarrow^{-1}$. For the N, $\rho_\uparrow = \rho_\downarrow$ so that $\rho_{N,\uparrow(\downarrow)} = 2\rho_N$. The impedance to spin currents through structures can be expressed in terms of spin resistances. This spin-impedance can be written for a length of material i as $(\rho_i\lambda_{s,i})/A_i$. The split in the chemical potentials at the interface has been shown to follow the interfacial spin resistance:

$$R_{i,s} = \frac{\mu_\uparrow - \mu_\downarrow}{eJ_e} = \frac{\alpha_{FM}^2\left(\rho_N\lambda_{s,N}\right)\left(\rho_{FM}\lambda_{s,FM}\right)}{\left(\rho_{FM}\lambda_{s,FM}\right) + \left(1-\alpha_{FM}^2\right)\left(\rho_N\lambda_{s,N}\right)}, \tag{1.55}$$

$$= \frac{\alpha_{FM}^2 R_{s,N}R_{s,FM}}{R_{s,FM} + (1-\alpha_{FM}^2)R_{S,N}}. \tag{1.56}$$

1.2.8 Tunnel Barrier Interfaces

Transport across tunnel barrier contacts is, in principle, easier to understand than transport across diffusive interfaces. The simplest treatment of such a system was introduced by Johnson and Silsbee [40]. A tunnel barrier placed at the interface of the FM and N prevents diffusion from the FM to N and *vice versa*, effectively decoupling transport in the two materials by mechanisms other than tunneling.

A bias applied across the interface will drive a charge current that injects spin-polarized electrons and generates spin accumulation, as discussed in §1.2.6 and depicted

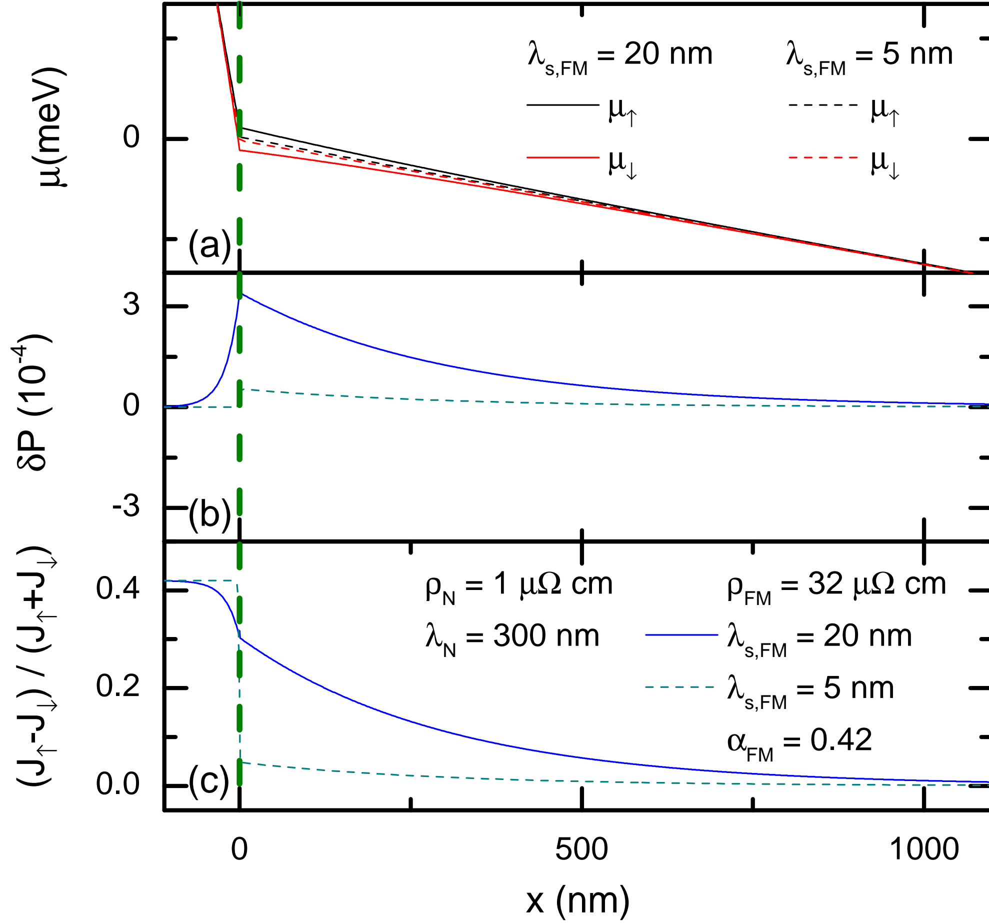

Figure 1.4: Calculated position dependence of (a) the spin-up and -down chemical potential, (b) non-equilibrium spin polarization, and (c) polarization of the spin current.

in Figure 1.3. The insertion of a tunnel barrier prevents the diffusion of injected non-equilibrium spins back into the FM, and subsequent relaxation, and leads to a larger spin accumulation.

1.2.9 Two Diffusive FM/N Interfaces - Giant Magneto Resistance

Valet and Fert addressed the case of two FM/N interfaces back-to-back, an FM-F-FM structure [14]. They derived expressions for the change in resistance across the structure when the relative orientation of the magnetization of the FMs is changed from parallel ($\uparrow\uparrow$) to anti-parallel ($\uparrow\downarrow$). The difference in resistance between magnetic configurations in the limit of the N thickness t_N much less than $\lambda_{s,N}$ and the FM thickness t_{FM} less than $\lambda_{s,FM}$ as written by Valet and Fert [14] is

$$R_{\uparrow\downarrow} - R_{\uparrow\uparrow} = \alpha_{FM}^2 \frac{(\rho_{FM} t_{FM})^2}{\rho_N t_N + \rho_{FM} t_{FM}}, \tag{1.57}$$

where the current polarization α_{FM} (Equation 1.8) is due to the difference in transport conductivities between the two spin sub-bands. As previously stated, α_{FM} is not necessarily equal to P_{FM}. Equation 1.57 is the same as is found using the two-channel model considering only the spin resistances of each sub-band.

The GMR ratio, which is often used as the measure of device performance, is expressed as

$$\left(\frac{R_{\uparrow\downarrow} - R_{\uparrow\uparrow}}{R_{\uparrow\downarrow}} \right) = \frac{2\alpha_{FM}^2 \lambda_{s,FM}}{(1 - \alpha_{FM}^2) t_{FM}}, \tag{1.58}$$

in the limit where $t_N \ll \lambda_{s,N}$, $t_{FM} \gg \lambda_{s,FM}$, and $\rho_N t_N \ll \rho_{FM} \lambda_{s,FM}$, which are satisfied for typical vertical GMR devices. Due to the dependence of the GMR ratio on α_{FM} and $\lambda_{s,FM}$, GMR experiments can be used to measure the spin-dependent transport properties of FMs. However, the functional form of Equation 1.58 provides difficulties in separating the two. Valet and Fert typically extracted α_{FM} and $\lambda_{s,FM}$ by fitting the dependence of the GMR ratio on t_{FM} [41].

CPP-GMR devices with increased t_N, on the order of $\lambda_{s,N}$, exhibit behavior due to spin relaxation in N. Although t_N can be fabricated to be similar to $\lambda_{s,N}$ for some materials in a vertical structure, this is experimentally undesirable since $\lambda_{s,N}$ is typically on the order of 100 nm for metallic films. To do this requires impractically thick N layers

to be deposited. Instead, lateral devices are more desirable for studies of $\lambda_{s,N}$, in which patterned devices give access to the relevant length scales.

1.2.10 Non-Local Detection of the Non-Equilibrium Spin Accumulation

The non-local device geometry used in this work is operationally similar to the CPP-GMR structure. Two FM/N interfaces are employed and a change in resistance between the $\uparrow\uparrow$ and $\uparrow\downarrow$ states is observed. These devices are lateral, however, comprised of wires running in the substrate plane. Lateral devices can be used in a local configuration in a manner similar to a CPP-GMR device with an N spacer layer determined by the separation between the FM contacts. However, the spacer in this case is much larger than the traditional vertical structure. In this work, they are used in a non-local configuration. An N channel is patterned and lies along the substrate with FM electrical contacts laterally spaced along the length of the N channel ans separated by distance d. This configuration is illustrated in Figure 1.5(a).

A charge current that passes through both FMs and the N channel in the local configuration leads not only to spin injection and the spin valve effect, but also to other magneto-resistive effects and a significant ohmic drop. In the non-local geometry, however, current flows through one FM (injector) but not the second FM (detector) as it is outside the current path. The absence of net charge current flowing through the device to the right of the injector prevents normal MR and AMR effects from appearing in the measured data.

Although a net charge current does not flow to the right of the injector contact, the injected non-equilibrium spins diffuse in all directions, along the current path as well as towards the FM detector contact. This is depicted in Figure 1.5(a), with the charge current flowing through the left hand side but spin current flowing left and right. The spin current will flow through all branches of the device until it relaxes, making analytical solutions of the differential spin diffusion equation intractable for the actual experimental geometry.

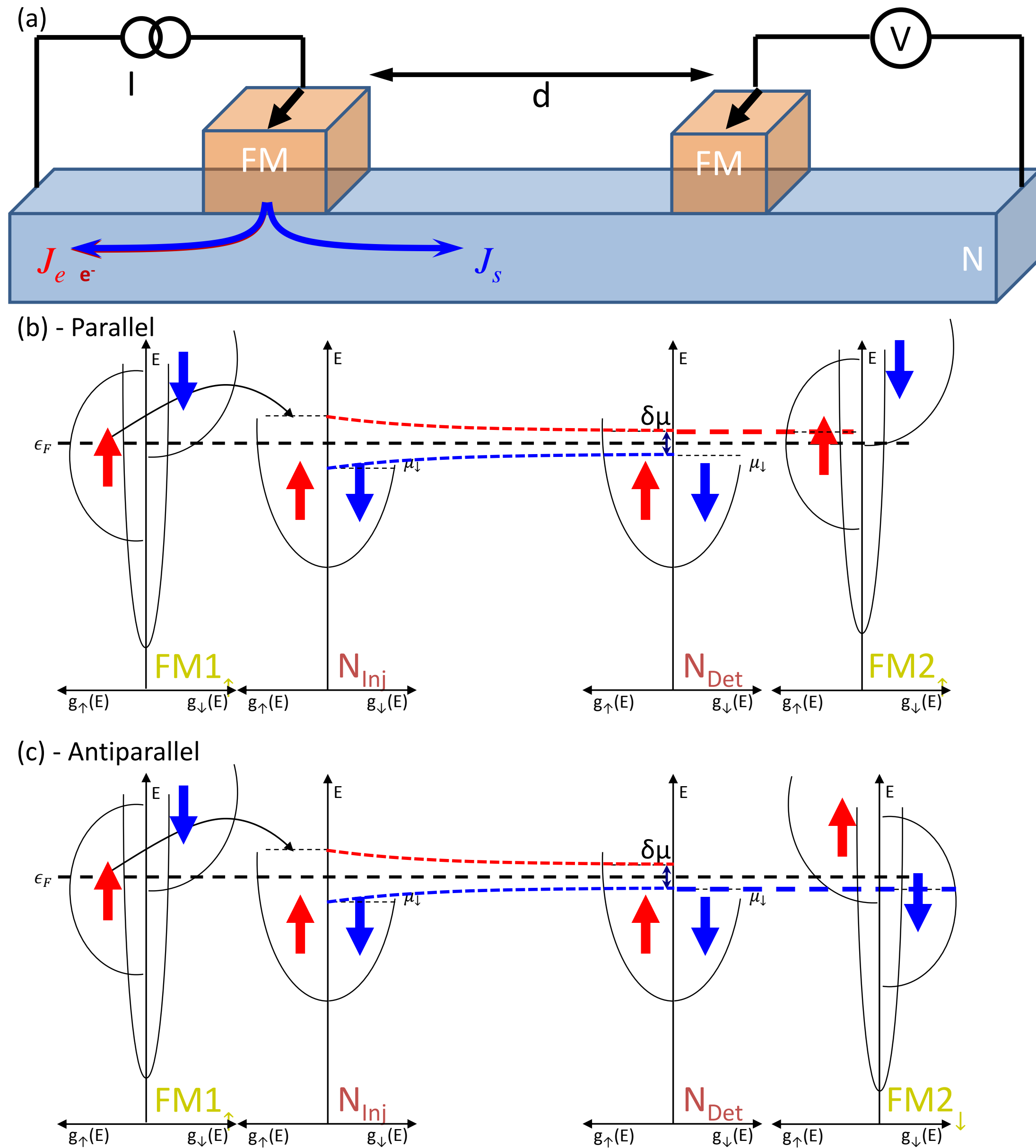

Figure 1.5: (a) Representative diagram of a non-local spin valve device with arrows representing the electron and spin currents, J_e and J_s, respectively. Depiction of spin injection and detection using spin dependent DOS diagrams for the (b) parallel and (c) anti-parallel magnetization states.

Non-Local Injection and Detection of the Spin Accumulation: DOS Representation

Extending the picture introduced in §1.2.6 to describe the injection of non-equilibrium spins can be used to understand spin detection, as well. This is illustrated by the series of DOS plots in Figure 1.5(b)-(c). Spin injection, shown in the left two DOS panels, leads to a spin accumulation in N. The injected non-equilibrium spin population relaxes and diffuses in the N channel from near the source, labeled in Figure 1.5 as N_{Inj}, to the region of N near the detector, N_{Det}. This is depicted by the spatial reduction of $\Delta\mu$ by the red and blue dashed lines from injector to detector.

The case in which the detector magnetization is parallel to the injector ↑ allows $\mu_\uparrow$ to be probed, depicted in Figure 1.5(b). The detector contact will undergo a potential shift to align with $\mu_\uparrow$ in the N at the detector, depicted in the figure by the $g_\uparrow(\varepsilon_F)$ for FM2. Likewise, if the detector magnetization is set ↓, $\mu_\downarrow$ is probed by the detector shifting to align with $\mu_\downarrow$ at the interface ($\mathrm{FM2}_\downarrow$). These potential shifts are measured by a voltmeter connected to the detector FM referenced to the N channel far from the detector and outside the current path. The difference in measured detector voltage V_{NL} between ↑↑ and ↑↓ measures the spin accumulation. This also holds for the opposite magnetization of the injector FM by reversing all the arrows.

1.2.11 Diffusive Non-Local Spin Transport: Spin-Resistor Network Solution

Instead of the general solutions to the spin diffusion equation in §1.2.7, a spin-resistor network is often used to analyze the spin transport in more complicated structures. The spin resistance R_s of each material depends on the product of ρ and λ_s, as well as the cross-sectional area A, defined by Kimura *et al.* [42],

$$R_{s,N} = 2\frac{\rho_N \lambda_{s,N}}{A_N}, \tag{1.59}$$

$$R_{s,FM} = 2\frac{\rho_{FM} \lambda_{s,FM}}{A_{FM}\left(1-\alpha_{FM}^2\right)}. \tag{1.60}$$

The spin resistances are used to set up an equivalent spin resistor network. A solution to the attenuated transmission line network for the magnitude of the spin valve signal

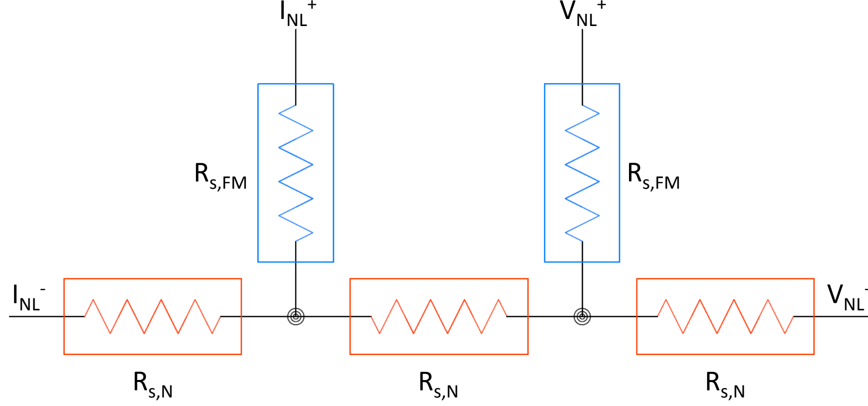

Figure 1.6: Layout of the non-local resistor network. The N and FM spin resistances are labeled with $R_{s,N}$ and $R_{s,FM}$, respectively. The non-local current and voltage connections are labeled as well.

in the non-local geometry is given by:

$$\Delta R_{NL} = \frac{\alpha_{FM} R_{s,N}}{2e^{d/\lambda_{s,N}}\left(2 + \frac{R_{s,FM}}{R_{s,N}}\right) + 4\sinh\left(d/\lambda_{s,N}\right)}, \tag{1.61}$$

which has a dependence on d which is not a purely exponential decay. This is typically approximated (e.g. Otani *et al.* [43]) as,

$$\Delta R_{NL} \approx \frac{\alpha_{FM}^2 R_{s,FM}^2}{2R_{s,FM} e^{d/\lambda_{s,N}} + R_{s,N} \sinh d/\lambda_{s,N}}. \tag{1.62}$$

This has been written in an alternate form [44, 45],

$$\Delta R_{NL} = \frac{2\alpha_{FM}^2 R_{s,N}}{\left(2 + \frac{R_{s,N}}{R_{s,FM}}\right)^2 e^{d/\lambda_{s,N}} - \left(\frac{R_{s,N}}{R_{s,FM}}\right)^2 e^{-d/\lambda_{s,N}}}, \tag{1.63}$$

which has an equivalent dependence on d to Equation 1.61.

These one-dimensional expressions of spin diffusion form the basis for understanding measurements of non-local spin valve effects. The measured d dependence of ΔR_{NL} can be fit to the spatial dependence given by this model, which is discussed in further detail in §4.4.

Non-Local Spin Transport: Tunnel Barrier FM/N Interfaces

The case of tunnel barrier contacts is treated using the framework introduced previously in this chapter. Due to the presence of tunnel barriers at the interfaces, the spin current flowing into the N from the FM injector will not back-diffuse and the spin-potential-splitting is given by:

$$\frac{2\mu_0}{e} = \left(-\frac{J_e}{2} - \frac{\mu_0 A_{FM}}{e\rho_N \lambda s, N}\right) R_{I,\uparrow} - \left(-\frac{J_e}{2} - \frac{\mu_0 A_{FM}}{e\rho_N \lambda s, N}\right) R_{I,\downarrow}, \tag{1.64}$$

where μ_0 is the equilibrium value of the electro-chemical potential, $R_{I,\uparrow}$ and $R_{I,\downarrow}$ are the spin-up and -down interfacial resistances. Using Equation 1.64, the spin-splitting of the chemical potential can be written,

$$\Delta\mu = \frac{J_e e R_{s,N} P}{1 + 2R_{s,N}/\left(R_{I,\uparrow} + R_{I,\downarrow}\right)}, \tag{1.65}$$

where the polarization at the interface can be expressed in terms of the spin-resolved interface resistances, $P_I = \left(R_{I,\uparrow} - R_{I,\downarrow}\right)/\left(R_{I,\uparrow} + R_{I,\downarrow}\right)$. Realistic tunnel barriers are treated in the limit where $R_I = \left(R_{I,\uparrow} + R_{I,\downarrow}\right) \gg R_{s,N}$ and, therefore, Equation 1.65 reduces to,

$$\Delta\mu = J_e e R_{s,N} P, \tag{1.66}$$

which can then be used to express the change of non-local trans-resistance between $\uparrow\uparrow$ and $\uparrow\downarrow$ states. This is written,

$$\Delta R_{NL} = \frac{\Delta V}{J_e} = \frac{P_{FM}^2 \lambda_{s,N} \rho_N}{A_N} e^{-d/\lambda_{s,N}}, \tag{1.67}$$

where the polarization P_{FM} of the injector and detector are the same for devices employing the same material for the injector and detector. This is the case for most experiments.

The expected magnitude of the non-local spin valve signal for tunnel barrier devices is given by Equation 1.67. This describes an exponential decay of the initial accumulation characterized by $\lambda_{s,N}$, given by Equation 1.66 with an extra factor of P_{FM} due to the detector. The purely exponential decay is due to the relaxation of spins within the N channel only due to the decoupling of the FMs from the N.

1.2.12 Characterizing Spin Relaxation: The Spin Diffusion Length

Spin Relaxation in Metals

A non-equilibrium population of spin polarized carriers relaxes with a characteristic length $\lambda_s = \sqrt{D\tau_s}$, as described previously. Although λ_s is the quantity used to characterize spin transport through the majority of this thesis, it is linked to τ_s through D. The spin lifetime is a property of the host material, and the physics that determines τ_s varies among different classes of materials.

The relaxation of spins in non-magnetic metals is believed to be caused by the spin-orbit (SO) interaction. The theory of this mechanism is attributed to Elliot and Yafet (EY) [46, 47]. Band structure calculations allow the Bloch eigenfunctions to be expressed as a linear combination of spin-up and -down states. Inclusion of the spin-orbit interaction in the calculation mixes the two states [48]. This results in a relation,

$$\frac{\tau_p}{\tau_s} \propto \left(\frac{\lambda_{SO}}{\Delta E_B}\right)^2, \tag{1.68}$$

where λ_{SO} is the spin-orbit coupling constant and ΔE_B is the average energy separation between the band and the adjacent band to which the state is spin-orbit coupled. This ratio of lifetimes is expected to be temperature-independent [47]. As a result, the ratio of momentum to spin-flip scattering can be expressed by a constant,

$$\alpha_{EY} \equiv \frac{\tau_p}{\tau_s}. \tag{1.69}$$

Using this relation, the expected temperature dependence of $\tau_p(T) \propto \rho(T)^{-1}$ can be used to express $\tau_s(T)$ using,

$$\tau_{s,N}(T) = \frac{m_e}{\alpha_{EY} n_{e,N} e^2 \rho_N(T)}, \tag{1.70}$$

for a bulk non-magnetic metal, where m_e is the electron mass and n_e is the carrier density. Since $\rho_N(T)$ can be measured experimentally, the residual resistivity ratio (RRR), the ratio of ρ at room temperature to that at low temperature [49], can also be determined. The measured RRR can be used to compute the ratio of expected spin lifetimes,

$$\frac{\tau_{s,N}(T = 5\text{ K})}{\tau_{s,N}(T = 292\text{ K})} = \frac{\rho_N(T = 292\text{ K})}{\rho_N(T = 5\text{ K})}, \tag{1.71}$$

which may be established within this theory with no knowledge of α_{EY}. Further, using Equation 1.40, the ratio of spin diffusion lengths can similarly be expressed,

$$\frac{\lambda_{s,N}(5\ \mathrm{K})}{\lambda_{s,N}(292\ \mathrm{K})} = \frac{\rho_N(292\ \mathrm{K})}{\rho_N(5\ \mathrm{K})}, \tag{1.72}$$

providing a useful test of Elliot-Yafet relaxation with no other knowledge required.

Additional knowledge of α_{EY} for a material allows τ_s to be explicitly calculated from Equation 1.70 and the measured $\rho_N(T)$. Monod and Beuneu used conduction-electron spin resonance (CESR) experiments to verify the temperature-independent relationship given in Equation 1.69 [50, 51]. The ratio of the half-width of the conduction electron spin resonance in magnetic field divided by the material resistivity $\Delta H/2\rho$ was measured to be $1.45 \pm 0.10\,\mathrm{G\,n\Omega^{-1}}$ for Cu and $0.75 \pm 0.10\,\mathrm{G\,n\Omega^{-1}}$ for Al [52]. The width of the resonance in CESR measurements are related to τ_s and, therefore, can be used to establish values of α_{EY} for various N [53]. Thee measured ratios of $\Delta H/2\rho$ allow the determination of α_{EY} to within 15 %.

Difficulty in Determining the Spin Diffusion Length in Nanostructures

The spin diffusion length $\lambda_{s,N}$ is typically measured in devices by varying the separation d between a spin injector and spin detector attached to a non-magnetic spin-diffusion channel. Measuring the relaxation of the spin accumulation along the length of the channel allows $\lambda_{s,N}$ to be determined. In principle it is possible to determine τ_s using the measured spin diffusion length with equation 1.40 if D is known and only intrinsic spin-relaxation mechanisms contribute. In practice, the ohmic FM contacts and extrinsic mechanisms in the N contribute to spin-relaxation, convolving all the relaxation mechanisms in the measurements of λ_s.

The relaxation of spins is due to the intrinsic spin relaxation described above, as well as extrinsic mechanisms. Extrinsic sources of relaxation, such as magnetic and high-atomic number impurities may contribute. Surface effects, which may not manifest in larger samples with dimensions larger than $\lambda_{s,N}$, appear as the the length scale of the device is reduced.

1.2.13 Spin-Relaxation at Surfaces

Enhanced spin-relaxation at the boundaries of normal metal channels is likely present in devices that have been patterned on length scales much less than the bulk $\lambda_{s,N}$. There are several possible origins of spin relaxation at surfaces. These include the spatial-symmetry breaking at the surfaces or changes of the materials properties near the surface. The Hamiltonian for the spin-orbit interaction is given by

$$H_{SOC} = \frac{\hbar^2}{4m^2c^2}(\nabla V \times \vec{p}) \cdot \vec{\sigma}_s, \tag{1.73}$$

where $\vec{p}$ is the momentum and $\vec{\sigma}_s$ is the spin. An important consequence of this is that the usual symmetries are broken. Time-reversal symmetry, $E(\vec{k},\uparrow) = E(-\vec{k},\downarrow)$, and space-inversion symmetry, $E(\vec{k},\uparrow) = E(-\vec{k},\uparrow)$ make the spin-bands degenerate. At surfaces the degeneracy is lifted at non-zero $\vec{k}$ due to the breaking of the space-inversion symmetry.

Increased spin-orbit splitting of the bands at material surfaces has been observed for several metals. This has been shown experimentally for metal surfaces such as Au(111), W(110), Mo(110), and Bi [54–57]. Further, the spin-lifetime from the symmetry breaking at the surface has been modeled quantum-mechanically using an equation-of-motion with the electronic structure represented by a tight-binding model. This showed an increase of the spin-relaxation rate in nanoscaled Cu [58]. In Cu nanoparticles with a resistivity of 3.2 µΩ cm, similar to the experimental resistivity measured in this work at room temperature, a spin diffusion length of 404 nm was calculated. In this calculation $\lambda_{s,N}$ was found to follow the expected Elliot-Yafet behavior as ρ_N was varied. As the simulated system size was reduced from an infinite system to one of finite size, consisting of 7 % surface atoms, $\lambda_{s,N}$ was reduced to 55 nm.

Although increased spin relaxation rates at surfaces have been invoked to explain unexpected experimental data, disagreement remains about the effect this has on the temperature dependence of $\lambda_{s,N}$ [43, 59]. The temperature dependence of the transport properties, such as the resistivity and mean-free path, will affect the contribution of spin relaxation rates at surfaces and in the bulk of N channels for finite spatial dimensions. To better understand the effect of enhanced spin relaxation at surfaces I have carried out numerical simulations of spin-diffusion and spin-relaxation in lateral non-local devices which are discussed in Chapter 5.

1.2.14 Spin Precession and Dephasing - the Electrical Hanle Effect

Electrons have a magnetic moment and therefore experience a torque in the presence of a magnetic field B which can be expressed as,

$$\vec{\Gamma}_B = -g\mu_B \vec{S} \times \vec{B}, \tag{1.74}$$

where $\vec{S}$ corresponds to the electron spin, $g \approx 2$ is the electron g-factor, and μ_B is the Bohr magnetron. This torque causes precession of the spins with a frequency given by,

$$\omega_L = \gamma B_\perp, \tag{1.75}$$

$$\gamma = g\mu_B/\hbar, \tag{1.76}$$

where γ is the gyromagnetic ratio and $B_\perp$ is the out of plane magnetic field, perpendicular to the FM magnetization $\vec{M}$. This effect is utilized in experimental techniques such as nuclear magnetic resonance, electron spin resonance (ESR), and muon spin resonance.

Spin precession can also be realized in lateral transport devices. In the case of spin-transport devices, the injected spins have $\vec{S} \parallel \vec{M}$, and $\vec{S}$ will precess due to an applied $B_\perp$. The spin current precesses while diffusing from source to detector, separated by a distance d. In the simplest case, that of ballistic transport with a fixed velocity v_F, electrons will travel from the source to the detector in a time $\tau_d = d/v_F$. During transit the spins will precess through an angle,

$$\theta_L = \omega_L \tau_d. \tag{1.77}$$

The signal due to spins arriving at the detector is proportional to the projection of $\vec{S}$ on $\vec{M}$, $R_{NL}(B_\perp) \propto +(-)\cos\theta_L$ for the detector magnetization parallel (antiparallel) to the injector. For a spin current that has precessed through $\theta_L = \pi$, the detected signal inverts, then returns to the initial value as the spins precess back through 2π. In practice, $B_\perp$ is swept to modulate the detected signal. In the case of ballistic transport, there will be a well-defined transit time and it follows that $R_{NL}(B_\perp) \propto +(-)\cos(\omega_L d/v_F)$.

In systems that are larger than the mean free path, the transport is diffusive. The simple sinusoidal behavior for ballistic transport does not hold in this regime. The spin transport in a one-dimensional N channel can be described by the differential equation

for spin diffusion,

$$\frac{\partial \vec{S}}{\partial t} = -v_d \frac{\partial \vec{S}}{\partial x} + D\frac{\partial^2 \vec{S}}{\partial y^2} - \frac{\vec{S}}{\tau_{s,N}} - \omega_L \times \vec{S}, \tag{1.78}$$

for the average spin polarization $\vec{S}$ in N. The terms on the right side of the equation are, from left to right, drift, diffusion, relaxation, and precession of the spins. For measurements made in the non-local geometry using metallic devices the drift velocity v_d is zero. The diffusion and relaxation terms have been discussed previously and are independent of the applied field. The final term accounts for precession resulting from the torque given by Equation 1.74 with precession frequency $\omega_L(B_\perp)$ from Equation 1.75.

For diffusive spin current, there is a distribution of transit times from source to detector. The distribution for a one-dimensional diffusion process is given by,

$$\mathcal{F}_\tau(\tau_d) = \sqrt{\frac{1}{4\pi D_N \tau_d}} e^{-d^2/4D_N\tau_d}, \tag{1.79}$$

so that, with Equation 1.77, a distribution of precession angles is expected. This distribution of precession angles dephases the signal for large diffusion times or large $B_\perp$. The distribution of transit times is modified due to spin relaxation by a factor of $e^{-\tau_d/\tau_s}$, reducing the weighting of large τ_d. By integrating Equation 1.79 with the factors for spin relaxation and precession over all diffusive transit times, the initial spin signal S_0 projected on the detector is:

$$S(B_\perp, d) = S_0 \int_0^\infty \mathcal{F}_\tau(\tau_d) \cos(\gamma B_\perp \tau_d) e^{\frac{-\tau_d}{\tau_{s,N}}}\, d\tau_d. \tag{1.80}$$

This gives the field-dependent detected signal. Since the contacts have finite width, the contact separation in Equation 1.80 can be replaced by integrals over the width of the injector x_I and detector x_D,

$$S(B_\perp) = S_0 \int_{x_{D,L}}^{x_{D,R}} \int_{x_{I,L}}^{x_{I,R}} \int_0^\infty \frac{1}{\sqrt{4\pi D_N \tau_d}} e^{\frac{-(x_D - x_I)^2}{4D_N\tau_d}} \cos(\omega_L \tau_d) e^{\frac{-\tau_d}{\tau_{s,N}}}\, d\tau_d\, dx_I\, dx_D, \tag{1.81}$$

to give the dependence of the detected signal on $B_\perp$. In this work, Equation 1.81 is used to analyze measured $R_{NL}(B_\perp)$.

Noteworthy are the following caveats to the application of this model. The first is that Equation 1.81 holds only for diffusive transport with a uniform spin lifetime.

Further, in this model, the source and detector FMs do not influence the detected signal; this is the case for experiments with tunnel barriers at the source and detector contact interfaces. This precession, relaxation, and dephasing of electron spins is known as the electrical Hanle effect.

Using Equation 1.81 the Hanle curves for parallel and antiparallel contact magnetization states can be computed. Hanle curves were computed for parameters which are similar to those of Al, $D = 6\,\mu m^2\,ns^{-1}$ and $\tau_{s,N} = 15\,ps$, and are shown in Figure 1.7(a). The contact separation used is $d = 2000\,nm$ and the contact widths are 200 nm and 100 nm for the injector and detector, respectively.

So far, Equation 1.81 accounts for the spin transport within the N channel but does not account for the out-of-plane rotation of the FM magnetization with the applied $B_\perp$. Typically, this is not a concern for experiments with semiconducting channels as the $|B|$ required for the measurements is much less than $4\pi M_s$. Experiments with metallic N channels, however, generally require much larger $B_\perp$. As a result, rotation of the FMs must be accounted for when using Equation 1.81 to fit the data. In this case, the rotation of the FMs out of plane is given by

$$S(B_\perp, \theta_{FM1}, \theta_{FM2}) = S(B_\perp) \cos\theta_{FM1} \cos\theta_{FM2} + |S(B_\perp = 0)| \sin\theta_{FM1} \sin\theta_{FM2}, \tag{1.82}$$

where the angles θ_{FM1} and θ_{FM2} are the out-of-plane angles of the FM contact magnetizations. The term with the factors of cosine suppress the magnitude of the Hanle oscillations due to the rotation of the FMs out-of-plane and the spin polarization becomes aligned along $B_\perp$. The term with the factors of sine lead to the background due to the rotation of the FMs into the out-of-plane parallel state. The model with FM magnetization rotation is shown in Figure 1.7(b).

1.3 Review of Spin Transport in Metals Experiments

A number of experiments have measured the transport and relaxation of spins in both ferromagnetic and non-magnetic materials. In this section we review some measured quantities that have been reported in the literature for a variety of metallic systems. Material parameters such as the spin diffusion lengths in both N and FM materials as well as P_{FM} have previously been studied in both vertical devices, composed of

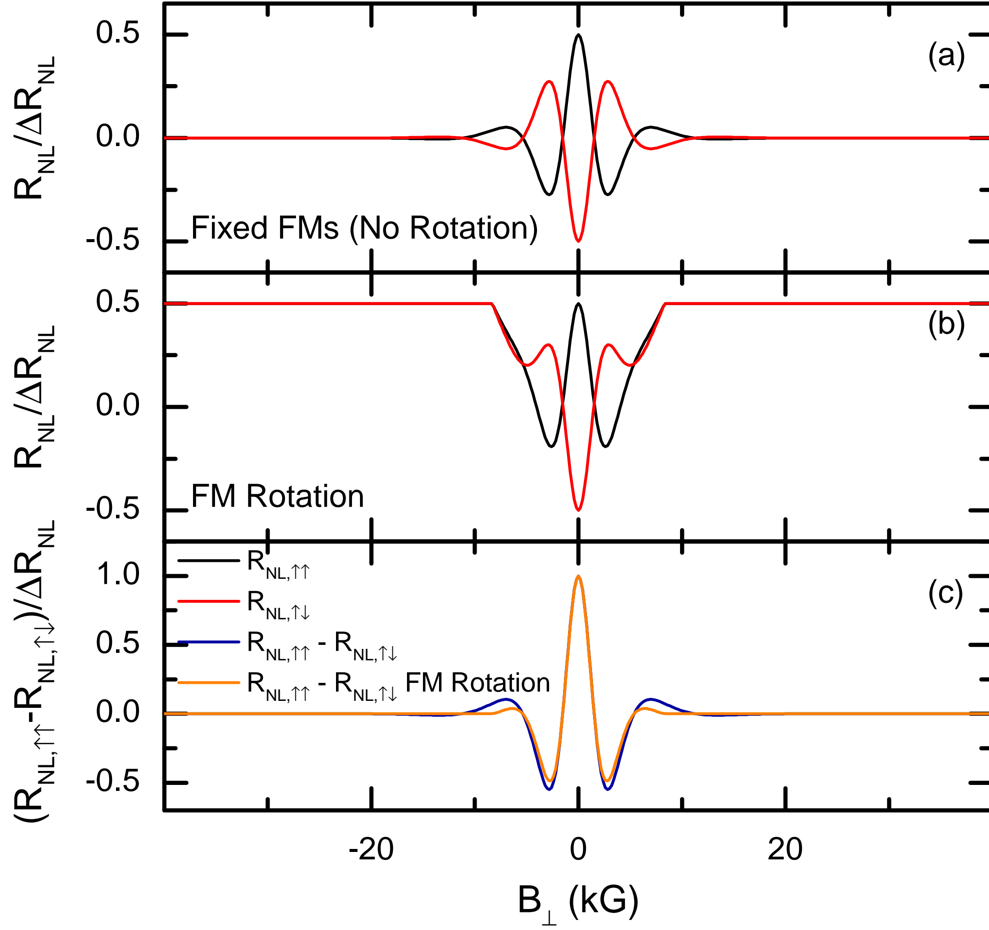

Figure 1.7: Modeled Hanle effect field sweeps of $R_{NL,\uparrow\uparrow}$ and $R_{NL,\uparrow\downarrow}$, normalized by the magnitude of the spin valve effect, for $D = 6\,\mu\text{m}^2\,\text{ns}^{-1}$, $\tau_{s,N} = 15\,\text{ps}$, and $d = 2000\,\text{nm}$ for (a) FM contacts with fixed magnetization, (b) for FMs that rotate out-of-plane, and (c) the difference between parallel and antiparallel magnetization configurations $(R_{NL,\uparrow\uparrow} - R_{NL,\uparrow\downarrow})/\Delta R_{NL}$ with(without) FM rotation plotted in orange(blue).

thin layers with thicknesses $\sim$ 10 nm, and lateral devices on $\sim$ 100 nm length scales. These experiments have used tunnel junctions to achieve spin injection, primarily for measuring P_{FM}, or low-resistance interfaces for measuring $\lambda_{s,FM}$. The lateral geometry has been used with either tunneling or low-resistance interfaces to measure $\lambda_{s,N}$ and possibly the FM parameters as well.

1.3.1 Vertical Devices - GMR and TMR

Spin transport models, reviewed in §1.2, have been applied to a number of experiments dealing with spin transport in metals. Tunneling experiments have been used to measure P_{FM}, although the values obtained are sensitive to the properties of the tunnel barriers. Spin tunneling into superconductors can be extremely useful for measuring P_{FM}. These measurements, however, are limited to a maximum temperature of the superconducting transition temperature. Despite the usefulness of tunneling devices for determining P_{FM}, the magnitude of the spin-dependent tunneling is independent of $\lambda_{s,FM}$. Tunneling experiments are therefore incapable of yielding information about $\lambda_{s,FM}$. To determine spin lifetimes or diffusion lengths in FM materials requires diffusive interfaces.

The polarizations of FMs taken from a variety of tunneling measurements are summarized in Table 1.1. Primarily, these are Meservey-Tedrow style tunneling experiments [60], where the conductance of tunneling from an FM strip into a superconducting (TSC) strip is used to determine the polarization of the ferromagnet. Values of P_{FM} obtained using point-contact Andreev reflection (PCAR) and tunneling magnetoresistance (TMR) between two FM layers are also shown.

The table of reported values show a low-temperature P_{FM} of Py near 45% for several Meservey-Tedrow style experiments, while a smaller value of 37% is observed by PCAR. The P_{FM} of Co, on the other hand, has been reported over a larger range from 34 % to 42 % among similar experiments. Since these techniques use a superconducting electrode, they are limited to temperatures below 5 K. Monsma *et al.* used Cu-doped Al to increase the critical field and temperature of the superconducting strip, but were still limited to low temperatures. Magnetic tunnel junctions, on the other hand, are capable of measuring to higher temperatures, potentially up to the magnetic transition temperature. Shang *et al.* measured a weak temperature dependence of P_{FM} for Co

Material	Geometry	T (K)	P_{FM} (%)	Ref.
Py	TSC	0.4	45	[61]
Py	PCAR-Nb	≤ 4.2	37 ± 5	[62]
Py	TSC	≤ 0.4	45	[63]
Py	MTJ	4.2 — 300	42 — 33 ± 3	[64]
Fe	TSC	0.4	44	[60]
Fe	PCAR-Nb	≤ 4.2	42 ± 2	[62]
Ni	TSC	0.4	11	[60]
Ni	PCAR-Nb	≤ 4.2	43 ± 2	[62]
Ni	TSC	≤ 0.4	31	[63]
Co	TSC	0.4	34	[60]
Co	PCAR-Nb	≤ 4.2	42 ± 2	[62]
Co	TSC	≤ 0.4	42	[63]
Co	MTJ	4.2 — 300	34 — 33 ± 2	[64]

TSC	Spin tunneling into superconducting strips
PCAR-Nb	Point contact Andreev reflection using Nb tip electrodes
MTJ	TMR measurements of magnetic tunnel junctions

Table 1.1: Experimentally-determined ferromagnetic polarizations from tunneling experiments.

MTJs over a range of temperatures from 4.2 K to room temperature [64]. The same set of experiments demonstrated a larger temperature dependence of the P_{FM} of Py. P_{FM} decreased by over 20% from $T = 4.2$ K to 300 K, which is more than twice the reduction of the corresponding bulk M_s. This has been attributed to soft-surface magnon modes having a stronger temperature dependence than bulk. Below 300 K, the temperature dependence of M_s for Py and Co is expected to be determined by the magnons and therefore follow the Bloch $T^{3/2}$ law. P_{FM} is expected to follow M_s so that,

$$P_{FM}(T) = P_0(1 - \alpha_B T^{3/2}), \tag{1.83}$$

where the coefficient α_B determines the strength of the temperature dependence. The value of α_B of bulk Py and Co ferromagnets is $\alpha_B \approx 10^{-6}\,\mathrm{K}^{-3/2}$ for Co and $\alpha_B \approx 10^{-5}\,\mathrm{K}^{-3/2}$ for Py [65]. The electron polarization at the ferromagnetic surface is suppressed by softer magnon modes, leading to a larger value of α_B which can be several times that of bulk. The measured value of α_B for Py from these magnetic tunnel junctions is $3 - 5 \times 10^{-5}\,\mathrm{K}^{-3/2}$ [64].

The spin diffusion length in ferromagnets $\lambda_{s,FM}$ can be determined from vertical GMR type structures. The experimentally determined $\lambda_{s,FM}$ tabulated for a variety of experiments is summarized in Table 1.2. The most common experimental technique used is the CPP-GMR measurement, although lateral non-local devices are also used and have been included in the summary. Different FM materials are included, especially those used within this thesis, at various temperatures. The measured $\lambda_{s,FM}$ from fitting experimental data are included with the corresponding ρ_{FM}, when available. Spin relaxation in N metals is expected to follow the Elliot-Yafet mechanism, however there is less of a consensus for the mechanism responsible for determining $\lambda_{s,FM}$. Nevertheless, one might expect the product $\rho_{FM}\lambda_{s,FM}$ to be constant for each material.

The FM metals and alloys have been found to follow an empirical relation consistent with an average $\rho_{FM}\lambda_{s,FM}$ across many elemental and alloyed ferromagnetic metals,

$$\lambda_{s,FM} = C_{FM}\frac{1}{\rho_{FM}}, \tag{1.84}$$

across materials and techniques with the exception of pure Co and Fe [66]. Using a survey of several experimental values reported in the literature [42, 43, 67–69], $C_{FM} = 6.74 \times 10^{-6}\,\mu\Omega\,\mathrm{cm}^2$. It turns out that this is empirically true for a large number of

materials with the exception being the large $\lambda_{s,FM}$, greater than 40 nm, for Co [41, 70] and the low ρ_{FM} of Fe despite $\lambda_{s,FM} < 10$ nm.

Material	Geometry	$\frac{T}{\mathrm{K}}$	$\frac{\rho_{FM}}{\mu\Omega\,\mathrm{cm}}$	$\frac{\lambda_{s,FM}}{\mathrm{nm}}$	$\frac{\rho_{FM}\lambda_{s,FM}}{\mathrm{p}\Omega\,\mathrm{cm}^2}$	Ref.
Py	CPP-NW	77		4.3 ± 1		[67]
Py	LNL/X	293	27.8	3	8	[42]
Py	LNL/X	79	23.6	14.5	34	[71]
Co	CPP-S	4.2	6.0	≥ 40	≥ 24	[70]
Co	CPP-NW	77	16.0 ± 2.0	59 ± 18	90	[41]
Co	CPP-NW	300	21.0 ± 3.0	38 ± 12	80	[41]
Fe	CPP-S	4.2	4.0	8.5 ± 1.5	3.4	[72]
Ni	CPP-S	4.2	3.3 ± 0.3	21 ± 2	7	[73]

CPP-NW	CPP-GMR using electrodeposited nanowire multilayers
CPP-S	LNL spin valve measurements with superconducting strips
LNL-X	LNL cross spin valve measurements with diffusive metallic contacts

Table 1.2: Experimentally determined ferromagnetic spin diffusion lengths.

1.3.2 Lateral Spin Valve Experiments

Lateral non-local spin valves offer much of the same functionality of GMR devices with the added ability to measure over a much larger range of geometries. Unlike GMR devices, the non-local geometry allows the measurement of a purely diffusive spin current. The models for such depend both on the N and FM spin-dependent properties: $\lambda_{s,N}$, $\lambda_{s,FM}$, and P_{FM}.

Previous experiments to extract $\lambda_{s,N}$ have been conducted by a variety groups on a subset of several different materials combinations. Some of the results for $\lambda_{s,N}$ for the most commonly used metals are shown in Table 1.3. The values tabulated here are taken primarily from lateral non-local spin valve measurements with a few vertical GMR devices included for comparison. As described, the Elliot-Yafet relaxation mechanism predicts the product $\rho_N \lambda_{s,N}$ to be constant for a material. The table demonstrates that this is not experimentally verified for the case of Cu. The inconsistencies of $\rho_N \lambda_{s,N}$ requires that either Elliot-Yafet does not hold or that an extrinsic relaxation mechanism

Material	Geometry	$\frac{T}{\mathrm{K}}$	$\frac{\rho_N}{\mu\Omega\,\mathrm{cm}}$	$\frac{\lambda_{s,N}}{\mathrm{nm}}$	$\frac{\rho_N \lambda_{s,N}}{\mathrm{p}\Omega\,\mathrm{cm}^2}$	Ref.
Cu	CPP-NW	77	3.1	140 ± 15	40	[74]
Cu	CPP-NW	300	2.0 — 6.5	36 ± 14	4 — 30	[75]
Cu	LNL-C	4.2	1.4	1000 ± 200	140	[23, 76]
Cu	LNL-C	293	2.9	350 ± 50	100	[23, 76]
Cu	CPP-VE	293		170 ± 40	≥ 24	[77]
Cu	LNL-X	293	2.1	500	110	[78]
Cu	LNL	293	2.1	700	150	[79]
Cu	LNL	4.2	3.4	920	310	[79]
Cu	LNL-H	4.2	3.4	546	190	[80]
Cu	LNL	10	1.36	200 ± 20	30	[81]
Cu	LNL	300	3.4	> 110	≥ 40	[81]
Cu	LNL	10	0.69	1000	69	[43]
Cu	LNL	40	≈ 0.7	1350	≈ 95	[43]
Cu	LNL	292	2.35	400	95	[43]

CPP-NW	CPP-GMR using electrodeposited nanowire multilayers
CPP-VE	CPP-GMR using EBL defined trilayer devices
LNL	LNL spin valve measurements with diffusive metallic contacts
LNL-H	LNL Hanle effect measurements with diffusive metallic contacts
LNL-X	LNL cross spin valve measurements with diffusive metallic contacts
LNL-C	LNL spin valve measurements with extra diffusive FM contacts

Table 1.3: Experimentally-determined non-magnetic metal diffusion lengths.

is present. The inconsistencies could be due to impurities, grain boundaries, or finite-size effects on the scattering. The inconsistency of $\rho_N \lambda_{s,N}$ and possible explanations can be systematically investigated by varying materials and geometry, which has been done as part of this work.

The lateral geometry can also be used to extract P_{FM} and $\lambda_{s,FM}$ from transport experiments as the magnitude of the spin valve signal depends on both. Data from a small subset of experiments using Py contacts is shown in Table 1.4 with a large range of reported values, both below and above the values determined from tunneling experiments. The difficulties of reliably extracting P_{FM} from lateral spin valves are discussed in §4.4.2.

Material	Geometry	T (K)	P_{FM} (%)	Ref.
Py	LNLSV	4.2	20	[76]
Py	LNLSV	300	25	[42]
Py	LNLSV	4.2 — 292	58 — 49	[43]

Table 1.4: Experimentally-determined ferromagnetic diffusion lengths.

1.4 Remarks

The experiments described in this thesis were designed to test the effects of nanostructuring on spin relaxation and diffusive transport across FM/N interfaces in the framework of the theory and previous experiments discussed in this chapter. The FM and N materials used are varied to explore the contributions from each in determining the spin-dependent transport in lateral spin valves. The investigation of the roles of various material properties were done using devices fabricated with the same technique for each material combination. Studying a variety of materials with one technique is an advantage of this work that has not been done elsewhere. In this work FM materials, Py and Co, were used with both Cu and Al channels.

Chapter 2

Experimental Techniques

2.1 Introduction to Experimental Techniques

The measurement of spin transport in lateral spin valves patterned on nanoscopic length scales requires precise experimental techniques. The ability to pattern devices on sub-micron length scales allows for the observation of materials physics that cannot be observed in bulk. To accomplish this, lithographic techniques with resolution beyond that of traditional optical lithography are required. Electron beam lithography (EBL) is well-suited for the task. In particular, the short wavelength of the electron beam can create patterns ($\sim$ 10 nm) that are small enough to allow the fabrication of metallic lateral spin-transport devices.

Controlling the quality of materials and interfaces is critical for the studies undertaken in this thesis. To achieve the necessary level of control, careful attention must be paid to the deposition source materials and to the vacuum environment in which samples are deposited. Ultra high vacuum (UHV) evaporation systems provide an ideal environment for the deposition of patterned devices. This chapter will describe the methods used to deposit multiple patterned materials in succession without breaking vacuum using a multi-angle shadow evaporation process.

Quantifying spin transport in the devices discussed in this thesis requires measuring voltages as small as 1 nV, making experiments sensitive to the measurement environment. At these small voltages, spin transport measurements require careful regulation of temperature T, applied magnetic field H, and minimization of background electronic

noise. The techniques described in this chapter provide the foundation for conducting these experiments successfully.

2.2 Sample Patterning Techniques

The lateral non-local spin valve device (L-NLSV), introduced in §1.2.10, is utilized extensively in the experiments described in this thesis due to its unique experimental advantages, which include the isolation of a pure spin current, as well as geometric and materials flexibility. The L-NLSV device fabrication technique has been designed to maximize reproducibility while maintaining the ability of the materials and geometry to be varied. The materials and thicknesses deposited through the prepared mask patterns can be varied to study the impact on spin transport.

Throughout Chapter 1, the sensitivity of spin transport to the FM/N interfaces was emphasized. Therefore, experimental FM/N interfaces must be controlled. Rather than attempt an etch process to clean the surface of a material before the deposition of the subsequent layer, as has been done elsewhere [76], we employ a multi-angle deposition technique similar to that employed in Reference [82]. This method employs deposition of the FM and N materials at different angles (§2.2.2) relative to the substrate, without breaking vacuum, to achieve the desired heterostructure. This technique has been dubbed *in-situ* deposition and allows for the FM/N interfaces to be prepared with minimal contamination, as described in §2.3.1.

2.2.1 Lithography

Lithography is at the heart of micro- and nano-device fabrication. The process comprises exposing and developing a polymer resist to pattern features. The patterned structures usually serve as templates for selectively adding or removing material, referred to as liftoff or etch processes respectively. Liftoff processing used in this work will be described later in this section. While an array of patterning techniques are now available, the bulk of these fit into the categories of electron beam lithography and optical lithography. Although electron beam lithography (EBL) is primarily used here, conceptually similar methods are used for photolithography.

The general scheme for a liftoff style fabrication is depicted in Figure 2.1. Each of

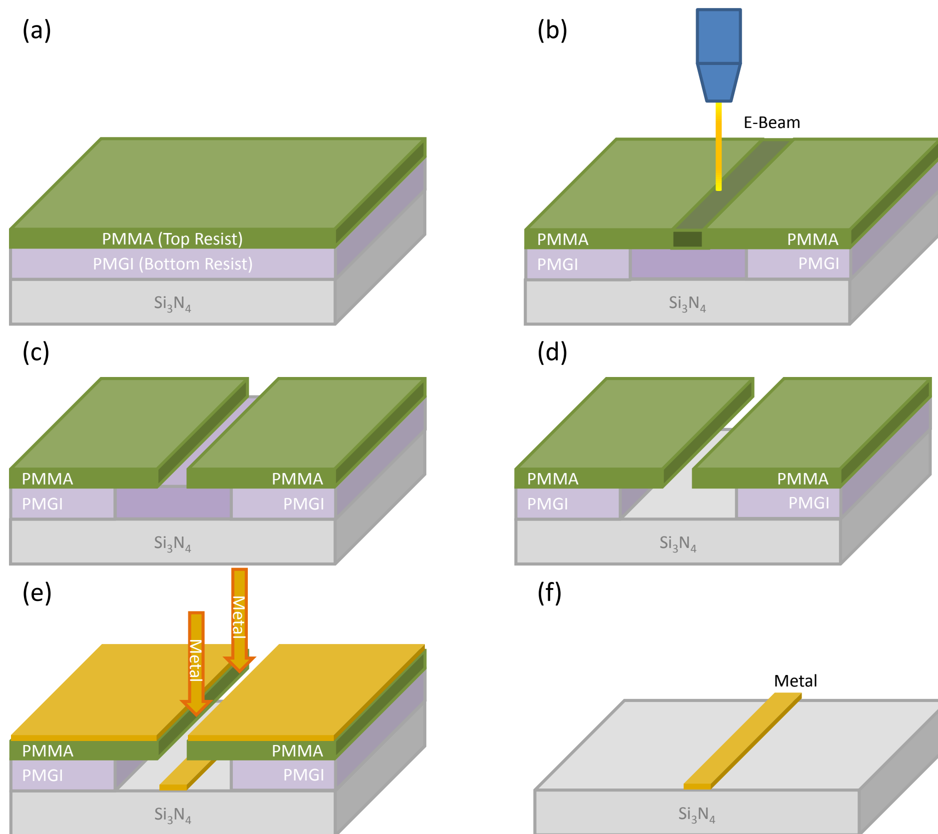

Figure 2.1: Graphical depiction of the generalized fabrication steps of electron beam lithography, deposition, and liftoff processes. (a) A resist bi-layer is spun onto a substrate then (b) exposed using a rastered electron beam depicted by darkened resist. (c) The top layer is developed first first followed by (d) the second layer which creates an undercut. (e) Materials are then deposited and (f) the excess material is removed by lift-off of the resist.

the basic steps required to lithographically fabricate a feature using a liftoff-type process is shown, resulting in the creation of a simple feature. A resist bi-layer is initially spun onto a substrate to a desired thickness, shown in (a). Using a rastered beam of high-energy electrons, the resist is then exposed, depicted by darkened resist in (b). In the case of a bilayer resist stack, with the appropriate combination of resists the two layers can be developed independently. Developing the top layer first (c), followed by the second layer (d), creates an undercut. Materials are then deposited (e) and the excess removed by stripping the resist, leaving the desired structure (f).

Resists

Polymer-based resists are used to create shadow masks used for fabricating the devices described in this thesis. Resists are exposed using photons or electrons, serving to either break down or cross-link the polymer chains. The breaking of positive resist chains during exposure, known as scission, makes resist easier to remove with chemical developer. After development, a patterned polymer template remains. Alternatively, exposure of negative resist crosslinks the polymers, hardening it against removal in developer. The energy-dependent exposure sensitivity varies by resist composition and must be chosen according to the method of exposure.

Prior to exposure, the resist is coated onto a substrate. Resist in a solvent is placed on a substrate and rapidly spun in plane to form a thin layer with thickness determined by the properties of the resist solution and the angular velocity of the spin. The coated substrate is then baked to remove the solvent and form a hardened film. This is typically done on a hot-plate at temperatures 100 °C to 200 °C for several minutes.

Two resist layers on a single substrate are often employed for lift-off processes; a bottom resist layer is first spun and baked followed by a second layer. Constituent resists for the bi-layer are chosen to avoid inter-solubility as well as to ensure compatibility of bake temperatures. This starting point is depicted in Figure 2.1(a). Details of the resists and fabrication recipes are given in Appendix B.

The resists used in this work to for the critical EBL patterns are formed of bi-layers, recipies for which can be found in §B.4 and §B.5. For the devices discussed in this thesis, a bi-layer resist was spun out on a p-type 10 Ω cm silicon substrate with a silicon-nitride layer nominally 200 nm thick. An underlayer of polydimethylglutarimide

polymer (PMGI) was spun first to 700 nm thick at 3200 RPM. The PMGI layer was baked at 150 °C for 20 minutes followed by 5 minutes at 180 °C. The PMMA layer is then added, spun at 5100 RPM to a thickness of 300 nm, and baked for 20 minutes at 180 °C.

Exposure

Optical lithography encompasses a broad range of operational methodologies and is frequently used. Standard optical techniques involve exposing resist simultaneously across large areas of the substrate surface. This is accomplished by flooding the substrate with light while some regions are shadowed by a mask plate in contact with the resist defining the pattern to be exposed. This technique is used to pattern $\sim 100\,\mu\text{m} \times 100\,\mu\text{m}$ bonding pads and interconnecting conducting channels, often referred to as vias.

The method used in this work to pattern the NLSV devices themselves is electron beam lithography. This uses a high-energy electron beam which is rastered across the resist to expose the desired pattern. This is depicted graphically in Figure 2.1(b) by a darkening of the resist in the exposed region. This technique is capable of feature sizes down to ≈ 10 nm.

The bulk of the lithography undertaken as part of this work was done using a Raith 150 EBL system unless specifically designated. This tool consists of a LEO/Zeiss scanning electron microscope (SEM) with additional stage leveling and beam control electronics to adapt it for lithography work. The electron beam voltages available for this system are similar to that of a typical SEM 1 – 30 kV. For a standard positive resist, such as PMMA, typical exposures of $300\,\mu\text{C}\,\text{cm}^{-2}$ are required in this energy range. For these exposures beam currents of 20 pA were used. Although this system is capable of the resolution required to make the desired structures, this hybrid machine is much less stable and reliable than purpose-built systems.

Towards the conclusion of this work a new 100 kV purpose-built Vistec EBPG 5000+ EBL system was made available and the process was adapted to it. Due to the much higher energy electrons used in this case the resolution is increased. The exposure through the resist depth is much more confined and provides a more columnar profile for higher energy electrons. In contrast, the lower voltage beams deposit energy as they traverse the resist and scatter, as a result the exposure tends to broaden laterally near

the bottom of the resist. This effect makes creating small features on think resist stacks at low beam energies difficult. At higher voltages, the sensitivity of resist to the incident electrons is reduced. Increasing the electron energy from 30 keV to 100 keV requires that the dosage be increased from approximately 300 to 950 $\mu C\,cm^{-2}$, so given a fixed beam current the exposure will take three times longer. This can be compensated for by using larger beam currents. Comparable devices patterned with this system use beam currents of 0.1 nA to 2 nA.

More details of photolithographic processes and EBL are given in §B.1.2.

Developing

Once exposed, the structure is developed using a wet chemical process. This requires placing the resist in a developer bath for a length of time followed by immersion in a stop bath, typically deionized water (DI H_2O) or isopropanol (IPA). Developing of positive resist removes the exposed resist. A bilayer resist stack with the appropriate choice of resists and developer selectivity allows only the top resist layer to be developed by the first round of developer shown in Figure 2.1(c). A second develop and stop can then be used to remove only the exposed bottom layer. With the ability to independently develop each layer, the bottom layer can be developed beyond that of the top layer, creating an undercut (shown in Figure 2.1(d)) necessary for liftoff-type processes. More details are found in §B.1.3.

The patterned resist bi-layers used in this work are selectively developed with two different developers. PMMA is developed using methyl isobutyl ketone in isopropanol (MIBK:IPA) at a volumetric ratio of 1:3 at room temperature, which is often used for high resolution feature development [83]. The patterned substrate is placed in IPA for 60 s to stop the develop process and gently blown dry with dry N_2 gas. After drying the sample, the PMGI underlayer is developed using Microposit® MF® CD-26 Developer in IPA with a volumetric ratio of 1:30. CD-26 is a proprietary developer formulation with 2.4% tetramethylammonium hydroxide (TMAH) in water [84]. Although ratios of CD-26:IPA of 1:3 are typically used, the process developed for this thesis requires strict control of the undercut rate so a ratio of 1:30 is used. The PMGI was developed for 35 s when exposed with 30 keV electrons. The develop time was increased to 50 s for patterns exposed with 100 keV electrons. Again the sample is placed in IPA for 60 s to

stop the develop process and gently blown dry with dry N_2 gas.

A final step prior to metallization is to descum the substrate surfaces using a reactive-ion etch. The etch increases adhesion of subsequently deposited materials to the substrate surfaces by stripping off residual resist that was not removed by the develop process. The etch typically employed is a short O_2 reactive ion etch, known as an O_2 ash. This was done using an oxygen plasma barrel etcher that achieves typical resist removal rates of 120 Å/min [85]. This is done for 20 s at pressures up to a ~ 1 Torr at applied radiofrequency power up to 100 W removing $\lesssim 40$ Å, the details of which can be found in §B.4 – B.5. This serves to descum the surfaces by reactively destroying the resist using energetic oxygen ions that then create carbon oxides which can be pumped away by a vacuum pump.

Deposition

After the develop and ash steps, the pattern is ready for materials deposition. This is typically done using a physical vapor deposition process such as evaporation or magnetron sputtering. In this work, electron beam evaporation was used, discussed in detail in §2.3.2 as part of a larger discussion of the vacuum deposition system employed (§2.3). The deposition of evaporated metal onto the patterned substrate is depicted in Figure 2.1(e).

Liftoff

The final step in the process is to liftoff the excess metal. This is accomplished by submersion in organic solvents to strip the resist and, with it, the material intended to be removed. After liftoff, only the desired structure remains, corresponding to the original patterning of the resist, shown in Figure 2.1(f).

The samples were immersed in N-methylpyrrolidone (NMP) for the liftoff of resists and excess metals. Due to the relatively low vapor pressure of NMP based solvents, 9.5 Torr at 80 °C for NMP compared to 1520 Torr for acetone [86], elevated temperatures of 80 °C for the NMP were used to accelerate the liftoff process. Agitation of the liftoff solvent in a sonicator was not used. A much less aggressive technique is employed in this work for EBL, using an eyedropper to gently move the solvent back and forth past the piece to be lifted off. This technique can significantly reduce the liftoff time while

avoiding damage to the structures. These devices required between 30 minutes and 45 minutes to liftoff. After removal from the NMP the structures were rinsed with acetone, MeOH, IPA, and blown dry with N_2 leaving only the desired structure, corresponding to the original patterning of the resist shown in Figure B.1(f).

Further details are included in Appendix B: §B.1.5.

Electron Beam Lithography Exposure Dosage

Electron beams are used to expose resist, as discussed in §2.2.1. The dosage required for the particular case of a bottom layer of resist with thickness $t_B \approx 750$ nm of PMGI and with top resist layer thickness $t_T \approx 300$ nm of high resolution PMMA is between $330\,\mu\mathrm{C\,cm^{-2}}$ (with beam energy 30 keV) and $950\,\mu\mathrm{C\,cm^{-2}}$ (at 100 keV). To properly expose a broad range of feature sizes requires a non-uniform dosage, which is determined by accounting for proximity effects. Adjusting for proximity effects allows the desired features to be patterned with reduced distortion, discussed further in §B.3.

2.2.2 Multi-Angle Deposition Lithography

The generic lift-off process described above has been used with a process of evaporating source materials at multiple angles relative to the substrate. The shadow masking of deposition materials sourced from different angles through a pattern can create overlapping material shadows, able to form multi-material device structures. This technique has been employed to create lateral spin valves without breaking vacuum, as depicted in Figure 2.2. A resist bilayer is prepared, as described in §2.2.1. The resist underlayer is overdeveloped, however, resulting in an extreme undercut. The materials are then evaporated from sources at angles θ_d relative to the substrate, depositing through tunnels created under the top layer by the undercut of the bottom resist layer. At large θ_d the finite thickness of the top layer t_T will prevent material from being deposited through gaps smaller than

$$y_F = t_T \sin \theta_d, \tag{2.1}$$

in the tilt direction. These materials will then overlap to create the desired structure. Consideration of these geometrical constraints goes into the pattern design to be exposed and the deposition angles to be used to create working devices, discussed further in

§2.2.3.

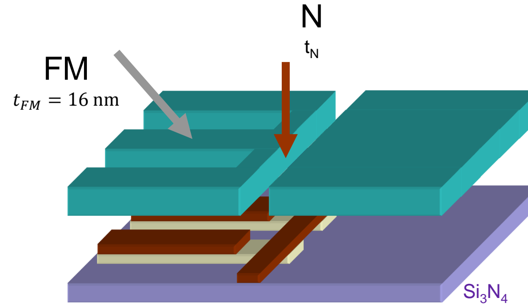

Figure 2.2: General scheme for the multi-angle shadow evaporation technique. A FM material is deposited at an angle relative to the substrate followed by an N material deposited at normal incidence so that they overlap to create a lateral spin valve.

Figure 2.2 depicts a suspended resist pattern which serves as a shadow mask for evaporated materials. The FM material is evaporated first, at an angle relative to the substrate normal. The resulting pattern follows the mask shape but is laterally translated by $t_B \tan\theta_d$. The N metal is then evaporated at normal incidence, creating a shadow pattern that overlaps with the deposited FM material, thus creating a lateral spin valve.

2.2.3 Non-Local Spin Valve Device Design

The pattern for each non-local device is exposed such that there exists an N channel and a pair of FM contacts to serve as the spin injector and detector. Since knowledge of the contact resistance is crucial, each FM contact has two connecting vias so that a quasi four-terminal measurement of the interface resistance R_I can be made, as discussed in §3.2.

Additionally, the coercive fields H_c of each FM contact must be sufficiently different to allow the FM contacts to be placed in the anti-parallel magnetization configuration via an applied magnetic field. This is accomplished by patterning the FM contacts to have different widths, resulting in different demagnetization factors. The design pattern

and deposition techniques employed allow each FM contact to be grown isolated from other FM material, resulting in increased H_c compared to that of large interconnected FM bonding pads, vias, and FM contacts. Each FM contact has a width w_{FM} ranging from 100 nm to 250 nm and a length $l_{FM} \approx 1\,\mu\text{m}$.

The magnetization reversal of FM structures, with cross-sectional dimensions on the order of the width of the domain wall, is not expected to follow coherent rotation, although the demagnetization factors [87] still serve as a guide to the dependence of H_c on w_{FM} and l_{FM}. Reversal is likely to occur via the nucleation and propagation of a domain wall through the FM contact. The field required to cause magnetic reversal in this case depends on the activation volume for a domain wall to nucleate in the FM, decreasing monotonically with increasing w_{FM}. For the regime where $l_{FM} \gg w_{FM} \gg t_{FM}$ the the reversal field follows approximately [88],

$$H_c \propto \frac{1}{w_{FM}}. \tag{2.2}$$

Although other physical phenomena, such as pinning, may contribute to the coercivities of the two FM contacts, the demagnetization field alone leads to different H_c for each FM. The measured difference of H_c between the two contacts is about 70 G in the case of Py and 150 G for Co at $T = 5\,\text{K}$. Measured values of the reversal fields are shown in §3.10.

Given these considerations, an exposure pattern that satisfies these design requirements is shown in Figure 2.3. The N regions are shown in blue which is coincident with the exposed resist, while the in-plane shifted FM regions are shaded red.

2.3 Deposition of Materials in Vacuum

The relevant materials are vacuum deposited through the masks described in §2.2. The use of high-purity source materials in a UHV environment minimizes the concentration of impurities in the deposited structures. The shadow-mask fabrication scheme requires the directional deposition of materials, which was done by electron-beam evaporation (§2.3.2), although the ability to evaporate transition metal ferromagnets by resistive thermal evaporation (§C.3) was added to the vacuum system.

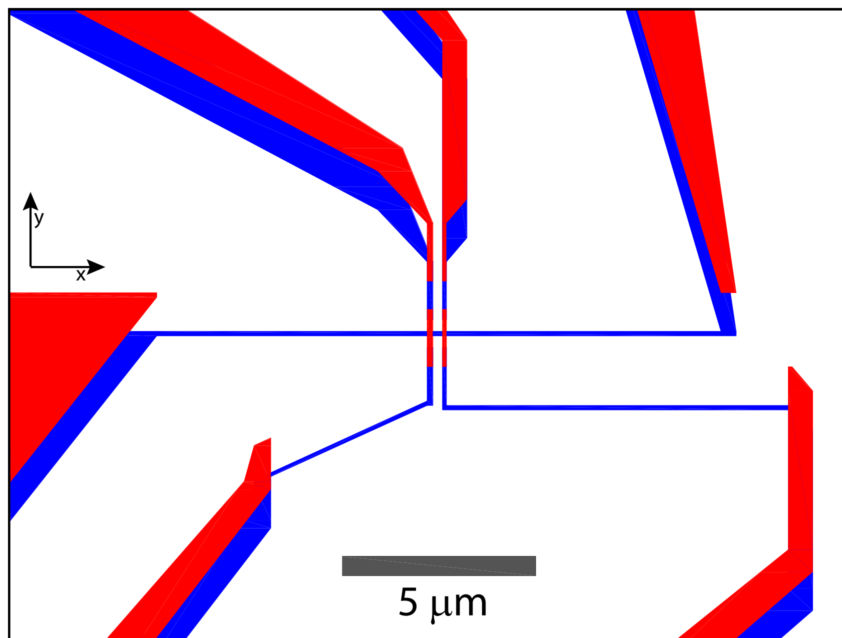

Figure 2.3: Non-local spin valve pattern layout for shadow evaporation (blue) and the FM projection due to deposition at an angle (red).

2.3.1 Ultra-High Vacuum Deposition System

The home-built UHV deposition system is capable of reaching pressures $\lesssim 10^{-11}$ Torr and has been described in its previous configuration by Lund and Leighton in Reference[89]. Many additional details of the system are given in Appendix C:

- §C.1 contains further discussion and details of the UHV vacuum system used for sample deposition.

  §C.1.1 gives information and background on the pumping systems used to achieve UHV.

  §C.1.2 provides basic operation details for vacuum gauges used to measure the pressure of the UHV system.

- §C.2 includes background information about electron beam evaporation techniques, beyond that provided in this chapter (§2.3.2).
- §C.2.1 gives further information about details of the evaporation onto resist coated substrates, and incidental exposure considerations that need to be made.
- §C.3 includes details of the thermal evaporation sources and capabilities of the system.
- §C.4 includes background information on the quartz crystal microbalance measurement of deposited film thicknesses.
- §C.5 describes the operation of two-evaporation-sources capable of co-deposition of two materials and the deposition of superlattices

2.3.2 Electron Beam Evaporation

The deposition of materials by evaporation is accomplished by creating a source vapor that is then condensed on a substrate. Directional deposition techniques are desirable for shadow mask deposition. This is generated if the mean free path of the gas molecules or atoms λ_g is much larger than the source to substrate distance d_{ss}. The mean free path can be written in the kinetic theory of gases as,

$$\lambda_g = \frac{k_B T}{\sqrt{2}\pi d_g^2 P_g}, \tag{2.3}$$

where k_B is the Boltzmann constant, T is the temperature of the gas, d_g is the diameter of the scattering gas particles, and P_g is the pressure.

In UHV, $\lambda_g \approx 3 \times 10^6\,\mathrm{m}$ for nitrogen ($d_g = 1.42\,\mathrm{Å}$) at $P_g = 10^{-10}\,\mathrm{Torr}$, larger than any realistic vacuum system. Alternatively, Ar sputtering processes, with typical $P_g = 2 \times 10^{-3}\,\mathrm{Torr}$, have $\lambda_g = 8\,\mathrm{cm} \lesssim d_{ss}$. In the case of the UHV system described here, $d_{ss} \approx 69\,\mathrm{cm}$ which is much less than λ_g. Due to the large d_{ss}, the distribution of arrival angles of the deposition material is $\leq 2°$.

An electron beam evaporator, generically shown in Figure 2.4, operates by heating a source ingot with an intense beam of electrons until it evaporates. The electrons are sourced from a filament by thermionic emission and then accelerated by an anode, in this case held at $V_a = 7\,\mathrm{kV}$. The electron beam is manipulated by a magnetic field created by permanent magnets via the Lorentz force so that it is incident on the source material. The energy of the bombarding electrons is then dissipated in the source, thereby locally heating it. The precise positioning of the beam is done by a pair of orthogonal coil sets. These steering coils are able to adjust the beam position on the source in both in-plane directions with the application of small fields. Continuously sweeping the beam over the source material provides uniform heating over a larger area. This is especially useful for materials with low thermal conductivities, for which a stationary beam may only evaporate material locally, drilling a hole through the ingot and making ineffective use of the source material. As shown in Figure 2.4, the source material is placed in a water-cooled copper hearth. Materials with high thermal conductivities are placed in a thermally-insulating crucible liner to isolate the material from the cooling of the hearth. The liner also prevents the inter-diffusion of source materials with the hearth.

To control the evaporation rate, the power P_W imparted to the source by the electron beam can be adjusted. This can be expressed simply as $P_W = I_e V_a$, where V_a is held fixed by the controller while the beam current I_e is adjusted to change the source temperature and, and thereby, the evaporation rate. A quartz crystal monitor (QCM) is used to monitor the thickness of the deposited material. I_e is controlled in order to keep the deposition rate monitored by the QCM fixed. Evaporation rates from $0.01\,\mathrm{Å\,s^{-1}}$ to $10\,\mathrm{Å\,s^{-1}}$ can be achieved. In the chamber configuration described above rates greater than $3\,\mathrm{Å\,s^{-1}}$ are difficult to achieve due to the large source-substrate distance.

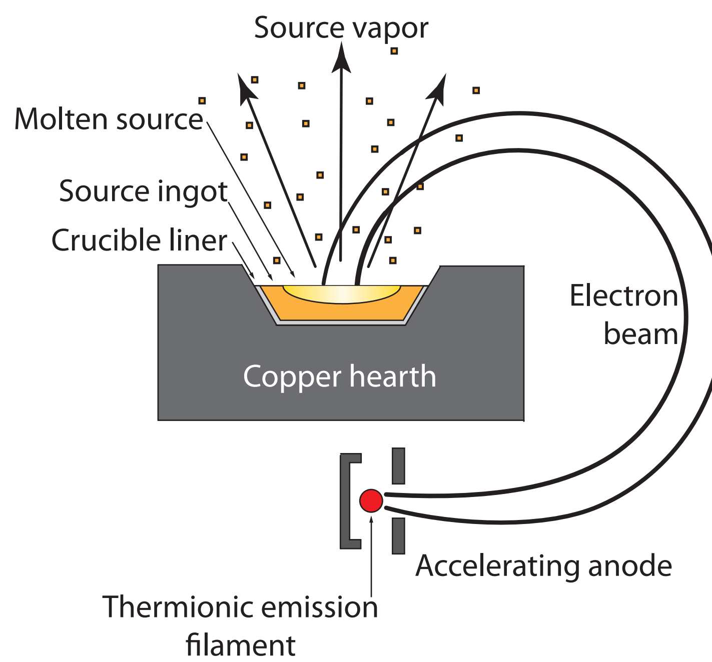

Figure 2.4: Graphical depiction of the main components of an electron beam evaporation source.

Deposition onto Resist-Patterned Substrates

Evaporating material from a molten metal source held at temperatures of about 1500 °C leads to radiative heating of the resist. For most resists, temperatures below 100 °C will not damage the patterning. However, if heated above the glass transition temperature T_g, which is 105 °C for PMMA [83] and 180 to 190 °C for PMGI [90], the resist will begin to reflow. This can occur in the form of lateral feature distortion or, equally troublesome, the undercut regions may collapse. To avoid this, depositions must be finished before the substrate temperature exceeds T_g of either resist. This is done by adjusting the deposition rate to ensure that the deposition time is sufficiently short. Due to the non-linear dependence of deposition rate on source temperature, the increase in heating of the substrate due to increased source temperature is small compared to the reduction in deposition time. Short depositions at increased rates will reduce the maximum temperature reached during deposition. For lateral spin valves, the FM materials are deposited at 0.5 Å/s and the N materials at 1.0 Å/s, keeping the final sample temperature below 65 °C, as measured by a thermocouple on the sample manipulator.

For a fixed residual pressure inside the vacuum system, and thus a fixed rate of impinging defect atoms or molecules on the growth surface, higher deposition rates allow a smaller number of impurities to be incorporated into the structure. Consequently, the concentration of impurities will be reduced.

One unfortunate consequence of using electron beam evaporation for depositing material in a EBL patterned resist mask is the effect of stray electrons on the mask itself. The high energy electron beam incident on the metallic source material serves as a source of secondary and back-scattered electrons that may reach the sample and cause undesired resist exposure.

A simple but effective solution to this problem is the application of a magnetic field along the path between the source and substrate. A magnetic field of sufficient magnitude orthogonal to the stray electron flux will deflect electrons transiting from the source to the substrate. In this case a magnetic field of $\geq 10\,\mathrm{G}$ applied over a $\approx 10\,\mathrm{cm}$ path of the stray electron flux is sufficient to deflect the electrons due to the Lorentz force and stop them from damaging the resist. This field is generated using a large solenoid external to the vacuum system. A marked improvement has been observed in the ability of the resist to withstand prolonged evaporation when the deflecting field is

present.

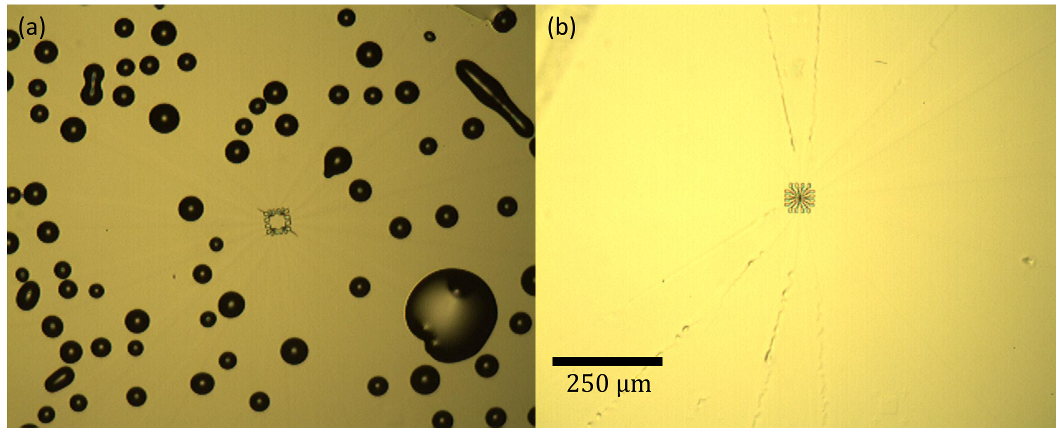

Figure 2.5: Optical micrographs of metal films on resist. (a) Blistering of resist due to secondary electrons. (b) Application of a magnetic field removes the secondary electron flux.

The resist in Figure 2.5(a) shows damage due to secondary electrons, with blisters evident below the metal film. Figure 2.5(b) shows a similarly prepared sample except for the application of a magnetic field to the chamber during growth, resulting in the absence of blistering.

2.3.3 Growth Control Shutters

The flux from the sources is controlled by a set of shutters, further discussed in §C.5.1. These shutters are constructed to block the direct path between the source and the substrate. The system is equipped with three shutters, one for each of the evaporators (e-beam and thermal), along with a master shutter positioned approximately 2 inches below the sample stage.

Normal operation of the master sample shutter is opened(closed) to begin(end) sample deposition. The shutter can also be opened to intermediate states, capable of shelding only a subset of samples loaded for deposition. During deposition, the shutter can be moved to alter the thickness of a layer, for example, while keeping all other growth parameters and materials constant. In this work the shutter was moved in $\approx 10°$ steps,

requiring less than 1 s to change the position, so that the thickness of adjacent samples on the platen can be incremented. The calibration procedure of this shutter is described in §C.5.1. A photograph of the sample holder (platen) and substrate with stepped growth contours are shown in Figure 2.6 along with the corresponding calibration plot. The thickness-dependence experiments contained in this thesis exploit this technique, applying it to fabricate non-local spin valves of varying channel thickness.

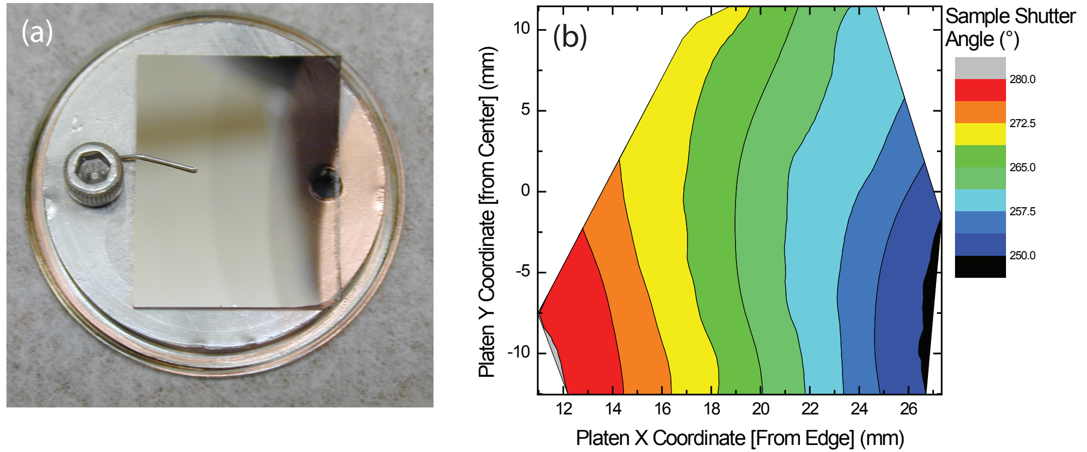

Figure 2.6: (a) A photograph of the sample platen and substrate with stepped growth contours. (b) An xy-plot of the calibrated contours due to intermediate positioning of the sample shutter.

2.3.4 Multi-Angle Deposition

The need to deposit materials at multiple angles relative to the substrate is explained in §2.2.2 and §2.2.3. The UHV deposition system (§2.3.1) was modified to accomplish this task. The stainless steel platen holder attached to the end of the load-lock transfer arm was replaced with a custom ring holder which grasps the platen only by the edges, shown in Figure 2.7. This leaves the sample area of the platen exposed, allowing it to be deposited on from below while remaining on the transfer arm, a side view for a normal incidence deposition is shown in Figure 2.7(c). Since the transfer arm rotates azimuthally about its long axis, the sample can be tilted such that the source material is now at an angle (θ_d) relative to the platen normal, the holder in this configuration is

shown in Figure 2.7(b). Dashed lines are drawn to illustrate where the sample platen is located for a growth. Angles up to $\theta_d \approx 55°$ may be used, which requires the ring to be very thin in the tilt direction. In order for the ring to serve it's standard purpose of transferring samples to and from the growth stage, the transfer arm can be rotated 180°. In this configuration it is capable of transferring the platen to and from the growth stage, shown in Figure 2.7(a).

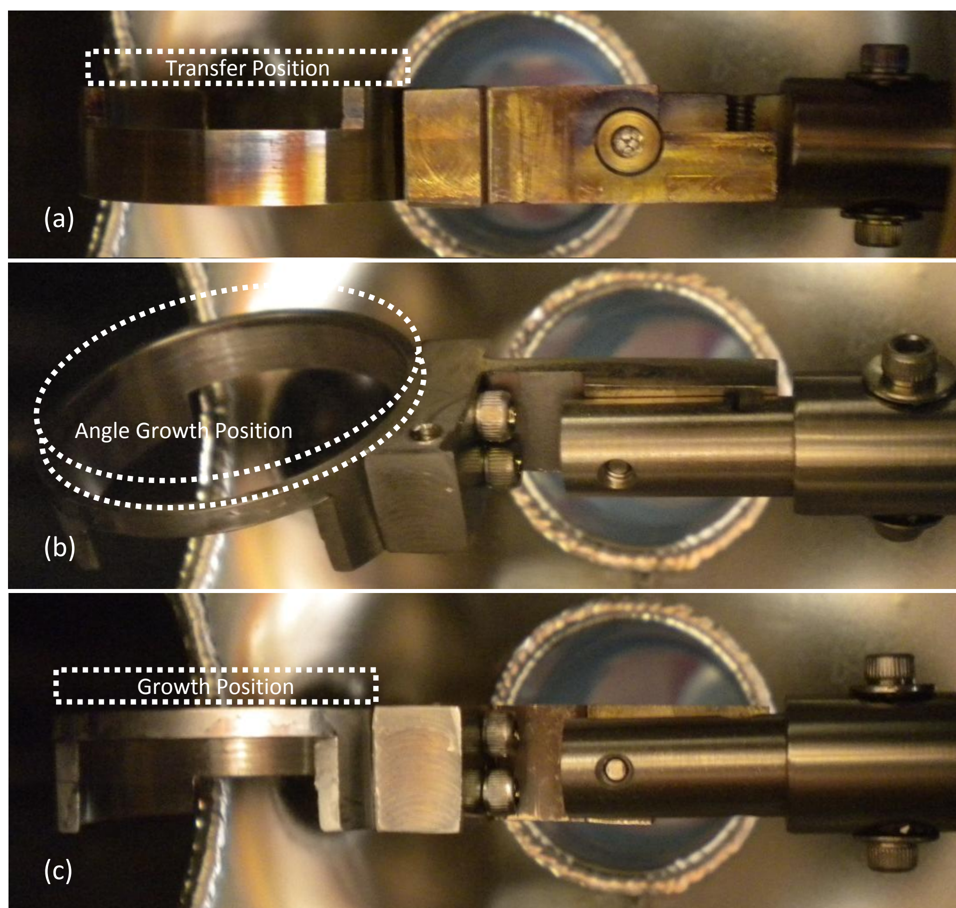

Figure 2.7: *In situ* photographs of the transfer arm taken from the side in the orientation used for (a) transfering platens to and from the manipulator, (b) deposition of materials at non-zero angle of incidence, and (c) deposition of materials at zero angle of incedence.

In-plane rotation of the sample platen allows for the sample's direction of tilt to be adjusted. This is accomplished by loading a stainless steel chuck with a raised

'tongue' and 'dovetail', fabricated specifically for this task, onto the growth stage. A sample platen with a groove on the back is used to mount the samples to be grown on the transfer arm. This allows adjustments of the in-plane angle of the platen on the transfer arm by lowering the vertical position of the growth stage chuck such that the 'tongue and groove' of the two are mated, and then rotated. The dovetail on the rotation chuck assures the chuck will rotate with the stage. The pieces are shown in Figure 2.8; the back of the growth platen is shown on the right and the rotation chuck is shown on the left.

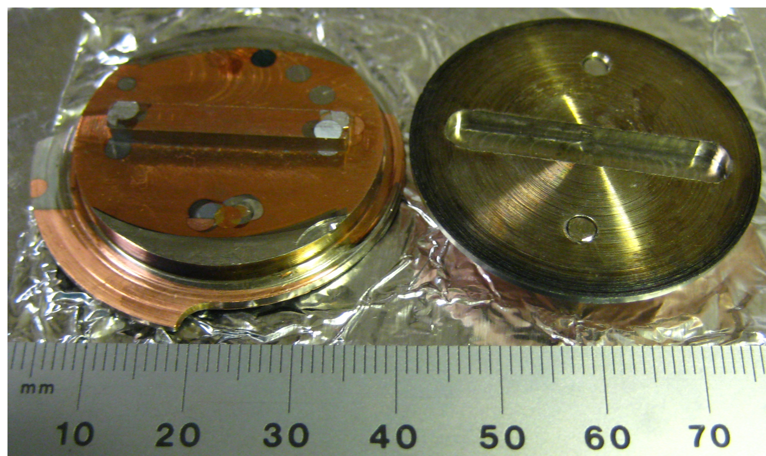

Figure 2.8: The chuck for adjusting inplane rotation (left) and the back of the growth platen (right).

2.4 Materials and Structural Characterization Techniques

A variety of characterization techniques have been employed. Primarily these have been aimed at imaging the device structure, the microstructure of the materials, or measuring the composition of the materials used. This was accomplished using a variety of techniques including x-ray techniques, neutron reflectometry, scanning electron microscopy, and atomic force microscopy.

2.4.1 X-Ray Diffraction

Scattering of x-rays scattering from the constituent atoms in a material leads to a wealth of information about the structure of the material. The angular dependence of the diffracted x-rays gives information about the crystal structure and planar spacings. It can provide information about the orientation of the crystalline components of the material, including the distribution of orientations of the crystallites that comprise a material. Since this technique is not extensively used in this work, further discussion is omitted but many in-depth discussions are available, for instance in References [91–93].

2.4.2 Grazing-Incidence X-Ray Reflectivity

Grazing-incidence x-ray reflectivity (GIXR) is widely used to characterize thin film materials. This technique utilizes collimated x-rays incident at small angles relative to the surface of a thin film. The x-rays undergo reflection from the interfaces between materials and interfere to give an angular dependence to the total reflected x-ray intensity. The angular period of the reflected intensity depends on the thickness of the film. As the thickness of the film is increased the angular period of the interference oscillations decreases, closely related to the Bragg interference condition,

$$n\lambda_i = 2t_f \sin\theta_i, \tag{2.4}$$

where n is the interference order, λ_i is the wavelength of the incident x-ray radiation, t_f is the layer thickness, and θ_i is the angle formed between the incident x-rays and the film surface. More correctly, the the critical angle θ_c below which the incident x-rays undergo total internal reflection in the film needs to be accounted for. In these experiments Cu K_α radiation, with a wavelength $\lambda_i = 1.542\,\text{Å}$, is used [94].

The typical experimental reflectometry geometry is shown in Figure 2.9. The incident probe beam with wavevector $\vec{k_i}$ impinges on the sample at an angle of θ_i with respect to the substrate. The beam is then reflected from each interface with wavevector $\vec{k_f}$ that makes an angle θ_f with the substrate. The change in wavevector of the incident and outgoing beams is

$$|\vec{q}| = \left|\vec{k_f} - \vec{k_i}\right| = \frac{4\pi}{\lambda_i}\sin\theta_i. \tag{2.5}$$

In these experiments specular reflection, $\theta_i = \theta_f$, is typically used.

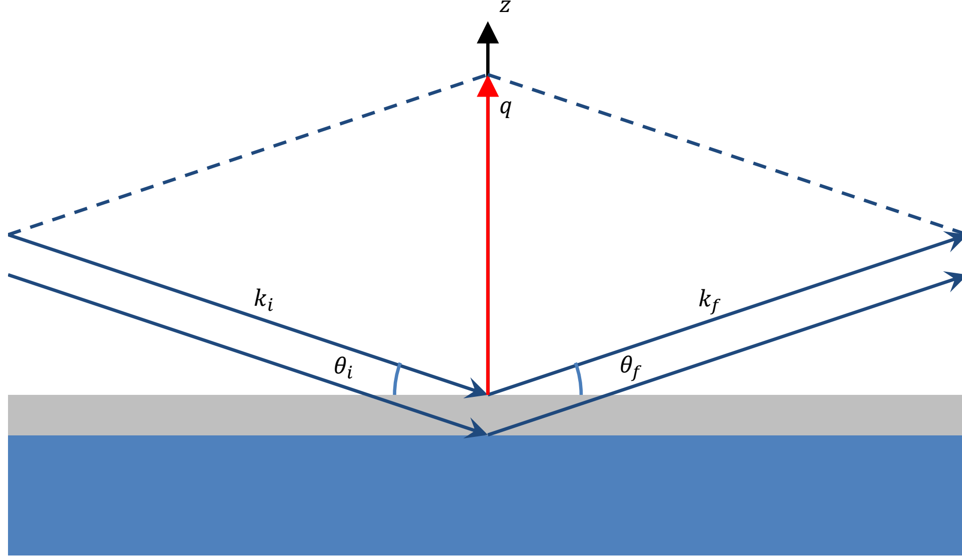

Figure 2.9: Diagrammatic geometry of a grazing-incidence scattering experiment.

The reflected x-ray intensity as a function of $|\vec{q}|$ also contains information about the layer density and interface roughness. The density of the layer will attenuate the intensity of x-rays passing through a film so that, for a fixed layer thickness, the amplitude of the reflection from the interior interfaces will be reduced more as the density is increased. The roughness of the layers will also serve to damp out the interference oscillations as θ_i is increased.

In GIXR measurements, $\theta_i \leq 10°$, so that $|\vec{q}|$ from Equation 2.5 is capable of probing the film thickness. The interference oscillations in GIXR measurements follow the relation [95],

$$\sin^2(\theta_i) = \left(\frac{(n + n_O)\,\lambda_i}{2t_f}\right)^2 + 2\delta \tag{2.6}$$

where the interference order n is offset by $n_O = 0$ ($n_O = 1/2$) in the case of constructive (destructive) interference leading to maxima (minima) of the reflected intensity. The interference order can be written,

$$n = 1 - \delta - \beta_x, \tag{2.7}$$

where δ can be expressed in terms of the critical angle θ_c below which total internal

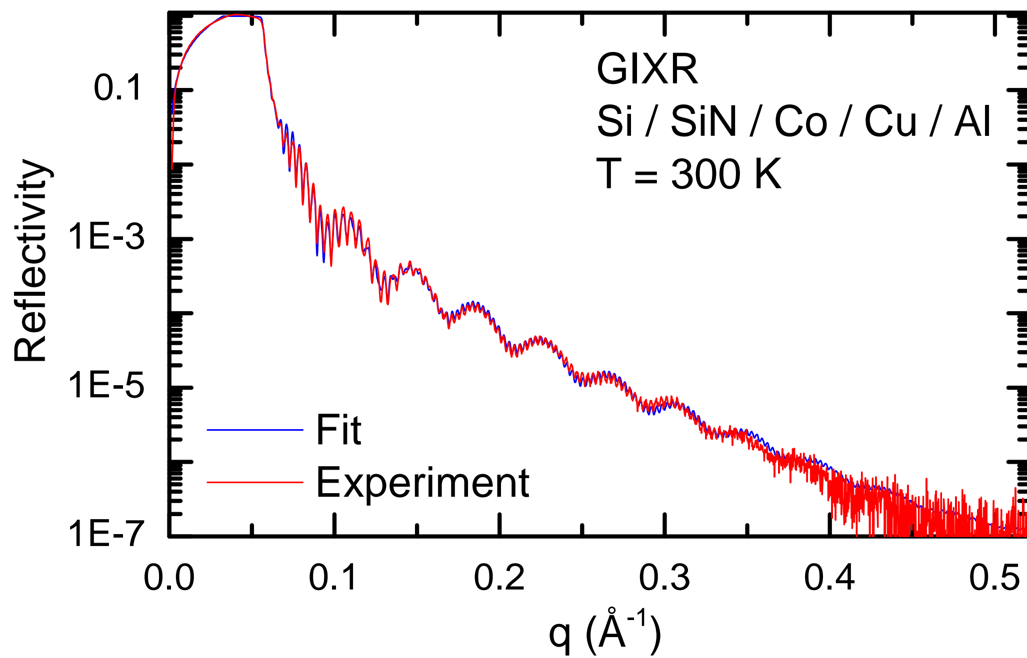

Figure 2.10: Example of grazing-incidence x-ray reflectivity data with corresponding fit for a thin film heterostructure comprised of the following layers with nominal growth thicknesses: Si / SiN (200 nm) / Co (16 nm) / Cu (100 nm) / Al (5 nm) and fitted thicknesses: Si / SiN (196 nm) / Co (15.1 nm) / Cu (94.2 nm) / Al (3 nm).

reflection occurs,

$$\theta_c = \sqrt{2\delta}. \tag{2.8}$$

The coefficient β_x is determined by the attenuation of electromagnetic waves by the film material and δ is related to the atomic scattering factor. Further, the precision of fitting GIXR data can be increased using the Fresnel equations to model the data [96, 97]. Surface roughness can be added to the Fresnel equations by adding a Gaussian distribution of film thicknesses for each layer. An optical fitting program, in this case PANalytical Reflectivity [98], can then be used to recursively fit the data, extracting values for the available parameters of layer thickness, density, and roughness. Films composed of multiple layers require three new parameters for each layer, increasing the complexity of fitting experimental data.

2.4.3 Polarized Neutron Reflectivity

Neutron reflectivity, like grazing-incidence x-ray reflectivity, is a small-incidence-angle technique. The de Broglie wavelength of the neutrons used is similar to that of the x-rays used in these scattering experiments, probing length scales $\sim 1\,\text{Å}$. Unlike x-rays, neutrons are sensitive to the nuclear potential and can be used to characterize properties of samples that are inaccessible to x-ray experiments. More importantly, the spin of the neutrons used to probe thin films may be polarized, allowing access to the magnetic properties of the film. Reflectivity data using polarized neutrons thus provides information about the depth profile of the chemical and magnetic properties of the materials. The interface roughness and material densities can also be determined.

The polarized neutrons interact with the jth layer of the film via an effective potential U_j, which is comprised of the nuclear interaction potential and a magnetic component which takes the form of a Zeeman interaction,

$$U_j = \frac{2\pi\hbar^2}{m_n} N_j b_j^{nuc} - \vec{\mu_n} \cdot \vec{B}_j, \tag{2.9}$$

where m_n and μ_n are the neutron mass and magnetic moment, respectively, N_j is the atomic density of the layer, b_j^{nuc} is the nuclear scattering length density, and $\vec{B}_j$ is the magnetic induction in the layer. This potential can be rewritten in terms of a scattering

length density due to the magnetic interactions,

$$U_j^{\pm} = \frac{2\pi\hbar^2}{m}\left(N_j b_j^{nuc} \pm N_j b_j^{mag}\right), \tag{2.10}$$

where b_j^{mag} is the magnetic scattering length density [99, 100]. It turns out that the magnetic and nuclear scattering length densities are typically of the same order of magnitude, making the technique sensitive to both.

The experiment is conducted using an incident neutron beam that passes through a series of neutron optics before reflecting from the sample and passing through a series of analyzing optics. The neutron experiments on our samples discussed in this thesis were conducted at the Spallation Neutron Source (SNS) by Liam O'Brien, R. Goyette, V. Lauter. At this facility, a pulsed 1 MeV proton beam is collided with a mercury target to generate neutron pulses. The energy of the neutrons must be reduced to make them usable, which is accomplished by passing them through a water moderator. Sets of slits are used to collimate the incident neutron beam. Measuring reflected neutrons with the polarizer set parallel or antiparallel (+ or $-$) to an applied magnetic field and the analyzer also set parallel or antiparallel (+ or $-$) allows four different reflectivities to be measured. These reflectivities are typically written as R^{++}, R^{--}, R^{+-}, and R^{-+}, with the first superscript denoting the state of the polarizer and the second superscript used to describe the analyzer.

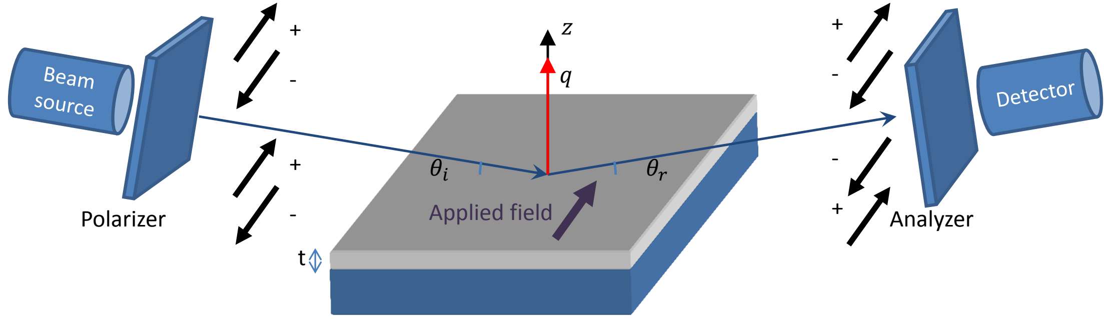

Figure 2.11: Geometry of a polarized neutron reflectivity experiment with the incident angle θ_i, reflected angle θ_r, and scattering wavevector q which is out-of-plane .

The R^{++} and R^{--} channels are the non-spin-flip channels and give information about the magnetization in the direction of the neutron polarization. The other two

channels involve the neutron flipping while reflecting from the sample. These spin-flip channels give information about components of the magnetization perpendicular to the neutron polarization, as well as the chemical properties. Both the chemical depth profile and magnetic depth profile can be accessed through only the non-spin-flip channels when an external field is applied to orient the magnetization.

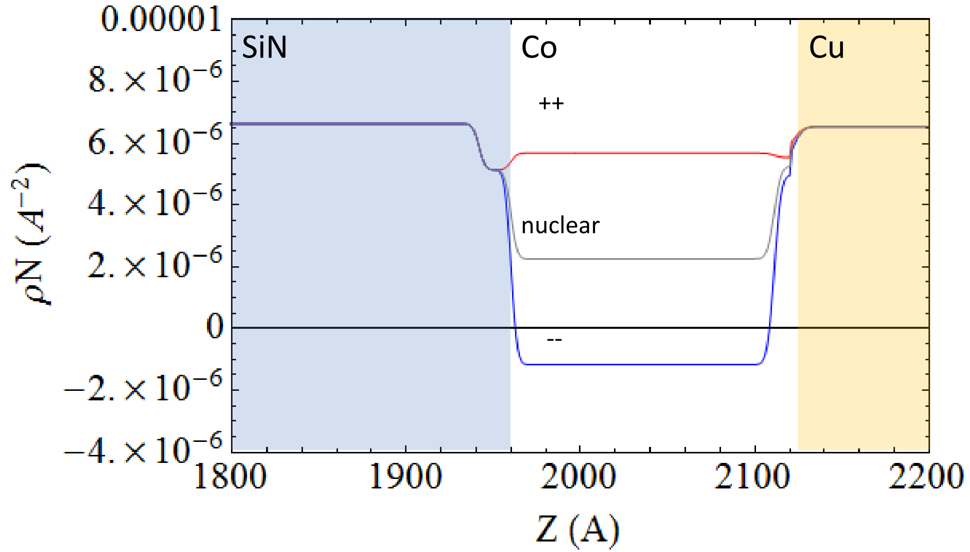

Figure 2.12: Schematic representation of the scattering length densities for R^{++} and R^{--} through the depth Z of a SiN/Co/Cu multilayer.

The depth profile of the nuclear and magnetic scattering length densities, which enter in Equation 2.10, determine the reflection of the neutrons from the sample. The neutrons are most strongly reflected from the interfaces where the change in scattering length density is the greatest. For the schematic scattering length density depth profile shown in Figure 2.12, the two polarizations are scattered differently. The $--$ neutrons are strongly scattered from the non-magnetic / magnetic interfaces and lead to q_z dependent interference whereas the $++$ neutrons are weakly scattered due to the lack of contrast in the scattering length density for this channel. This leads to strong interference oscillations in the R^{--} channel and weak oscillations in the R^{++} channel. Employing simulations that take into account the described scattering and the addition of diffuse or rough interfaces, the chemical and magnetic depth profile can be extracted as in

Reference [101].

Figure 2.13 shows PNR data for both the R^{++} and R^{--} channels for a multilayer with Co FM and Cu N materials with fitted(nominal growth) thickness for the FM / N bilayer $t_{FM} = 15.1\,\text{nm}(16\,\text{nm})$ and $t_N = 94.2\,\text{nm}(100\,\text{nm})$. Like the non-local devices there is an Al cap 3 nm(5 nm) thick. These data correspond closely to the above discussion and a representative depth profile of the scattering length density shown in Figure 2.12. The magnetic layer structure determined from PNR fitting can be compared with the chemical depth profile determined from GIXR fitting to glean information about the magnetism at interfaces and through the depths of the chemically distinct layers. GIXR

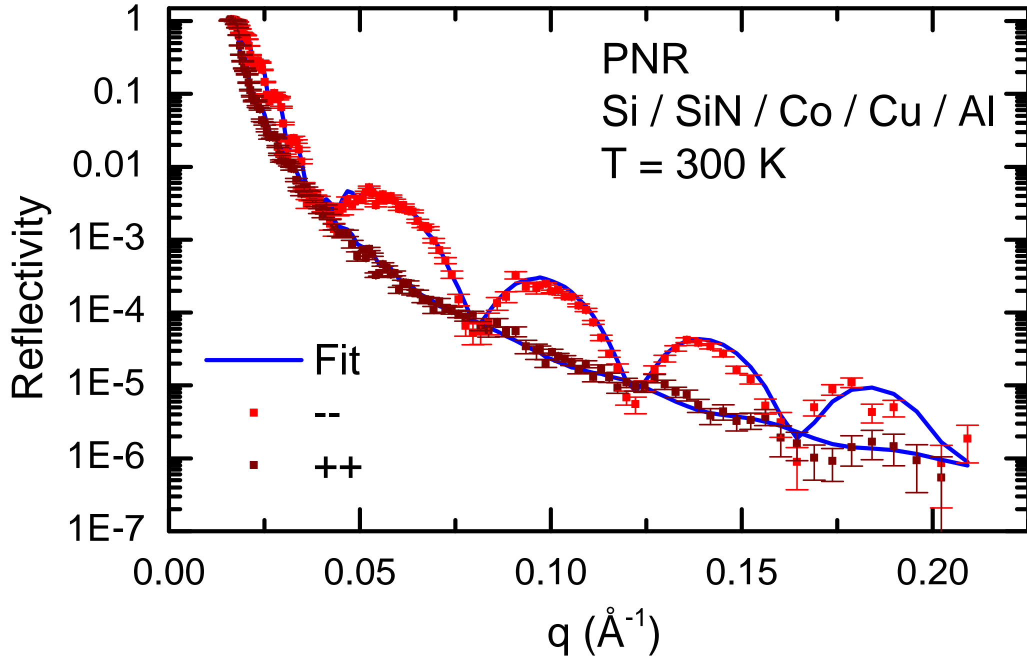

Figure 2.13: Example R^{++} and R^{--} PNR data with corresponding fits for a thin film heterostructure comprised of the following layers with nominal growth thicknesses: Si / SiN (200 nm) / Co (16 nm) / Cu (100 nm) / Al (5 nm). The fitted values are Co (15.1 nm) / Cu (94.2 nm) / Al 3 nm) with a 9 Å thick FM/N interlayer with $M_s = 260\,\text{emu/cm}^3$.

and PNR measurements have given us infomation about the magnetism of the interdiffused layers. The thickness, roughness, and magnetization of interdiffused layers for

Py/Cu, Co/Cu, and Py/Cu that has been annealed are discussed in §6.4.2. Fits of PNR data have allowed us to determine that the interfaces of Py/Cu samples are smooth, with a roughness of 6 ± 2 Å, and with no measurable interlayer. Co/Cu and annealed Py/Cu do show the formation of a magnetic interlayer, 0.9 ± 0.2 nm and 4.2 ± 0.2 nm thick, respectively. The roughness for the interlayers of the Co/Cu and annealed Py/Cu samples from the PNR measurements are 0.7 ± 0.2 nm and 3.1 ± 0.2 nm, respectively.

2.4.4 Scanning Electron Microscopy

Scanning electron microscopy is an indispensable technique for characterizing and visualizing structures fabricated on sub–micron length scales. The need for such a technique is immediately evident since the wavelength of optical light is large relative to the feature sizes involved. From the Rayleigh criterion, Equation B.3, the minimum resolvable feature size by an optical microscope is approximately 350 nm for $\lambda_e = 555$ nm, the most sensitive wavelength to the human eye, and a numerical aperture of 0.95. Using the shortest visible wavelength, violet $\lambda_e = 400$ nm, the minimum feature size is reduced to ≈ 250 nm. Neither of these vales are sufficient to resolve anything but the largest features of a metallic lateral spin valve, where contact separations of 200 nm are typical. Going to the much shorter wavelength of high-energy electrons in a scanning electron microscope (SEM) reduces the resolution limit to nanometer length scales.

The technique is very similar to that used in electron beam lithography §2.2.1 until the incident electron beam intersects the sample to be imaged. A complex set of electron optics are used to generate a highly-focused electron beam. This beam is then rastered across the surface of the sample, generating several signals that can be detected. By correlating the detected signals to the location of the electron beam at the time of detection, an image of the sample can be generated.

Secondary Electron Imaging

The detected signals in a typical SEM, among others, can be secondary electrons, backscattered electron, x-rays, Auger electrons, or cathodoluminescence generated by the high-energy electron beam interacting with the sample. The latter two will not be discussed further as they are not utilized in this work. Secondary electron detection is the most commonly used method to produce images in an SEM. Electrons incident

on the sample scatter inelastically, liberating electrons bound to atoms in the sample. These secondary electrons have kinetic energies of less than 50 eV and are typically detected by acceleration through a series of biased stages. The secondary electrons are accelerated from where they originate to a positively-biased grid held at $\approx 400\,\mathrm{V}$. Once the electrons move through the grid, they are accelerated to higher energies of a few kiloelectron volts, where they collide with a scintillator and are detected.

Secondary electrons emitted from flat surfaces orthogonal to the incident beam will appear different than those from regions with vertical surfaces. The beam generates secondary electrons uniformly about the incident beam, a fraction of which leave the sample and reach the detector. When electrons are generated near vertical feature surfaces the number of these secondary electrons able to leave the sample is increased. As a result edges or vertical surfaces typically appear brighter than flat surfaces, resulting in images that appear three-dimensional.

Additionally, the layout of the SEM chamber typically places the detector off to one side of the sample stage. In combination with the increased secondary electron emission from vertical features, this creates the appearance of shadows from the vertical surfaces as if illuminated from the side of the detector. This allows for the high resolution of the electron imaging to be combined with information about the out-of-plane topography of the sample. A non-local spin valve imaged with secondary electrons in a SEM is shown in Figure 2.14.

SEM micrographs of lateral devices are taken after the transport measurements have been done. We have observed for formation of contamination on the imaged surface due to residual hydrocarbons in the SEM vacuum system, affecting the spin-transport measurements. If the sample vacuum of the SEM is clean, less than 7×10^{-7} Torr, with an electron beam current of $\leq 10\,\mu\mathrm{A}$, and a minimal detector bias voltage, the measured spin-transport signal changed by less than 5 % after taking an SEM image. Care must be taken, however, to minimize the exposure of the sample to the beam in the event further transport measurements need to be made.

Backscattered Electron Imaging

Rather than use secondary electrons to image a sample, the incident electrons that are elastically backscattered can be detected instead. These backscattered electrons are of

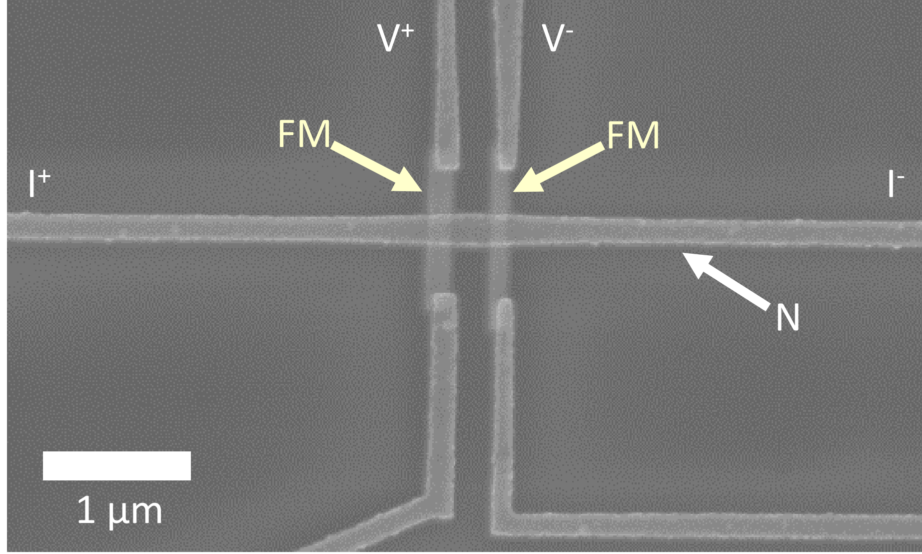

Figure 2.14: Scanning electron micrograph of a fabricated lateral spin valve with the non-local wiring configuration labeled.

higher energy than secondary electrons ($> 50\,\text{eV}$), typically greater than half the energy of the incident electron beam energy, and backscatter with an atomic number-dependent probability. The probability of electron backscatter over the entire hemisphere is given by

$$\eta_{BS} = \frac{\pi e^4 Z^2 N_A}{4(4\pi\epsilon_0)^2 A E_e^2}\rho_f t_f, \tag{2.11}$$

where Z is the atomic number, N_A is Avogadro's number, ϵ_0 is the permittivity of vacuum, A is the atomic weight, E_e is the energy of the bombarding electrons, and where ρ_f and t_f are the mass density and thickness of the film respectively. Due to the fact that $\eta_{BS} \propto Z^2/A$, backscattered electrons are capable of showing Z contrast of the sample. Although the spatial resolution is lower than that of secondary electron imaging, the elemental contrast of samples can still be imaged. The backscattered electrons can be directly detected by a scintillation or solid state detector around the incident electron beam optics column, as the higher energy backscattered electrons are ineffectively deflected by the grid bias on the secondary electron detector. A Centaurus Scintillator Backscattered Electron Detector has been used here.

Energy-dispersive X-ray spectroscopy

Energy-dispersive X-ray spectroscopy (EDS) is a technique that allows for the elemental composition of a sample to be measured. The interaction of 5 keV to 30 keV electron beam with the sample leads to inner-shell electrons being knocked out by inelastic scattering, as described above. This vacancy in the inner orbitals can then be filled by an electron relaxing from a higher energy level and emitting an x-ray photon. The difference of the energy levels determines the energy of the emitted photon. Since the energy levels depend on the element (i.e. Z), x-rays generated from the sampled volume can be collected to form an EDS spectrum, from which the elemental composition can be determined.

X-rays emitted from the sample are then detected using an energy dispersive spectrometer. Two types of detectors are used in this work: the more traditional Si(Li) detector and the newer silicon drift detector (SDD). The Si(Li) detector is composed of a specially-engineered P-I-N diode, a pulse processor, and analyzer electronics. The diode has a lithium compensated silicon layer several millimeters thick with a p-type silicon layer on one side and an n-type layer on the other. Metalized contacts on both sides are used to bias the diode to around 1000 V. The Si(Li) layer is normally non-conducting, but when exposed to x-rays it generates a pulse of electron-hole pairs that are drifted apart by the high bias and measured by a pulse processor. These detectors must be cooled to 77 K to reduce the dark (unexposed) leakage current of the detector. The x-ray energy determines the number of electron-hole pairs created, which are amplified and shaped by a pulse processor as well as separated from other pulses by a discriminator. The output is then fed to analyzing electronics to construct an energy spectrum. Further discussion can be found elsewhere, such as References [102, 103].

The SDD technique is very similar, but rather than the large P-I-N diode, it relies on a much smaller Si wafer with very low leakage currents. A transverse bias is applied by a series of electrodes and current is collected by a small anode. Interacting x-rays generate carriers that are drifted by the bias field to the detector, and the resulting pulse is processed in the same fashion as in the Si(Li) detector. Due to the small leakage current for these detectors, they need not be cooled by liquid nitrogen. Instead SDD detectors typically use a Peltier cooler. These detectors have lower capacitances than the Si(Li) detectors and increased active detection areas, which leads to increased

pulse throughput and higher count rates, resulting in better statistics.

Both the traditional Si(Li) detector and the newer SDD have been used in this work for measuring the EDS spectra. A set of example spectra for Cu and Al N channels, as well as Py and Co FMs, are shown in Figure 2.15. The K_α peaks for Fe, Co, Ni, and Cu are visible near 10 keV. The L_α peaks are visible below 2.5 keV along with the large peak for Si. A spectra such as this can be used to verify the purity of materials as well as to check the composition of Py and other alloys.

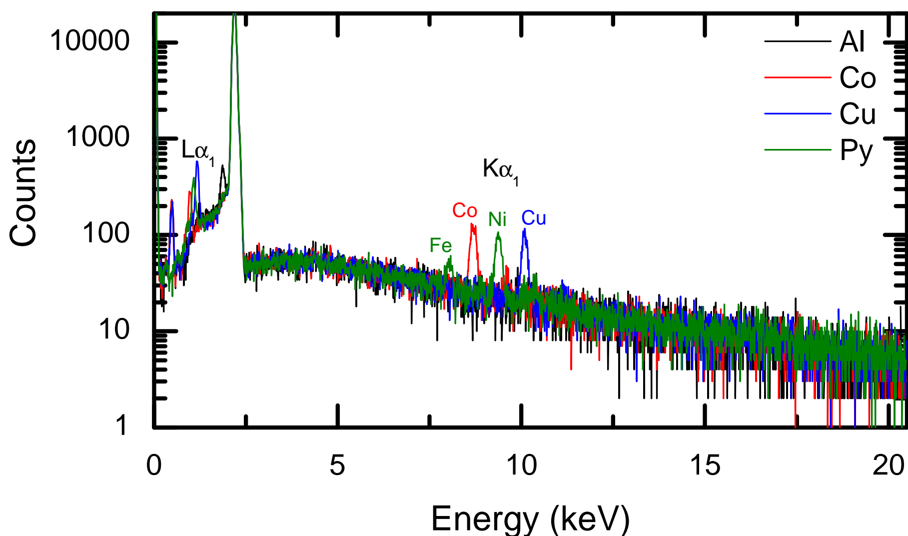

Figure 2.15: Energy-dispersive X-ray spectra of Cu, Al, Py, and Co thin films deposited on doped Si/SiO_x. The Lα and Kα lines of the transition metals are labeled.

2.4.5 Atomic Force Microscopy

Atomic force microscopy (AFM) is a scanning probe microscopy (SPM) technique that utilizes a sharp Si tip, with a radius of curvature on the order of nanometers, which is scanned over a sample surface. The tip is mounted at the end of a micro-cantilever, which is rastered over the sample while the tip interacts with the sample surface. Forces between the tip and the sample determine the deflection of cantilever. The deflection of the tip is measured using the changing reflection of a laser from the back of the cantilever by a grid of photodiodes. The deflection of the silicon-based cantilever Δy

follows Hooke's law,

$$F_t = -k_t \Delta y \tag{2.12}$$

where k_t is the spring constant of the tip, and F_t is the force applied to the tip. As a result, the force applied to the tip can be measured via its deflection. This technique was developed by Binnig *et al.* and further details can be found in Reference [104].

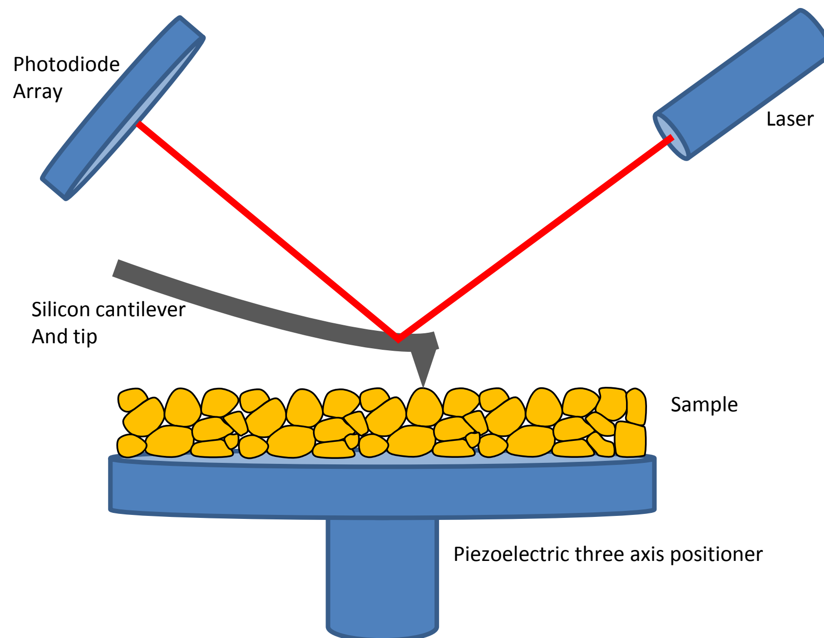

Figure 2.16: Depiction of the components of an atomic force microscope including the piezoelectric scanner, sample, AFM tip, laser, and photodiode array.

The tip is scanned using piezoelectric elements that are capable of positioning the tip to greater than nanometer precision. Using these elements, the sample can be positioned under the tip and rastered across the sample. Rather than operate with the cantilever at constant height above the sample, the probe tip is operated in a constant force mode. Using a feedback loop, the deflection of the tip is held constant by adjusting the vertical position of the sample while scanning. The vertical position is recorded while scanning in this mode and the three-dimensional topographic surface of the sample can be measured. In addition, measurements of the horizontal deflection of the tip while scanning can give information about the friction of the surface.

Further, instead of operating in constant contact mode, the tip can be oscillated towards and away from the sample. This is called tapping mode and can provide further information about the surface interactions. This mode is ideally suited for working with softer materials such as patterned polymers. The AFM also forms the basis for the magnetic force microscope (MFM), where a magnetic tip is used to probe the spatial variations of magnetic interactions with a sample.

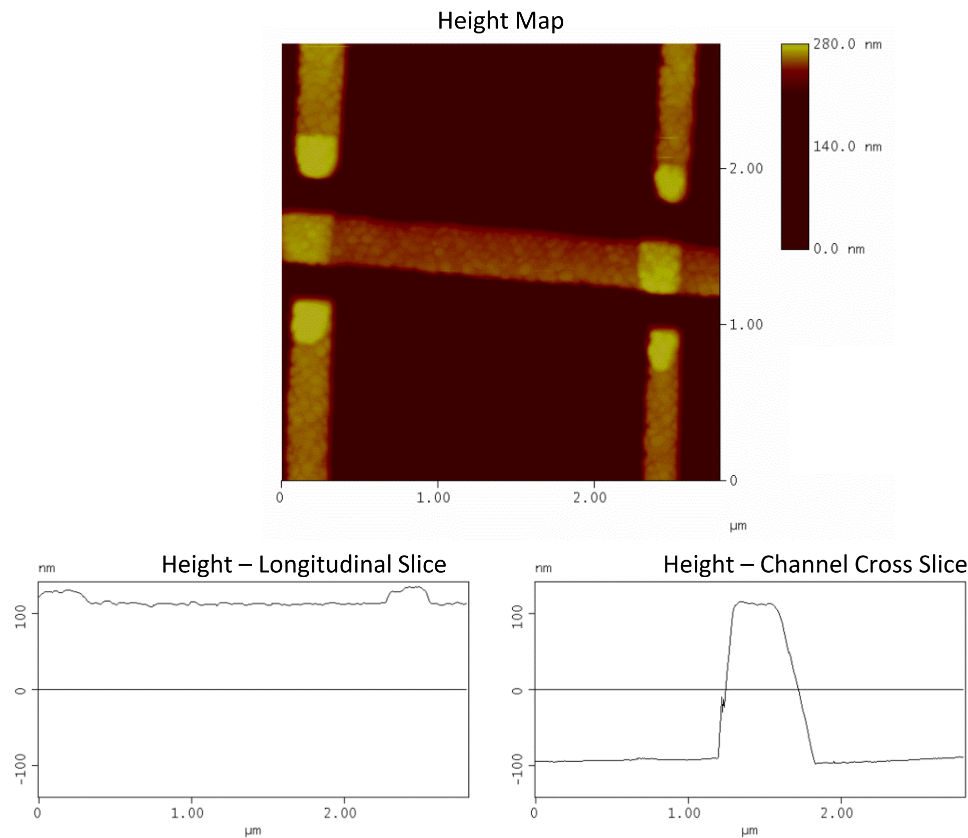

Figure 2.17: Atomic force microscope spatial height map of a Py/Cu non-local spin valve with measured geometric parameters $t_N = 202$ nm, $w_N = 260$ nm, and $d = 1970$ nm.

Figure 2.17 contains a map of the measured height profile of a Py/Cu non-local spin valve measured by AFM. The surface topology, visible in the height map, contains information about surface roughness and grain structure. The geometry of the device may also be measured, for this device $t_N = 202 \pm 5\,\text{nm}$, $w_N = 260 \pm 10\,\text{nm}$, and $d =$

$1970 \pm 10\,\text{nm}$.

2.5 Transport Measurements

Spin-transport measurements of fabricated and characterized devices are carried out at various applied magnetic fields and temperatures. Samples are loaded into the bore of a helium-vapor cryostat, discussed in §2.5.1, which provides a low-noise environment for measurement where the applied magnetic field and temperature can be controlled. The orientation of the magnetic field relative to the device can also be controlled by rotating the sample.

The low resistance and nanoscale cross sections of the samples mean small electrostatic discharges can lead to current densities large enough to destroy the structures. In §2.5.2, precautions to prevent electrostatic discharge through devices are discussed.

2.5.1 Helium-Vapor Cryostat Operation

Low-temperature transport measurements are conducted using a custom sample mount constructed to load samples into a helium vapor magneto cryostat (SuperVariMag) manufactured by the Janis Research Company. The cryostat vaporizes liquid helium which then flows over a sample to control its temperature between 1.2 K and 325 K. At temperatures less than 4.2 K it is possible for the sample to be immersed in liquid He rather than vapor. Further information regarding cryostat design and operation is found in Appendix E (§E.5).

A magnetic field is applied by flowing current through a superconducting solenoid immersed in the liquid He (LHe) bath of the cryostat. Although the application of large magnetic fields is unnecessary for the spin valve measurements described in §1.2.10, Hanle effect measurements (§1.2.14) require the application fields up to several Tesla. The NbTi superconducting magnet used here is capable of large field, up to $\pm 9\,\text{T}$. The solenoid provides a relatively uniform magnetic field varying by between $\pm 0.01\%$ and $\pm 0.5\%$ over a 1 cm region. Since the magnet is only capable of generating magnetic fields in a fixed direction (vertical), experiments requiring fields applied in other directions necessitate *in situ* rotation of the sample instead. A probe capable of rotational positioning of samples must also provide measurement wiring and thermometry. Such

a probe was designed and built as part of this work and is described in §2.5.2.

2.5.2 Measurement Probe Design

Sample Holder Design

The design of the sample probe is critical for making accurate and precise transport measurements. A precision thermometer, heater, and magnetic field sensor (which also aids in orienting the sample rotation) are mounted in or on a copper block onto which the sample is affixed. The copper block provides good thermal contact between the sample and the temperature regulation components while allowing the magnetic field to be measured. Explanation of the sample stage construction is given in Appendix E (§E.3).

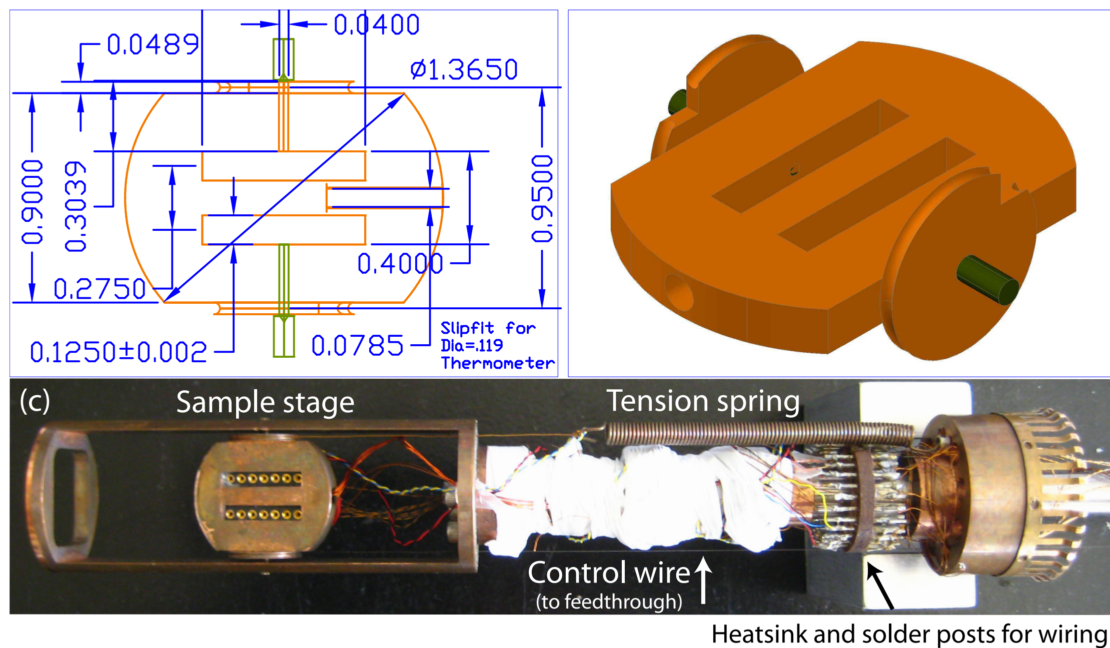

Figure 2.18: Schematic drawings of sample stage (a) above the sample position and (b) 3D rendering of the stage with dimensions labeled in inches. (c) Picture of stage held in place at end of sample probe with electrical wiring, sample rotation wires, and tension spring in place.

Sample Stage Rotation

The copper sample block with the accompanying thermometer, heater, and sample electrical connections must be affixed to the probe in such a way that it can be rotated. This is accomplished by mounting stainless steel pivot points on opposite sides of the sample block. The points are seated into a pair of spring-loaded sapphire pivot cups which secure the sample block but allow free rotation due to the very low coefficient of friction between stainless and sapphire. The sapphire pivots are mounted into brass screws, which are threaded into opposite sides of a copper cage attached to the end of the probe.

A pair of pulley wheels are attached coaxially with the pivot points, as shown in Figure 2.18. A wire is wound around each pulley with one end attached to the sample block and the other to either a linear positioner or a BeCu coil spring above. In the case of the former, the wire is passed up the sample stick to a linear feedthrough which rotates the sample block about the pivots when pulled. The stage rotates in the opposite direction when the feedthrough is lowered. To keep the stage stable, the pulley on the opposing side is oppositely wound and connected to a Be-Cu coil spring mounted above. The wires pulling in opposite directions stabilize sample rotation, with the position of the linear feedthrough defining the sample angle.

Since a bipolar magnetic field can be applied, the sample typically does not need to be rotated by more than 90°. The diameter of the pulleys is 1.863 cm (0.733") so that translating 5.852 cm (2.304") will rotate the sample through 360°. Pulleys with larger circumference allow for the sample angle to be set with greater precision due to the fixed resolution of the linear positioner which drives the actuating wire. The maximum probe dimensions, however, limit the pulley size to the diameter specified above. Photographs of the rotation stage are shown in Figure 2.19. Further information including schematics and photographs of the rotation stage materials can be found in Appendix E, including an example calibration of the rotation in §E.4.

Probe Wiring

Wiring is required to connect the low temperature sample environment to laboratory equipment. Electrical measurement leads exist for thermometry, heating, and field

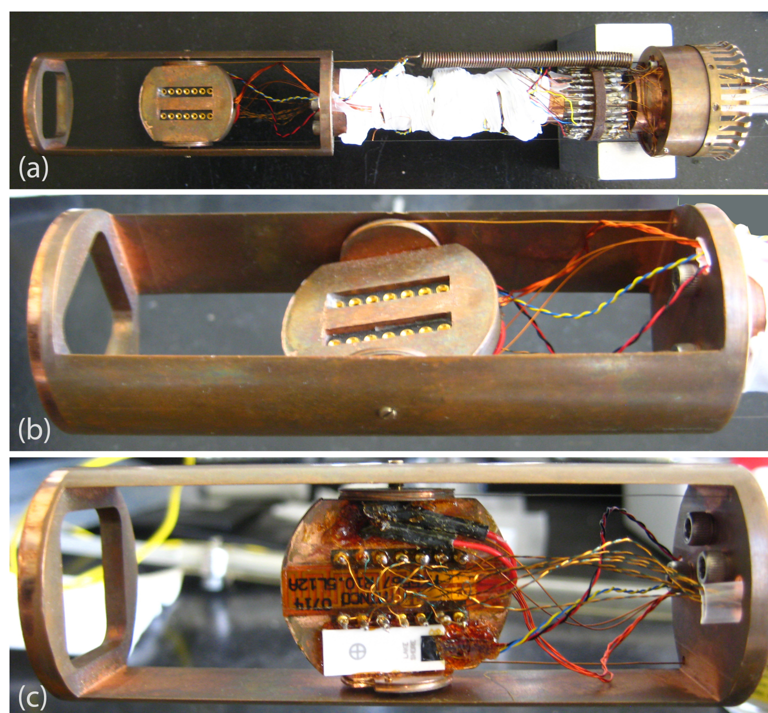

Figure 2.19: Photographs of the sample stage, electrical socket, and retaining apparatus. (a) Overhead image shows the socket, heatsink for electrical connections, and the BeCu centering spring with (b) a closeup of the rotation stage from an oblique angle. (c) A photograph of the back side of the rotation stage showing twisted-pair wiring for the sample leads, foil resistive heater, and cryogenic Hall sensor.

sensing. The connections between the He sample space and the external environment are made via Detoronics™ hermetically-sealed 19-pin Military Standard connectors (Detoronics P/N DTO2H-14-19PN). The wires provide low-noise, low-resistance connections while minimizing heat leaks due to thermal conduction in the wires between the sample and room temperature. The Wiedemann-Franz law provides an approximate relation between the thermal κ_T and electrical σ conductivities:

$$\frac{\kappa_T}{\sigma} = LT, \tag{2.13}$$

where the product of the Lorenz number $L = 2.44 \times 10^{-8}\ W\,\Omega\,K^{-2}$ and temperature T is the constant of proportionality between κ_T and σ. Copper and alloys such as phosphor bronze (copper with tin and phosphorus), Nichrome (nickel with chromium), and Manganin (copper with manganese and nickel) are often used for cryostat wiring. Manganin and phosphor bronze are used here to balance the tradeoffs of κ_T and σ. A compiled table of the transport properties of some popular wire materials is included in Table E.1, which is found in the appendices.

Magneto-resistive effects also constrain the choice of wire material for magnetic-field dependent measurements. The susceptibilities χ_m^{SI} and magnetoresistances MR for each wire are also shown in Table E.1 from References [105, 106]. The magnetoresistance is defined here as

$$MR = \frac{R(B) - R(0)}{R(0)}, \tag{2.14}$$

where $R(B)$ and $R(0)$ are the resistances at finite applied field B and zero field, respectively, for a given temperature. Due to the desirable combination of relatively low residual resistivity ratio (RRR) and magneto-resistance, phosphor bronze was chosen for wiring. The wires were twisted to aid in the rejection of unwanted electro-magnetic coupling along the length of the probe. The wires are connected to a low-temperature heat sink near the bottom of the probe, 13 cm above the sample stage, to minimize thermal loading of the sample.

Additional wires were installed for the thermometer, heater, and magnetic field sensor. The thermometer and field sensor were both connected to a pair of twisted-pair phosphor bronze wires facilitating four-terminal measurements; one pair carries excitation current while the other probes voltage. The only component wired differently is the heater. Here, larger diameter wire was used to minimize Joule heating

in the wires supplying current to the sample heater's resistive heating element (Minco HK5566R15.0L12A).

Sample Grounding - Electrostatic Discharge Protection

Due to the susceptibility of nanoscale devices to damage from electrostatic discharge, the sample cannot be directly connected to the probe wiring without taking steps to protect the samples first. For example, voltages as small as 0.6 V are capable of driving enough current to destroy a sample. Therefore, the socket on the probe must be grounded while the sample package is inserted into the probe stage receptacle. This ground must be maintained while the probe and sample are loaded into the cryostat. Once loaded, the system is configured to make transport measurements of the sample by opening a set of switches connected to each of the sample measurement wires and a common bus. The bus is, in turn, connected to ground via a switch. By sequentially opening the switches the lines between sample and measurement apparatus are safely isolated. A diagrammatic layout of this grounding system is shown in Figure 2.21.

The sample must be re-grounded for protection before permuting connections or removing the sample from the cryostat. The re-grounding is done by closing the switches to the common bus, which is floating at this point. Now that the sample lines are at equipotential via the common bus; the bus can be grounded to simultaneously ground all lines. Each of these switches provides a less than 1 Ω path to ground when closed, and isolate each line to greater than 10 GΩ when open.

Rotation Stage Hall Probe

The rotation stage is also equipped with a low temperature Hall probe, which provides a useful tool to monitor both the applied field and the orientation of the sample, further described in §E.4. The field sensor operates using the well-known Hall effect, whereby a charge current flowing in a material is deflected by the Lorentz force given by,

$$\vec{F_e} = e\left(\vec{v_d} \times \vec{B}\right), \tag{2.15}$$

where e is the carrier charge, $\vec{v_d}$ is the drift velocity of the carriers, and $\vec{B}$ is the applied magnetic field which generates a transverse electric field. The Hall effect geometry, shown in Figure 2.20, relies on a charge current bias and a resulting transverse Hall

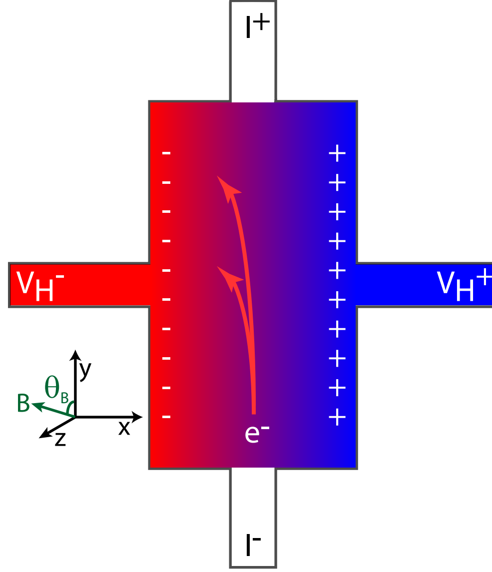

Figure 2.20: Diagram of the operational scheme of a Hall probe as a magnetic field sensor.

voltage. Electrons are deflected in-plane by the Lorentz force orthogonal to an out-of-plane magnetic field $B_\perp$ and drift velocity $\vec{v_d}$ described by the cross product in Equation 2.15. If the field is directed along $\vec{v_d}$, $\vec{F_e}$ goes to zero; if $\vec{B}$ is along the Hall arms, then $\vec{F_q}$ is out-of-plane. As a result, this configuration is insensitive to in-plane components of the magnetic field. The measured transverse Hall voltage can be written,

$$V_H = V_H^+ - V_H^- = \eta_H B \sin\theta_B, \tag{2.16}$$

where θ_B is the angle of the B field relative to the plane of the Hall sensor, shown in Figure 2.20, and η_H is the sensitivity of the sensor.

The cryogenic LakeShore MCT-3160 which we used is made from a high mobility InAs semiconductor. It has an active area of 0.8 mm^2 and, for a sensor current of 100 mA, a Hall voltage develops with sensitivity $\eta_H = 0.688\,\mathrm{mV\,kG^{-1}}$. At zero field, there is a DC offset voltage of 2.5 µV. Further, when the sensor is operating between 1.5 - 350 K, η_H has a minimal temperature dependence, changing by less than ±0.010 %/°C and deviating by less than 0.3% below 200 K. Due to the relative temperature independence of η_H, the Hall sensor is capable of providing a measure of the sample orientation

in the applied field at various temperatures. Using this sensor, the rotational positioner can be calibrated or adjusted to compensate for the thermal expansion of the probe materials, thus maintaining the desired sample angle. An example calibration curve is shown in §E.8.

Noise Considerations

Electrical noise in the measurement system must be minimized to allow low-noise measurements to be conducted on reasonable time scales. The probe wiring and connector cable is connected so that no grounding loops exist among the interconnected measurement apparatus, which could contribute to noise or other erroneous transport measurements. Twisted-pair probe wiring is used to minimize coupling to external fields; this is further enhanced by individually shielding the twisted-pairs on the connecting cables between the cryostat and the measurement equipment.

A spectrum analyzer was used to characterize noise contributions from the measurement circuit components. The noise in the system was verified using a low-resistance dummy load consisting of $1\,\Omega$ and $100\,\Omega$ metal-foil resistors with measurement leads connected at the junctions between resistors and mounted on the sample probe. A Stanford Research 560 Low-Noise Preamp was used to measure the RMS voltage noise over a fixed bandwidth, which is a useful figure of merit defined as,

$$V_N \equiv V_{RMS}/\sqrt{B_V}, \tag{2.17}$$

where V_{RMS} is the root mean square (RMS) AC voltage and B_V is the bandwidth of the measurement (more information can be found in Reference [107]). For example, between $1\,\mathrm{Hz}$ and $10^6\,\mathrm{Hz}$, V_{RMS} is $5\,\mu\mathrm{V}$, giving a system noise of $V_N = 5\,\mathrm{nV/Hz^{1/2}}$, which is also the noise floor of the measurement equipment. This measurement was repeated periodically to check the noise of the system and samples.

2.5.3 Transport Measurement Techniques and Apparatus

The samples to be measured, the probe, and other apparatus are all connected to measurement equipment, including resistance bridges, temperature controllers, superconducting magnet supplies, voltmeters, and current sources. Most importantly, a resistance bridge with a low-noise preamp is used for measuring sample transport, but in

some cases standard lock-in or DC measurements are compared for verification. Further, the lock-in or DC techniques may be employed to monitor simultaneously the applied magnetic field component on the Hall sensor.

AC measurements

The primary measurement technique used in this work employs a low-frequency alternating current (AC) resistance bridge. An AC current with root mean square amplitude J_e is driven though a sample at 16.2 Hz with the resulting sample voltage measured by a resistance bridge and/or lock-in amplifier. The system used a LakeShore 370 Resistance Bridge and Lakeshore 3708 ultra-low noise preamp was integrated into the system. The preamp is capable of measuring at a noise floor of $2\,\mathrm{nV}/\sqrt{\mathrm{Hz}}$ and also serves as a channel scanner capable of switching between eight independent sets of resistance measurement leads. The 3708 channel scanner is capable of switching between channels such that samples are not destroyed during switching. Ideally, this is done in a "make before break" configuration to minimize the risk of electrostatic discharge through the sample. When switching channels the 3708 box reduces the excitation current to zero, sends commands to the relays to connect to the next channel and disconnect from the previous channel. The excitation current is then ramped to the desired value from zero. A block diagram of the measurement system is laid out in Figure 2.21 with wiring and system grounds included.

Figure 2.21 depicts the sample probe configured as inserted into the bore of a helium vapor cryostat with the sample surrounded by a superconducting solenoid immersed in a liquid helium bath. Phosphor bronze wires carry transport signals to the top of the cryostat, in turn connected to a cable bundle of individually shielded twisted pairs connected to a breakout box. The breakout box can be connected to the preamplifier/resistance bridge or other measurement electronics. Digitized transport data, along with temperature and magnetic field information from their respective controllers, are fed into a computer to be recorded. All equipment and shields are connected to a common earth ground at the breakout box. Cables are all shielded with grounds provided at the breakout box and broken on the opposite side to avoid ground loops.

Standard lock-in techniques, again using an AC current source, are also employed. In this case, however, a lock-in is used. A Signal Recovery, formerly EG&G, 7265 lock-in

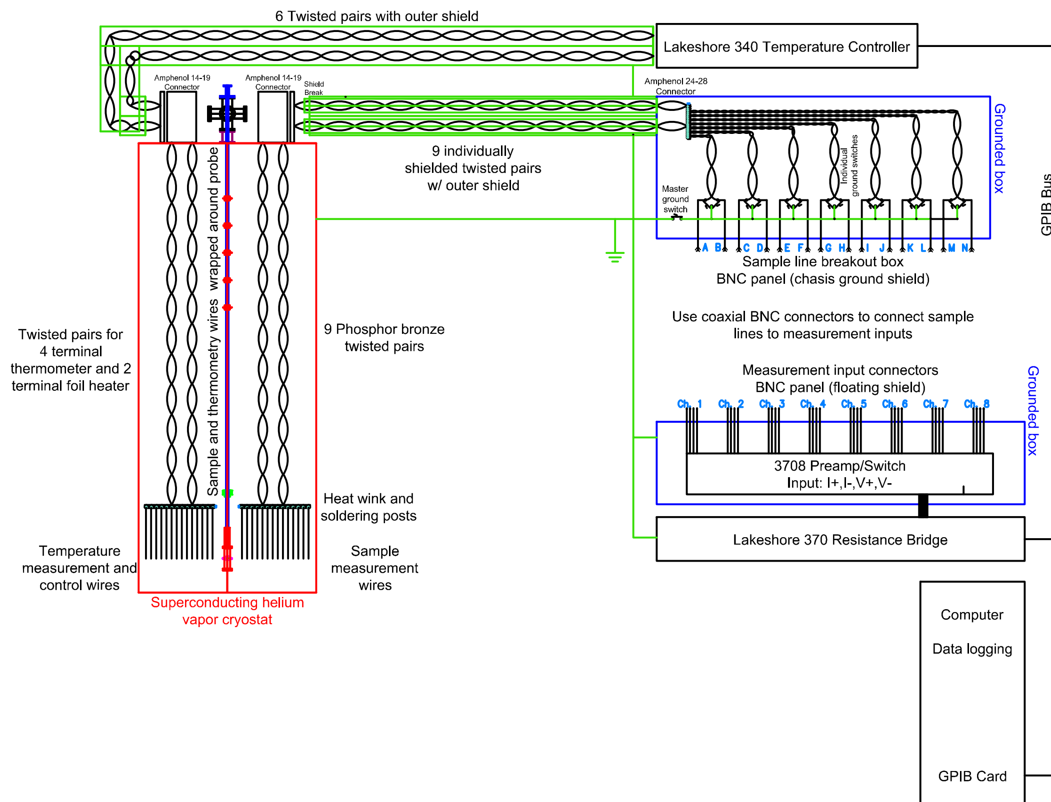

Figure 2.21: Block diagram of the low-temperature measurement system used in this work.

amplifier is employed and is sometimes used in conjunction with a Stanford Research 560 Low Noise Preamp. The preamp is used in differential mode with a built-in variable band-pass filter and gain stage. Depending on the configuration, the noise floor is between 2 and 5 nV/$\sqrt{\text{Hz}}$. For the internal lock-in pre-amplifiers, field effect transistors on the lock-in have a high input impedance, but a noise floor of 5 nV/$\sqrt{\text{Hz}}$ whereas the bipolar input gain stage has a lower impedance and a noise floor of 2 nV/$\sqrt{\text{Hz}}$. Lockin measurements works well for small voltage signals on a small background, but the dynamic range is insufficient for measurements with larger backgrounds. Therefore, the 3708 resistance bridge is most often used.

DC measurements

The sensitivity and noise rejection of AC techniques are excellent. Straightforward direct current (DC) measurements are useful for understanding transport. In this case serving as an important verification of AC measurements. A Keithley 220 precision current source was used to supply direct current (DC) excitation I_{DC}. A Keithley 2182 Nanovoltmeter, or Keithley 2002 voltmeter, was used to measure DC voltages V_{DC}.

Background voltage removal techniques may be used so spurious voltages are ignored. As an example of a quasi-AC technique, the current source is ramped to $+I_{DC}$ and held constant for several seconds before V_{DC}^{+} is recorded. The current is then ramped to $-I_{DC}$ and V_{DC}^{-} is again recorded after several seconds. The sample resistance can then be computed, assuming linear response, with background voltages that are not due to the excitation current removed:

$$R_{DC} = \frac{V_{DC}^{+} - V_{DC}^{-}}{2I_{DC}}. \tag{2.18}$$

The average of the two polarities of I_{DC}, $R_{DC,Ave} = V_{DC}^{+} + V_{DC}^{-}/2I_{DC}$, gives a thermoelectric voltage.

Samples with low resistance interfaces show the same spin-dependent transport whether measured by AC or DC techniques at $J_e = 1\,\text{mA}$. This is unsurprising, owing to the low-frequency AC excitation used, but it does serve as an important validation of AC measurements. Trusting the AC techniques becomes increasingly important when signals less than 10 nV are to be measured; standard DC techniques are incapable of resolving these signals.

2.5.4 Data Acquisition Software

The above equipment was interfaced using custom National Instruments LabVIEW software. The software interfaces the LakeShore 340 temperature controller, Cryomagnetics CS-4 (or Oxford IPS-120) superconducting magnet supply, Keithley 220 precision current source, Keithley 2000, 2002, or 2182 (nano-)voltmeters, and LakeShore 3708 AC resistance bridge. The software also interfaces with the cryogen level meter to ensure the cryostat is sufficiently filled with cryogens. This software allows a detailed magnetic field sweep to be programmed and executed at defined temperatures, which it will automatically stabilize before proceeding. The temperature stability and other parameters are configurable within the software user interface.

The tools, techniques, and apparatus built to make the devices and measurements required to study spin transport in metals is described in this chapter. In most cases sufficient information is given in this chapter but further information to understand this work can be found in the accompanying appendices. There are areas for which further reading may bring insight, with many references given throughout the thesis.

Chapter 3

Transport Measurements and Basic Characterization

Non-local spin valve devices were fabricated using the process described in §2.2.3, the deposition methods described in §2.3, and measured using the instrumentation introduced in §2.5. High purity Cu and Al non-magnetic N metal spin transport channels with permalloy Py and Co ferromagnetic FM contacts are the focus of the experiments in this thesis. In this chapter the basic characterization and transport measurements of the materials used and the lateral devices are discussed and shows some corresponding data.

Measurements used to characterize the charge and spin transport in these systems were conducted in several geometries including in-line, non-local, and three-terminal configurations. This chapter describes the basics of these techniques.

3.1 Four-Terminal Channel Resistance Measurement

The four terminal in-line measurement is used to measure the resistivities ρ of the non-magnetic N and ferromagnetic FM materials. The resistivity of a material is determined using Ohm's law by measuring the potential drop V due to the charge current flowing through a material. Therefore, determining ρ requires knowledge of the current density j_e and the distance over which the voltage drop is measured d.

The resistivities ρ of the N and FM materials, designated with subscripts as ρ_N and

ρ_{FM}, respectively, are central to understanding the transport in these lateral FM/N heterostructures. Polycrystalline thin films have much larger resistivities than bulk single crystals of the same material. Metallic wires patterned on sub-micron length scales have further increased resistivities over unpatterned films, due in part to surface effects. In Cu, for example, the grain microstructure has been shown to change with thickness contributing to changes in the measured resistivities [108]. The increased resistivities of films and nanowires over bulk materials has been observed here and by others, with examples given in References [109, 110]. Therefore $\rho_N(T)$ and $\rho_{FM}(T)$, which appear in the theoretical description of spin transport presented in Chapter 1, need to be measured for the patterned materials used in this work.

The lateral spin valve geometry, depicted in Figure 3.1, is used to measure the resistivity of the patterned N channel. Doing so allows ρ_N to be measured directly for each spin-transport device. The charge current is experimentally controlled by a current source driving electrons through the N channel, as depicted. The N width w_N and thickness t_N, labeled in Figure 3.1(a), are used to compute $j_e = J_e/(t_N w_N)$, where w_N and t_N are measured using SEM and QCM. V is measured between the FM contacts separated by a distance d, allowing ρ_N to be directly calculated using Ohm's law in the following form:

$$\rho = \frac{V t_N w_N}{J_e d}. \tag{3.1}$$

ρ_{FM} is determined in a similar fashion to that used for ρ_N, as described above. ρ_{FM}, however, cannot be measured directly using the lateral spin valves due to the presence of only three in-line terminals along the FM. Rather, patterned FM nanowires, with the requisite four in-line terminals, were used to determine ρ_{FM}. The nanowires were patterned to be $200 \pm 20\,\mathrm{nm}$ wide, $16 \pm 1\,\mathrm{nm}$ thick, and with several voltage contacts spaced at $15\,\mu\mathrm{m}$ along the wire. An SEM micrograph of one such structure is shown in Figure 3.2. The device shown has several contacts for measuring V over various segments of the device and varying d.

The temperature dependence of the resistivity further characterizes charge transport in materials. In metals, as T is lowered from room temperature, the scattering due to phonons is reduced, leaving only the contribution due to impurity defect scattering ρ_0 at low T. The RRR, discussed on Page 26, gives a direct measure of the quality of the metal. Higher quality metals exhibit larger RRR due to the reduction of ρ_0 resulting

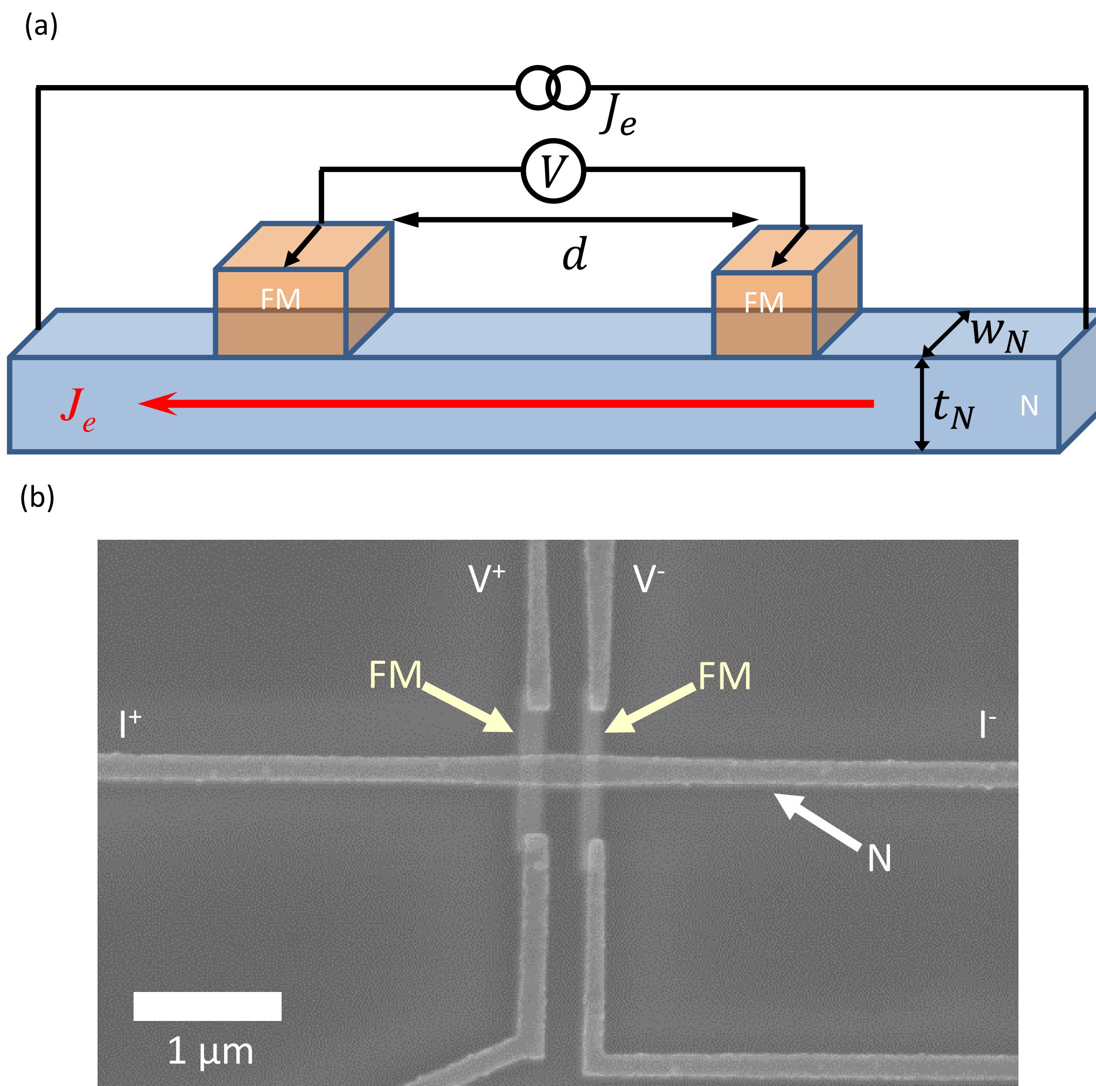

Figure 3.1: Illustration of the four-terminal measurement configuration (a) used for measuring channel resistivities with an SEM micrograph (b) of a lateral device from which w_N is measured.

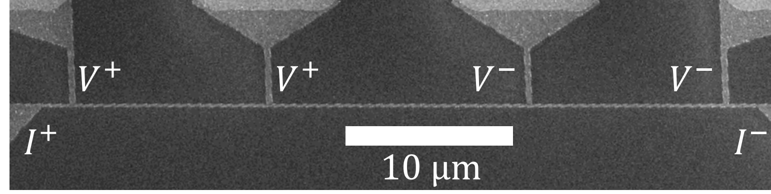

Figure 3.2: SEM micrograph of a patterned nanowire used for measuring $\rho_{FM}(T)$.

from reduced impurity scattering at low temperature. $\rho(T)$ is experimentally determined by measuring V as a function of T while J_e is held constant. The temperature dependent resistivities for Cu, Al, Co, and Py nanowires are shown in Figures 3.3, 3.4, and 3.5.

The resistivities of the metals used in this thesis depend on the thickness and in-plane dimensions of thin films and patterned wires. The measured $\rho_{FM}(T)$ for Co and Py thin films and nanowires are shown in Figure 3.3 and summarized in Table 3.1. As the thickness of the deposited materials is reduced, ρ_{FM} increases and the RRR decreases as the scattering rate increases. The resistivity further increases when films are patterned into nanowires. The resistivities of patterned nanowires, with $t_{FM} = 16\,\text{nm}$, are approximately a factor of 3 larger than unpatterned films with $t_{FM} = 100$ nm. The non-local devices employ $t_{FM} = 16\,\text{nm}$ FM nanowires, so the nanowire ρ_{FM} is used.

Material	Thin film		$w_N \approx 200$ nm
t_{FM}	100 nm	16 nm	16 nm
ρ_{Py} $(T = 5\,\text{K}, 292\,\text{K})$	11.8, 24.4 μΩ cm	20.6, 30.3 μΩ cm	30.3, 41.4 μΩ cm
Py RRR	2.1	1.5	1.4
ρ_{Co} $(T = 5\,\text{K}, 292\,\text{K})$	5.6, 12.3 μΩ cm	16.9, 24.0 μΩ cm	18.8, 27.1 μΩ cm
Co RRR	2.2	1.4	1.5

Table 3.1: Typical values of ρ_{FM} at $T = 5\,\text{K}$ and $292\,\text{K}$ with RRR measured using films and patterned wires $w_{FM} \approx 200\,\text{nm}$.

The thickness dependence of $\rho_N(T)$ for Cu is shown in Figure 3.4. As just described, the measured ρ_N increases with decreasing t_N.

Representative experimental values of $\rho(T)$ for each of the patterned materials used throughout this thesis at $T = 5\,\text{K}$ and $292\,\text{K}$ are summarized in Figure 3.5 and Table

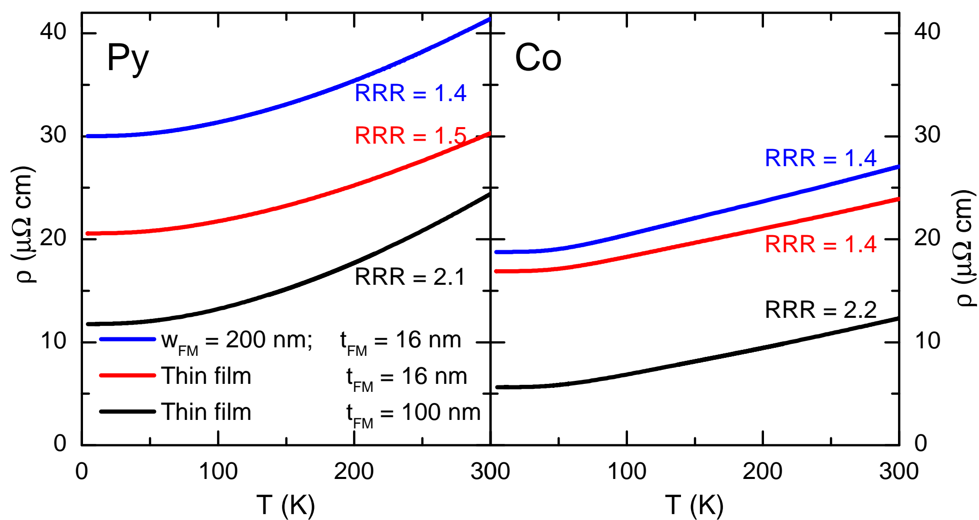

Figure 3.3: Typical temperature dependent resistivites of FM thin films and patterned nanowires of Py (permalloy) and Co.

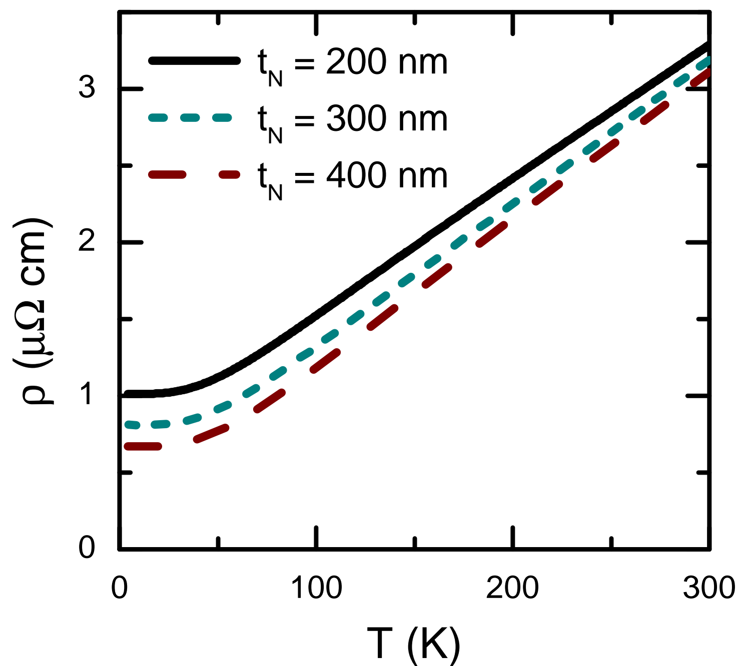

Figure 3.4: Typical temperature dependent resistivites of the Cu channel for several t_N.

3.2. The measured $\rho(T)$ of each material can be compared; Cu has the lowest ρ_N with Al a factor of 3 to 4 larger, depending on temperature. The resistivities of the FMs are much larger than the Ns. The maximum ρ_N is $8\,\mu\Omega\,\text{cm}$ and the minimum ρ_{FM} is $19\,\mu\Omega\,\text{cm}$, and therefore an axis break has been included to make the T dependence easier to observe. The measured resistivities, as described in this section, will be used for the analysis of the spin transport data.

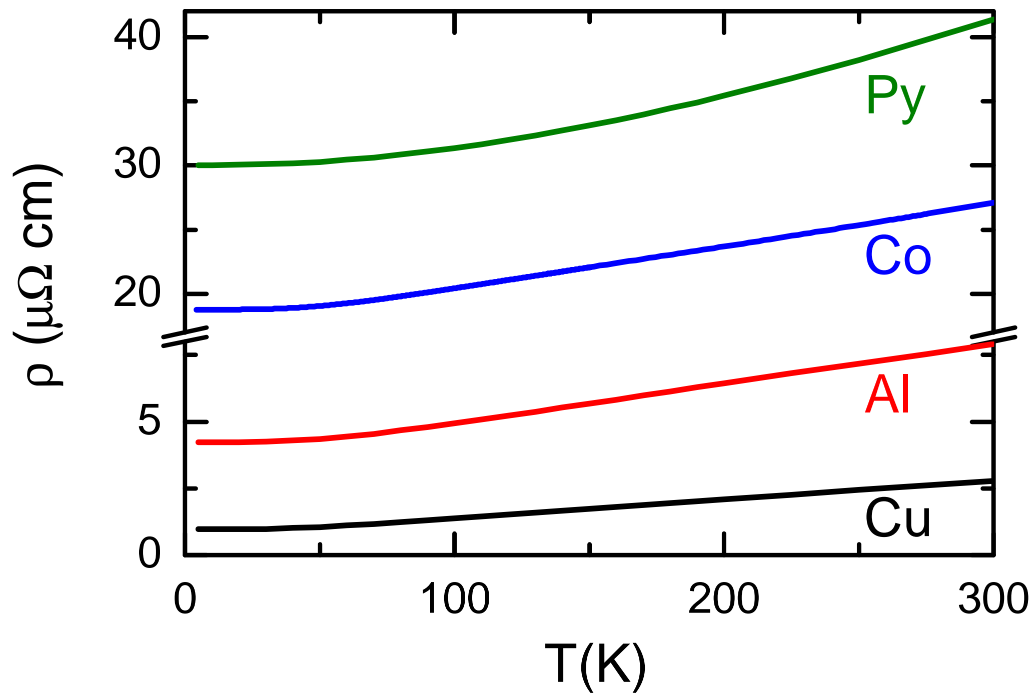

Figure 3.5: Typical temperature-dependent resistivites of the materials used in this thesis that have been patterned into nanowires and devices.

Material	$\rho_N(T = 5\,\mathrm{K}, 275\,\mathrm{K})$	$\frac{\rho_N(275\ \mathrm{K})}{\rho_N(5\ \mathrm{K})}$
Py/Cu	1.0, 3.1 µΩ cm	3.1
Co/Cu	1.1, 3.2 µΩ cm	2.9
Py/Al	4.2, 7.9 µΩ cm	1.9
Co/Al	4.3, 8.1 µΩ cm	1.9

Table 3.2: Typical values of ρ_N measured using patterned lateral non-local devices, with both FM materials serving as contacts.

3.2 Measurement of the Ferromagnet-Normal Metal Interface Resistance

Beyond characterizing transport through the individual patterned materials, the interfaces of the NLSV structures were also examined. The focus of this thesis is spin transport in lateral devices with diffusive transport across FM/N interfaces. Remarkably, the interfacial resistance R_I has rarely been reported in previous lateral transport experiments. Some of the previously-reported work on lateral spin valves describe fabrication techniques that result in interfaces of indeterminate quality. One fabrication technique used elsewhere employs multi-step lithography and materials deposition with argon-ion milling between layers to clean the FM/N interfaces. Even for fabrication techniques that minimize the possibility of the formation of an interfacial contamination layer, such as the multi-angle shadow evaporation technique used here (§2.3.4), it is important to characterize R_I.

The non-local lateral devices used in this work are fabricated with an additional electrical connection to the FM contact. This second FM connection, which has not typically been included in the work of others, allows one current source and voltage connection to be made to the same FM contact with the counter electrodes connected to opposite ends of the N. This measurement electrode configuration is referred to here as a 'three-terminal' measurement, depicted in Figure 3.6(a). The configuration shown allows R_I to be measured with contributions from the resistance of the surrounding materials contributing to the experimentally measured interface resistance:

$$R_{I,E} = \frac{V^+ - V^-}{J_e} = \frac{\Delta V_I}{J_e}. \tag{3.2}$$

Due to the finite size of realistic lateral devices, the measured voltage drop resulting from J_e includes contributions from the materials on either side of the interface, which can make R_I difficult to determine as the experimentally measured $R_{I,E}$ may be drastically different from the actual interface resistance R_I.

If R_I is much larger than the resistance of the surrounding materials, R_I can be estimated directly from the experimental $R_{I,E}$. In the opposite limit, where R_I is similar or less than the surrounding material resistances, the experimentally measured interface resistance must be separated from that due to the nearby materials. Since ρ_N and ρ_{FM} have been measured, the contributions to the measured resistance can be calculated. Modeling of the charge current through lateral non-local devices is described in §3.5.

The lateral devices used in this thesis are designed so that a four-terminal measurement of the interfaces can be made. This is accomplished by attaching the current source and voltmeter in a cross configuration about the interface, as labeled in Figure 3.6. The resistance measured in this configuration, for the case of a Co/Cu device, is -16 mΩ. For the case of large R_I, relative to the surrounding materials, a positive value will be measured. As R_I decreases the measured interface resistance will become negative due to the contribution of the current spreading at the intersection of the FM and N. The calculated potential has a negative background, a contour plot is shown in Figure 3.14(c) comparing the potential difference for the different lead configurations. The calculated background resistance due to current spreading $R_{I,M}$ is subtracted from the measured resistance $R_{I,E}$, allowing for an estimate of R_I. For the example Co/Cu case, $R_I \approx R_{I,E} - R_{I,M} \approx 5\,\mathrm{m}\Omega$. The product of R_I with the interface area A_I characterizes the interface, in this case $R_I A_I \approx 0.3\,\mathrm{f}\Omega\,\mathrm{m}^2$. This procedure can be repeated for devices with each of the materials combinations shown in Table 3.3, resulting in an upper bound of $R_I A_I \lesssim 0.6\,\mathrm{f}\Omega\,\mathrm{m}^2$ for all measured materials combinations. In Chapter 1 the spin resistance of a material was given, $R_s = \rho\lambda_s/A$, where λ_s is the spin diffusion length and A is the cross sectional area of a material. For these materials $R_{s,N} \geq 4\,\mathrm{f}\Omega\,\mathrm{m}^2$ and $R_{s,FM} > 1.6\,\mathrm{f}\Omega\,\mathrm{m}^2$. These devices are in the diffusive interface regime, as the estimated interface resistances here are of the same order or less than the characteristic spin resistances of the materials.

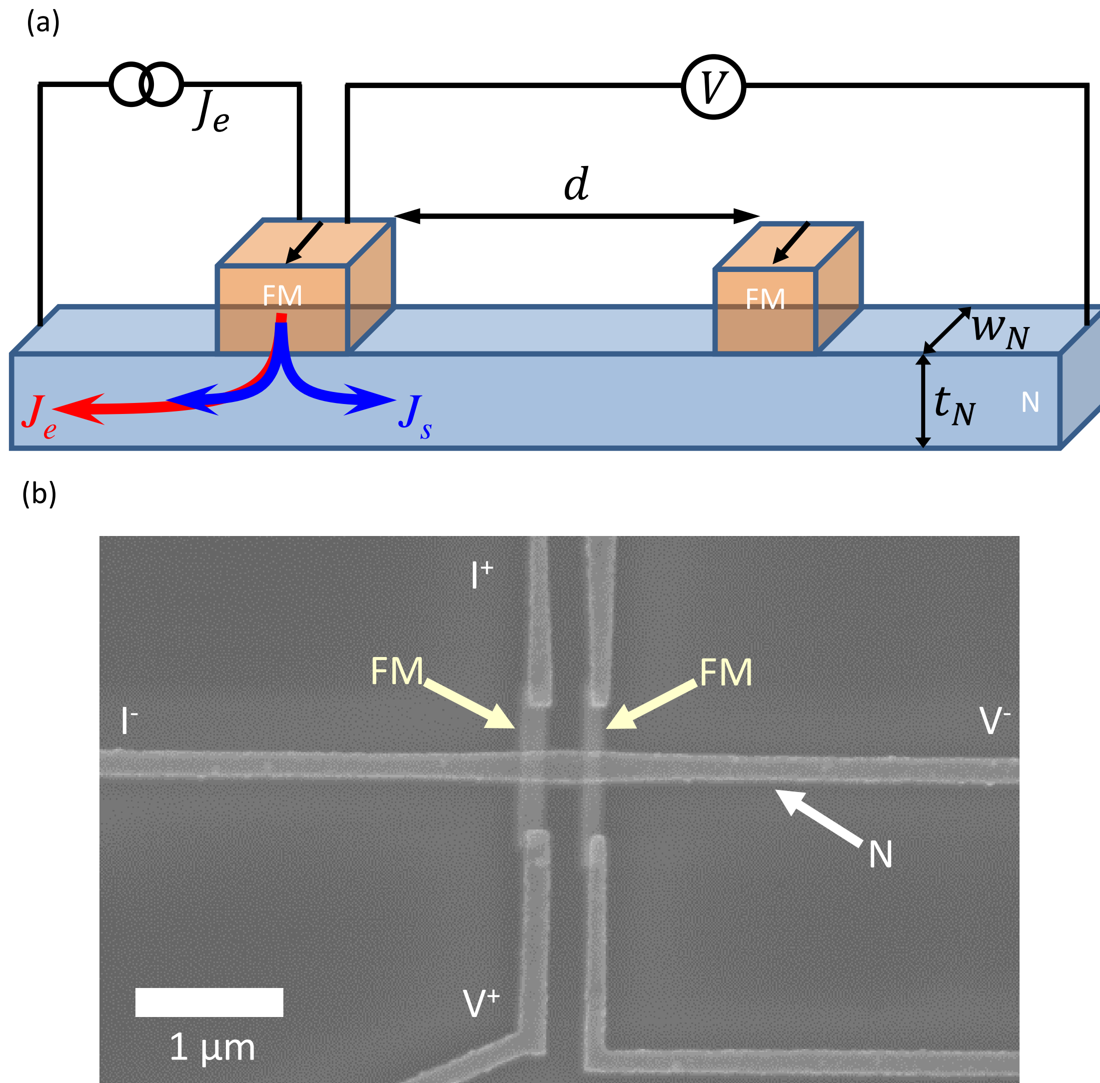

Figure 3.6: (a) Diagram of the three-terminal measurement configuration for interface resistance measurements also (b) labeled on a plan view SEM micrograph.

Material	$R_{I,E}$(mΩ)	$R_{I,M}$(mΩ)	$R_{I,E} - R_{I,M}$(mΩ)	$R_I A_I$(fΩ m^2)
Py/Cu	-8	-14	6	0.4
Co/Cu	-11	-16	5	0.3
Py/Al	-12	-22	10	0.5
Co/Al	-14	-25	11	0.6

Table 3.3: Typical values of experimentally measured $R_{I,E}$, calculated background $R_{I,M}$, and the resulting R_I after accounting for current spreading.

3.3 Non-Local Spin Transport Measurements

The techniques described in §3.1 and §3.2 characterize the charge-transport properties of each material. This section describes the measurement of spin transport in these structures, utilizing two different techniques. Each was conducted in the non-local measurement geometry, introduced in §1.2. This configuration is depicted in Figure 3.2(a) with an accompanying SEM micrograph of a lateral device in Figure 3.2(b). The SEM micrograph is labeled with the non-local configuration of the current source and voltage measurement connections.

3.4 Non-Local Spin Valve Measurement

By sweeping an applied magnetic field along the easy axis of the ferromagnetic contacts, which is the long axis of the FM shown in Figure 3.7, leads to the spin valve effect described in §1.2.10. At large positive magnetic fields both FM electrodes are aligned along the applied field in a parallel state (↑↑). As the magnetic field is swept from large positive to negative field, the magnetization of the FMs flip. The coercive field H_c of each FM contact is different so that during the field sweep one FM contact will flip before the other, putting the FMs in an antiparallel (↓↑) configuration. Subsequently, as the sweep continues the second FM flips, leaving the contacts in the opposite parallel state (↓↓). This process is the same for the opposite field sweep direction, and is repeated to obtain a second measurement of the antiparallel state. This process is then repeated at various T for each device.

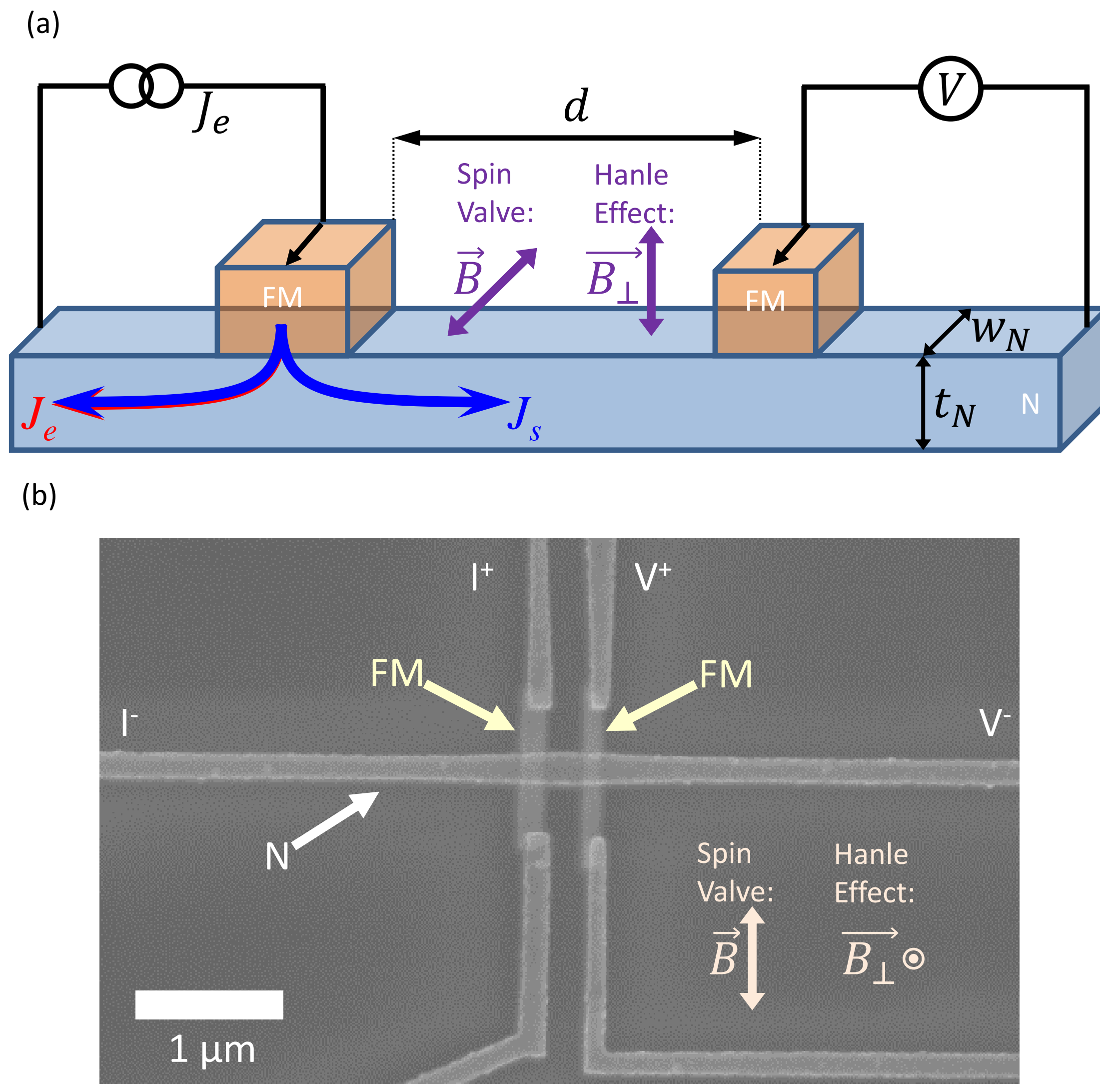

Figure 3.7: (a) Diagram of low-temperature measurement used in this work. (b) SEM micrograph with the current source and voltmeter connections and magnetic field orientations labeled.

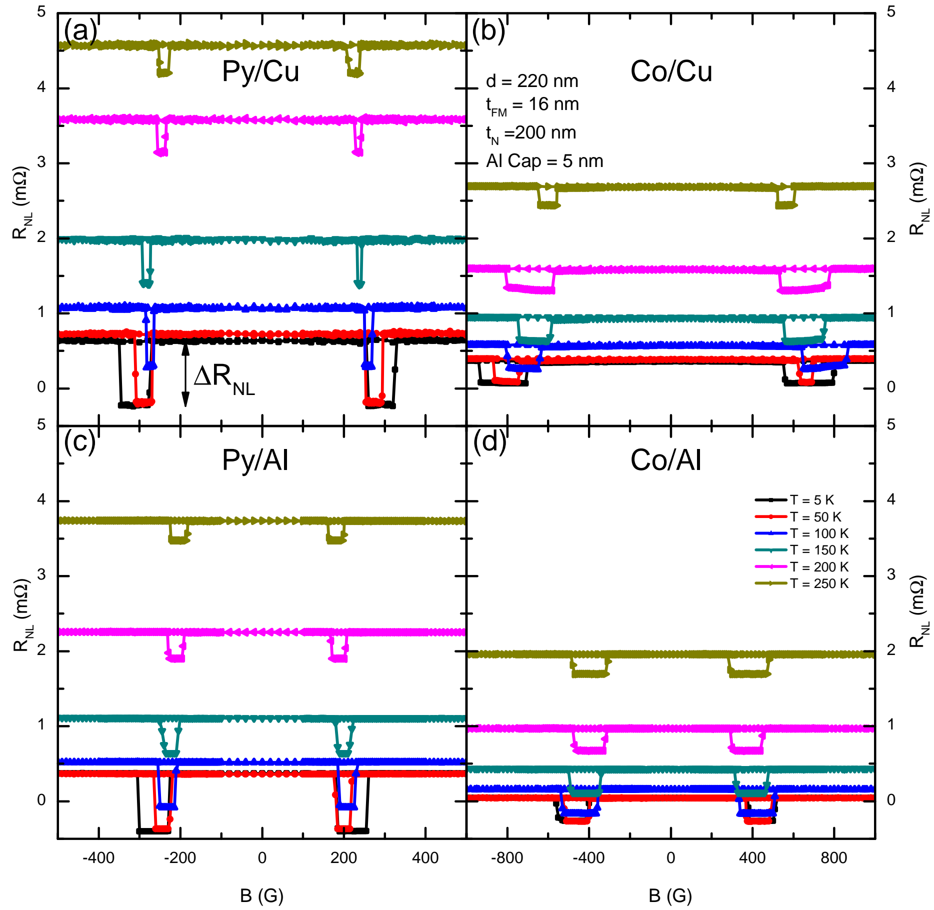

Figure 3.8: Measured non-local resistance R_{NL} vs magnetic field B showing the spin-valve effect. Measurements are shown for (a) Py/Cu, (b) Co/Cu, (c) Py/Al, and (d) Co/Al at $T = 5$, 50, 100, 150, 200, 250 K, $J_e = 1$ mA, and $d \approx 220$ nm.

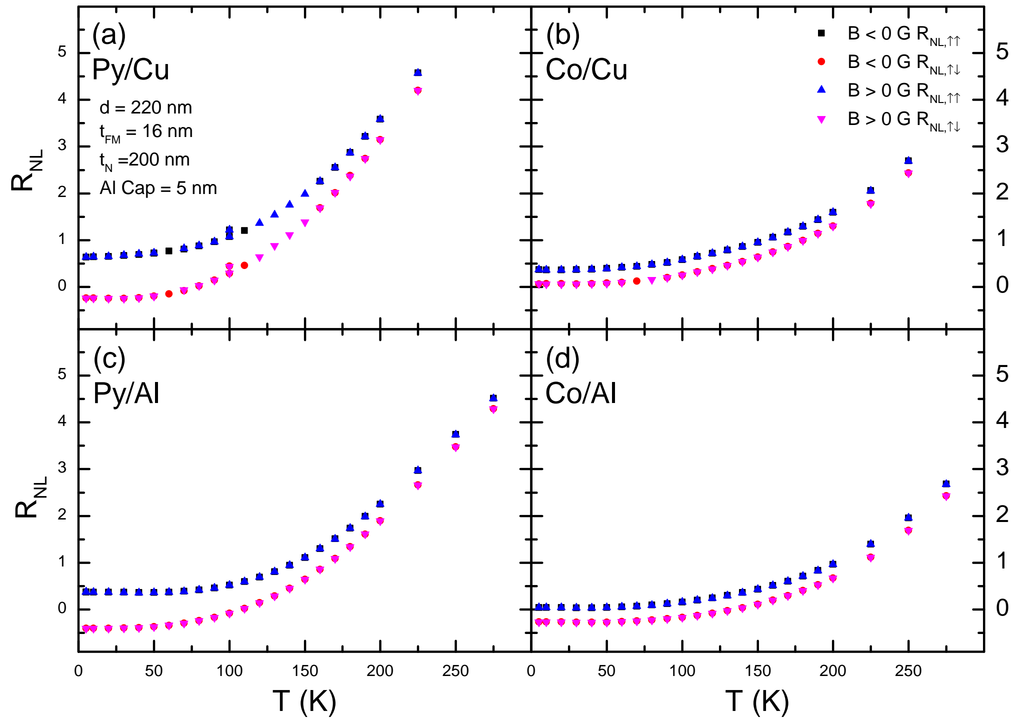

Figure 3.9: Measured non-local resistance for the parallel state $R_{NL,\uparrow\uparrow}$ and antiparallel state $R_{NL,\uparrow\uparrow}$ for both the descending field sweep ($B < 0\,\mathrm{G}$) and the ascending field sweep ($B > 0\,\mathrm{G}$) as a function of temperature for (a) Py/Cu, (b) Co/Cu, (c) Py/Al, and (d) Co/Al at $J_e = 1\,\mathrm{mA}$, and $d \approx 220\,\mathrm{nm}$.

Field-dependent transport measurements of lateral spin valve devices in the non-local configuration lead to typical non-local spin valve effect data, as shown in Figure 3.8. The critical feature of the data is the difference in magnitude between parallel and antiparallel states. The parallel and antiparallel non-local resistances are shown in Figure 3.9. The non-local resistances for the descending part of the field sweep are indistinguishable from the ascending one. These curves differ by less than $5\,\mu\Omega$ in most cases. By inspection, the difference between the two curves changes more with temperature for Py devices than Co. This difference in non-local spin resistance ΔR_{NL} is written,

$$\Delta R_{NL} \equiv \frac{V_{\uparrow\uparrow} - V_{\uparrow\downarrow}}{J_e} = \frac{\Delta V_{NL}}{J_e} = R_{NL,\uparrow\uparrow} - R_{NL,\uparrow\downarrow}, \tag{3.3}$$

where $V_{\uparrow\uparrow}$ and $V_{\uparrow\downarrow}$ are the parallel and antiparallel detector voltages, respectively. When $V_{\uparrow\uparrow}$ and $V_{\uparrow\downarrow}$ are divided by the excitation current J_e this yields $R_{NL,\uparrow\uparrow}$ and $R_{NL,\uparrow\downarrow}$, which are the parallel and antiparallel non-local resistances.

The magnetic field dependence of this transresistance shows switching between parallel and antiparallel states at $H < 0$ G for the descending field sweep direction and likewise at $H > 0$ G for the ascending sweep direction. Contributions to the data from an Ohmic drop as well as ordinary and anisotropic magnetoresistances are small compared to the signal due to the purely diffusive spin current flowing from the injector to the detector. Other transport effects are generally avoided in this configuration. In §3.5 it is shown that current spreading in metallic devices may extend beyond the injection electrode into the detection circuit area and lead to background voltages. Thermoelectric effects may also appear in this configuration, although the simplest cases are not expected to appear in the first harmonic of an AC lockin measurement but rather in the second harmonic.

The field-sweep data shown in Figure 3.8 show switching at fields consistent with reversal of the sub-micron patterned Py and Co. Although the field scale is too small to be consistent with single-domain coherent rotation of the FMs, the magnitude of the field is reasonable for nucleation and propagation of a domain wall. The coercive field H_c is dependent on the FM contact width and follows $H_c \propto w_{FM}^{-1}$, as discussed in §2.2.3. Differences in H_c observed in the data shown in Figure 3.8, are determined by the contact width. The wider contact was used for the spin injector while the narrower one is used is the detector. As a result it is expected that the magnetization

of the injector should switch first, followed by the detector contact. The switching fields decrease weakly with increasing temperature. H_c is shown as a function of temperature in Figure 3.10. The switching fields decrease with increasing temperature because the reversal is a thermally activated process. There is neither a particular feature at any temperature nor a significant difference between Py/Cu and Py/Al.

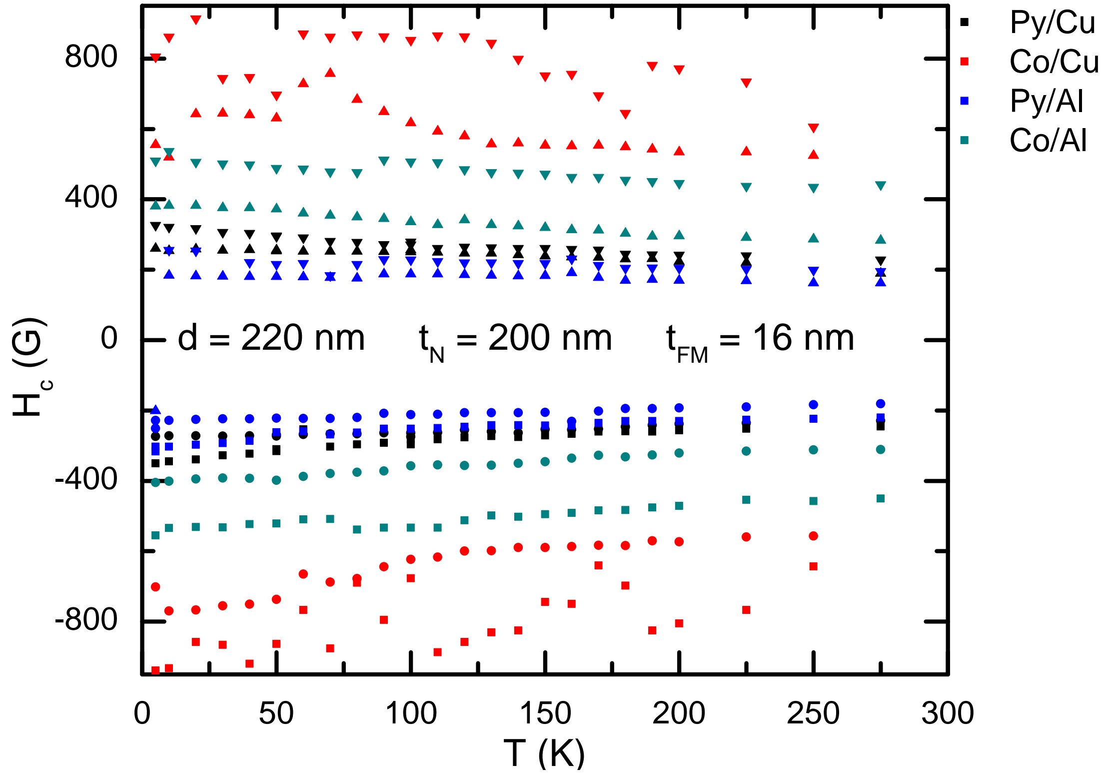

Figure 3.10: Measured coercive fields H_c, one for each contact for both ascending and descending field sweeps, as a function of temperature for Py/Cu, Co/Cu, Py/Al, and Co/Al non-local devices with $d \approx 220\,\text{nm}$.

3.4.1 Dependence of Spin Accumulation on Injection Current

NLSV experiments utilize charge currents up to $J_e = 1$ mA to inject spins, which is equivalent to $j_e = 3 \times 10^7$ A cm^{-2} for the wider contact while $j_e = 6 \times 10^7$ A cm^{-2} for the narrower contact. A threshold $J_e \approx 3$ mA ($j_e \approx 2 \times 10^8$ A cm^{-2}) has been found, above which FM break-down is likely due to "fuse-wire" like melting of the contact,

corresponding to a Joule heating power density of 10^{12} W cm^{-3}. SEM micrographs of destroyed devices confirm the "fuse-wire" failure mode.

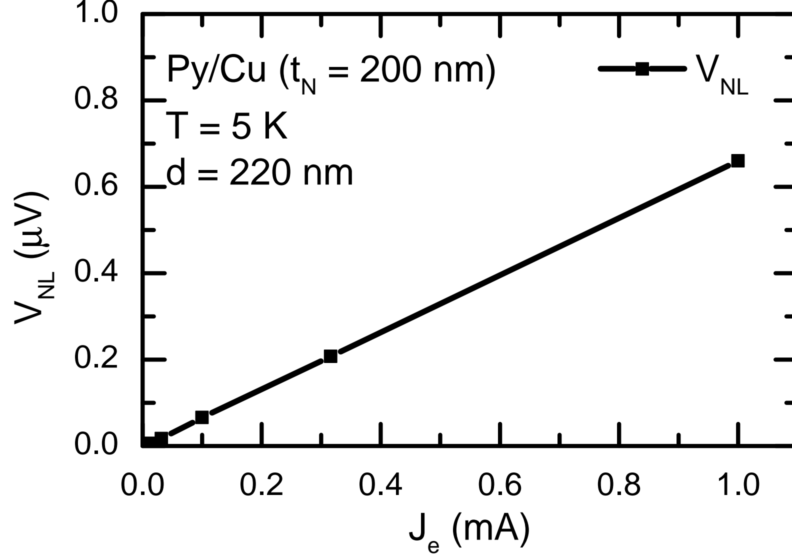

Figure 3.11: Dependence of the non-local detector voltage V_{NL} on the injector bias current J_e.

The diffusive transport across FM/N interfaces is expected to obey Ohm's law. The measured non-local voltage V_{NL} is shown in Figure 3.11. V_{NL} depends linearly on J_e and has an intercept of zero. ΔV_{NL} measured using devices with diffusive FM/N interfaces is expected to be linear with J_e also. Repeated field sweeps at various excitation currents confirm that, up to $J_e = 1\,\mathrm{mA}$, ΔV_{NL} remains linear, with a constant ΔR_{NL}, as shown in Figure 3.12. In the case of this Py/Cu device ΔR_{NL} is $0.7\,\mathrm{m}\Omega$ at $T = 5\,\mathrm{K}$. The magnitude of this signal is less than has been observed for similar low-resistance interface Py/Cu devices by Kimura *et al.* [43]. The value of ΔR_{NL} measured in this work, however, is larger than has been reported in most other low-resistance devices such as the experiments reported in References [45, 78, 82]. This linear response has also been confirmed for J_e below several milliamps for devices of similar dimensions by Casanova *et al.* [44]. Due to the sensitivity of ΔR_{NL} on T for Py/Cu, which will be shown in §4.1, this also serves as a test of Joule self-heating of the sample.

A second test of sample self-heating was conducted by cooling the sample to low

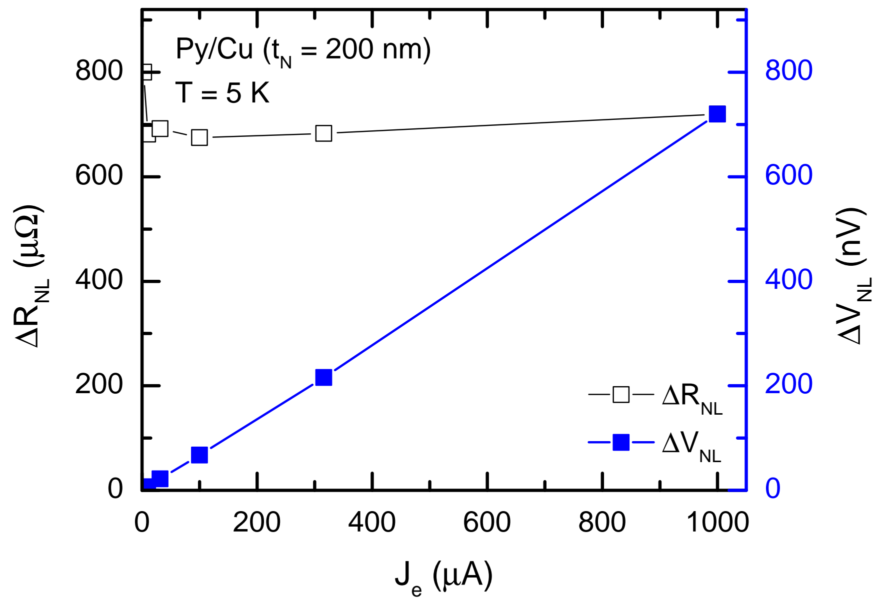

Figure 3.12: Dependence of the non-local detector voltage ΔV_{NL} and resistance ΔR_{NL} on the injector bias current J_e.

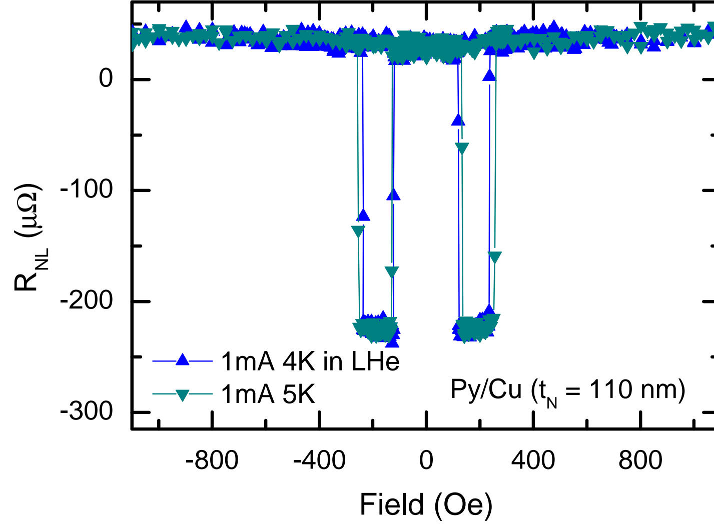

Figure 3.13: Comparison of non-local spin valve field sweeps either immersed or not immersed in liquid He.

temperatures and measuring ΔR_{NL} as the sample was immersed in liquid helium. The results of one such test are shown in Figure 3.13 where the magnitude of the non-local resistance is independent of whether the samples is immersed in liquid helium or remains in vapor. This confirms that the sample is in good thermal contact with the helium-vapor cryostat and is capable of keeping the sample from appreciably self heating for $J_e \leq 1\,\mathrm{mA}$.

3.5 Origin of the Non-Local Background

The background V_{NL} is expected to be zero for purely diffusive spin transport in the ideal lateral non-local device. The detected V_{NL} should increase or decrease from zero by equal amounts, depending on whether the spins are parallel or antiparallel to the detector magnetization. The background,

$$R_{NL,B} = \frac{V_{NL,B}}{J_e} = \left(R_{NL,\uparrow\uparrow} + R_{NL,\uparrow\downarrow}\right)/2, \tag{3.4}$$

should equal zero in the absence of other effects. However, the raw non-local field sweep data shown thus far in this thesis have non-zero backgrounds. This is due to contributions from spin-independent and -dependent mechanisms.

3.5.1 Spin-Independent Background Due to Charge Current Spreading

Background voltages generated from the charge current path depend on the precise geometry of the device and the resistivities of the constituent materials. Due to the spatial asymmetry of the non-local measurement, the voltage probes do not lie along lines of equipotential. Using the measured ρ and device geometry, the magnitude of the Ohmic background can be calculated.

Numerical calculation of current spreading

The geometries of the fabricated devices are sufficiently complicated that calculating the potential difference between the non-local detector voltage probes analytically is difficult, although it has been addressed by others [111]. Rather, numerical methods are a straight forward way to determine the background detector voltages due to current spreading. A finite-element method was used to calculate this background.

The finite-element method uses a grid of points laid out over the geometry of the device to calculate specific quantities at each point. The solution must satisfy the continuity equation. A solution to Poisson's equation,

$$\nabla^2 V = -\frac{n_e}{\epsilon}, \tag{3.5}$$

is determined iteratively for each point in the mesh for the electric potential V, where n_e is the density of charge carriers, and ϵ is the permittivity of the medium. For the case of planar conductors, Equation 3.5 can be written for the two orthogonal in-plane Cartesian coordinates $\hat{x}$ and $\hat{y}$,

$$\frac{\partial}{\partial x}\left(\frac{1}{\rho_x}\frac{\partial V}{\partial x}\right) + \frac{\partial}{\partial y}\left(\frac{1}{\rho_y}\frac{\partial V}{\partial y}\right) = 0, \tag{3.6}$$

where the ρ_x and ρ_y are the in-plane components of the resistivity tensor. For these experiments, the N metals are isotropic ($\rho_N = \rho_{N,x} = \rho_{N,y}$) and, therefore, only one

resistivity needs to be specified. For the FM materials, however, this is not necessarily the case. Due to anisotropic magnetoresistive effects, $\rho_{FM,x} \neq \rho_{FM,y}$ with the two differing by a few percent in typical transition metal FMs [112, 113].

Boundary conditions are also required to complete the calculation. A fixed potential V_E is set between the end of the FM injector and N channel, labeled in Figure 3.14(c), defining an applied potential to drive current through the injector. At all other boundaries, the charge current perpendicular to the surface must be zero.

Once Poisson's equation has been satisfied for the specified boundary conditions, the current density j_e can be recovered from

$$\vec{j_e} = -\frac{1}{\rho}\nabla V. \tag{3.7}$$

Summing j_e across the cross section allows the total current flowing through the device to be calculated. V_E is varied iteratively to achieve the desired J_e to model experiments. Figure 3.14 shows a typical finite-element solution for a Co/Cu lateral non-local device at $T = 292$ K using the measured ρ_N and ρ_{FM}. Figure 3.14(a) shows j_e, which is constant through the N and FM far from the N/FM interface. Near the interface, however, the current spreads out into the N towards the FM injector as well as into the detector contact resulting in a drop in j_e. Panels (b) and (c) show the potential plotted, (b) with full scale ($\approx 2.9\,\mathrm{mV}$) and (c) a narrow ($5\,\mu\mathrm{V}$) subrange to show the background. A potential gradient is observed extending into the detector region, generating a spin-independent voltage between the FM detector (V^+) and the detector reference (V^-) contact, which is far away on the N channel. The voltage measured between V^+ and V^- is approximately $1\,\mu\mathrm{V}$ at $J_e = 1\,\mathrm{mA}$ for the case of Co/Cu at room temperature which corresponds to $R_{NL} \approx 1\,\mathrm{m}\Omega$. The modeling also indicates that the voltage measured between the FM detector from the contact on the opposite side to the voltage reference ($V^+_{Opp} - V^- \approx 1\,\mu\mathrm{V}$) should be of the same order with a sign reversal. Additionally, in this model, if the N channel resistivity is reduced, the background voltage due to current spreading is reduced. The above magnitude, sign change with V^+_{Opp}, and the dependence on ρ_N are all consistent with experimental observations. The spin-independent background is demonstrated experimentally by measuring R_{NL} for a device with the FM material replaced by a non-magnetic metal. $R_{NL}(T)$ for an all-copper device is shown in Figure 3.15 .

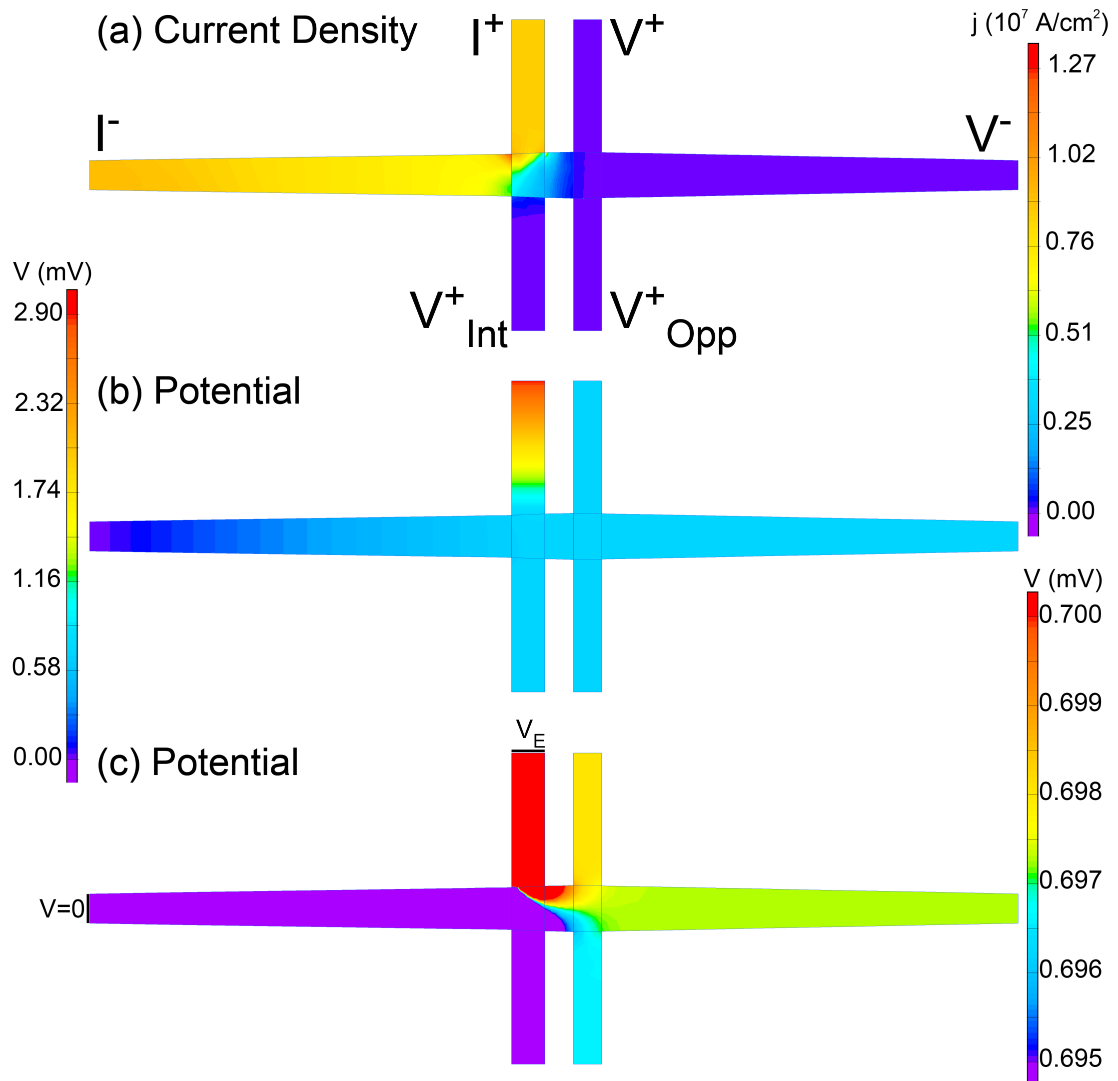

Figure 3.14: Modeled charge transport through a non-local spin valve with (a) the spatial current density and the spatial potential shown with (b) a 2.9 mV scale and (c) a 5 µV scale.

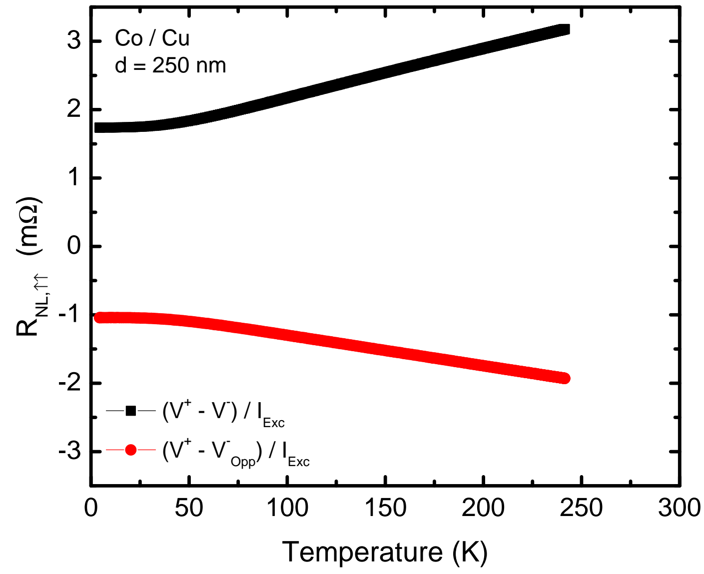

Figure 3.15: Non-local resistance as a function of temperature for an all-copper device measured using each of the leads attached to the detector (V^- and V^-_{Opp}).

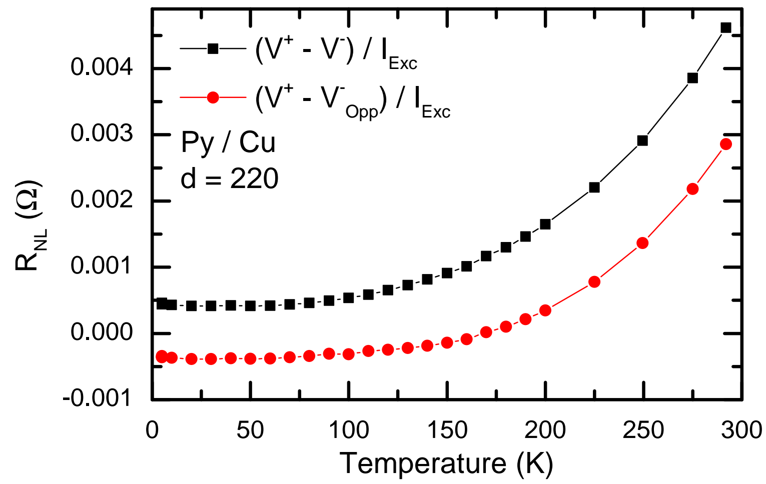

Figure 3.16: Non-local resistance as a function of temperature for a Py/Cu device measured using both of the leads attached to the detector (V^- and V^-_{Opp}).

3.5.2 Non-Local Background - Thermoelectric Effects

Thermoelectric effects are another likely source of background effects. Thermoelectric effects that are spin-independent as well as spin-dependent may contribute to the background. Bakker *et al.* [114] described contributions from spin-based thermoelectric effects that induce offsets to the measured non-local background.

The non-local background, given by Equation 3.4, can have contributions from charge current spreading as well as thermoelectric effects. The contribution due to current spreading should decay exponentially with d. The data in Figure 3.17, however, are not purely exponential. The thermoelectric origin would follow from the heat generated at the injector due to the charge current flow. In this case, due to the differences of the Peltier coefficients of the FM and N materials this may lead to heating or cooling of the injector interface depending on the sign of the charge current. The resulting thermal gradient will also be present at the detector. Now, due to the Seebeck effect, a detector voltage will be present. Originating from the Peltier effect, rather than only the Joule heating, makes it possible for this effect to manifest in a standard lockin measurement at the first harmonic.

Thermal gradients on the order of $\sim 2\,\mathrm{K}$ between source and detector have been found for FM/N/FM nanostructures with similar current densities [115]. The magnitude of the thermoelectric non-local background increases with temperature gradient and can be as large as $\sim 10\,\mathrm{m}\Omega$ near room temperature. For smaller current densities the relevant detector voltage decreases, and thus non-local background resistance can be on the order of $1\,\mathrm{m}\Omega$. Thermal gradients may contribute to the temperature dependence of the non-local background which has been observed as part of this work for various contact separations, shown in Figure 3.17 Differences among the materials combination shown in Figure 3.18 may also have contributions from thermoelectric effects.

3.6 Non-Local Electrical Hanle Effect Measurement

The Hanle effect, as described in §1.2.14, allows for the measurement of the source-detector transit time of the diffusive spin-current, and more importantly, the spin lifetime $\tau_{s,N}$. Rather than acquiring spin-relaxation information by measuring ΔR_{NL} at several different d to measure the spatial dependence of the spin relaxation, Hanle effect

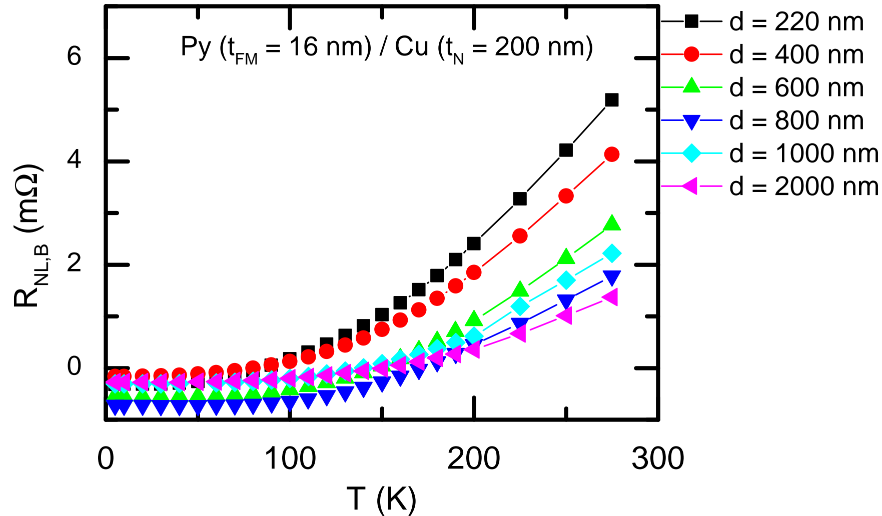

Figure 3.17: Measured non-local background resistance as a function of temperature for Py/Cu non-local devices with various contact separations.

measurements are sensitive to the spin precession and dephasing of the diffusive spin current about a perpendicular magnetic field. The Hanle effect experiments on Al devices with diffusive interfaces presented here produce Hanle curves qualitatively similar to those observed in semiconductors [5] or a limited number of experiments with Al channels in References [4, 116, 117] with tunnel barrier interfaces. Hanle curves have also been measured using Py/MgO/Ag devices with large separations $d = 2\,\mu\text{m}$ and $6\,\mu\text{m}$ [118]. Hanle experiments were also undertaken on the Cu devices, in this case, a full Hanle curve is difficult to measure due to the larger diffusion constant than in Al resulting in broad Hanle curves. A previous attempt to measure Hanle effects for Cu with tunnel barriers [80], and to some extent Ag [59], only measured partial curves limited to small fields. Some of the first Hanle effect measurements and analysis of diffusive interfacial transport through Cu and Al channels are shown in this thesis.

The electrical Hanle effect in the non-local geometry requires the current source and voltmeter to be connected in the same manner as for spin valve experiments in §3.3. The difference between these measurements is that the applied magnetic field $H_\perp$ is now perpendicular to the FM magnetization, and thus perpendicular to $\vec{S}$. As a result

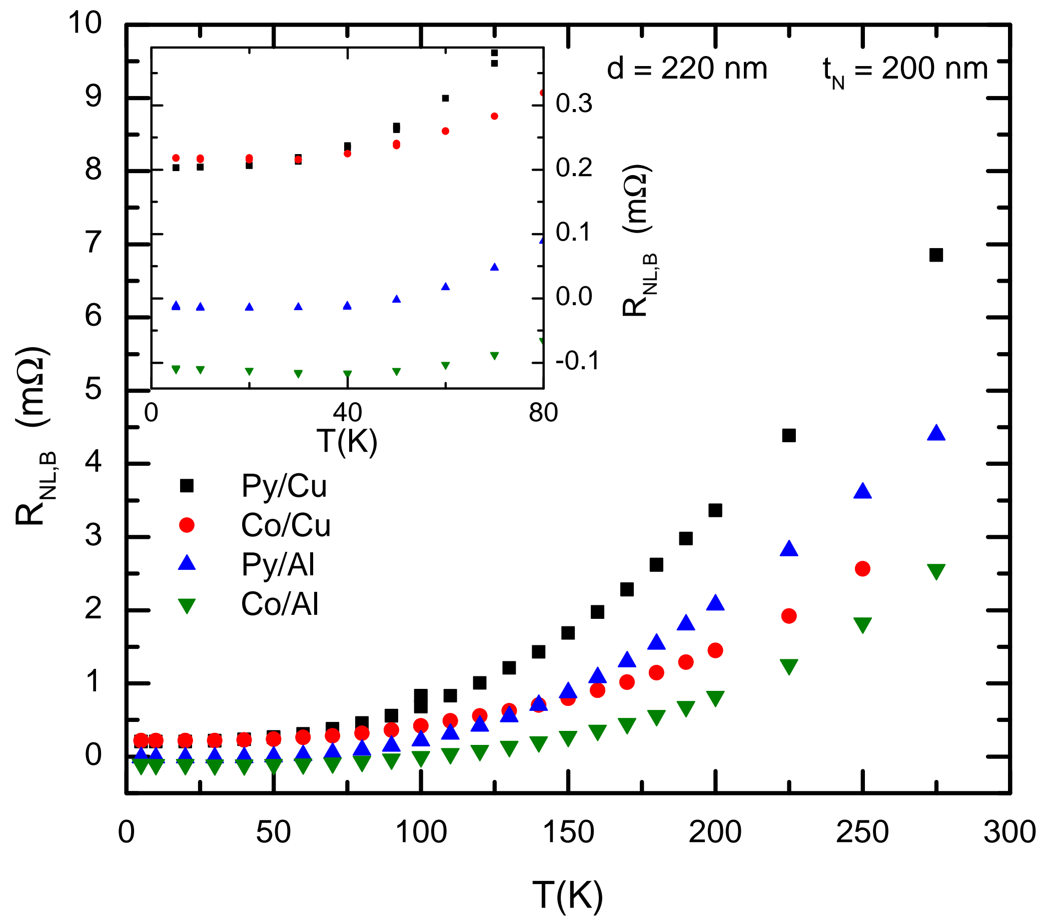

Figure 3.18: Measured non-local background resistance as a function of temperature for Py/Cu, Co/Cu, Py/Al, and Co/Al non-local devices with $d \approx 220\,\text{nm}$.

the diffusive spin current is precesses and dephases.

Al devices, with diffusion constant $D_N \sim 60\ \mathrm{cm}^2/\mathrm{s}$ and spin lifetime $\tau_{s,N} \gtrsim 15$ ns at $T = 5\,\mathrm{K}$, produce Hanle widths sufficiently narrow such that they may be experimentally observed with transition metal FM injectors and detectors. Figure 3.19 shows Hanle effect data for a Py/Al device with $d = 2000$ nm at $T = 5$ K which was prepared in either the parallel ($\uparrow\uparrow$) or antiparallel ($\uparrow\downarrow$) FM magnetization states using partial in-plane field sweeps. The NLSV device is initialized into the parallel state by sweeping the applied field to $B = 4\,\mathrm{kG}$ then back to zero field and the parallel resistance $R_{NL,\uparrow\uparrow}$ is confirmed. The antiparallel state is initialized similarly but rather than end at $B = 0\,\mathrm{G}$ the field is swept through zero until the one contact has reversed, then brought to $B = 0\,\mathrm{G}$. The observed antiparallel spin valve resistance $R_{NL,\uparrow\downarrow}$ at the end of this process is stable. In both cases the sample is then rotated 90° such that $H_\perp$ can be applied to measure the Hanle effect. Analysis of these field sweep data will be discussed in §4.5, where the application of analytical models that include transport in the N only are used, and §5.2.4 where a numerical model including the FMs and spin relaxation at surfaces is used.

The results of the systematic measurements of charge and spin transport of non-local spin transport devices, as described in this chapter, are discussed in Chapter 4. The temperature and spatial dependences of the spin-valve signal are discussed for various materials combinations. The analysis of these data to determine parameters associated with the spin diffusion length and lifetime are also included.

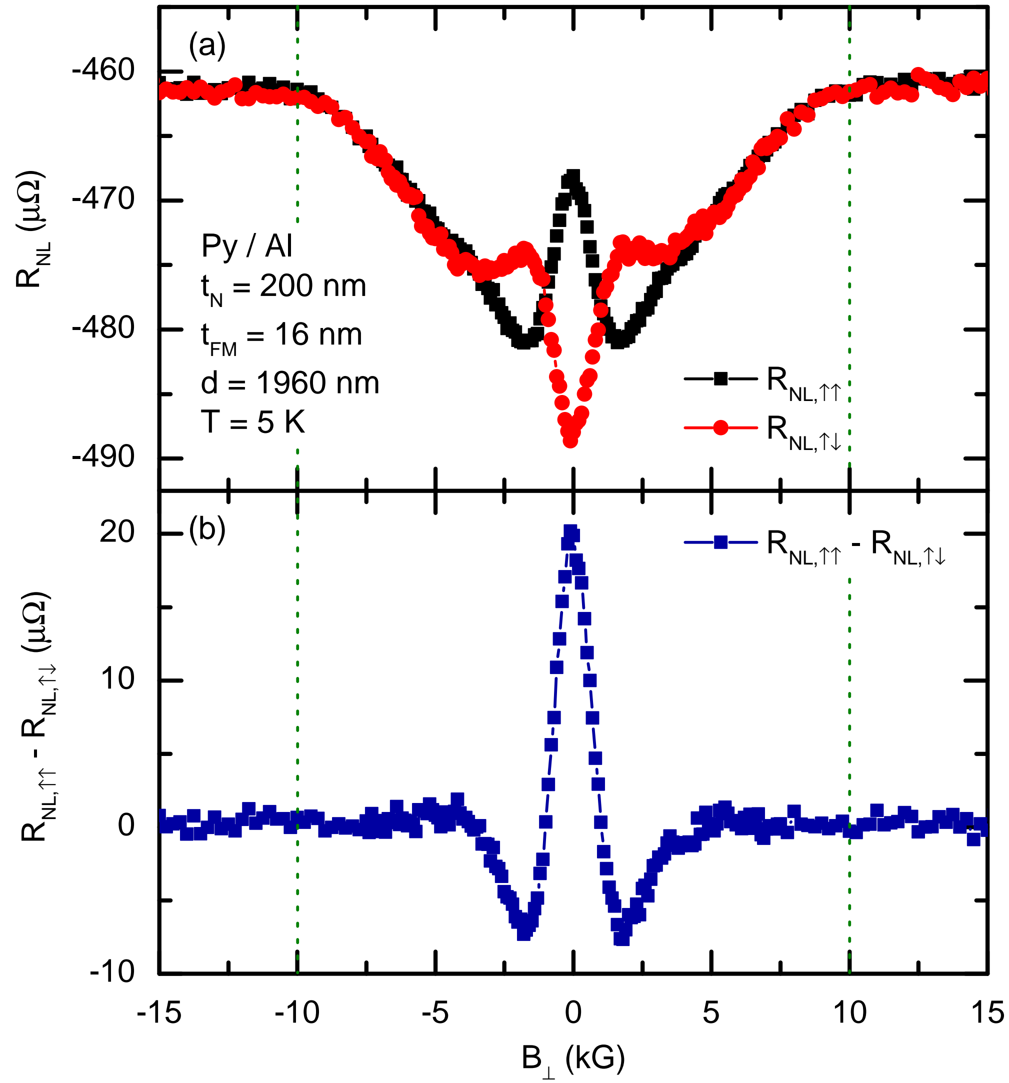

Figure 3.19: (a) Raw Hanle effect data of $R_{NL,\uparrow\uparrow}$ and $R_{NL,\uparrow\downarrow}$ as well as (b) the difference between parallel and antiparallel magnetization configurations ($R_{NL,\uparrow\uparrow} - R_{NL,\uparrow\downarrow}$) for a Py/Al device.

Chapter 4

Spin Transport Results and Analysis

The results of spin-transport measurements using lateral non-local spin valves (L-NLSV) are reported in this chapter. The devices were fabricated as described in Chapter 2 and measured as outlined in Chapter 3. Field sweeps of the non-local resistance R_{NL} vs. applied field B, such as those shown in Figure 3.8, were used to measure the difference between R_{NL} in the parallel and anti-parallel states (ΔR_{NL}). These measurements were repeated at various temperature T, FM contact separation d, and for different FM/N material combinations.

4.1 Temperature Dependence of ΔR_{NL}

Field sweeps were used to measure the difference of the non-local resistance between the parallel and anti-parallel FM contact magnetization states, $\Delta R_{NL} = R_{NL,\uparrow\uparrow} - R_{NL,\uparrow\downarrow}$, as a function of temperature for each of the materials combinations Py/Cu, Co/Cu, Py/Al, and Co/Al. These data are shown for $d = 220 \pm 10\,\mathrm{nm}$ in Figure 4.1.

The most striking feature of the data in Figure 4.1 is the two very different temperature dependences, showing a correlation between ΔR_{NL} and the FM materials employed in the NLSV fabrication. $\Delta R_{NL}\,(T)$ for both the Co/Cu and Co/Al devices display a weak temperature dependence, changing by less than 20% as T is increased from 5 K to 275 K. In contrast, Py/Cu and Py/Al lateral spin valves show a reduction of $\Delta R_{NL}\,(T)$

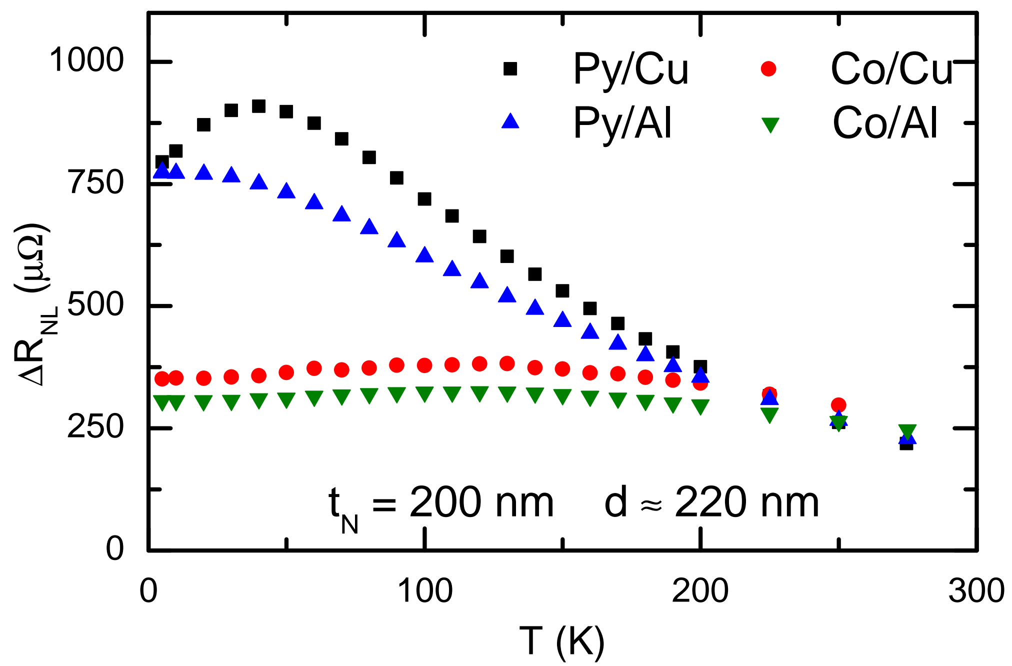

Figure 4.1: Temperature dependence of the difference of the non-local resistance between the parallel and anti-parallel contact magnetization states ΔR_{NL} for Py/Cu, Co/Cu, Py/Al and Co/Al devices with a source-detector separation of $d = 220 \pm 10\,\text{nm}$.

by nearly 75% over the same temperature range. Devices composed of Py/Cu appear to present a special case with a pronounced peak at $T \approx 50\,\mathrm{K}$. Very recent data collected by my collaborators show a similar peak for the case of Fe FMs with Cu channels. Our Py/Cu $\Delta R_{NL}\,(T)$ data are very similar to those of Kimura *et al.* [43], who focused solely on the role of the N channel. However, the marked differences that we find between Co and Py contacts reveal a strong dependence of spin transport on the FM properties in addition to those of the N channel. The comparison of all four material combinations clearly demonstrates that the unusual temperature dependence in the Py/Cu case cannot be ascribed to a property of either material alone but rather to the interplay of both, i.e. the interface between the FM and N.

These $\Delta R_{NL}(T)$ data can be compared to what is expected using the spin-transport theory discussed in Chapter 1. ΔR_{NL} can be expressed as [44, 45],

$$\Delta R_{NL} = \frac{2\alpha_{FM}^2 R_{s,N}}{\left(2 + \frac{R_{s,N}}{R_{s,FM}}\right)^2 e^{d/\lambda_{s,N}} - \left(\frac{R_{s,N}}{R_{s,FM}}\right)^2 e^{-d/\lambda_{s,N}}}, \tag{4.1}$$

which depends on the spin resistances $R_{s,FM}$ of the FM and $R_{s,N}$ of the N. The spin resistances used here,

$$R_{s,N}(T) = \frac{\rho_N(T)\lambda_{s,N}(T)}{A_N}, \tag{4.2}$$

$$R_{s,FM}(T) = \frac{\rho_{FM}(T)\lambda_{s,FM}(T)}{A_{FM}}, \tag{4.3}$$

depend on the resistivities ($\rho_N(T)$ and $\rho_{FM}(T)$), spin diffusion lengths ($\lambda_{s,N}(T)$ and $\lambda_{s,FM}(T)$), and cross sectional areas (A_N and A_{FM}). The magnitude of $\Delta R_{NL}(T)$ can be estimated from Equation 4.1, making use of measured and literature values for key material parameters. $\Delta R_{NL}(T = 5\,\mathrm{K}) = 3\,\mathrm{m}\Omega$ is estimated for the Py/Cu case using the measured ρ_N and ρ_{FM} as well as $\lambda_{s,Cu} = 1000\,\mathrm{nm}$, $\lambda_{s,Py} = 5\,\mathrm{nm}$, and $P_{Py} = 45\%$ which are consistent with the literature values tabulated in §1.3. The case of Py/Al, again using $\lambda_{s,Al} = 1000\,\mathrm{nm}$, $\lambda_{s,Py} = 5\,\mathrm{nm}$, and $P_{Py} = 45\%$, yields a smaller $\Delta R_{NL}\,(T = 5\,\mathrm{K}) = 1.5\,\mathrm{m}\Omega$ due to the fact that ρ_{Al} is approximately four times greater than ρ_{Cu}. If $\lambda_{s,N}$ used in the estimate is reduced from 1000 nm to 400 nm it leads to a reduction of $\Delta R_{NL}\,(T = 5\,\mathrm{K})$ from $1.5\,\mathrm{m}\Omega$ to $1.3\,\mathrm{m}\Omega$ for Al and $3\,\mathrm{m}\Omega$ to $2.1\,\mathrm{m}\Omega$ for Cu. To match experimental data with the magnitudes calculated from this model requires a reduction below the literature values of one or more of the parameters, $\lambda_{s,N}$, $\lambda_{s,FM}$, or

. Separating these parameters is impossible, however, when only one injector detector distance is used.

Shown in Figure 4.2 is $\Delta R_{NL}(T)$ measured for each combination of materials with several nominal contact separations: 220, 400, 600, 800, 1000, and 2000 ± 20 nm. The

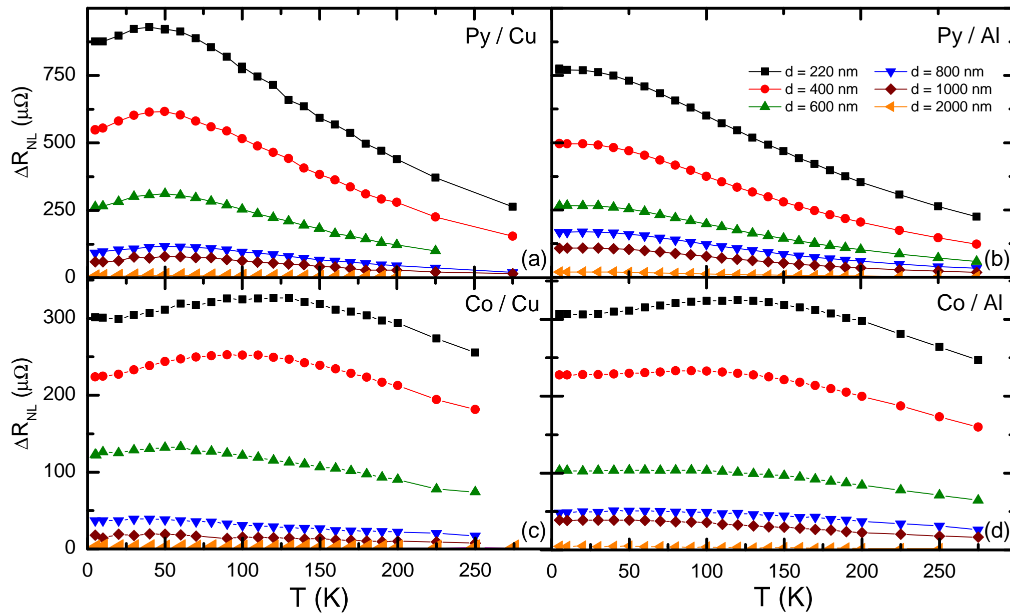

Figure 4.2: Temperature dependence of ΔR_{NL} for (a) Py/Cu, (b) Py/Al, (c) Co/Cu, and (d) Co/Al at FM contact separations ranging from 220 nm to 2 µm.

overall observed temperature dependence of ΔR_{NL} for each material at $d = 220 \pm 10$ nm, in Figure 4.1, persists for larger d but with reduced magnitude due to spin relaxation. This includes the $T \approx 50$ K peak of the ΔR_{NL} data, unique to Py/Cu, which also persists for all measured d at approximately the same T.

4.2 Separation Dependence of ΔR_{NL}

The spin diffusion length $\lambda_{s,N}$ of the channel material is determined by measuring the spatial decay of the non-equilibrium spin accumulation along the length of an N channel. $\lambda_{s,N}$ can be determined from the spatial dependence of the non-equilibrium spin accumulation. $\lambda_{s,N}$ has been reported by others to range from 40 nm to 100 µm for various N channel materials, as discussed in §1.3. In contrast, $\lambda_{s,FM}$ is smaller than $\lambda_{s,N}$ for all but high atomic number N materials like Pt. $\lambda_{s,FM}$ is determined from fitting the magnitude of the spin valve effect, typically of GMR measurements [2]. Although values up to 60 nm have been reported for Co [41], $\lambda_{s,FM}$ is typically less than 10 nm, as listed in Table 1.2.

The data of Figure 4.2 can also be plotted as a function of d rather than T. ΔR_{NL} plotted as a function of d is shown in Figure 4.3 for Py/Cu, Co/Cu, Py/Al, and Co/Al devices with $t_N = 200 \pm 10\,\text{nm}$ at $T = 5.000 \pm 0.005\,\text{K}$. The magnitude of ΔR_{NL} decreases with increasing d, similar to an exponential decay. Despite the differences in the magnitude of these ΔR_{NL} data, the spatial decay is similar for each of the material combinations used.

The decay of ΔR_{NL} with d is not expected to follow a pure exponential and requires the inclusion of diffusive spin transport across FM/N interfaces in the model. Contributions to spin-relaxation from diffusion of spins back into the FMs modifies the spatial dependence to that of Equation 4.1 where ΔR_{NL} decreases faster than $e^{-d/\lambda_{s,N}}$ for $d \lesssim \lambda_{s,N}$. A purely exponential decay of ΔR_{NL} is recovered for this model for $d \gg \lambda_{s,N}$. It is difficult to discern visually the increased decay rate of these data for small d given the experimental range measured in this work. To extract meaningful quantitative information from these data the d dependence must be fit with a diffusive interface model, the details and results of which are shown in §4.4.

4.3 Dependence of ΔR_{NL} on Channel Thickness

Changing the cross sectional dimensions of the N channel allows the effect of finite size on spin relaxation to be probed. This change of cross section was done by varying the thickness of the N channel t_N. To minimize differences among fabricated samples,

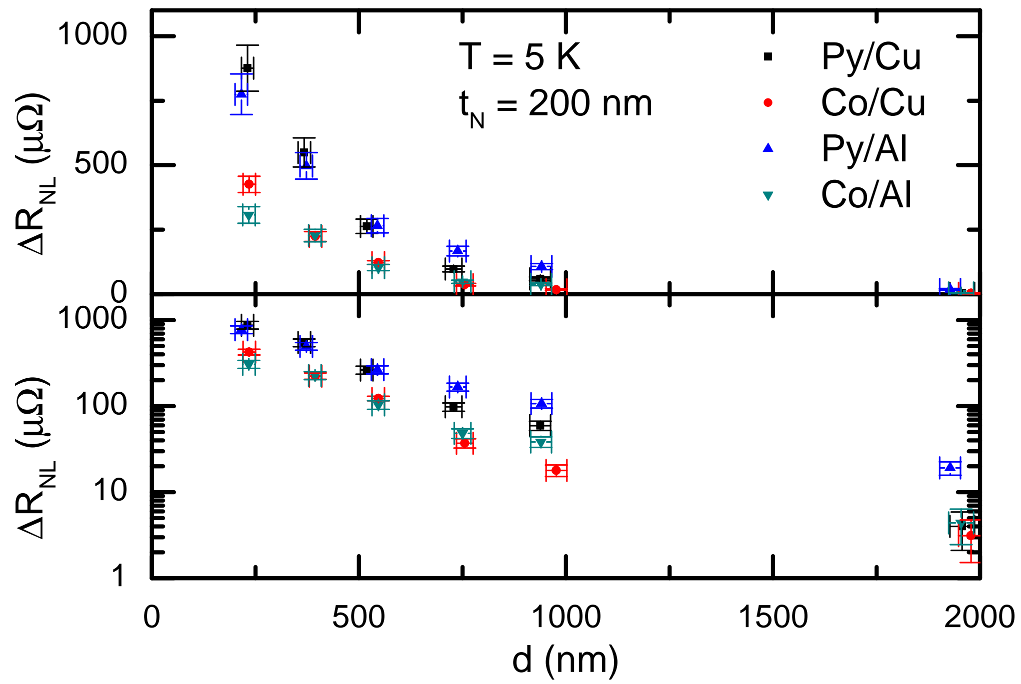

Figure 4.3: ΔR_{NL} measured for Py/Cu, Co/Cu, Py/Al, and Co/Al as a function of contact separation for $t_N = 200\,\text{nm}$ at $T = 5\,\text{K}$.

identical patterns were created using the EBL method given in Chapter 2. The deposition of 16 nm of Py was followed by Cu using the sample shutter to sequentially block patterns from the source such that devices with $t_N = 200$ nm, 300 nm, and 400 nm were deposited, as described in §2.3.3. The simultaneous patterning and deposition of samples with various t_N, ensured that the FM contacts, FM/N interfaces, and the first 200 nm of Cu were as identical as experimentally possible. Shown in Figure 4.4 is ΔR_{NL} as a function of T for these devices with $t_N = 200$, 300, and 400 ± 10 nm and $d = 220$, 800, and 2000 ± 20 nm. $\Delta R_{NL}(T)$ data for Co/Cu with $t_N = 200 \pm 10$ nm is overlaid for comparison.

The magnitude of $\Delta R_{NL}(T)$ increases with larger t_N for $d \geq 400$ nm and all measured temperatures. Conversely, $\Delta R_{NL}(T)$ changes little with t_N for the smallest d, which is smaller than $\lambda_{s,N}$ and $d \lesssim t_N$. The differences between ΔR_{NL} measured among the samples with various t_N decreases as T increases.

The increase of the measured $\Delta R_{NL}(T)$ with larger t_N could be due to an improvement of the effectiveness of spin injection and/or an increase of the effective $\lambda_{s,N}$ for the patterned device N channel. The effective $\lambda_{s,N}$ is the spatial decay length of the spin current resulting from spin relaxation in the interior of the channel, impurities, and at the surfaces. To distinguish between the case of increased spin injection or spin diffusion, $\lambda_{s,N}$ was extracted from fits to the separation dependence of ΔR_{NL} at various T, which is discussed in §4.4.

The effect of temperature on the spin transport for various t_N can be compared by normalizing and overlaying these $\Delta R_{NL}(T)$ data for each t_N. When normalized by $\Delta R_{NL}(T = 50\,\mathrm{K})$, the general temperature dependence of ΔR_{NL} is independent of t_N for all T, as shown in Figure 4.5. The peak near $T = 50$ K, shown previously for Py/Cu devices with $t_N = 200$ nm, persists as t_N is increased, and varying the thickness does not change the temperature at which the peak appears within 10 K. The magnitude of $\Delta R_{NL}(T = 50\,\mathrm{K}) - \Delta R_{NL}(T = 5\,\mathrm{K})$ changes by $\lesssim 10\%$ after normalization. A temperature-dependent reduction of the effective injection efficiency across the FM/N interface below 50 K is one potential explanation, which is discussed further in Chapter 6.

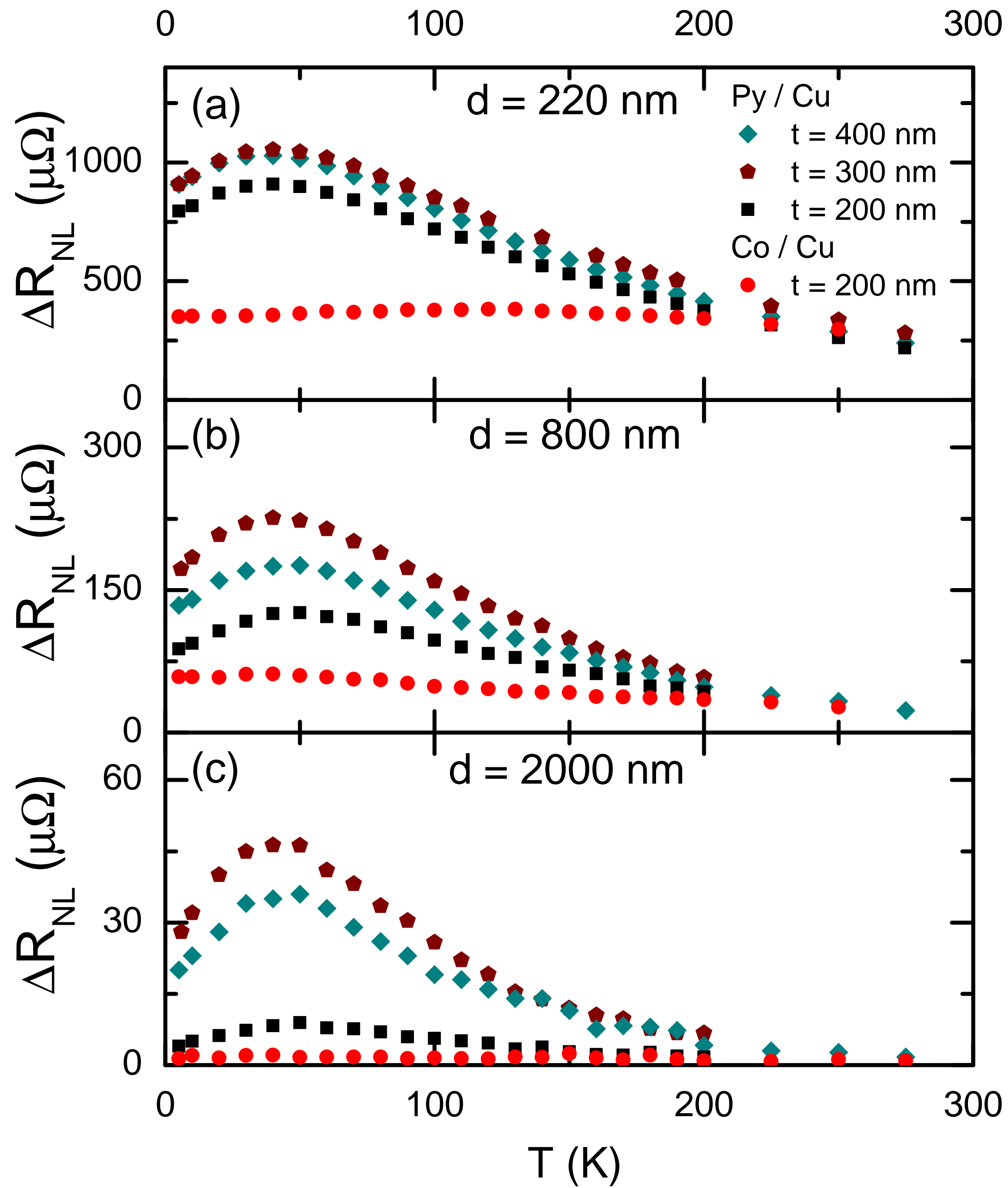

Figure 4.4: Temperature dependence of ΔR_{NL} measured for Py/Cu devices with $t_N =$ 200 nm, 300 nm, and 400 nm at (a) $d = 220$ nm, (b) 800 nm, and (c) 2000 nm.

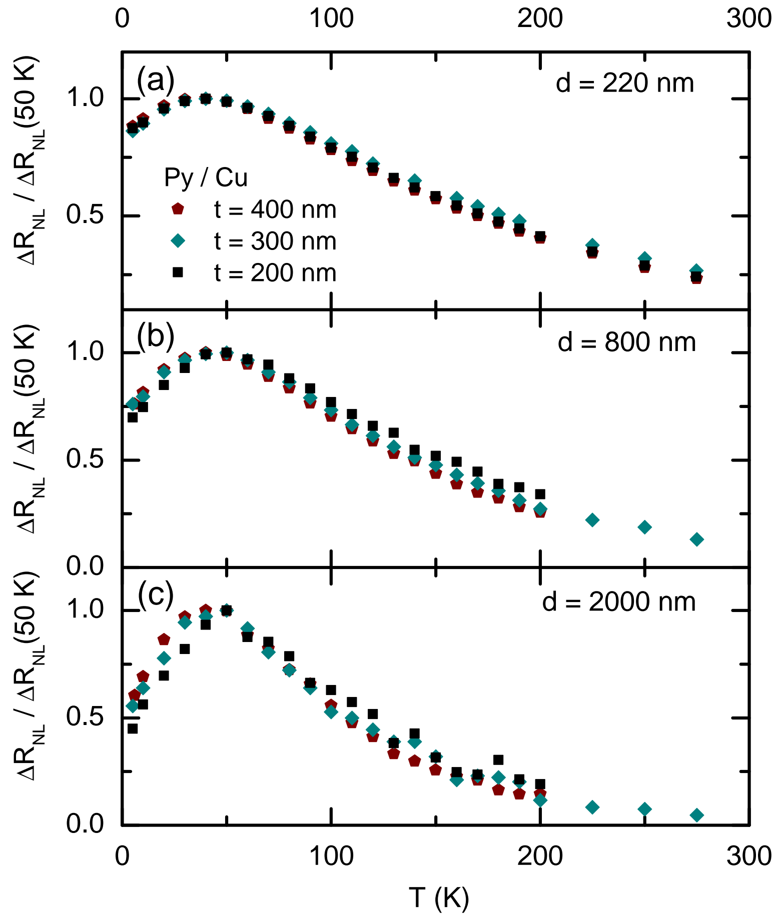

Figure 4.5: Temperature dependence of ΔR_{NL} normalized by $\Delta R_{NL}(50\,\mathrm{K})$ for Py/Cu devices for $t_N = 200\,\mathrm{nm}$, $300\,\mathrm{nm}$, and $400\,\mathrm{nm}$ at (a) $d = 220\,\mathrm{nm}$, (b) $800\,\mathrm{nm}$, and (c) $2000\,\mathrm{nm}$.

4.4 Non-Local Spin Valve Effect Fitting

The measurements of ΔR_{NL} shown in §4.1, §4.2, and §4.3 were fitted using theoretical models of spin transport in order to determine spin-dependent transport properties of the N and FM. The fitting procedure and results are discussed in this section.

4.4.1 Application of Transparent Interface Modeling to the Dependence of ΔR_{NL} on d

The dependence of ΔR_{NL} on d, such as that shown in Figure 4.3, can be fit to determine the spin-dependent transport parameters of a device. ΔR_{NL} data for Py/Cu as a function of d at $T = 5\,\mathrm{K}$ are shown in Figure 4.6 on both linear and semi-logarithmic scales. The solid curves are fits to the transparent interface and tunnel barrier models (simple exponential). Equations 1.61 and 1.67 are used to fit the contact separation dependence data with the transparent interface model and the tunnel barrier models, respectively. In this case, the free parameters for each fit are λ_N and α_{FM} while ρ_N, ρ_{FM}, A_N, and A_{FM} were determined by independent experimental measurements and $\lambda_{s,Py}$ is set to 5 nm, consistent with literature values [67].

In §3.2, upper bounds were placed on the interface resistance R_I, confirming that the devices are in the diffusive FM/N interface regime, satisfying the criteria that $R_{s,N}$ and $R_{s,FM}$ are greater than R_I. In this limit, the transparent interface model (Equations 1.61 – 4.6) is expected to apply, shown in Figure 4.6 as a solid red line; a tunnel barrier fit $\Delta R_{NL} = C_I e^{-d/\lambda_{s,N}}$ (blue dashed line) is shown for comparison. Both fits follow within $2\,\mu\Omega$ of a pure exponential for $d \gtrsim 400\,\mathrm{nm}$, which coincides with the majority of the experimental range, and differ significantly only for $d < 400\,\mathrm{nm}$. For this data set, $\lambda_{s,N} = 360 \pm 15\,\mathrm{nm}$ using the exponential model fit (tunnel barriers) and $\lambda_{s,N} = 370 \pm 12\,\mathrm{nm}$ using the diffusive model constrained as described in §4.4.1. The reduced chi-squared χ_r^2 is 1.8 and 3.4 for the diffusive interface and simple exponential fits, respectively.

The spin transport in an NLSV device with tunneling FM contacts is described by Equation 1.67, with $C_I = \alpha_{FM}^2 \lambda_{s,N} \rho_N / A_N$ in the exponential expression above. Although $\lambda_{s,N}$ is in agreement for fits using both tunnel barrier and transparent interface models, the value of α_{FM} determined for the case of tunnel barriers is much lower

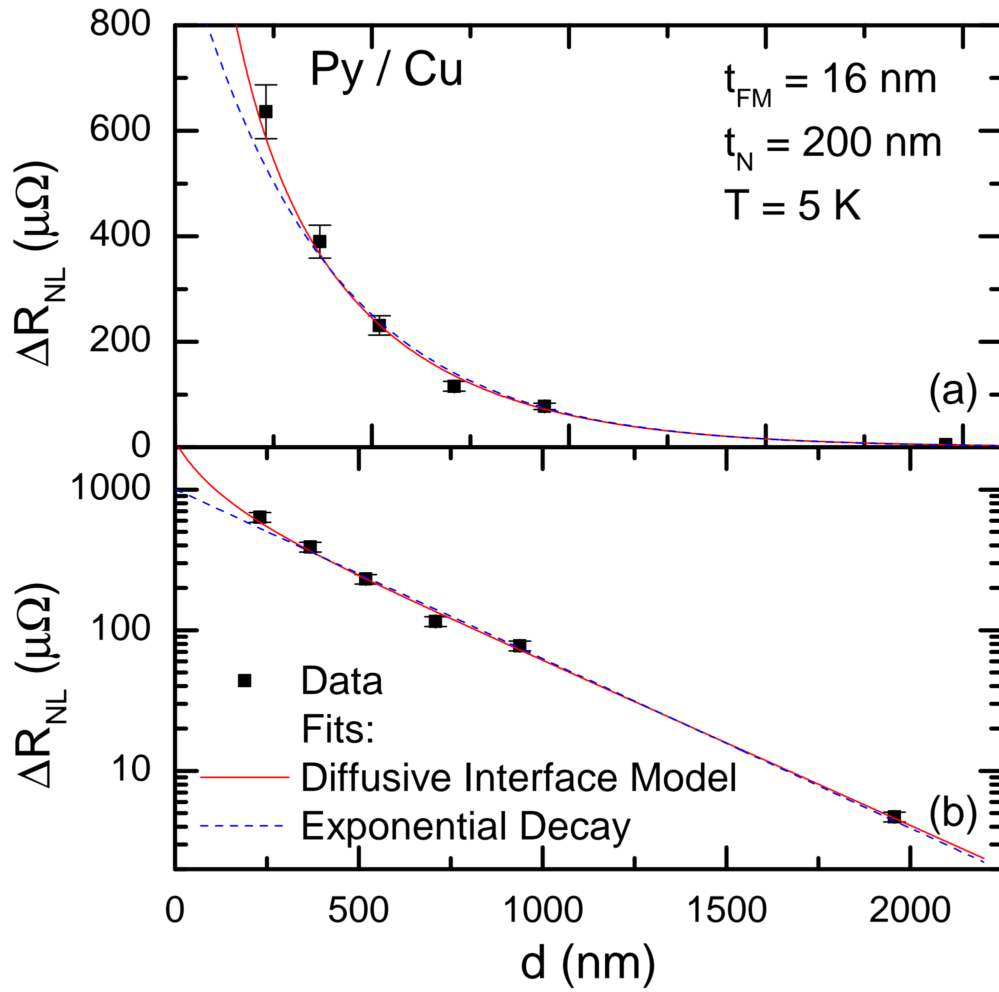

Figure 4.6: Plots of FM injector-detector separation dependence of ΔR_{NL}, plotted on (a) linear and (b) semi-logarithmic scales.

than for the case of diffusive FM/N interfaces. The value obtained from the simple exponential model is also lower the range of α_{FM} reported in the literature for the materials used. In this case $P_{Py} = 12\%$ results from the application of the tunnel barrier model, less than expected and illustrating the danger of applied the tunneling model, as some have done, when barriers are not present. In contrast, $P_{Py} = 25\%$ to 45% using the transparent-interface model, depending on the value of $\lambda_{s,Py}$ used. This range corresponds to $\lambda_{s,Py}$ between 5 nm and 2 nm, consistent with other experiments [42, 67, 76]. Despite the interdependence of ΔR_{NL} on α_{FM} and $\lambda_{s,FM}$, as discussed further in §4.4.2, the values of α_{FM} for the diffusive interface fit are similar to those found in tunneling experiments using a vertical geometry [62, 64, 119].

The application of the tunnel-barrier model to describe the devices in this work would result in α_{FM} that is half the value typically found elsewhere. The $\lambda_{s,N}$ found for this data depends weakly on the model whereas the ferromagnetic spin-dependent transport parameters depend strongly on the model applied. The appropriate model, that incorporates diffusive transport through FM/N interfaces, must be applied to produce reliable fit parameters for $\lambda_{s,FM}$ and α_{FM}.

Independently Determined Fit Parameters

These ΔR_{NL} vs d data, such as those shown in Figure 4.3, were fit using several independently determined parameters to reduce the number of free parameters for the fits of the 1D transparent-interface model given by Equation 1.63. These fits allow the determination of parameters, llisted in Table 4.1, for the different materials combinations at various T and t_N, which is reported through the remainder of this chapter. Four of the seven parameters used to model spin transport through diffusive interfaces were determined experimentally in order to reduce the number of free parameters. Using one further parameter fixed to literature values reduces the number of free parameters used to fit these data sets to two.

Specifically, the resistivities ($\rho_N(T)$, $\rho_{FM}(T)$) and geometric parameters (A_N, A_{FM}) were determined from independent measurements. The resistivities $\rho_N(T)$ of the N metals were measured using the NLSV device channels themselves. Ferromagnetic metals that were patterned into nanowires with width $w_{FM} = 200$ nm and thickness $t_{FM} = 16$ nm, as described in §3.1, were measured in order to determine $\rho_{FM}(T)$. SEM

Parameter	Method used to determine parameter
$\rho_N(T)$	Measured $\rho_N(T)$ of N channel
$\rho_{FM}(T)$	Measured $\rho_{FM}(T)$ of companion FM nanowire
$\lambda_{s,N}(T)$	Free parameter
$\lambda_{s,FM}(T)$	Free parameter
$\alpha_{FM}(T)$	Fixed to literature values
A_N	Measured $w_N \times t_N$
A_{FM}	Measured $w_{FM} \times w_N$

Table 4.1: Fit parameters for the 1D spin transport model in the diffusive FM/N interface limit.

micrographs were used to determine N channel widths w_N and FM contact widths w_{FM} for each device by measuring the in-plane geometry of the devices. The values of w_N and w_{FM} were combined with QCM, tilted-SEM, or AFM measurements of the thicknesses to determine the cross sections A_N and A_{FM}, as discussed in §2.4.4 and §2.4.5.

The magnitude of ΔR_{NL} depends on the remaining parameters $\lambda_{s,N}$, $\lambda_{s,FM}$, and α_{FM}. The spatial dependence of the six $\Delta R_{NL}(d)$ data points, ranging from $d = 200\,\text{nm}$ to $2000\,\text{nm}$, determine $\lambda_{s,N}$ but $\lambda_{s,FM}$ and α_{FM} cannot be independently determined from the experimentally available d. Separately determining $\lambda_{s,FM}$ and α_{FM} is described in further detail in §4.4.2.

4.4.2 Interdependence of ΔR_{NL} on $\lambda_{s,FM}$ and α_{FM}

To elucidate the difficulty of separately determining the FM parameters, $\lambda_{s,FM}$ and α_{FM}, the contact separation dependence of ΔR_{NL} for Py/Cu devices at $T = 5\,\text{K}$ was fitted using two methods for comparison. Using Equation 1.63, fits were performed while allowing $\lambda_{s,N}$ and one of the FM parameters, either $\lambda_{s,FM}$ or α_{FM}, to be free. The solid black curve in Figure 4.7 shows a fit with $\lambda_{s,N}$ and $\lambda_{s,FM}$ as free parameters and with α_{FM} fixed for which $\chi^2_r = 1.8$. The dashed red curve is the fit with free parameters $\lambda_{s,N}$ and α_{FM} with $\lambda_{s,FM}$ fixed, which has $\chi^2_r = 2.2$. The dotted blue curve shows the difference between the aforementioned fits as a function of d with α_{FM} and $\lambda_{s,FM}$ fixed.

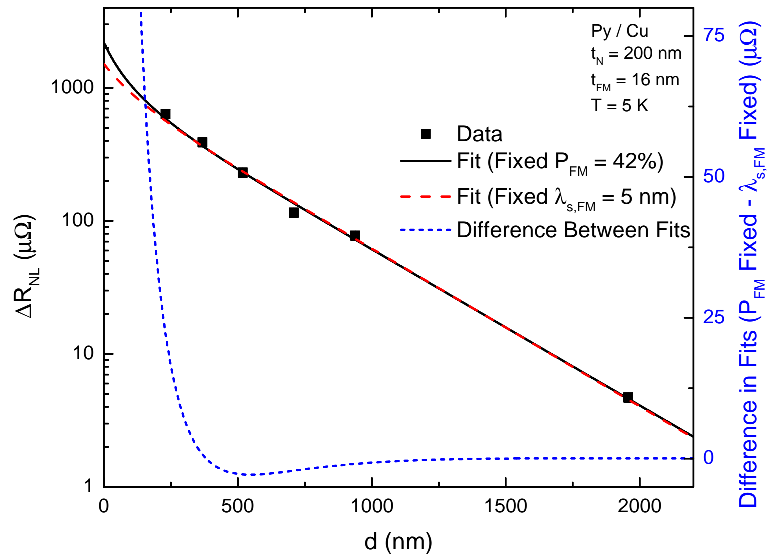

Figure 4.7: Comparison of fits to the NLSV ΔR_{NL} data as a function of contact separation d using either α_{FM} (solid black) or $\lambda_{s,FM}$ (dashed red) as the additional fixed parameter. The difference between the fits, with α_{FM} or $\lambda_{s,FM}$ fixed, is shown with short blue dashes.

χ_r^2 is 22 % larger for the fit in which $\lambda_{s,FM}$ has been set to a fixed value compared to that in which α_{FM} has been fixed. In each case, $\chi_r^2 \approx 2$, making it difficult to determine one fit as a significant improvement over the other. The difference between the fits, using a fixed α_{FM} or fixed $\lambda_{s,FM}$, is overlaid as the blue dotted curve in Figure 4.7. The difference between the two fits for $d > 250\,\mathrm{nm}$ is less than $16\,\mu\Omega$, which is similar to, or less than, the uncertainty of the geometric contributions to ΔR_{NL} associated with the experimental uncertainty of measuring the physical dimensions of the L-NLSVs. If experimental measurements of ΔR_{NL} could be made for several devices with $d \ll 250\,\mathrm{nm}$, it may be possible to distinguish between these cases. However, at the time of device fabrication for this work it was not possible to create devices much smaller than 250 nm. Newer 100 kV EBL tools now available allow d to be decreased, possibly to the extent that $\lambda_{s,FM}$ and α_{FM} could begin to be resolved. If a similar Py/Cu device were fabricated to measure ΔR_{NL} at $d = 50\,\mathrm{nm}$ the difference between the two fits would be $280\,\mu\Omega$, which is experimentally resolvable.

In addition to higher voltage EBL tools, a technique to fabricate non-planar non-local devices on film edges with $d < 100\,\mathrm{nm}$ has been developed by McCallum and Johnson [120]. They were able to create prototype devices with $d = 42 \pm 2\,\mathrm{nm}$, significantly shorter than planar L-NLSVs. This film edge technique has not yet been used to characterize the dependence of ΔR_{NL} on $d < 200\,\mathrm{nm}$ to determine $\lambda_{s,FM}$ or α_{FM}.

The same analysis was conducted for the case of Co/Cu devices, for which controversy remains over the value of $\lambda_{s,Co}$. The spin diffusion length in FM metals and alloys has been found to follow an empirical relation,

$$\lambda_{s,FM} = C_{FM} \frac{1}{\rho_{FM}}, \tag{4.4}$$

across materials and measurement geometries with the exception of pure Co and Fe in GMR structures [66]. Using a survey of several experimental values reported in the literature [42, 43, 67–69], $C_{FM} = 67.3\,\mathrm{nm}\,\mu\Omega\,\mathrm{cm}$ was found. Table 4.2 includes values of $\lambda_{s,Cu}$, $\lambda_{s,Co}$, or P_{Co} obtained from fitting spin-valve effect data with one parameter fixed to literature values, denoted in the first column. The other columns contain the values of the parameters obtained from the fitting, including the value of χ_r^2 for each fit. The symbol † marks the use of the approximate value obtained from the empirical relation given by Equation 4.4 to determine $\lambda_{s,FM}$.

Fixed Parameter	α_{FM}	$\lambda_{s,FM}$	$\lambda_{s,N}$	χ^2_r
α_{FM}	**42%** [63]	3.8 ± 0.4 nm	330 ± 40 nm	1.4
$\lambda_{s,FM}$	36 ± 3 %	**5 nm** †	327 ± 35 nm	1.4
$\lambda_{s,FM}$	9.4 ± 1.7 %	**40 nm** [70]	312 ± 30 nm	1.3

Table 4.2: Fitting parameters α_{FM}, $\lambda_{s,FM}$, and $\lambda_{s,N}$ along with the corresponding χ^2_r from fitting ΔR_{NL} as a function of d for Co/Cu devices with the one FM parameter held fixed shown in bold. Each line of the table represents a different fit.

The magnitude of $\lambda_{s,N}$ determined from fitting depends weakly on which FM parameter is held constant. Using a fixed value of $P_{Co} = 42\%$ [63] leads to a short $\lambda_{s,FM} = 3.8 \pm 0.4$ nm which is similar to that found using the empirical relationship of Equation 4.4 with the measured ρ_{FM}. The fit results shown in Table 4.2, with $\lambda_{s,FM} \leq 5$ nm, have values of α_{FM} from 36% to 42%, which are consistent with experiments conducted elsewhere [60, 62–64]. The magnitude of all parameters are consistent with the values found in the literature, given the measured ρ_{FM}, except in the case where a long $\lambda_{s,FM}$ of 40 nm is specified for the fit, which was taken from CPP-GMR measurements [70]. In this case yielding $\alpha_{FM} = 9.4\%$, which is lower than expected.

4.4.3 Temperature-Dependent λ_s from Spin Valve Effect Fitting

$\lambda_s(T)$ Determined from ΔR_{NL} vs d

ΔR_{NL} data, for various d as a function of T, were shown previously in Figure 4.2 and are replotted in Figure 4.8 with d as the abscissæ. The contact separation dependence was fit at each temperature, using the model for diffusive transport through FM/N interfaces (transparent interfaces) with ρ_N, ρ_{FM}, A_N, A_{FM}, and α_{FM} fixed experimentally.

Since it is unfeasible to determine both $\lambda_{s,FM}$ and α_{FM} from fits of the spatial dependence of the spin valve effect over the experimental range of d available here, methods similar to that given above for a single value of T have been adopted to examine the temperature dependence. External measurements of α_{FM} from the literature are used to fix the values of α_{FM} for fitting, available from a variety of techniques and device measurements including MTJs, vertical GMR, and point contact Andreev reflection (PCAR), which are summarized in Table 1.1. Measurements of $\lambda_{s,FM}$ have been reported less

frequently than for α_{FM}, typically being determined only by measurements of diffusive FM/N interface devices such as in CPP-GMR and NLSV measurements [41, 42, 67, 70–73]. The difficulties in fitting NLSV experiments outlined here make extracting $\lambda_{s,FM}$ unreliable unless α_{FM} is known. Therefore, using values of α_{FM} reported in the literature to constrain fitting is chosen to begin the discussion of the analysis. The small range of d available makes fitting difficult and that α_{FM} and $\lambda_{s,FM}$ cannot both be determined unambiguously.

For consistency, α_{FM} is chosen from values in the literature, measured using tunneling experiments. Values of $P_{Py} = 45\%$ and $P_{Co} = 42\%$ are used, which have been obtained from a single set of experiments by Monsma and Parkin [63]. We start by showing fits with temperature independent α_{FM} fixed to the above values. The data and fits for each combination of N and FM materials (Py/Cu, Co/Cu, Py/Al, and Co/Al), at various temperatures from $T = 5\,\text{K}$ to 250 K, are shown in Figure 4.8.

The fits of the contact separation dependence of ΔR_{NL} are characterized by mean χ_r^2 over all measured temperatures of 1.1, 0.7, 1.2, and 0.6 for Py/Cu, Co/Cu, Py/Al, and Co/Al devices, respectively. These values are close to unity in each case, indicating that the analysis based on the transparent interface model fits these data appropriately. The free parameters of $\lambda_{s,N}(T)$ and $\lambda_{s,FM}(T)$ determined from these fits are shown in Figure 4.9. The temperature dependence of $\lambda_{s,N}$ resulting from spin valve fitting, shown in Figure 4.9(a), is similar for each materials combination. The values of $\lambda_{s,N}$ range from $260 \pm 20\,\text{nm}$ to $390 \pm 20\,\text{nm}$ for Cu and from $290 \pm 40\,\text{nm}$ to $540 \pm 50\,\text{nm}$ for Al, with a weak temperature dependence when compared to the expectation for metals that $\lambda_{s,N}(T) \propto 1/\rho_N(T)$ for Elliot-Yafet-type spin relaxation. Given the measured $\rho_N(T)$ in Figure 3.5, $\lambda_{s,N}$ is expected to vary by a factor of three(two) over the experimental temperature range for Cu(Al). Therefore, Elliot-Yafet relaxation with only bulk scattering is incapable of producing the observed $\lambda_{s,N}(T)$, independent of the value of $\alpha = \tau_p/\tau_s$ (Equation 1.69).

The temperature dependence of the spin diffusion length in Cu at $T \approx 10\,\text{K}$ and 300 K has been reported in other lateral experiments to be 920 nm to 700 nm [121], 200 nm to 110 nm [122], and 1000 nm to 350 nm [23]. These $\lambda_{s,N}$ are also *inconsistent* with the measured RRR for each case: 1.6, 2.5, and 2.1, respectively. These experiments were limited in scope and utilized a variety of fabrication and fitting techniques; the

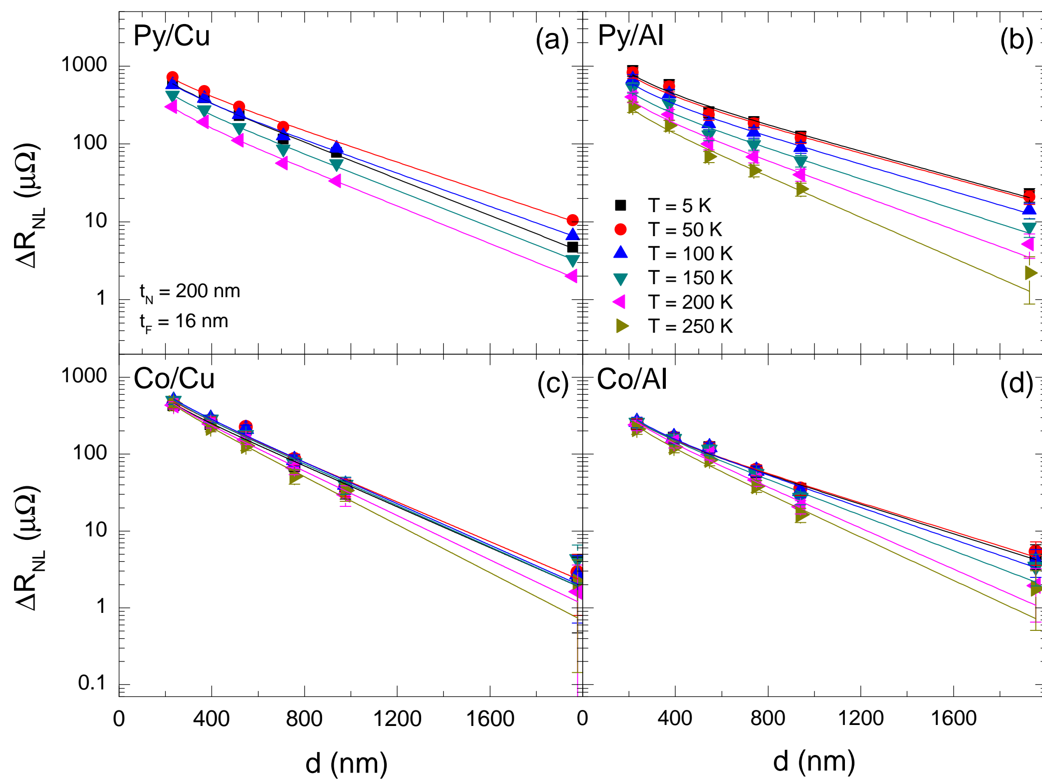

Figure 4.8: ΔR_{NL} as a function of injector-detector separation d plotted for several temperatures between 5 K and 250 K for different combinations of FM and N (a) Py/Cu, (b) Py/Al, (c) Co/Cu, and (d) Co/Al with the accompanying transparent interface model fits.

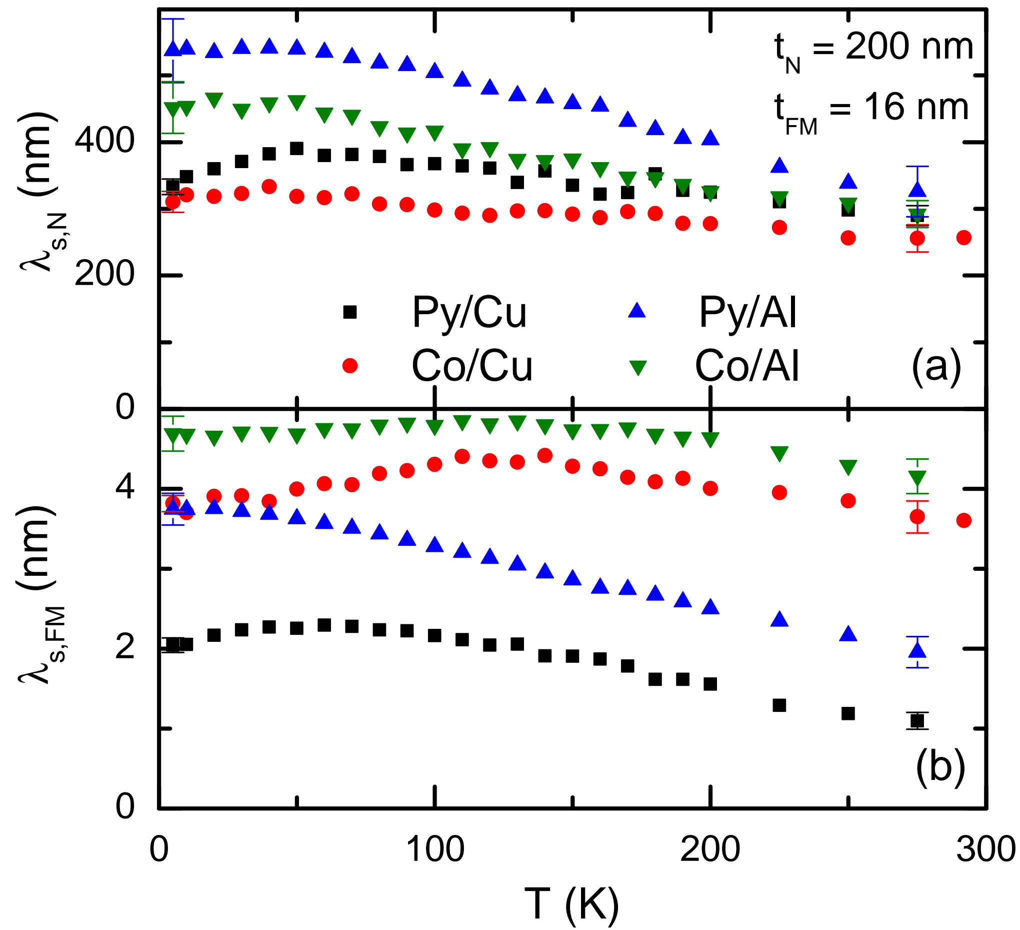

Figure 4.9: Free fit parameters (a) $\lambda_{s,N}(T)$ and (b) $\lambda_{s,FM}(T)$, resulting from constrained fitting of ΔR_{NL} vs. d, using the model incorporating transparent interfaces for each materials combination with $P_{Py} = 45\,\%$ and $P_{Co} = 42\,\%$ fixed and all other parameters experimentally determined.

material properties and geometry are inconsistent across experiments, and the resulting fitted $\lambda_{s,N}$ was sensitive to the details of the fitting procedure [66]. Although instructive, a comparison of these results from different experiments is less useful than from a single analysis of a set of experiments conducted using the same fabrication technique, as has been done in this work and described in this thesis.

$\lambda_{s,FM}(T)$ was determined from the fitting process discussed above, and is shown in Figure 4.9(b). $\lambda_{s,FM}(T)$ measured in this work is similar in magnitude for each FM material and ranges from 2 nm to 5 nm. For the case of Py/Cu, $\lambda_{s,Py}$ is 2.1 ± 0.1 nm to 1.2 ± 0.1 nm at 5 K and 275 K, respectively. The values reported elsewhere range from 2 nm to 6 nm [42, 43, 67]. Unlike the case of Py, the magnitude of $\lambda_{s,Co}$ from Co/Cu devices is weakly dependent on temperature. We find $\lambda_{s,Co}$ is 3.9 ± 0.1 nm at $T = 5$ K increasing to a weak maximum of 4.4 ± 0.1 nm at $T \approx 140$ K before decreasing to 3.7 ± 0.1 nm at $T = 275$ K. Values of $\lambda_{s,FM}$ found using CPP-GMR measurements range from 40 nm to 60 nm, although for Co alloyed with 9% Fe, a reduced $\lambda_{s,CoFe}$ of 12 nm has been found [68]. From the measured values of $\rho_{Co}(T)$ and Equation 4.4 with C_{FM} determined from literature values, $\lambda_{s,Co}$ is expected to be 5.2 nm at 5 K and 2.5 nm at 300 K. These values of $\lambda_{s,Co}$ found using ρ_{Co}, are consistent with the values obtained from fitting ΔR_{NL} vs. d in this work, as reported above. In the case of $T = 275$ K, the value of $\lambda_{s,FM}$ expected from Equation 4.4 is shorter than measured in this work.

Similarly, for the case of Py/Al, $\lambda_{s,Py}$ has a stronger temperature dependence than $\lambda_{s,Co}$ for the case of Co/Al. $\lambda_{s,Py}$ determined from fitting ΔR_{NL} vs. d is 3.8 ± 0.2 nm at 5 K and 2.0 ± 0.2 nm at 275 K. The magnitude of $\lambda_{s,Co}$ from Co/Al devices is also only weakly dependent on temperature. We find $\lambda_{s,Co}$ to be 4.7 ± 0.1 nm and 4.2 ± 0.2 nm at 5 K and 275 K, respectively. There is a weak and broad peak reaching 4.9 ± 0.1 nm that appears in the temperature dependence at $T \approx 140$ K, similar to that found in for Co/Cu.

The spin diffusion length of FMs have a stronger temperature dependence for Py based devices than for Co. Although there is no clear expectation for the temperature dependence of $\lambda_{s,FM}$, there is greater understanding of $\alpha_{FM}(T)$. The expectation is that α_{FM} should change with temperature more for materials with lower Curie temperatures, in this cases Py is expected to change more than Co.

So far the values of α_{FM} used for fitting have been temperature independent. α_{FM},

however, is expected to be temperature dependent following the Bloch $T^{3/2}$ form for $T < 300\,\mathrm{K}$. In this case,

$$P_{FM}(T) = P_0(1 - \alpha_B T^{3/2}), \tag{4.5}$$

where the coefficient α_B is the strength of the temperature dependence. The values of α_B for bulk Co and Py are $\alpha_B \approx 10^{-6}\,\mathrm{K}^{-3/2}$ and $10^{-5}\,\mathrm{K}^{-3/2}$, respectively [65]. Magnetic tunnel junction experiments have found the polarization of $P_{Py}(T)$ to vary with temperature more than has been measured in bulk. This idea has been discussed by the authors in References [123–126]. The spin polarization at the ferromagnetic surface may be affected by softer magnon modes, leading to a larger value of α_B, which can be several times that of bulk.

Shang *et al.* measured the value of α_B for Py from magnetic tunnel junctions to be 3-5 $\times\, 10^{-5}\,\mathrm{K}^{-3/2}$ [64]. $\lambda_{s,FM}(T)$ was fit ΔR_{NL}vs. d was fit using the α_{FM} given by Equation 4.5 with $\alpha_B = 1 \times 10^{-6}\,\mathrm{K}^{-3/2}$ and $P_0 = 42\,\%$ for Co and $\alpha_B = 5 \times 10^{-5}\,\mathrm{K}^{-3/2}$ and $P_0 = 45\,\%$ for Py in order to determine $\lambda_{s,FM}(T)$. The temperature dependent $\lambda_{s,FM}$, determined for each material combination using this method, is shown in Figure 4.10. In each case $\lambda_{s,Py}(T)$ has a weaker temperature dependence using the Bloch $\alpha_{FM}(T)$ for Py. Using this method, $\lambda_{s,FM}$ changes by less than 4 % for Py/Al and Co/Al and less than 18 % from 5 K to 275 K. For the Py/Al and Py/Cu fits, using the temperature independent α_{FM}, $\lambda_{s,FM}(T)$ changes by 50 %.

The Bloch temperature dependence of α_{FM}, with the larger α_B for Py, is consistent with a nearly temperature independent $\lambda_{s,FM}(T)$. The fitting is repeated using a fixed temperature independent value of $\lambda_{s,FM} = 4\,\mathrm{nm}$ with $\alpha_{FM}(T)$ free. The resulting $\alpha_{FM}(T)$, shown in Figure 4.11, resemble the Bloch from, except for the case of Py/Cu. The $\alpha_{FM}(T)$ resulting from the spin valve fitting can in turn be fit using the Bloch $T^{3/2}$ form, Equation 4.5, to determine $P_{0,FM}$ and α_{FM}. The results of fitting $\alpha_{FM}(T)$ to the Bloch $T^{3/2}$ form are given in Table 4.3.

4.4.4 Fitting the Channel Thickness Dependence of ΔR_{NL} vs. d for Py/Cu Spin Valves.

Although variations of the resulting $\lambda_{s,N}(T)$, from fitting ΔR_{NL} vs. d, exist among the measured NLSV material combinations discussed in §4.4.3, each N metal has a

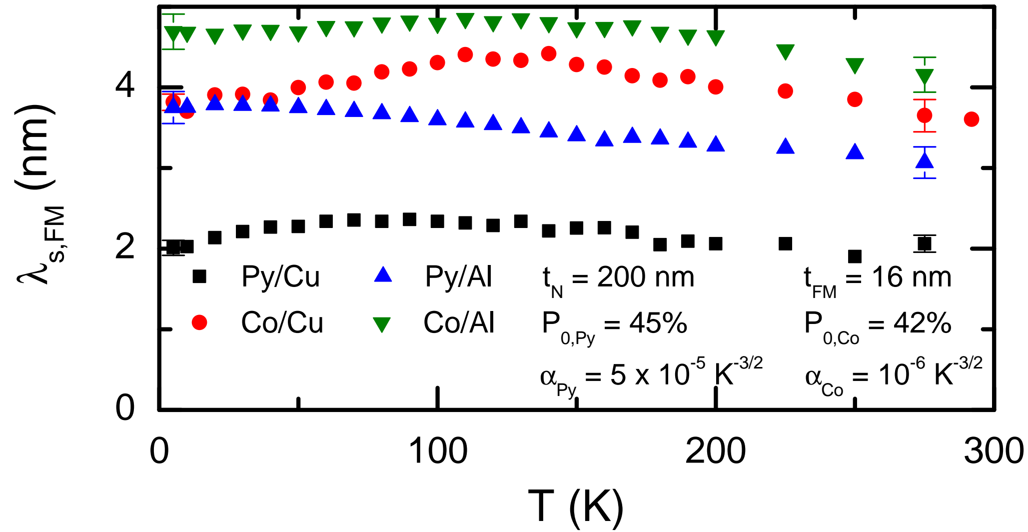

Figure 4.10: Fit parameter $\lambda_{s,FM}(T)$, resulting from fits of ΔR_{NL} vs. d using the model incorporating transparent interfaces, for each materials combination with a temperature dependent $\alpha_{FM}(T)$ specified to be the Bloch $T^{3/2}$ form.

NLSV Materials	$P_{0,FM}$	α_B
Py/Cu	$31 \pm 1\,\%$	$9 \pm 1 \times 10^{-5}\,\mathrm{K}^{-3/2}$
Co/Cu	$39 \pm 2\,\%$	$0 \pm 5 \times 10^{-6}\,\mathrm{K}^{-3/2}$
Py/Al	$41 \pm 1\,\%$	$9 \pm 1 \times 10^{-6}\,\mathrm{K}^{-3/2}$
Co/Al	$39 \pm 2\,\%$	$0 \pm 3 \times 10^{-6}\,\mathrm{K}^{-3/2}$

Table 4.3: The Bloch $T^{3/2}$ law parameters: the 0 K FM polarization $P_{0,FM}$ and temperature coefficient α_B from fits of $\alpha_{FM}(T)$ determined from fitting of ΔR_{NL} vs d for non-local spin valves of various FM/N combinations.

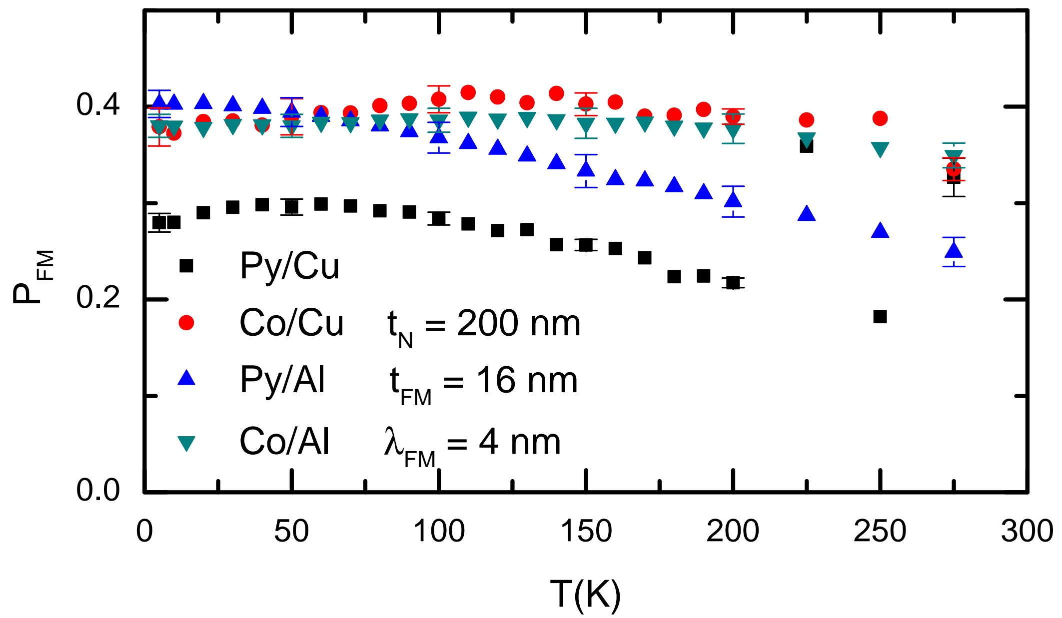

Figure 4.11: Fit parameter $\alpha_{FM}(T)$, resulting from fits of ΔR_{NL} vs. d using the model of spin transport incorporating transparent interfaces for Py/Cu, Co/Cu, Py/Al, and Co/Al material combinations with a temperature independent $\lambda_{s,FM} = 4\,\text{nm}$.

weaker temperature dependence and a reduced magnitude of $\lambda_{s,N}(T)$ relative to that measured in bulk materials. Assuming Elliot-Yafet is the correct spin-relaxation mechanism for bulk N metals, which there is strong theoretical and experimental evidence for, an extrinsic mechanism contributing to spin-relaxation is required to match the experimentally obtained $\lambda_{s,N}(T)$. In order to test the dependence of spin-relaxation on the N channel cross section, the same fitting analysis described previously in §4.4.2 is repeated for the Py/Cu devices with increasing Cu channel thicknesses of $t_N = 200\,\text{nm}$, 300 nm, and 400 nm. The resulting ΔR_{NL} vs. d was fit to extract $\lambda_{s,N}$, as described in §4.3, now for each t_N and T.

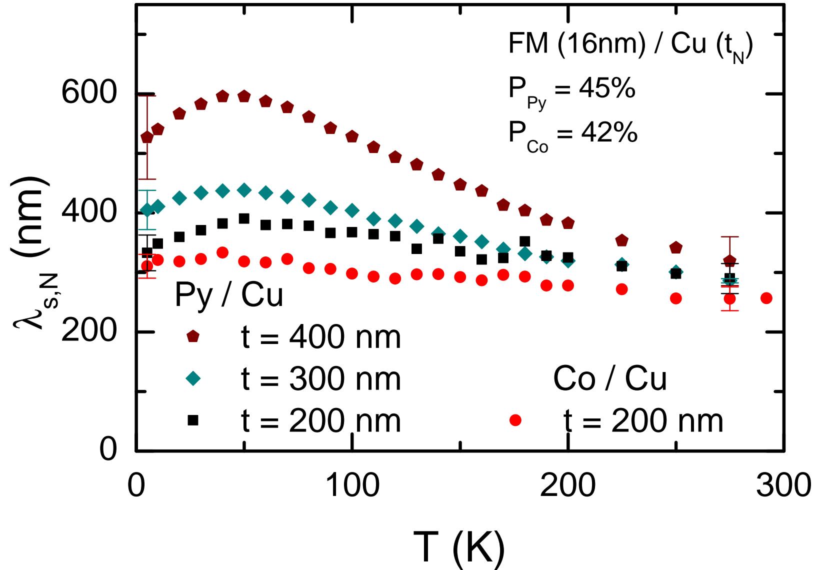

Figure 4.12: $\lambda_{s,N}$ vs. T for Py/Cu NLSVs with $t_N = 200\,\text{nm}$, 300 nm, and 400 nm determined by fitting of $\Delta R_{NL}(T)$ vs. d with the model for transparent FM/N interfaces.

$\lambda_{s,N}$ at $T = 5\,\text{K}$ increases from $330 \pm 20\,\text{nm}$ to $530 \pm 60\,\text{nm}$ with larger t_N from 200 nm to 400 nm, as shown in Figure 4.12. At $T = 275\,\text{K}$, $\lambda_{s,N}$ increases from $290 \pm 20\,\text{nm}$ to $320 \pm 40\,\text{nm}$ with increasing t_N from 200 nm to 400 nm. This demonstrates that the increase of the observed $\Delta R_{NL}(T)$ is not simply due to an increase in spin injection efficiency. Others have attributed the increase of ΔR_{NL} with increasing t_N to a geometry-dependent change in the effective injection polarization [45]. Other

experiments focusing on NLSVs using Py with Ag or Cu N channels implicate increased surface relaxation [43, 59]. The form and details of this mechanism, however, are incomplete or differ in each case. N channel thickness-dependent data, presented in Figure 3.4, shows a 35% reduction of $\rho_{Cu}(T = 5\,\mathrm{K})$ as t_N is increased from 200 nm to 400 nm which could be due, in part, to surface scattering and relaxation. The measured RRRs are not consistent with the changes observed in $\lambda_{s,N}(T)$ for each t_N. The observed dependence of spin diffusion on t_N and T cannot be explained within simple Elliot-Yafet relaxation for bulk Cu; an extrinsic process must be present.

The change of both ΔR_{NL} and $\lambda_{s,N}$ with varying t_N are reduced at higher temperatures. Although $\Delta R_{NL}(T)$ is largely determined by the material resistivities, the observed magnitude and suppression of the temperature dependence of $\lambda_{s,N}(T)$ for each t_N is *inconsistent* with bulk behavior or the measured change in $\rho_N(t_N)$. However, the measured $\lambda_{s,N}(t_N, T)$, discussed further in §5.2.3, can be understood through enhanced spin-relaxation rates at surfaces.

4.5 Hanle Effect Results and Analysis

For diffusive spin transport, the distribution of source-detector transit time and, more importantly, the spin lifetime can be measured using the electrical Hanle effect, described in §1.2.14. Rather than determining spin relaxation through the spatial decay of the spin accumulation by fitting the measured ΔR_{NL} at several different d, Hanle effect measurements rely on measuring precession and dephasing of electron spins about a perpendicular magnetic field $B_\perp$ as the diffusive spin current travels from source to detector.

The Hanle effect experiments shown in this thesis primarily use Al devices with transparent interfaces (§4.5.1). The measured Hanle curves are qualitatively similar to those observed in semiconductors [5] or a limited number of experiments with Al channels with tunnel barrier interfaces [4, 116, 117]. Hanle effect experiments were also conducted using Cu-based non-local devices, discussed in §4.5.3. It is much more difficult in this case to measure a full Hanle curve to a sufficiently large $B_\perp$ to fully dephase electrons, as the field required to do so is comparable to $4\pi M_s$ of the FM contacts. Previous attempts to measure Hanle effects for Cu [80] and Ag with resistive

contact interfaces [59, 118] only measured partial curves to small fields, $|B_\perp| \leq 3$ kG. Shown here are some of the first Hanle effect measurements and analysis with diffusive interfacial transport with Cu and Al channels.

4.5.1 Hanle Effect Data for Aluminum Channels

Al devices, with diffusion constant $D_N \sim 60$ cm^2/s (6×10^{-3} m^2 s^{-1} or 6 µm^2 ns^{-1}) and spin lifetime $\tau_{s,N} \gtrsim 15$ ns at $T = 5$ K, produce Hanle widths sufficiently narrow in applied magnetic field such that the full Hanle curve may be observed with transition metal FM injectors and detectors for the larger experimental contact separations used in this work. Figure 4.13 shows Hanle effect data for a Py/Al device with $d = 1960 \pm 20$ nm and $t_N = 200 \pm 10$ nm at $T = 5.000 \pm 0.005$ K prepared in either the parallel ($\uparrow\uparrow$) or antiparallel ($\uparrow\downarrow$) FM contact magnetization states using partial in-plane spin valve field sweeps, as described in §3.6.

The difference between $R_{NL,\uparrow\uparrow}$ and $R_{NL,\uparrow\downarrow}$, shown in Figure 4.13(b), at $B_\perp = 0$ G is the ΔR_{NL} measured in the spin valve configuration. As $|B_\perp|$ is increased, the spins precess and dephase; at $|B_\perp| = 2$ kG the diffusing spins have precessed through an average angle of π. The magnetization of each FM contact points out of plane for $|B_\perp| \gtrsim 10$ kG, consistent with $4\pi M_s \approx 10$ kG for Py, returning the device to the parallel configuration, which is now out of plane.

One feature of these $R_{NL,\uparrow\uparrow}(B_\perp)$ and $R_{NL,\uparrow\downarrow}(B_\perp)$ data, which has not been observed previously for Al devices with FM/N interfacial tunnel barriers [116], is the non-zero difference between $R_{NL,\uparrow\uparrow}(B_\perp = 0\,\text{kG})$ and $R_{NL,\uparrow\uparrow}(B_\perp = 10\,\text{kG})$. This offset appears in both the $\uparrow\uparrow$ and $\uparrow\downarrow$ configurations, so that ΔR_{NL} remains unchanged from that measured using the field-in-plane NLSV configuration. By subtracting $R_{NL,\uparrow\uparrow}$ and $R_{NL,\uparrow\downarrow}$ the background can be removed, leaving the changes of R_{NL} due to the spin precession and dephasing components.

Due to the presence of this background, using a model for the electrical Hanle effect which accounts for spin precession and dephasing only within the N channel, described in §1.2.14, to fit $R_{NL,\uparrow\uparrow} - R_{NL,\uparrow\downarrow}$ is simpler than fitting either $R_{NL,\uparrow\uparrow}$ or $R_{NL,\uparrow\downarrow}$ separately. The fitting can be used to extract $\tau_{s,N}$, and since D_N can be determined from ρ_N, $\lambda_{s,N} = \sqrt{D_N \tau_{s,N}}$ can be computed. Shown in Figure 4.14 is $R_{NL,\uparrow\uparrow}$, $R_{NL,\uparrow\downarrow}$, and $R_{NL,\uparrow\uparrow} - R_{NL,\uparrow\downarrow}$ for Co/Al devices which produce similar Hanle data to Py/Al and are

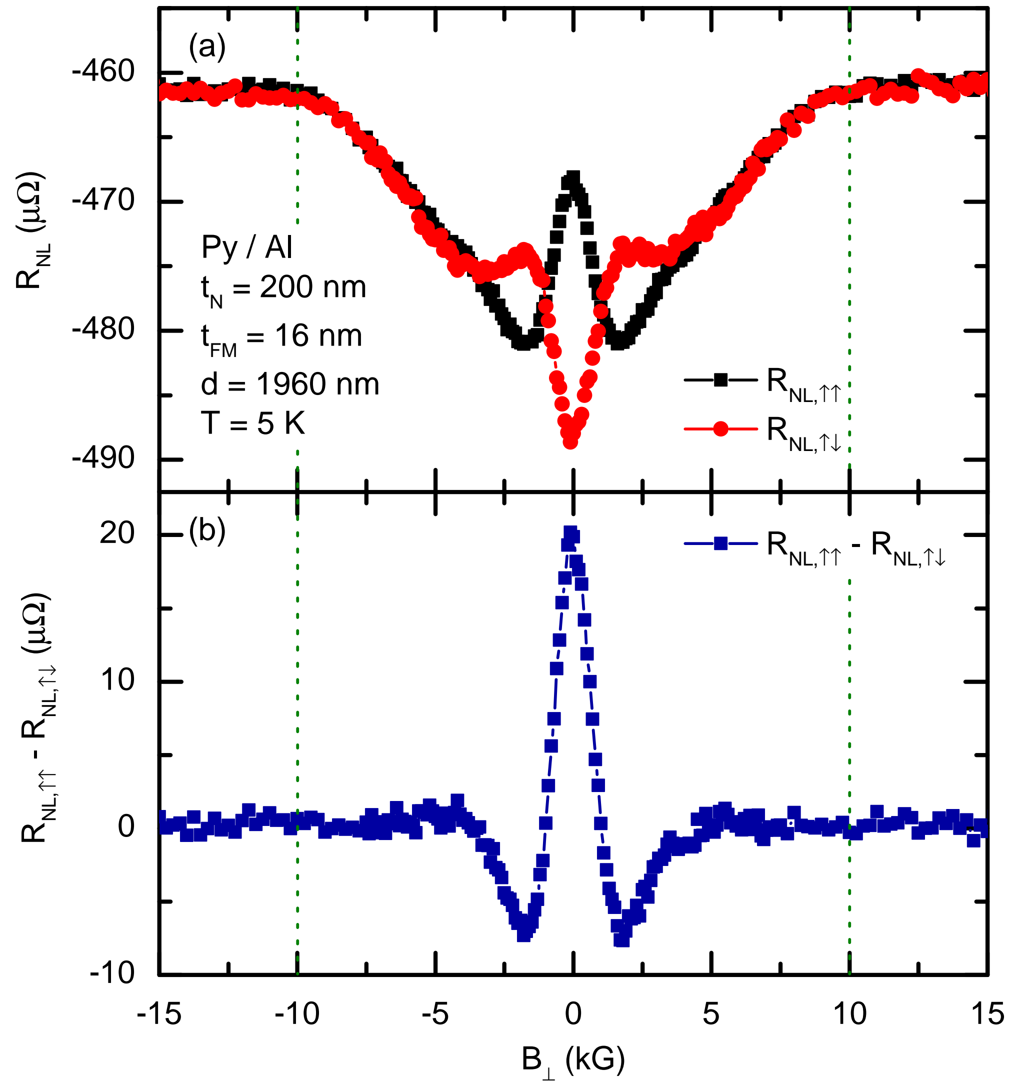

Figure 4.13: (a) Raw non-local Hanle effect data for parallel ($R_{NL,\uparrow\uparrow}$) and antiparallel ($R_{NL,\uparrow\downarrow}$) FM magnetization configurations as well as (b) the difference between the two ($R_{NL,\uparrow\uparrow} - R_{NL,\uparrow\downarrow}$) for a Py/Al device with $d = 1960 \pm 20\,\text{nm}$.

treated similarly except that $4\pi M_s \approx 17$ kG rather than 10 kG for Py.

4.5.2 Hanle Effect Analysis: Aluminum

Hanle effect field sweeps, such as those shown in Figures 4.13 and 4.14, are fit using the model discussed in §1.2.14. The expression for $R_{NL}(B_\perp)$ in this model, given by Equation 1.81, includes the diffusion, precession, and relaxation of spins in the N channel only. The model depends on the quantities d, D_N, and $\tau_{s,N}$ to determine the dependence of R_{NL} on $B_\perp$. The measured sample geometry is used to determine d, and $D_N(T)$ is set using the measured value of ρ_N and the Einstein relation, Equation 1.22. The fits of $R_{NL}(B_\perp)$ data were used to determine the value of $\tau_{s,N}$ which was measured using only one device unlike fits of R_{NL} vs. d, which requires multiple devices.

Hanle effect fits to the difference between the non-local resistance in the parallel and anti-parallel states ($R_{NL,\uparrow\uparrow} - R_{NL,\uparrow\downarrow}$) as a function of $B_\perp$ are shown for Al channels with both Py and Co FMs at $T = 5\,\mathrm{K}$ in Figure 4.16. The fitted curves are shown for Py/Cu with both D_N determined from ρ_N, shown in red, and for D_N as a free fitting parameter, shown in blue. The width of the central peak for each of the fits changes little with D_N either fixed or free. Larger differences appear for the minima near $|B_\perp| = 8\,\mathrm{kG}$, however. Setting $D_N(T)$ to a value using the measured $\rho_N(T)$, as done previously, allows both the resulting $\tau_{s,N}$ to be determined by the width of the central peak and maintains consistency with the method used previously to determine $\lambda_{s,N}$ from spin valve fitting.

Hanle effect fitting, as discussed previously, was repeated for several measurement temperatures on Py/Al and Co/Al devices with nominal $d = 800\,\mathrm{nm}$. The value of $\tau_{s,N}(T)$ obtained from these fits can be taken with $D_N(T)$ to compute $\lambda_{s,N} = \sqrt{D_N\,\tau_{s,N}}$. $\lambda_{s,Al}(T)$ from Hanle effect fitting is plotted, along with the values obtained from spin valve effect fitting, in Figure 4.17. $\lambda_{s,N}(T)$ obtained from the Hanle effect fitting has a weak temperature dependence, which is in agreement with the temperature dependence of spin valve measurements of $\lambda_{s,N}(T)$. However, the magnitudes of $\lambda_{s,N}(T)$ obtained from the two methods do not agree. Numerical simulations of spin injection, diffusion, relaxation, and precession will show that this discrepancy is resolved by a Hanle effect model which includes diffusive FM/N interfaces and spin relaxation at surfaces, discussed in §5.2.4.

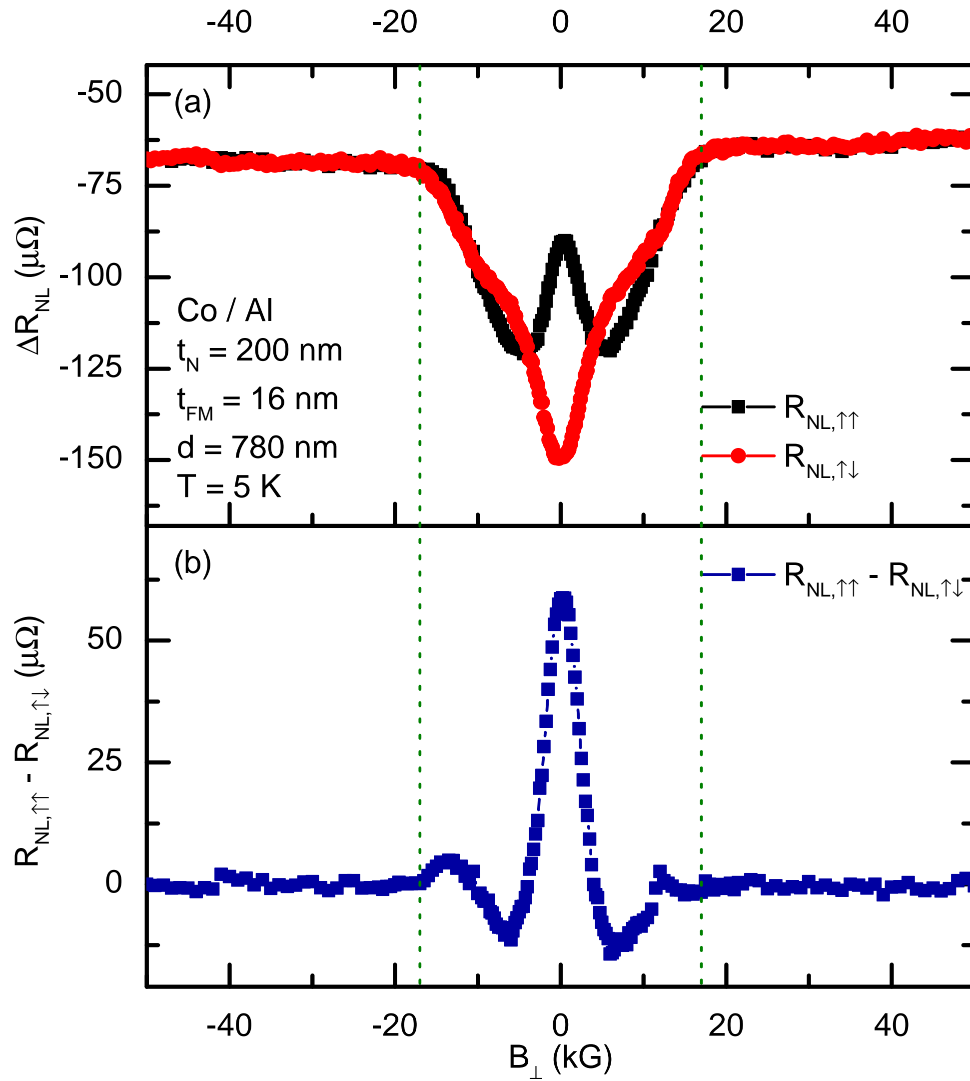

Figure 4.14: Raw Hanle effect data: (a) $R_{NL,\uparrow\uparrow}$ (black) and $R_{NL,\uparrow\downarrow}$ (red), and (b) $R_{NL,\uparrow\uparrow} - R_{NL,\uparrow\downarrow}$ as a function of $B_\perp$ for a non-local Co/Al device with $d = 780 \pm 20\,\mathrm{nm}$.

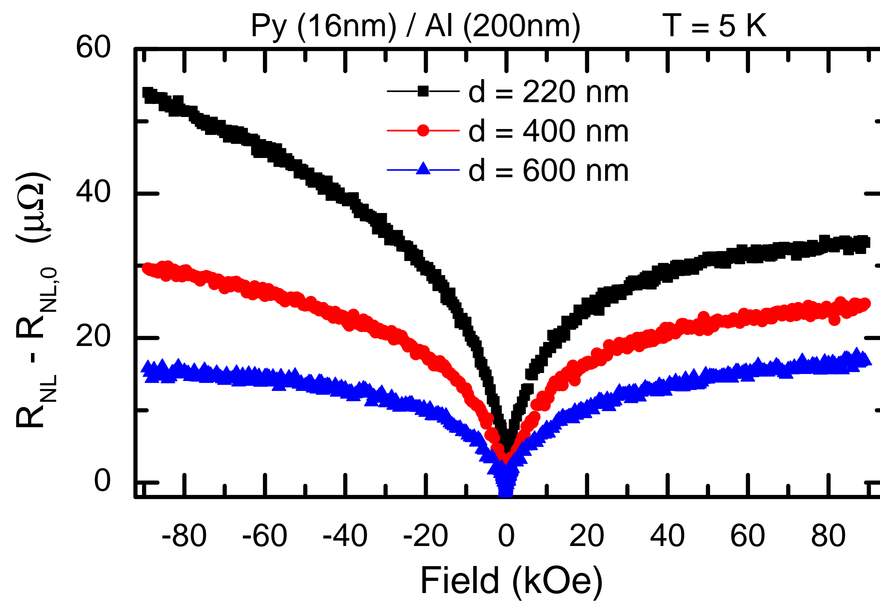

Figure 4.15: Non-local resistance R_{NL} measured to $\pm 9\,\mathrm{T}$ with the offset at $B = 0\,\mathrm{T}$ $R_{NL,0}$ subtracted. Data from devices with contact separations $d = 220\,\mathrm{nm}$, $400\,\mathrm{nm}$, and $600\,\mathrm{nm}$ are shown at $T = 5\,\mathrm{K}$.

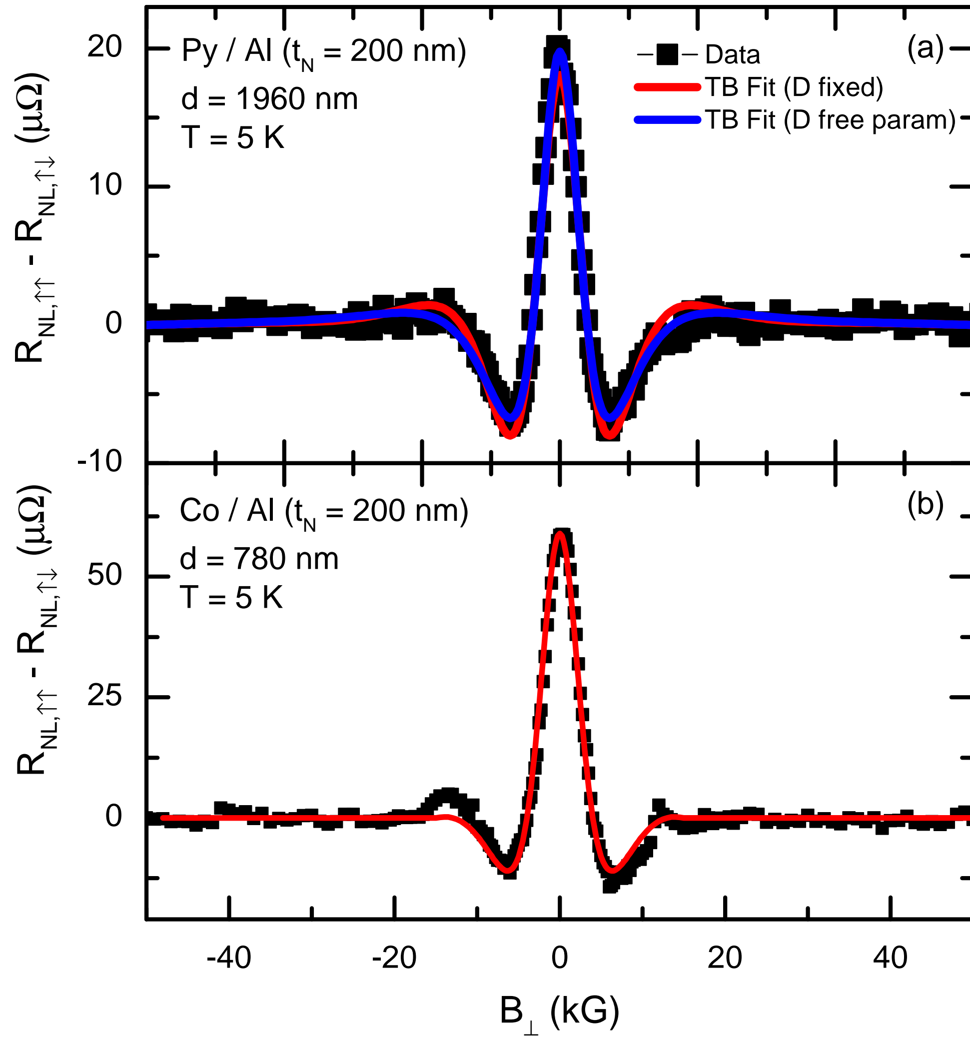

Figure 4.16: Hanle effect data $R_{NL,\uparrow\uparrow} - R_{NL,\uparrow\downarrow}$ for (a) a Py/Al lateral non-local device and (b) a Co/Al lateral non-local device, with corresponding fits to the analytic model of diffusion and relaxation in the N channel only, which includes diffusion, relaxation, and precession.

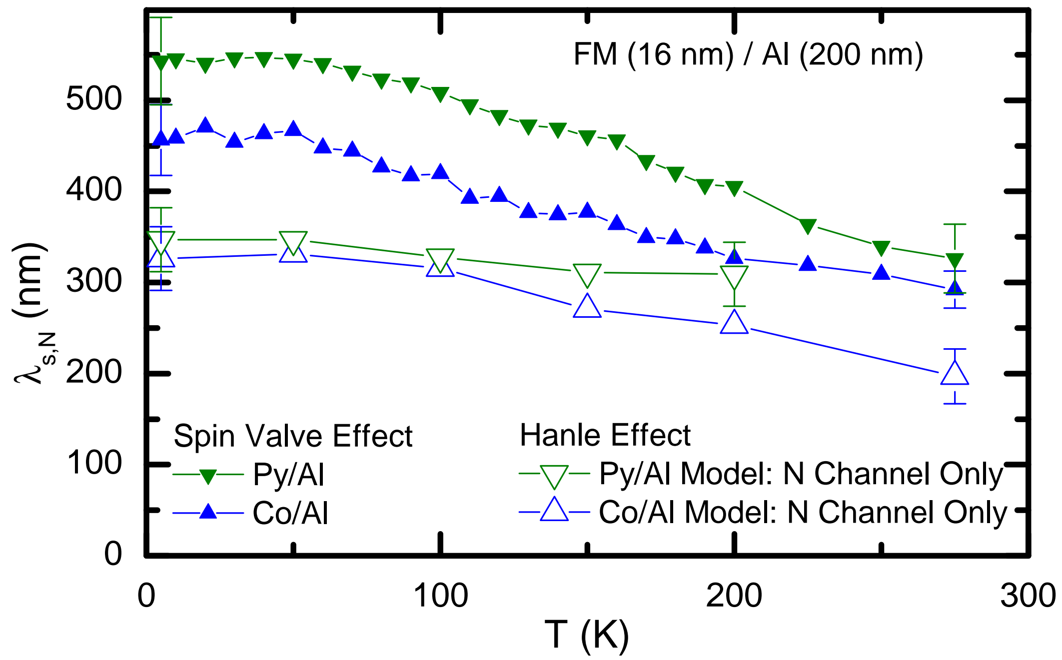

Figure 4.17: $\lambda_{s,Al}$ computed from fits to Hanle effect data using the model for precession, relaxation, and diffusion within the N only (open symbols).

4.5.3 Hanle Effect Analysis: Copper

Experimental Hanle effect data for devices with Cu channels are more difficult to measure and analyze than for the Al counterparts. $\tau_{s,Cu}$ is $\sim 5\,\mathrm{ps}$, smaller than that of Al, while D_N for Cu channels is $\sim 300\,\mathrm{cm^2\,s^{-1}}$, larger than that of Al. The values of these parameters for Cu produce a Hanle widths larger than that of Al, with the minima due to a mean precession through π occurring at $|B_\perp| \gtrsim 10$ kG for Cu. These minima occur at approximately $4\pi M_s$ of Py and approaching $4\pi M_s \approx 17\,\mathrm{kG}$. Measurements and fitting are possible, although, the results of quantitative fitting should be interpreted cautiously.

The fields below that required to saturate Py FMs out-of-plane ($B_\perp < 10$ kG) is too small to observe a sufficient window of the Hanle width. As a result, only data from Co/Cu devices are shown. Similar to Al Hanle effect data, a background appears for Cu devices with transparent interfaces, although the magnitude is much larger. The background depends on $B_\perp$ non-linearly, so that the Cu $R_{NL,\uparrow\uparrow}(B_\perp)$ Hanle data cannot be fit without subtracting the background first. This background is present in the spin valve configuration as well, as seen in the Co/Cu spin valve measurements shown in Figures 3.8 and 4.19. However, the background changes little for $|B_\perp| < 1\,\mathrm{kG}$ compared to ΔR_{NL}.

The fitting of Hanle effect measurements of $R_{NL,\uparrow\uparrow}$ for Co/Cu devices requires the background R_{NL} to be measured as a function of the in-plane field $B_\parallel$, the same geometry as spin valve measurements except the maximum field is larger, so that the in-plane background can be subtracted from R_{NL} vs. $B_\perp$. Figure 4.18 shows non-local field sweeps under applied out-of-plane magnetic fields $B_\perp$ (left column) and in plane $B_\parallel$ (right column), for $d = 400, 600, 800\,\mathrm{nm}$ and $T = 5, 50, 100, 150, 200\,\mathrm{K}$ with the FMs initialized into the $\uparrow\uparrow$ state. The offset of $R_{NL}(B = 0\mathrm{G})$ is removed from each plot, allowing the data to be overlaid. The same offset appears in both the Hanle ($B_\perp$) and background ($B_\parallel$) field sweeps. These measurements were the first observation of a background of this form. Later, similar measurements have been made by others on Py/Ag devices. This has been attributed to the formation of oxide clusters at the interface forming magnetic impurities in the N [127]. Mihajlovic *et al.* argued these magnetic impurity clusters are randomly magnetized at zero applied field and therefore provide additional spin-relaxation. As the applied field is increased the strength of

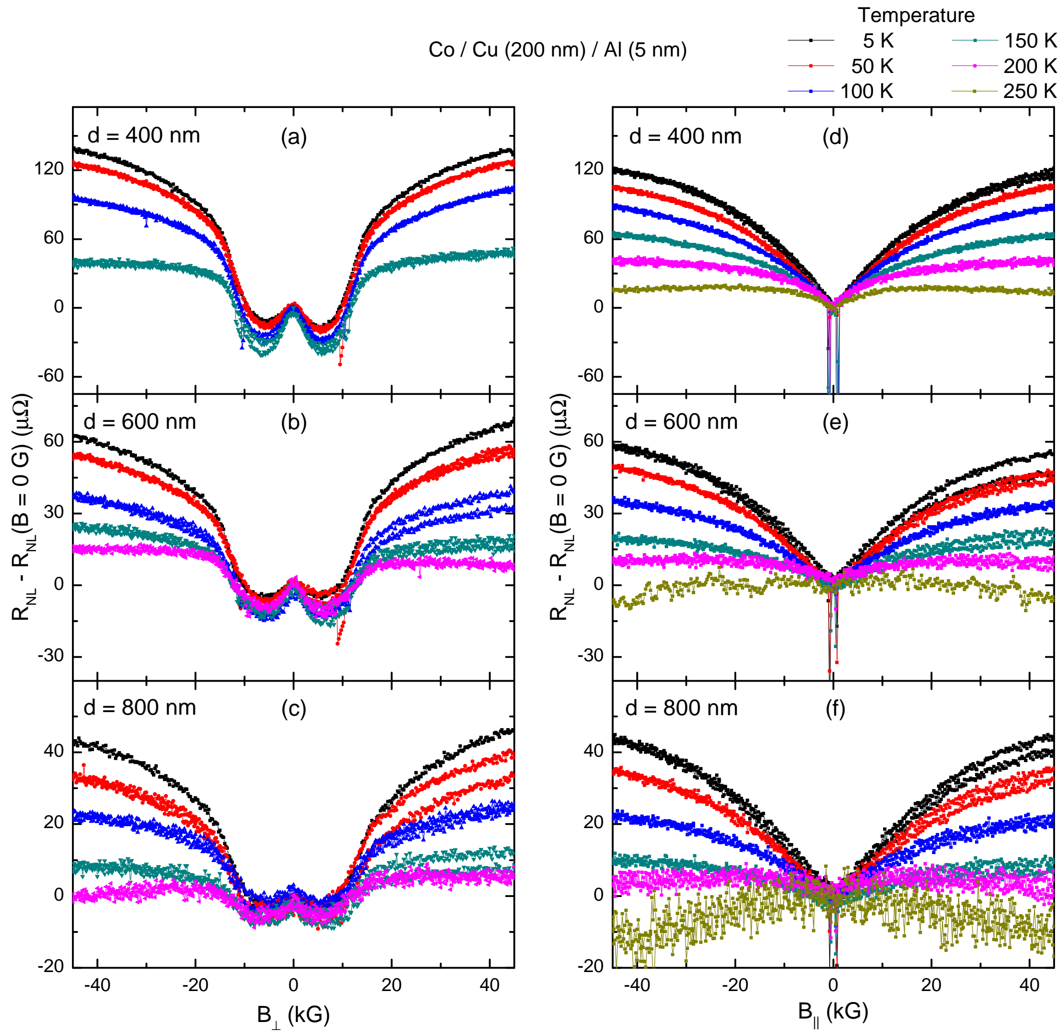

Figure 4.18: $R_{NL,\uparrow\uparrow}$ data for large applied field for Co/Cu devices with the magnetic field applied out-of-plane ($B_\perp$) for (a) $d = 400\,\mathrm{nm}$, (b) $600\,\mathrm{nm}$, and (c) $800\,\mathrm{nm}$ and in-plane ($B_\parallel$) for (d) $400\,\mathrm{nm}$, (e) $600\,\mathrm{nm}$, and (f) $800\,\mathrm{nm}$, with $R_{NL}(B = 0\,\mathrm{G})$ subtracted.

the spin-relaxation is reduced. This explanation, which depends on FM oxide clusters near the FM/N interface, does not seem to be consistent with the similarity of the background observed here for both Co/Cu and Py/Cu systems as the interdiffusion and oxide formation of Ni, Fe, and Co are different. The magnitude of the background decreases with increasing T, so that at $T = 200\,\mathrm{K}$ it appears nearly flat for $B_\perp > 10\,\mathrm{kG}$. Further, the background at a fixed field of 4.5 T decreases linearly with temperature. In addition to the Co/Cu large field background data, shown in Figure 4.18, the background was also measured for a Py/Cu device with $d = 400\,\mathrm{nm}$ to be $R_{NL}(45\,\mathrm{kG}) - R_{NL}(0\,\mathrm{kG}) = 100\,\mu\Omega$ at 5 K. The magnitude for this background is similar for both Py/Cu and Co/Cu devices, which is much larger than that of Al devices. For Al devices the magnitude of this high field background is a factor of 20 smaller than devices with Cu channels. The dependence on channel material indicates that this effect depends primarily on the N channel rather than the FM material alone.

In-plane field sweeps of R_{NL} for both Co/Cu and Co/Al devices are shown in Figure 4.19. These Co/Cu data, shown in Figure 4.19(a), have a field-dependent background. The slope of this background in the parallel-magnetization state for $|B| < 4\,\mathrm{kG}$ is $|5.2 \pm 0.2\,\mathrm{n\Omega\,G^{-1}}|$. For the Co/Al data the slope of this background in the parallel-magnetization state is $|0.4 \pm 0.2\,\mathrm{n\Omega\,G^{-1}}|$. The slope of the low-field background switches sign with the contact that reverses at larger coercive field, i.e. with the reversal of the FM detector, rather than at $B = 0\,\mathrm{G}$. The slope of this background in the anti-parallel-magnetization state is $|12 \pm 6\,\mathrm{n\Omega\,G^{-1}}|$ for Co/Cu and $|0.1 \pm 0.2\,\mathrm{n\Omega\,G^{-1}}|$, consistent with the magnitudes of the slopes in the parallel state.

Figure 4.20 shows the Hanle data of Figure 4.18 after subtraction of the measured background. The data after background subtraction are qualitatively similar to that expected for devices where tunnel barriers are present, i.e. spin diffusion in the N channel only. The magnitude is weakly dependent on T, consistent with the previously-measured $\Delta R_{NL}(T)$ from spin valve experiments. Further, the observed width of the Hanle curve does not change significantly with T. To gain better estimates of $\tau_{s,N}$ and $\lambda_{s,N}$, the background-subtracted data were fitted. Quantitative analysis was done for Cu Hanle data, shown below.

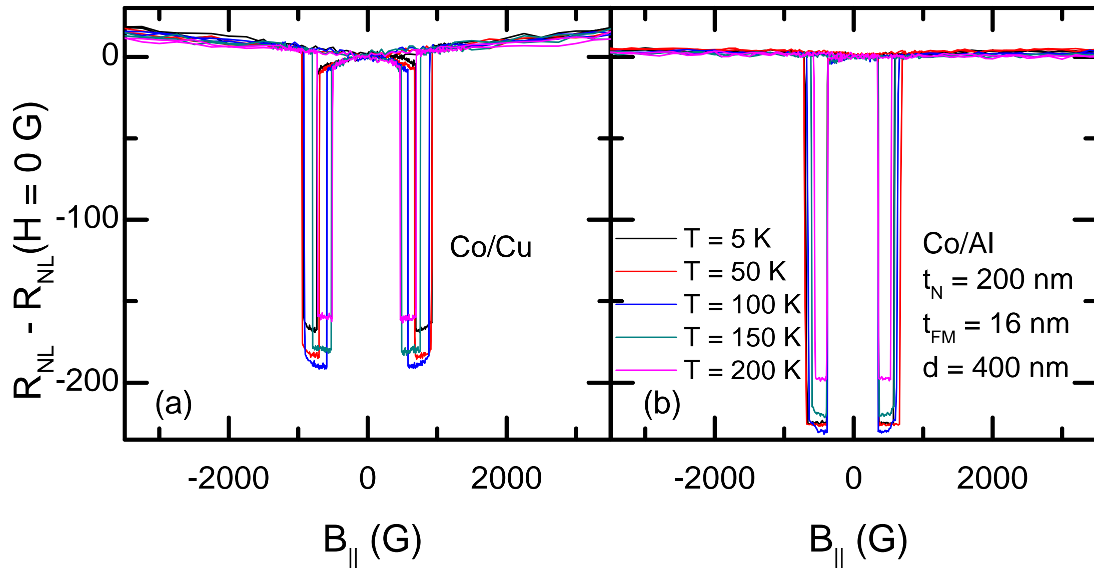

Figure 4.19: In-plane field sweep data of R_{NL} for (a) Co/Cu and (b) Co/Al devices with $d = 400\,\mathrm{nm}$ at various temperatures and an offset $R_{NL}(B = 0\,\mathrm{G})$.

4.5.4 Fitting Hanle Data for Devices with Copper Channels

Unlike the devices with Al channels, the Cu-based devices have a width of the central Hanle peak too wide to make extracting the magnitudes of $\tau_{s,N}$ and $\lambda_{s,N}$ accurate. However, the relative change of the Hanle width as a function of T remains a useful indicator of the temperature dependence of spin relaxation. Using $D_N(T)$ determined from $\rho_N(T)$, fits of the background subtracted $R_{\uparrow\uparrow}$ vs $B_\perp$ Hanle field sweeps were performed, the results of which are shown in Figure 4.21.

Similar to the case of Al, described in §4.5.2, $\lambda_{s,Cu}(T)$, is shown in Figure 4.22, and computed from the Hanle effect fitting results at various temperatures. The graph also includes $\lambda_{s,N}$ obtained from Co/Cu spin valve effect fitting from a sister device fabricated simultaneously. Similar to the results from Al channels, Hanle effect fitting for Cu devices confirms a weak temperature dependence of $\lambda_{s,N}(T)$. The oscillations of the Hanle signal measured for Al devices allows $\tau_{s,N}$ to be determined with smaller systematic errors than for devices in which only partial oscillations are observed. Since these oscillations are unavailable for Cu devices, the fitting is limited to the central

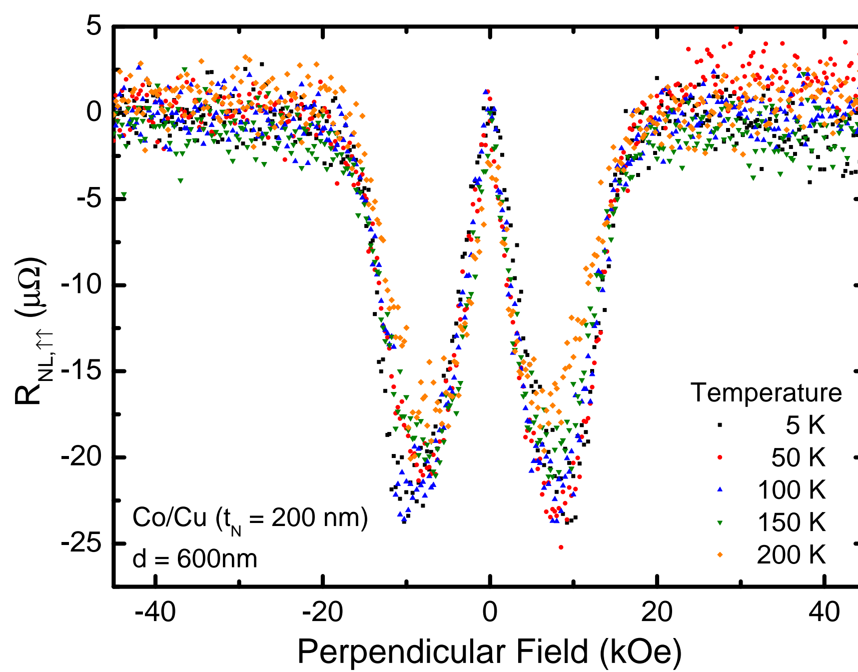

Figure 4.20: Temperature-dependent Hanle effect data $R_{NL,\uparrow\uparrow}$ for a Co/Cu device with $d = 600 \pm 20\,\text{nm}$ and a background of the form shown in Figure 4.18 subtracted.

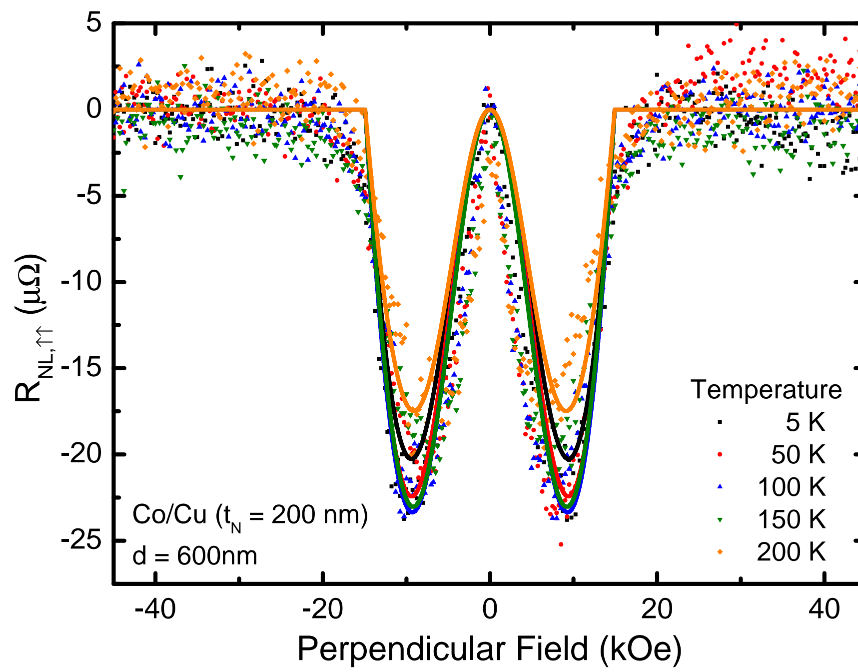

Figure 4.21: Hanle effect data $R_{NL,\uparrow\uparrow}$ and 1D diffusion model fits at various T for a Co/Cu device with a background subtracted.

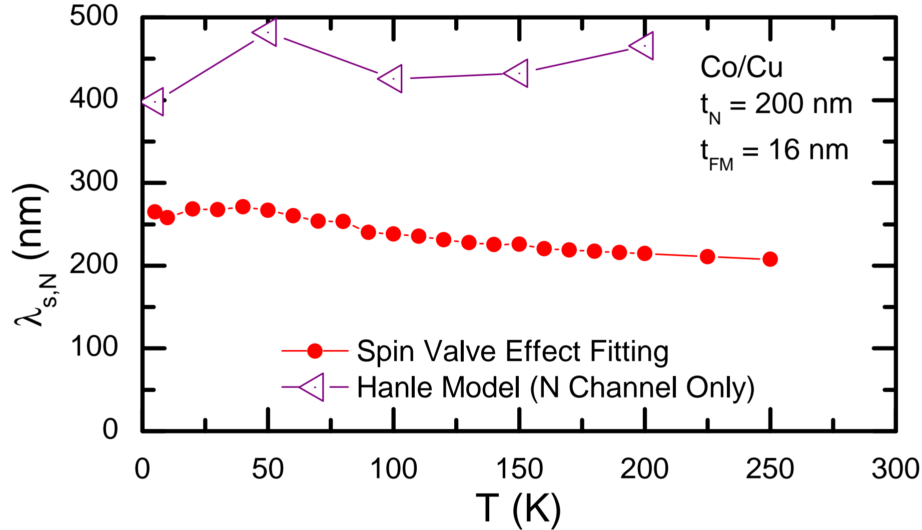

Figure 4.22: $\lambda_{s,Cu}$ from the fitting of Hanle effect data $R_{NL,\uparrow\uparrow}(B_\perp)$ (open triangles) for a Co/Cu device at various T with $\lambda_{s,Cu}$ from spin valve effect fitting of measurements of the same device set (closed circles).

region of the Hanle peak resulting in the magnitude of $\tau_{s,N}$ having larger systematic errors than for Al devices. The magnitude of $\lambda_{s,N}$, with the systematic error shown, determined using spin valve effect experiments or from Hanle experiments disagree.

Examining $\tau_{s,N}(T)$ rather than $\lambda_{s,N}(T)$ shows a surprising result: $\tau_{s,N}$ increases with increasing T. Shown in Figure 4.23, $\tau_{s,N}$ increases with T, independent of the choice of $D_N(T)$ or whether Hanle or spin valve effects are used. This contradicts the expectation for Elliot-Yafet spin relaxation in bulk metals, for which $\tau_{s,N} \propto \rho_N^{-1}$. Broadly, for metals $\tau_{s,N}$ is expected to decrease with increasing T.

The only way to resolve this apparent contradiction is for the total number of spins relaxing per unit time to decrease with increasing T. The discussion in Chapter 5 shows that the presence of enhanced spin relaxation at surfaces can allow this decrease of overall relaxation rate of the spin accumulation sampled by the detector. This proposed mechanism is compatible with the experimental observations presented in this chapter. Increased T leads to reduced diffusion of spins that scatter at the surfaces, where spin polarization relaxes quickly. An increased proportion of the spin polarization relaxes in

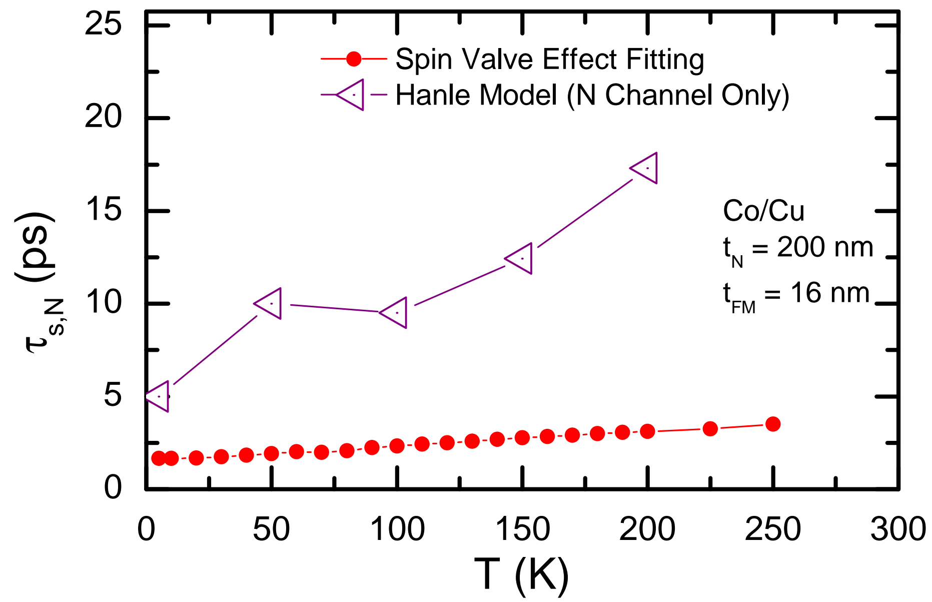

Figure 4.23: Spin lifetime $\tau_{s,N}$ found by fitting Hanle effect $R_{NL,\uparrow\uparrow}$ data and spin valve effect data for Co/Cu devices.

the bulk than at surfaces for increasing temperature. Numerical modeling discussed in §5.2 demonstrate this result.

The spin lifetime can also be plotted for devices with Al channels, as shown in Figure 4.24. In this case $\tau_{s,N}(T)$ in remains approximately constant. This is also inconsistent with the expected Elliot-Yafet spin relaxation behavior for metals. The expected $\mathrm{d}\tau_{s,N}/\mathrm{d}T$ from theory and experiment for Al is smaller than for Cu, which coincides with the electronic mean free path being shorter for Al than Cu, leading to reduced surface scattering.

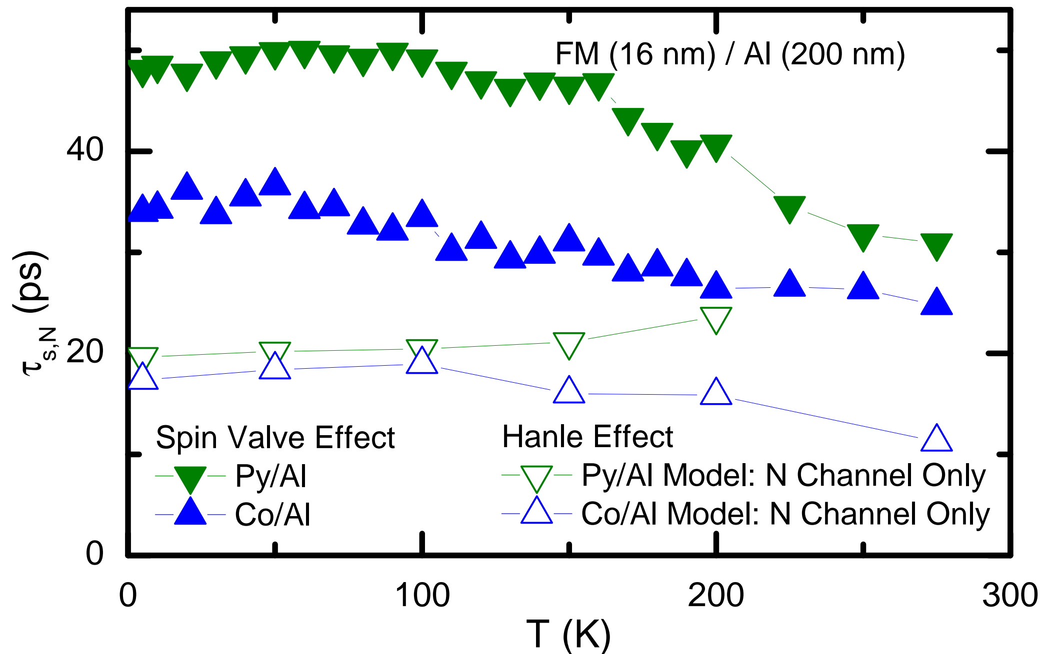

Figure 4.24: Temperature dependence of the spin lifetime $\tau_{s,N}$ found by fitting Hanle effect. $R_{NL,\uparrow\uparrow} - R_{NL,\uparrow\downarrow}$ and spin valve effect data for Al lateral non-local devices.

In this chapter the results of both spin valve effect measurements and Hanle effect measurements have shown that $\lambda_{s,N}$ has a weak temperature dependence, as well as a reduced magnitude, relative to that expected from the bulk resistivities. For bulk Elliot-Yafet relaxation in the N channel only, the weak temperature dependence of

$\lambda_{s,N}$ requires that $\tau_{s,N}$ increase with T to be consistent with the measured $\rho_N(T)$ and $\lambda_{s,N}(T)$. One explanation is heterogeneous relaxation of spins, where they relax faster at surfaces than in the bulk of the channel. This possibility was tested using numerical calculations, described in Chapter 5.

A unique $\Delta R_{NL}(T)$ was shown with a peak near 50 K for Py/Cu devices which did not appear for any other measured material combination. This did not appear in $\lambda_{s,N}(T)$ from fitting beyond the systematic fitting errors. Since the measured $\lambda_{s,Cu}(T)$ is monotonic, the Py/Cu $T \approx 50$ K peak is likely due to a peak in the effective spin-injection rate into the channel.

Chapter 5

Spin Diffusion and Relaxation Simulations

The experiments in this work have focused on spin-transport in nanostructured lateral spin valves. The measured temperature dependence of the spin diffusion length $\lambda_{s,N}$ of lateral spin-transport devices was found to be inconsistent with the accepted relaxation mechanisms for non-magnetic metals. The accepted spin-relaxation mechanism for metals, first proposed by Elliot and Yafet, gives a spin lifetime $\tau_{s,N}$ that is proportional to the momentum scattering time $\tau_{p,N}$. The temperature-*independent* constant of proportionality is defined as:

$$\alpha \equiv \frac{\tau_{p,N}}{\tau_{s,N}}\,. \tag{5.1}$$

The Elliot-Yafet mechanism, as discussed in §1.2.12, leads to $\lambda_{s,N}(T) \propto \rho_N(T)^{-1}$, which varies with temperature T. Materials for which Elliot-Yafet spin relaxation applies should satisfy the relation

$$\frac{\lambda_{s,N}(T_1)}{\lambda_{s,N}(T_2)} = \frac{\rho_N(T_2)}{\rho_N(T_1)}, \tag{5.2}$$

which is not observed in this work. The failure of experimental data to satisfy Equation 5.2, as discussed below, demonstrates the need for an additional relaxation mechanism to describe this data.

The relationship given in Equation 5.2 was evaluated using the measured values of $\rho_N(T)$ and $\lambda_{s,N}(T)$ determined by fitting $\Delta R_{NL}(T)$ vs. d, presented in Chapter 4. The spin diffusion length $\lambda_{s,N}$ of the spin-polarized electrons was measured for

nanostructured N channels with width $w_N = 270 \pm 30\,\text{nm}$ and thicknesses t_N ranging from 200 to 400 nm. For devices with N channels 200 nm thick, values of $\lambda_{s,N}$ are given in Table 5.1. The corresponding typical resistivities, previously given in §3.1, are also listed in the table. Included in the table are the corresponding ratios of each of these parameters over the same range of temperatures, $\lambda_{s,N}(5\,\text{K})/\lambda_{s,N}(275\,\text{K})$ and $\rho_N(275\,\text{K})/\rho_N(5\,\text{K})$. These ratios should agree, satisfying Equation 5.2. However, the experimental values in Table 5.1 do not.

Material	$\rho_N(5\,\text{K}, 275\,\text{K})$	$\frac{\rho_N(275\,\text{K})}{\rho_N(5\,\text{K})}$	$\lambda_{s,N}(275\,\text{K}, 5\,\text{K})$	$\frac{\lambda_{s,N}(5\,\text{K})}{\lambda_{s,N}(275\,\text{K})}$
Py/Cu	1.0, 3.1 µΩ cm	3.1	290, 390 nm	1.2 (1.3†)
Co/Cu	1.1, 3.2 µΩ cm	2.9	260, 333 nm	1.3
Py/Al	4.2, 7.9 µΩ cm	1.9	330, 540 nm	1.6
Co/Al	4.3, 8.1 µΩ cm	1.9	290, 465 nm	1.5

Table 5.1: The ratio of measured ρ_N from §3.1 and fitted $\lambda_{s,N}$ from §4.4.3 at $T = 5\,\text{K}$ and 275 K for lateral NLSV devices with transparent interfaces.

For Cu devices, the measured ratios $\lambda_{s,N}(5\,\text{K})/\lambda_{s,N}(275\,\text{K})$ and $\rho_N(T = 275\,\text{K})/\rho_N(T = 5\,\text{K})$ are 3.0 ± 0.1 and 1.3 ± 0.1, respectively. These ratios for Al devices are 1.9 ± 0.1 and 1.5 ± 0.1. Since Equation 5.2 is not satisfied for either Cu or Al, it is clear that a non-bulk relaxation mechanism is present in the nanostructured N channels.

Enhanced spin-relaxation at the boundaries of the normal metal is likely present due to increased spin-orbit interaction from the symmetry breaking at the surface [55, 58] or material properties that are different at surfaces, as discussed in §1.2.13. Enhanced spin relaxation at surfaces may be a possible mechanism to resolve the inconsistency regarding the experimental temperature dependence. Although spin relaxation at surfaces has been invoked to explain unexpected experimental data, disagreement remains about the effect this has on the temperature dependence of $\lambda_{s,N}$ [43, 59]. To better understand the effect of enhanced spin relaxation at surfaces, I have carried out numerical simulations of spin-diffusion and spin-relaxation in lateral non-local devices.

5.1 Spin-Transport Simulation Details

Numerical simulations of diffusive spin-transport in lateral FM/N devices were performed. These simulations were used to determine the spin accumulation due to diffusion in three-dimensions in non-local spin valve structures. The simulations were set up to allow enhancement of spin-relaxation at material surfaces to be included, with the resulting spin accumulation and spin diffusion length then modeled.

Numerical Monte Carlo simulations of spin transport in lateral devices were conducted using MATLAB®. The simulations were written to model non-equilibrium spin diffusion described by the diffusion equation given in Chapter 1,

$$D\frac{\partial^2 (\mu_\uparrow - \mu_\downarrow)}{\partial x^2} = \frac{\mu_\uparrow - \mu_\downarrow}{\tau_s}, \tag{5.3}$$

using a three-dimensional random walk.

A simulated device is populated with electrons which diffuse within the device via randomized steps of length Δr. The direction of each random-walk step is uniformly distributed about the unit sphere, leading to isotropic diffusion. The randomized step-length is given by the distribution $f(\Delta r)$:

$$f(\Delta r) = \frac{1}{\sqrt{2\pi\varsigma^2}} e^{\frac{-\Delta r^2}{2\varsigma^2}}, \tag{5.4}$$

$$\varsigma = \sqrt{6}\lambda_p. \tag{5.5}$$

The distribution depends on the mean free paths $\lambda_{p,N}$ and $\lambda_{p,FM}$ of the N and FM materials, respectively, which are computed from the measured $\rho_N(T)$ and $\rho_{FM}(T)$. The magnitude of the mean free path of metals λ_p, given by $v_F\tau_p$, ranges in this work from 66 nm to 22 nm for Cu and 14 nm to 7 nm for Al, with the Fermi velocity v_F taken from the literature for each material [49]. Since the mean free path is material dependent, the random walk step size depends on position within the heterostructure.

Each simulated electron undergoes a random walk with the step size of the i$^{\text{th}}$ iterative step given by the distribution in Equation 5.4. The experimental devices consist of three-dimensional rectangular regions of N and FM materials, so for convenience Cartesian coordinates are used in the simulations to specify positions $\vec{r}(x, y, z)$. The Cartesian coordinates used here are chosen with $\hat{x}$ along the length of the N channel, $\hat{y}$ out-of-plane along the thickness (i.e. the growth direction) of the channel, and $\hat{z}$ the

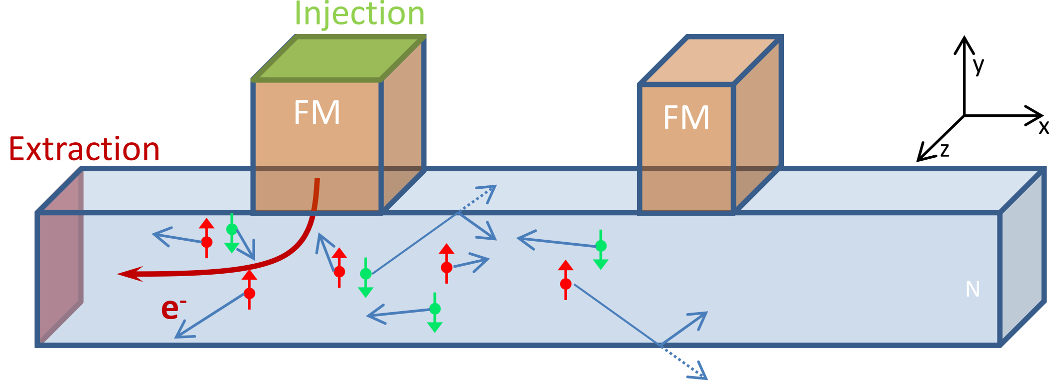

Figure 5.1: The simulation geometry of a non-local spin valve. Boundaries shaded green(red) mark the current injection(extraction) surface with spin-up and spin-down electrons shown with representative vectors depicting random steps, some of which scatter specularly from surfaces.

in-plane direction orthogonal to the N channel length. For this coordinate system, the N channel cross section is in the yz-plane, as shown in Figure 5.1. The distribution given in Equation 5.4 is used to generate a random step $\Delta\vec{r}_i$ from the position at the beginning of the i$^{\text{th}}$ step $\vec{r}_i$ to the position after the step $\vec{r}_{i+1}$. The length of the step for the i$^{\text{th}}$ step is recorded in terms of three Cartesian coordinates composed of the component in each direction $\Delta x_i\ \hat{x}$, $\Delta y_i\ \hat{y}$, and $\Delta z_i\ \hat{z}$,

$$\Delta r_i = \sqrt{(\Delta x_i)^2 + (\Delta y_i)^2 + (\Delta z_i)^2}, \tag{5.6}$$

which is used to compute the new position after an iteration. The new position $\vec{r}_{i+1}(x_{i+1},\ y_{i+1},\ z_{i+1})$ after the i$^{\text{th}}$ step is given by:

$$\vec{r}_{i+1}(x_{i+1}, y_{i+1}, z_{i+1}) = \Delta\vec{r}_i + \vec{r}_i(x_i, y_i, z_i). \tag{5.7}$$

The random walk simulation is subject to boundary conditions. These boundary conditions are implemented to constrain the diffusion of carriers within the physical geometry of the device. Random walk steps are physically bounded by enforcing specular reflection from the vacuum boundaries. Specular reflection from the boundaries confines diffusion within the device without changing the randomized-step length in the plane of the boundary. Random walk steps within a lateral spin valve are depicted graphically in

Figure 5.1. The specular reflection of a random step across a boundary in the xy-plane, for example, is given by,

$$\vec{r}_{i+1} = x_{i+1}\hat{x} + y_{i+1}\hat{y} + (2z_{BC} - \Delta z_i)\hat{z}, \tag{5.8}$$

where the xy-boundary is located at z_{BC}. This condition can be applied to x or y for boundaries in the yz- or xz-planes as well, simply by permuting x or y with z in Equation 5.8.

Random walk steps between the FM and N materials were treated by scaling the step length in each material by the mean free paths $\lambda_{p,i}$ of the initial material to the final material $\lambda_{p,i+1}$. The transport across the material boundaries is due to both the charge flow and the diffusion of carriers. The scaling of the step size ensures that the mean free path is properly averaged over the length of the randomized step by the properties of the FM and N materials. This is required for detailed balance, i.e. the probability of moving from $\vec{r}_i$ to $\vec{r}_{i+1}$ is identical to $\vec{r}_{i+1}$ to $\vec{r}_i$. Incorrect enforcement of this condition will lead to a non-physical accumulation on one side of the interface.

The distribution given in Equation 5.4 depends on λ_p, which is determined for the simulations by the experimentally determined ρ. Since ρ varies with temperature, the distribution in Equation 5.4 also varies with T. For a simulation of a particular set of FM and N materials at a particular temperature, $\lambda_{p,N}$ and $\lambda_{p,FM}$ are determined by the experimental $\rho_N(T)$ and $\rho_{FM}(T)$ of the constituent materials.

The charge current flowing through the simulated device is defined by the boundary of the FM injector and N channel through which the current flows, shown for the non-local spin valve configuration in Figure 5.1. This is done by injecting a number of electrons N_i per iterative time step dt at a fixed rate N_i/dt at the end of the FM injector and extracted at the same rate $-N_i/dt$ on the end of the N channel. The geometric layout of this is depicted in Figure 5.1, with the boundary where electrons are added shaded green and the boundary where electrons are extracted shaded red. The total current flowing in the simulated device is then given by:

$$J_e = \frac{eN_i}{dt}. \tag{5.9}$$

Simulations, with an applied current, were run until the non-equilibrium densities δn have converged. δn is computed by dividing the number of non-equilibrium electrons

per simulation cell. The cell size is a fraction of λ_p in each material, on the order of nanometers, and each region of the device contains an integer number of cells.

The resulting shift in chemical potential $\delta\mu$ from the zero-current equilibrium can be found using,

$$\delta\mu = \frac{\delta n}{g(\epsilon_F)}, \tag{5.10}$$

where the density of states at the Fermi level $g(\epsilon_F)$ is taken as the bulk value for each material from Reference [49]. The simulated charge current is computed along the current path to confirm that the results of the calculation are consistent with what is expected from the material resistivities.

Simulations of transport through heterostructures, with three materials placed in-line, confirm that the modeling produces the expected potential profiles due to the charge current. Shown in Figure 5.2(a) is an FM-N-FM linear test structure used to demonstrate correct calculation of the spin-independent charge current. The charge current density can be computed from the spatial derivatives of the chemical potential. The current density in the $\hat{x}$ direction is given by,

$$j_e = \frac{1}{e\rho}\frac{\partial\mu}{\partial x}, \tag{5.11}$$

which was computed for the simulation shown in Figure 5.2(b) at $j_e = 2.4 \times 10^7\ \mathrm{A\,cm^{-2}}$, in agreement with the expected value. Having shown this to be correct, the simulation was extended to include the spin degree of freedom.

5.1.1 Spin-Dependent Diffusion Simulations

The simulations were expanded to include the spin degree of freedom following the two-channel model described in §1.2.1. A subscript $\uparrow$ or $\downarrow$ is appended to the spin-independent equations to give the spin-dependent equations for each spin-band:

$$\mu_{\uparrow,\downarrow} = -eV + \frac{\delta n_{\uparrow,\downarrow}}{g_{\uparrow,\downarrow}(\epsilon_f)}, \tag{5.12}$$

$$\delta n_{\uparrow,\downarrow} = n_{\uparrow,\downarrow} - n_{0\uparrow,\downarrow}, \tag{5.13}$$

$$j_{\uparrow,\downarrow} = \frac{1}{e\rho}\frac{\partial\mu}{\partial x}. \tag{5.14}$$

By incorporating spin-dependent transport and spin-flip scattering, the simulation can model diffusive spin transport and produce chemical potentials for the up and down

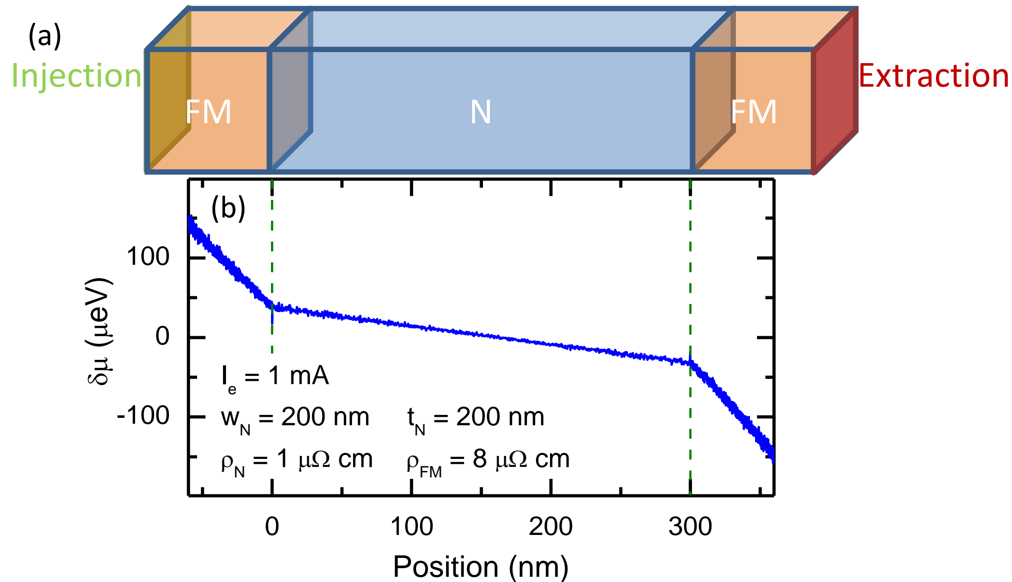

Figure 5.2: (a) Graphical representation of the three-dimensional linear FM-N-FM simulation geometry with (b) the resulting shift $\delta\mu$ due to the simulated charge current J_e.

spin bands. Diffusion within both the spin-up and spin-down bands is treated similarly to the spin-independent simulations but with random-walk properties that are spin-dependent. The simulations model the charge current as well as the diffusive transport within materials and across material interfaces. The interfacial diffusion includes the back-diffusion of injected spin-polarized electrons back from the N to the FM where they relax quickly. The spins may also flip from one spin band to the other, treated by Elliot-Yafet type relaxation. For each momentum scattering event, corresponding to a random step, the simulated electrons have a certain probability of flipping from one spin-subband to the other, given by $p_{\uparrow\downarrow}$.

For diffusion in the spin-up band, the probability of flipping to the spin-down band for a momentum scattering step is given by $p_{\uparrow\downarrow}$. Likewise, if starting in the spin-down band, the probability of flipping to the spin-up band is given by $p_{\downarrow\uparrow}$. These spin-flip probabilities depend on the position after a random-walk step $r_{i+1}(x, y, z)$. This is done such that for $r_{i+1}(x, y, z)$ within the N, the probability is given by $p_{\uparrow\downarrow,Bulk}$. If the step crosses the surface and specularly reflects from the N surface, the probability of spin-flip

is given by $p_{\uparrow\downarrow,Sur}$. Finally, if $r_{i+1}(x,y,z)$ is in the FM the spin-flip probability is given by $p_{\uparrow\downarrow,FM}$.

Detailed-balance was discussed in §1.2.5, in which

$$\frac{g_{\uparrow}(\epsilon_F)}{\tau_{\uparrow\downarrow}} = \frac{g_{\downarrow}(\epsilon_F)}{\tau_{\downarrow\uparrow}}. \tag{5.15}$$

For N materials $\tau_{\uparrow\downarrow,N} = \tau_{\downarrow\uparrow,N}$ since the densities of states for the spin-up and spin-down bands, $g_{\uparrow}(\epsilon_F)$ and $g_{\downarrow}(\epsilon_F)$ are equal and satisfying detailed balance. The simulations were done in terms of the spin-flip probabilities, that of flipping from spin-up to spin-down $p_{\uparrow\downarrow}$ and of flipping from spin-down to spin-up $p_{\downarrow\uparrow}$, which are equal for the N. For FM materials, however, $\tau_{\uparrow\downarrow,FM} \neq \tau_{\downarrow\uparrow,FM}$ in order to satisfy Equation 5.15 due to the inequality of $g_{\uparrow}(\epsilon_F)$ and $g_{\downarrow}(\epsilon_F)$. The difference between the spin-up and -down DOS divided by the total density of states gives the equilibrium polarization of the FM, $P_{FM} = (g_{\uparrow}(\epsilon_F) - g_{\downarrow}(\epsilon_F))/(g_{\uparrow}(\epsilon_F) + g_{\downarrow}(\epsilon_F))$, which can be used to set up the simulations to compare with experimental parameters. The spin-flip probabilities in the FM $p_{\uparrow\downarrow,FM}$ and $p_{\downarrow\uparrow,FM}$ are determined by the values of $\tau_{\uparrow\downarrow,FM}$ and $\tau_{\downarrow\uparrow,FM}$ so that $\lambda_{s,FM}^{-2} = \lambda_{s,FM\uparrow}^{-2} + \lambda_{s,FM\downarrow}^{-2}$ is specified. In this framework $\tau_{\uparrow\downarrow} = \tau_{p,\uparrow}/p_{\uparrow\downarrow}$ and $\tau_{\downarrow\uparrow} = \tau_{p,\downarrow}/p_{\downarrow\uparrow}$ were used to determine the spin flip probabilities for a given P_{FM}. Using these expressions, $p_{\uparrow\downarrow}$ and $p_{\downarrow\uparrow}$ were calculated so that $g_{\uparrow}(\epsilon_F)$ and $g_{\downarrow}(\epsilon_F)$ give the desired P_{FM} and total spin lifetime to compare with experiment. These spin-flip probabilities change with temperature to satisfy the temperature dependent $P_{FM}(T) = P_0(1 - \alpha_B T^{3/2})$ of the Bloch form, as well as the the magnitude of the ferromagnetic spin-diffusion length.

Just as $\mu(x)$ was calculated previously for charge transport only, the spin-resolved $\mu_{\uparrow}(x)$ and $\mu_{\downarrow}(x)$ were calculated numerically for FM/N/FM structures. Simulations for the linear FM/N/FM structure are shown in Figure 5.2 for both spin bands. The resulting $\mu_{\uparrow}(x)$ and $\mu_{\downarrow}(x)$ are shown in Figure 5.3. The simulations are shown for $T = 5\,\text{K}$ with $J_e = 1\,\text{mA}$ and resistivities $\rho_N = 1\,\mu\Omega\,\text{cm}$ and $\rho_{FM} = 32\,\mu\Omega\,\text{cm}$, and spin diffusion lengths $\lambda_{s,FM} = 5\,\text{nm}$, $\lambda_{s,N} = 300\,\text{nm}$, and $d = 500\,\text{nm}$. The output of the spin-dependent simulations can be compared to the analytical model for a linear FM/N/FM spin valve discussed in §1.2.9. The results of the analytical calculation are shown using solid curves in Figure 5.3.

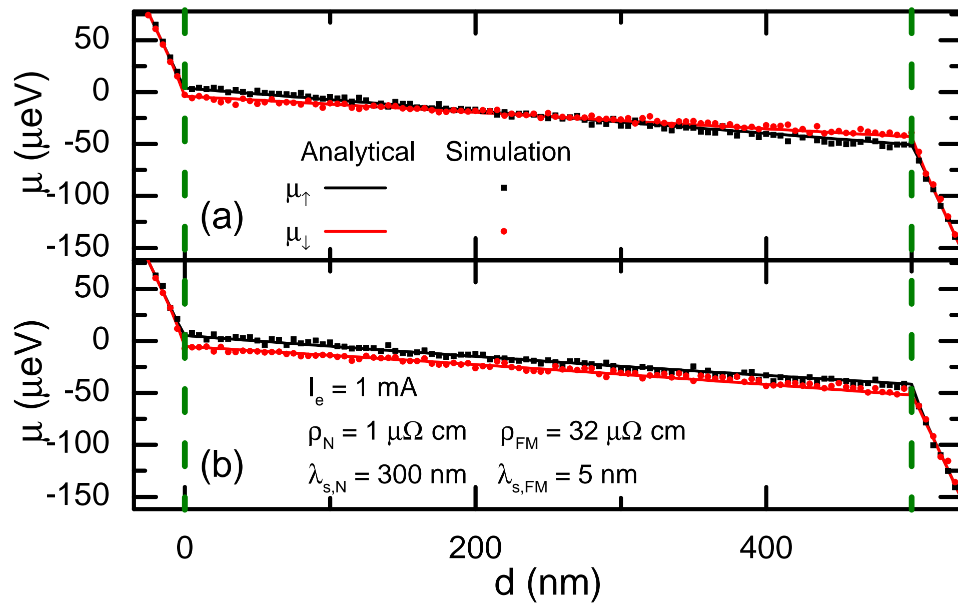

Figure 5.3: Simulated spin-dependent chemical potentials $\mu_\uparrow$ and $\mu_\downarrow$ and the analytical solution for a FM-N-FM structure with the FMs in the (a) parallel (↑↑) and (b) antiparallel (↑↓) states.

5.2 Non-Local Spin Transport Simulations: Results

Monte Carlo simulations of spin diffusion allow the effect of spin-relaxation at surfaces to be computed numerically. The simulation techniques described in §5.1 were used to explore the effect of increased probabilities of spin-flip scattering for scattering from material boundaries on the overall spin-transport in non-local structures. The interplay of the temperature-dependent properties of each material that contribute to determining spin transport were tested using these numerical calculations. In addition to calculating the temperature dependence of the spin accumulation on T the dependence on the geometric parameters d and t_N was also examined. The results of simulations allow $\Delta R_{NL}(T)$ and $\lambda_{s,N}(T)$ to be calculated as shown in the following sections §5.2.1 and §5.2.2.

Simulations were done using values of the ratio of momentum scattering time to the spin lifetime α_{EY}, defined in Equation 5.1, determined from conduction electron spin resonance experiments. Using the experimental α_{EY}, the probability of spin-flip for momentum scattering in the N channel within the simulation was set to $p_{\uparrow\downarrow,Bulk} = \alpha_{EY}$. The probabilities used were $p_{\uparrow\downarrow,Bulk} = 1/950$ for Cu and 1/3900 for Al [52, 53]. An increased relaxation probability for momentum scattering at surfaces is used, with the enhanced surface relaxation $p_{\uparrow\downarrow,Sur}$ varied to compare with experiments.

The spin accumulation was computed at various temperatures to determine $\lambda_{s,N}(T)$ as a function of the probability of surface spin-flip scattering $p_{\uparrow\downarrow,Sur}$ while the probability of bulk spin-flip scattering remained fixed. The measured $\rho_N(T)$ and $\rho_{FM}(T)$ were used to compute the distribution $f(\Delta r)$ for each material, Equation 5.5. The temperature-dependent $P_{FM}(T) = P_0(1 - \alpha_B T^{3/2})$ of the Bloch form found in Chapter 4 was used with a P_0 of 42 % for Co and 45 % for Py and α_B of $10^{-6}\,\mathrm{K}^{-3/2}$ for Co and $6 \times 10^{-5}\,\mathrm{K}^{-3/2}$ for Py. These values are consistent with those found in this work as well as by others [64, 65]. Due to the limitations of measuring $\lambda_{s,FM}$, discussed in §4.4.3, a temperature independent value was used. $\lambda_{s,FM}$ was set to 5 nm to match the experimental measurements in this work. $\lambda_{s,N}$ simulated for different values of $p_{\uparrow\downarrow,Sur}$ are plotted in Figure 5.4. In this case the abscissa is the ratio of $p_{\uparrow\downarrow,Sur}/p_{\uparrow\downarrow,Bulk}$ with the effective $\lambda_{s,N}$ from the d dependent simulations as the ordinate. Vertical bars indicate the experimental $\lambda_{s,N}$, reported in Chapter 4, which are placed near $p_{\uparrow\downarrow,Sur}/p_{\uparrow\downarrow,Bulk} \approx 30$

as this value shows agreement between the simulations and experiment. This important result gives the region of phase space for which simulations and experiment agree and are used to compare the modeled temperature dependencies of $\Delta R_{NL}(T)$ and $\lambda_{s,N}(T)$ with experiment in §5.2.1 – §5.2.3.

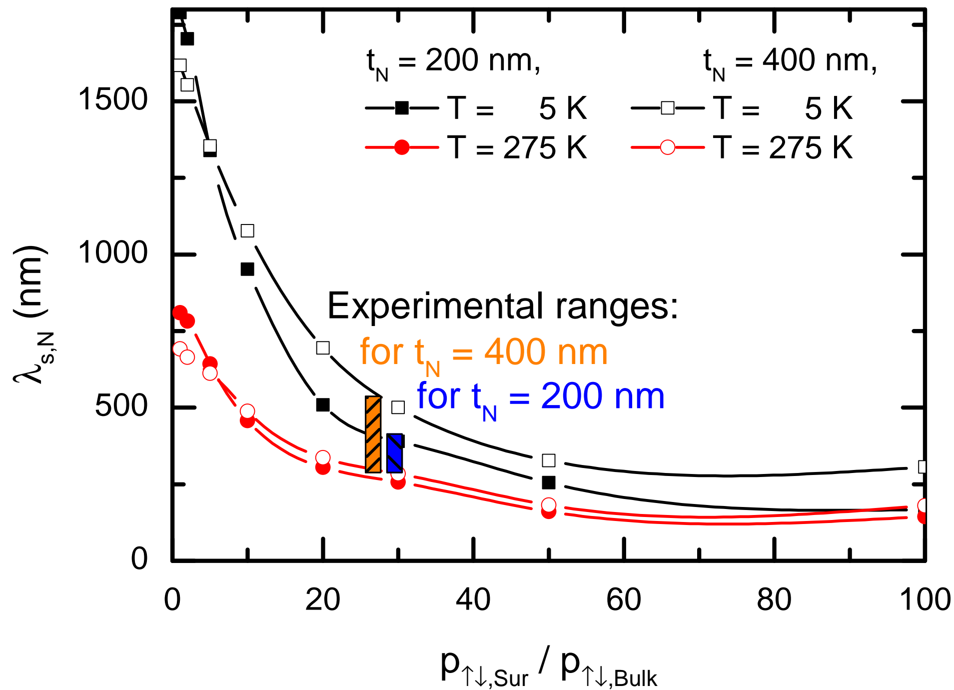

Figure 5.4: The simulated $\lambda_{s,N}$ for various T and t_N as a function of the ratio of surface to bulk spin-flip scattering probabilities $p_{\uparrow\downarrow,Sur}/p_{\uparrow\downarrow,Bulk}$.

5.2.1 Simulated Temperature Dependence of ΔR_{NL}

$\Delta R_{NL}(T)$ was calculated using the numerical model described in this chapter for all four material combinations Py/Cu, Co/Cu, Py/Al, and Co/Al with the corresponding experimental device geometries. The resulting $\Delta R_{NL}(T)$ are shown as a function of T in Figure 5.5 using $t_N = 200\,\text{nm}$, $d \approx 220\,\text{nm}$.

The simulation results shown in Figure 5.5(a) have the same general features as

the experimental data shown in Figure 5.5(b), which was presented in Chapter 4. The simulated $\Delta R_{NL}(T)$ match the overall T dependence for each of the FM/N material combinations. For the case of Py/Cu, however, the peak observed in the experimental data near $T = 50\,\mathrm{K}$ is not observed. Rather, the simulated $\Delta R_{NL}(T)$ are approximately constant for $T \lesssim 50\,\mathrm{K}$. The general temperature dependence of the numerically calculated $\Delta R_{NL}(T)$ agrees with that measured in experiment. The simulated magnitude is within 20 %, but larger than, that which was measured experimentally. In the cases shown here the calculated ΔR_{NL} are 50 to 250 µΩ larger than the experimental values. The calculations do reproduce the general temperature dependence and differences among materials properties, demonstrating consistency of the bulk properties and surface relaxation mechanisms with the observed $\Delta R_{NL}(T)$. The ratio of $\Delta R_{NL}(5\,\mathrm{K})$ to $\Delta R_{NL}(275\,\mathrm{K})$ is 1.3 and 1.2 for the modeling and experiment, respectively, for the Co based devices and 2.5 and 3.5 for Py based devices. This ratio is sensitive to all material properties, including the FMs and surface relaxation rates.

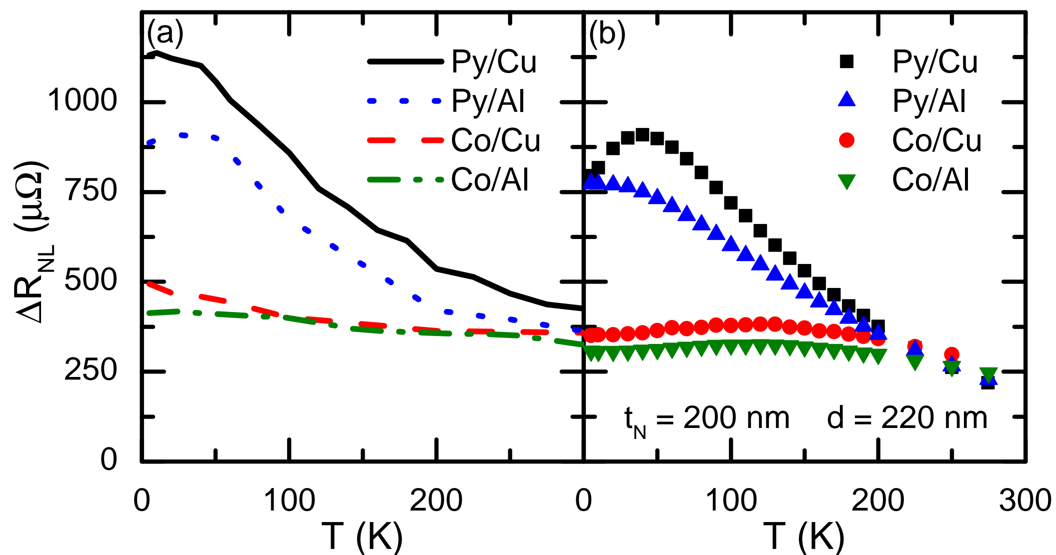

Figure 5.5: Temperature dependence of (a) the simulated and (b) measured ΔR_{NL} at a source-detector separation of $d \approx 220\,\mathrm{nm}$.

5.2.2 Simulated Temperature Dependence of the N Spin Diffusion Length in NLSVs

The same simulations which produced the $\Delta R_{NL}(T)$ in §5.2.1 were run for various d to determine $\lambda_{s,N}(T)$. Fitting the simulated $\Delta R_{NL}(T)$ vs contact separation, as was done for the experimental data in Chapter 4, allows the effective $\lambda_{s,N}(T)$ to be determined.

$\lambda_{s,N}$ calculated as a function of temperature for each material combination is shown in Figure 5.6(a). The magnitude of $\lambda_{s,N}(T)$ is similar to the experimentally determined values shown in Figure 5.6(b), ranging from 300 nm to 500 nm. The magnitude changes by less than 30 % from 5 K to 300 K, which is consistent. These changes with temperature are less than expected for the bulk channel material using the measured $\rho_N(T)$. The consistency between experiment and the simulated $\lambda_{s,N}$, as well as ΔR_{NL}, show the importance of enhanced surface relaxation in determining the spin transport behavior of non-local spin transport devices.

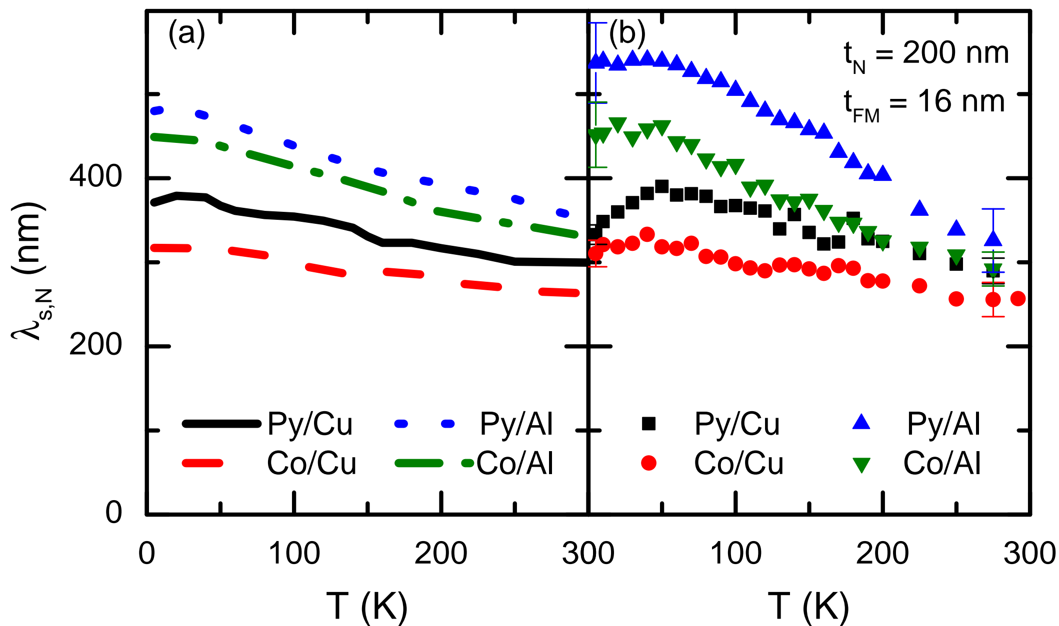

Figure 5.6: (a) Simulated temperature dependence of the effective $\lambda_{s,N}$ for devices with each of the material combinations Py/Cu, Co/Cu, Py/Al, and Co/Al for $t_N = 200\,\text{nm}$ for comparison with the measured $\lambda_{s,N}$ shown in panel (b).

These simulations show the effect of increased surface spin relaxation on the overall spin transport in a variety of material systems which have been patterned on a similar length scale to the momentum scattering length, 3 to $20 \times \lambda_{p,N}$. At low temperatures, the mean free path is long, and the non-equilibrium spins diffuse to the surface more readily. As the temperature increases, and the mean free path is reduced and non-equilibrium spins reach the surface less frequently. The fraction of spin-flip scattering occurring at N channel surfaces drops monotonically by 40 % as the temperature increases from 5 K to 275 K. The fraction relaxing in the interior of the N correspondingly increases. The ratio $\lambda_{s,N}(5\,\mathrm{K})/\lambda_{s,N}(275\,\mathrm{K})$ is 1.3 for the modeling and 1.6 for the experiment for Al based devices. The experimental ratio is 1.2 for the Cu based devices. This ratio is particularly sensitive to the surface relaxation rate.

5.2.3 Simulated Thickness Dependence of the Spin Transport in Cu

A series of simulations were run in which the channel cross section was varied by changing t_N. This was done to match the t_N of samples that were measured, as discussed in §4.4.4. Simulations were conducted of Py/Cu devices with N thickness $t_N = 200$, 300, and 400 nm and at various d matching the experimental sample geometries.

ΔR_{NL} as a function of temperature for various t_N is shown in Figure 5.7(a)-(c). The measured $\rho_N(T)$ and $\rho_{FM}(T)$ are used in each spin-diffusion simulation. In addition, the surface-relaxation probabilities from §5.2.1 – §5.2.2 were used, $p_{\uparrow\downarrow,Sur} = 30\,p_{\uparrow\downarrow,Bulk}$. The magnitude and temperature dependence of the simulation results are again consistent with experiment. The most critical observation is the simultaneous suppression of the total change with temperature of both ΔR_{NL} and $\lambda_{s,N}$ with decreasing t_N. Again, a peak near $T = 50$ K does not appear for any of the simulated conditions.

The simulated spin accumulation, due to the charge current flowing through diffusive interfaces, is similar to the experiment, apart from the low-temperature behavior. $\lambda_{s,N}(T)$ generated from the accumulation is shown in Figure 5.8. A surface relaxation effect in the N channel alone has not produced a peak in $\Delta R_{NL}(T)$ for any choice of parameters, independent of channel width, thickness, and the strength of the surface spin-flip probability. The overall spin accumulation is determined by the temperature-dependent transport properties of each material, including the polarization of the FMs.

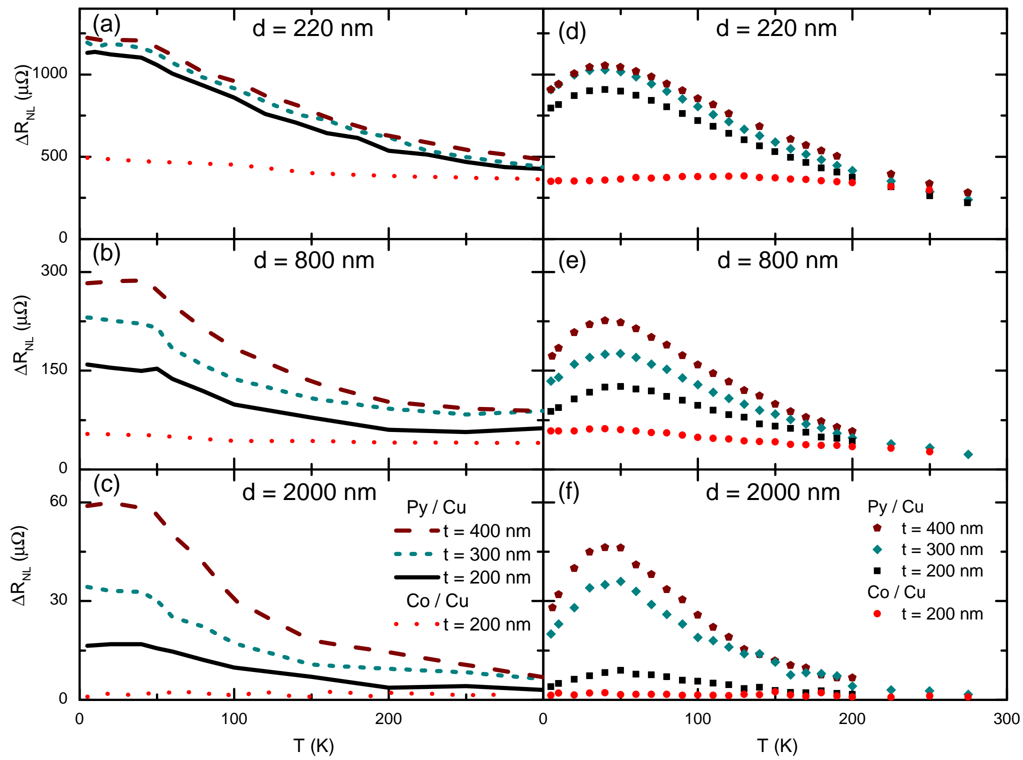

Figure 5.7: Temperature dependence of the simulated ΔR_{NL} at source-detector separations of (a) 220, (b) 800, and (c) 2000 nm for t_N = 200, 300, and 400 nm. The corresponding experimental data are shown in panels (d), (e), and (f).

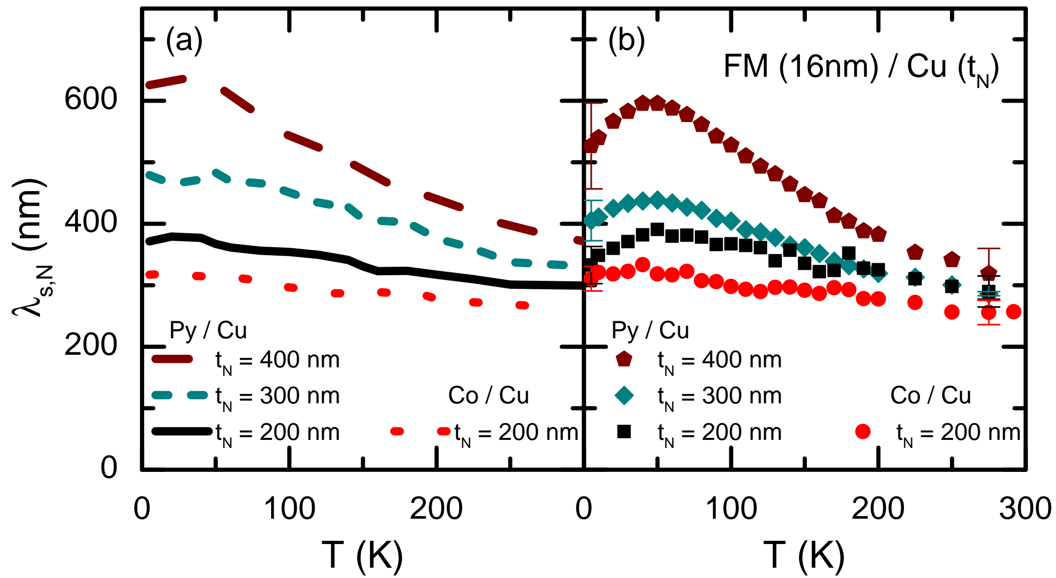

Figure 5.8: Temperature dependence of (a) the simulated and (b) measured $\lambda_{s,N}$ at $t_N = 200$, 300, and 400 nm for Py/Cu devices and $t_N = 200$ nm for Co/Cu devices.

However, this peak remains unexplained in both the simulations and experiments but suggests the presence of an interfacial effect modifying the effectiveness of spin injection, especially for the case of Py/Cu.

5.2.4 Hanle Effect Simulation Results

The electrical Hanle effect, described in §1.2.14, was used as a complementary measure of spin-relaxation. The analysis of Hanle experiments, introduced in §4.5, shows a weak temperature dependence of $\lambda_{s,N}$, similar to that observed using spin valve experiments. The magnitudes, however, do not agree. Since the magnitude of $\tau_{s,N}$ determined from Hanle effect measurements is very sensitive to the model used to fit the data, and therefore $\lambda_{s,N}$ is as well, a more accurate analysis of the Hanle width was made using the Monte Carlo simulations.

The simulations were run with a perpendicular field $B_\perp$ applied. The electrons precess through an angle $-e/m_e c\, B_\perp \mathrm{d}t$ per iterative step. The total component of the diffusive spin current is projected on the $\vec{M}$ of the detector. The top panel of Figure 5.9 shows an experimental Hanle curve measured on a Py/Al device with $d \approx 2000$ nm

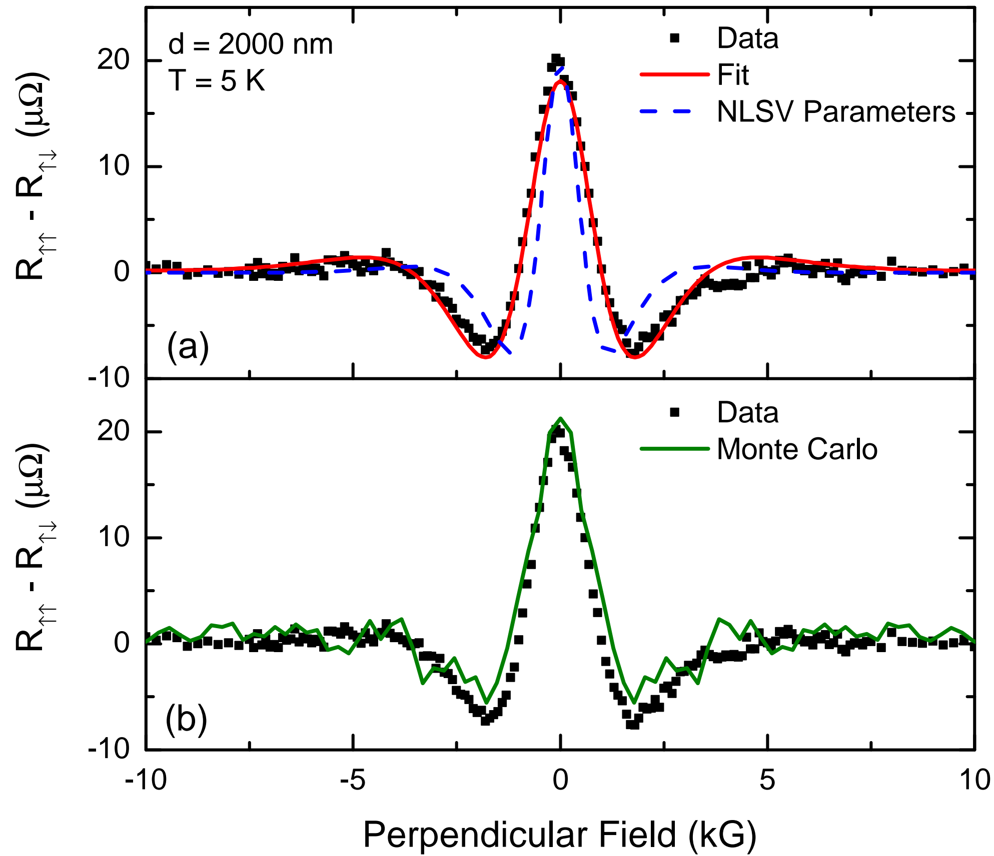

Figure 5.9: (a) $R_{NL,\uparrow\uparrow} - R_{NL,\uparrow\downarrow}$ Hanle effect data for Py/Al devices (solid symbols) with the fit without FMs or surface relaxation (red) as well as a modeled curve using $\lambda_{s,N}$ fixed from spin valve fitting (blue dashed). Panel (b) shows the data with the results of Monte Carlo simulated spin diffusion including FMs and surface relaxation.

at $T = 5\,\mathrm{K}$. A fitted Hanle curve, using the model that incorporates the N channel diffusion and relaxation only, is shown with the solid red curve. The $\lambda_{s,N}$ from this fit is smaller than expected from the separation dependence of the spin valve effect. A model Hanle curve is shown with blue dashes using the value of $\lambda_{s,N}$ obtained from spin valve fitting (§4.4.3). The width of the curve using the previously measured $\lambda_{s,N}$ is too narrow to match the experimental data.

An example of a Monte Carlo simulated Hanle curve with diffusive FM contacts and enhanced surface relaxation is plotted along with the experimental data in Figure 5.9(b). The Hanle simulations incorporate the back-diffusion of the injected spin polarized electrons back into the FM injector and detector as well as enhanced spin-flip scattering at the material boundaries. The parameters of the surface relaxation are taken from those previously shown to match spin valve experiments, $p_{\uparrow\downarrow,Sur}/p_{\uparrow\downarrow,Bulk} = 30$. Agreement is shown between the experimental and simulated Hanle curves, again demonstrating the critical importance of the FM contacts and relaxation at material boundaries in determining spin transport in lateral nano-scale devices.

The numerical simulations were used to interpret the T dependence of the experimental Hanle data, the result of which is shown in Figure 5.10. The experimental Hanle data fit using the simulations are shown as partially filled symbols. The apparent difference between the spin valve and Hanle experiments has been resolved. The resolution of this difference further supports spin relaxation at surfaces but does not resolve the unexplained injection efficiency for Py/Cu, namely the peak of $\Delta R_{NL}(T)$ near $T = 50\,\mathrm{K}$.

The results of the numerical simulations of spin transport in non-local devices with enhanced relaxation at surfaces agree with the experimental data for each material combination and t_N, except for Py/Cu devices. Modeling of Py/Cu devices does not show the experimentally observed peak near $50\,\mathrm{K}$. We conclude that the enhanced spin-relaxation at surfaces is important in determining the overall device behavior. It also suggests that the origin of the Py/Cu peak is *not* due to spin relaxation at the boundaries of the Cu channel. Some possible explanations, and ways to explore them, are discussed in Chapter 6.

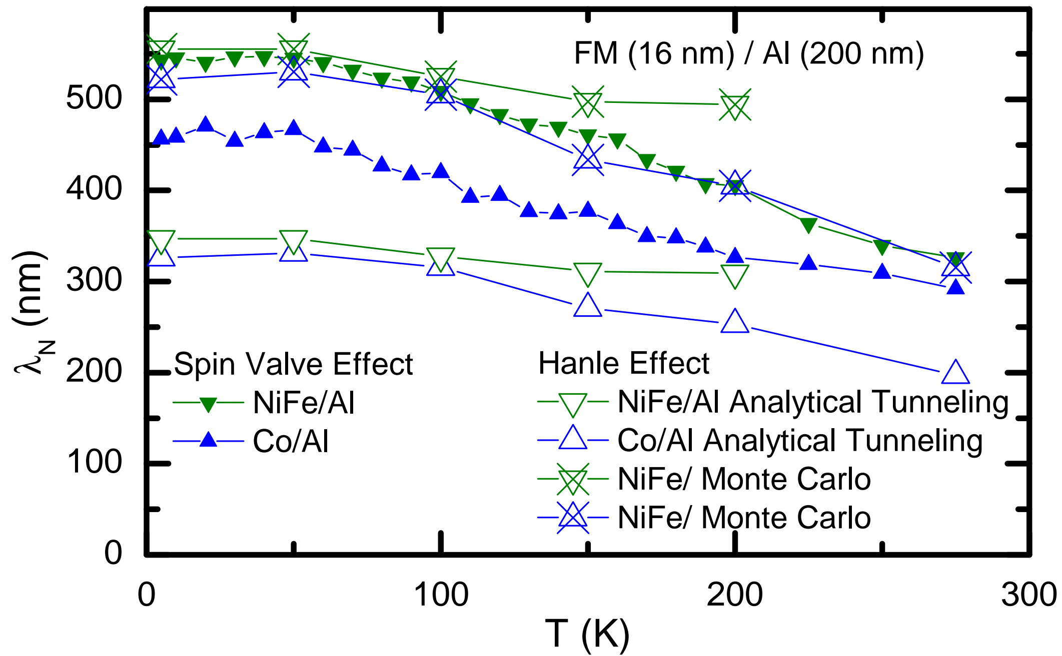

Figure 5.10: Spin diffusion length for Py/Al and Co/Al devices found in three different ways: spin valve effect vs contact separation (closed symbols), Hanle effect fits using channel diffusion and precession only (open symbols), and the interpretation of data using simulated Hanle effect including surface relaxation and diffusive FMs (half-filled symbols).

Chapter 6

Work in Progress and Future Research

6.1 Tunnel Barriers

Throughout the work described in this thesis the transport of electrons through the FM/N interface has been diffusive. The incorporation of tunnel barriers at the FM/N interfaces reduces the back diffusion of non-equilibrium spin-polarized electrons into FM and subsequent rapid relaxation, as described in §1.2.8. The removal of this relaxation mechanism should lead to ΔR_{NL} vs d following a pure exponential and simplify interpretation of the data. This simpler system will be useful for the case of large contributions from extrinsic spin-relaxation mechanisms, such as enhanced relaxation at surfaces.

The results from this work allow us to anticipate that $\lambda_{s,N}$ will continue to vary weakly with T, as presented in Chapter 4, when FM/N tunnel barriers are inserted. The magnitude of ΔR_{NL} will also be weaker than expected if using only the temperature dependence of the resistivities and FM polarizations. An estimate of $\Delta R_{NL}(T)$ is shown in Figure 6.1 which was calculated for devices with tunnel-barriers or transparent interfaces with the temperature dependence of the resistivites that are shown in Figure 3.5. $\Delta R_{NL}(T)$ computed similarly for transparent interfaces is shown as well.

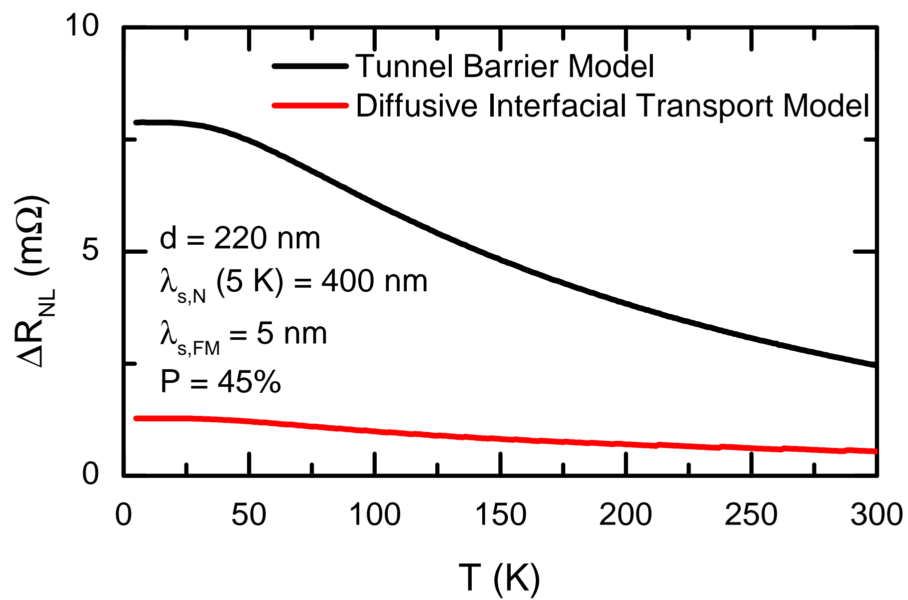

Figure 6.1: Calculated ΔR_{NL} vs. T for the tunnel barrier model as well as the case of transparent interfaces using the measured $\rho(T)$ shown in Figure 3.5, along with $\lambda_{s,N}(5\,\mathrm{K}) = 400\,\mathrm{nm}$, $\lambda_{s,FM} = 5\,\mathrm{nm}$, and $P_{FM} = 45\%$.

6.2 Novel Ferromagnets for Lateral Spin Valves

The role of diffusive spin-transport through FM/N interfaces has the potential to be investigated further by utilizing FMs with low Curie temperatures T_c or high FM spin-polarizations P_{FM}. The temperature dependencies of α_{FM} and $\lambda_{s,FM}$ have been studied, as discussed in §4.4.3, although modifying $P_{FM}(T)$ significantly could aid our understanding of the role of each parameter in determining ΔR_{NL}. The differences among the temperature dependencies of the transport properties of the different FMs was understood in terms of the Bloch $T^{3/2}$ law. For example, Py was found to have a stronger temperature dependence then Co. The temperature dependence of P_{FM} is expected to be even greater for FMs for which T_c is within, or close to, the measurement temperature range. FM materials with low and variable T_c should allow the effect of $P_{FM}(T)$ on $\Delta R_{NL}(T)$ to be better understood.

6.2.1 Cu_xNi_{1-x}

The T_c of copper-nickel alloys, Cu_xNi_{1-x}, can be altered from the bulk value $T_c = 630\,K$ of Ni down to 0 K near $x = 0.6$. Cu-Ni alloys have T_c reduced below that of the FMs used in this work, $T_c = 730\,K$ for Py and $T_c = 1400\,K$ for Co. The temperature dependence of the polarization in the latter two cases is expected to be much weaker for $T \leq 300\,K$ than for Cu_xNi_{1-x}.

The initial work to prepare thin films of Cu_xNi_{1-x} alloys of various Ni concentrations x has been undertaken. Depositing materials from the electron-beam evaporator (§2.3.2) and the vacuum-furnace source (§C.3) simultaneously, Ni and Cu can be co-deposited. Controlling the rate of each source allows Cu_xNi_{1-x} alloys to be deposited with a desired x.

The deposited thin films were characterized using EDS, GIXR, XRD, and temperature-dependent magnetometry. Using EDS, spectra similar to the example shown in Figure 2.15 were measured, allowing the composition to be determined against standard films of Ni and Cu of the same thickness. Using the standard and sample film spectra, a reliable value of x was found using an analysis similar to that used by Lund [103]. The measured values of T_c and M_s are plotted vs. x determined from EDS, shown in Figure 6.2 for a series of Cu_xNi_{1-x} thin films.

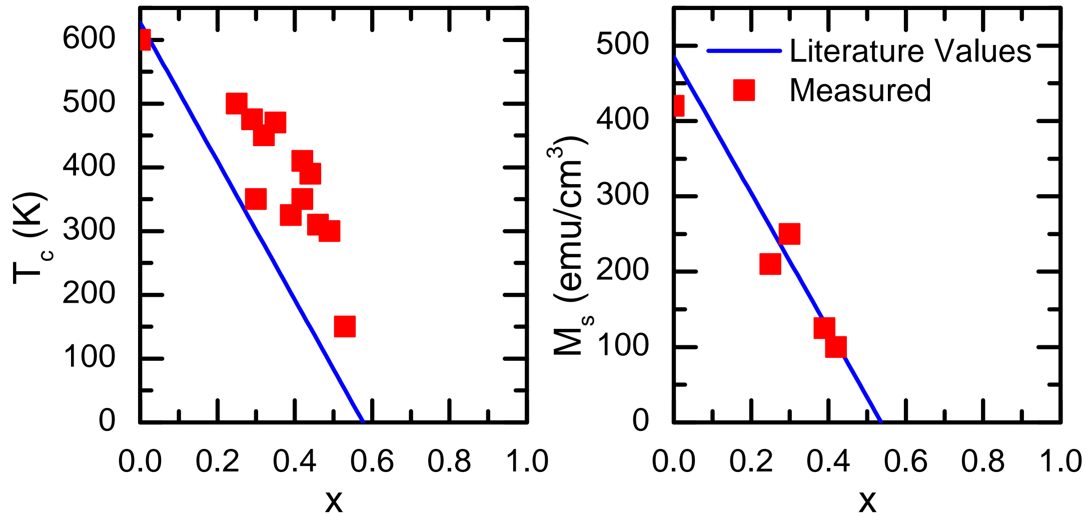

Figure 6.2: (a) T_c and (b) M_s (red squares) as a function of Cu composition x. The blue lines are fits to values reported in the literature [128, 129].

The measured T_c and M_s of $\mathrm{Cu_xNi_{1-x}}$ at $x = 0$ are 600 K and 420 emu/cm^3, respectively. When Cu concentration reaches $x \approx 0.6$, $T_c = 0\,\mathrm{K}$ and $M_s = 0\,\mathrm{emu/cm^3}$. T_c and M_s at intermediate values of x ($0 \leq x \leq 0.6$) lie somewhere between these two limits, following an approximately linear relation. These data are similar to those found elsewhere, for example to the values reported in References [128, 129]. A linear fit based on these references is overlaid on Figure 6.2, shown using a blue line.

The low T_c of Ni and $\mathrm{Cu_{1-x}Ni_x}$ alloys leads to an M_s that changes more than for either Py or Co for $T \leq 300\,\mathrm{K}$. As a result $P_{FM}(T)$ and $\alpha_{FM}(T)$ are also expected to change more dramatically. The effect of the stronger temperature dependence of $P_{FM}(T)$ and $\alpha_{FM}(T)$ on the expected $\Delta R_{NL}(T)$ is shown in Figure 6.3 calculated for transparent and tunnel-barrier interfaces. In order to calculate $\Delta R_{NL}(T)$ in Figure 6.3 $P_{FM}(T)$ and $\alpha_{FM}(T) \propto M_s(T)$ are used with either the tunneling or transparent interface models, Equations 1.67 and 1.63. To understand the differences in each case, devices with tunnel barriers may be needed to determine $P_{FM}(T)$ in addition to transparent interface devices.

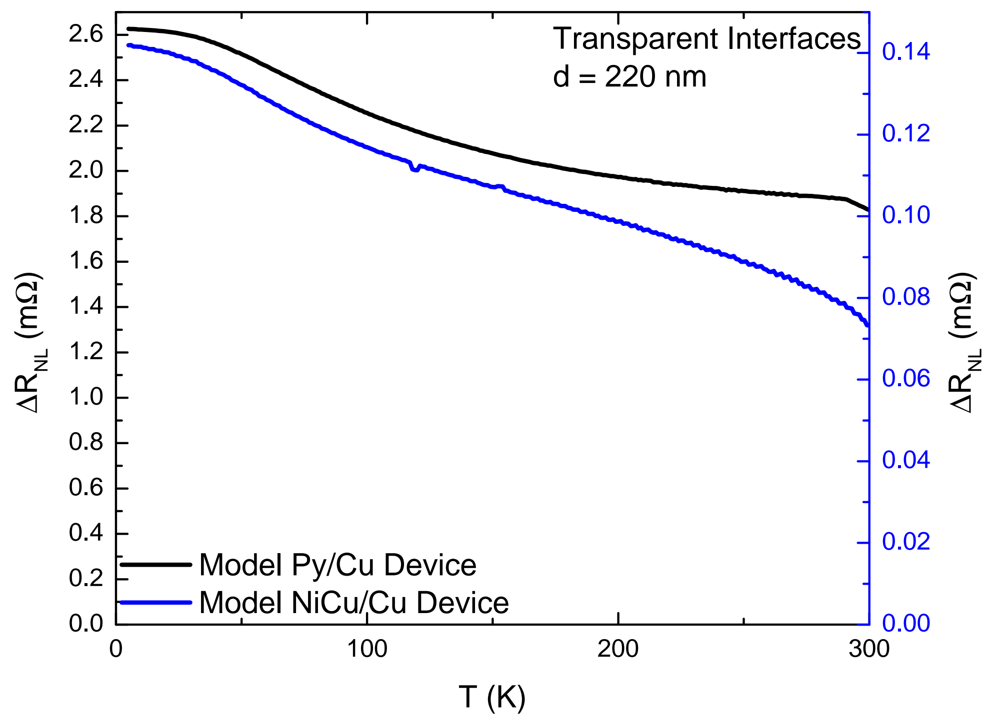

Figure 6.3: Predicted temperature dependence of ΔR_{NL} for a CuNi/Cu lateral NLSV with $d = 220\,\mathrm{nm}$.

6.2.2 Cobalt-Based Disulfides ($CoS_2 - Co_{1-x}Fe_xS_2$)

Another FM system that has the potential to be very interesting for studies of spin transport is $Co_{1-x}Fe_xS_2$ due to the capability of reaching large P_{FM}. The system provides a means for tuning P_{FM} by changing x. This ability to tune P_{FM} would allow the dependence of ΔR_{NL} on P_{FM}, and the related α_{FM}, to be measured and better understood.

Coupled to the change of P_{FM} with x will also be changes of $\rho_{FM}(T)$. $\rho_{FM}(T)$ for these materials has already been measured by Manno *et al* in Reference [130] to be 80 to 450 µΩ cm for films 160 to 180 nm thick with $x = 0.00$ to 0.14, respectively. These films are much thicker, however, than has been used for the FMs fabricated as part of the NLSVs in this work, in which the $t_{FM} = 16$ nm FM layer was deposited first. Manno *et al.* have measured a 30 nm thick film with $x = 0.00$ to have ρ_{FM} that is non-monotonic with T in the range from 400 µΩ cm to 550 µΩ cm for T between 5 K and 300 K. This resistivity is more than an order of magnitude larger than Co or Py.

In collaboration with Manno, patterned Co was sulfidized to create CoS_2 nanowires. The resistivity of a CoS_2 thin film and nanowire is shown in Figure 6.4 as a function of temperature. When patterned into a nanowire, many of the same characteristic features are observed for CoS_2 as have been observed in Reference [130], including the transition at $T_c \approx 122$ K. The very large ρ_{FM} of CoS_2 will play a role in determining ΔR_{NL}, as described in Equations 1.61 – 1.63 for diffusive spin-transport across interfaces. Employing these CoS_2 nanowires as the FM contacts, with either Cu or Al N channels, is in the regime of $R_{s,FM} \gg R_{s,N}$.

The polarization of $Co_{1-x}Fe_xS_2$ alloys has been measured by Wang *et al.* using PCAR [131, 132] who found P_{FM} ranging from 57% to 85% for $x = 0.00$ to 0.15. Little is known, however, about the use of $Co_{1-x}Fe_xS_2$ for spin-injection into metals or semiconductors. Further, the spin diffusion length is unknown for these sulfide-based FM materials. One would expect that $\lambda_{s,FM}$ is less than 10 nm, as with other FMs. Given the very high resistivity of $Co_{1-x}Fe_xS_2$ polycrystalline thin films, $\lambda_{s,FM}$ may be less than 1 nm if the empirical trend of $\lambda_{s,FM}$ to ρ_{FM}^{-1}, given in Equation 4.4, holds. Using the measured Al transport properties, reported in Chapter 4, with $\rho_{FM} = 400$ µΩ cm, $\lambda_{s,FM} \sim 1$ nm, and $P_{FM} = 90\%$ then ΔR_{NL} is expected to be about 150 mΩ using Equation 1.62.

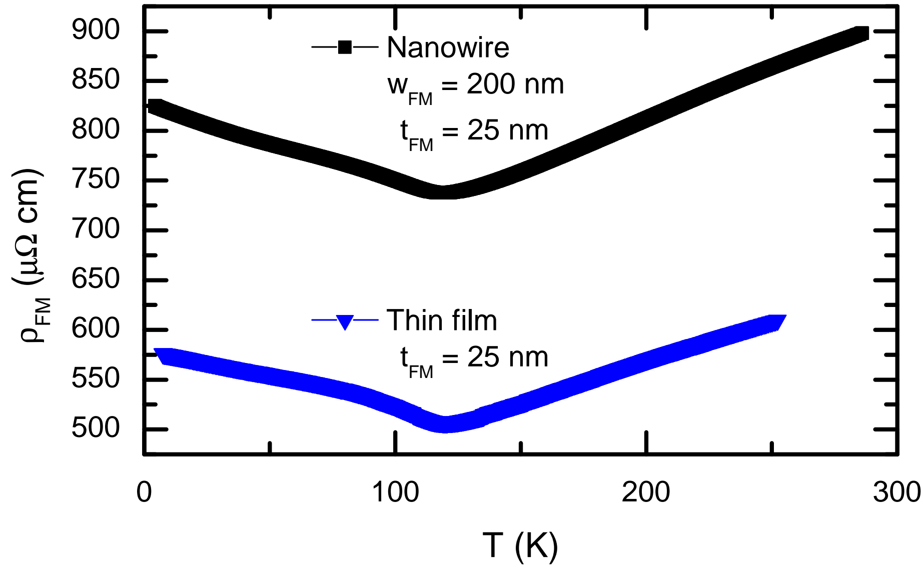

Figure 6.4: Temperature dependence of ρ_{FM} of CoS_2 for $t_{FM} = 25\,\text{nm}$ thin films and $w_{FM} = 200\,\text{nm}$ nanowires.

Preliminary work has been done on the fabrication and measurement of CoS_2/Al NLSVs. The fabrication steps involved are similar to what has been done for other devices in this work except that after patterning and depositing Co nanowires, the Co was removed from the vacuum system, lifted off, and annealed in a sulfur atmosphere at 350 °C for 8 h, as described in Reference [133]. After the sulfidation step, a channel was patterned using EBL across the CoS_2 followed by the deposition of an Al channel. Al was chosen for the N because a separate batch of Al nanowires were exposed to the same sulfur annealing as the Co without showing changes in the measured ρ_N.

An SEM of a completed CoS_2/Al lateral spin valve is shown in Figure 6.5. The CoS_2 FM contacts are labeled in the figure along with the Al transport channel. The Co was deposited on Ti(5 nm)/Au(20 nm) lithographic wires to allow electrical measurements, which are shown at the top of Figure 6.5 with clusters of sulfur resulting from the sulfidation process.

Transport through the device was measured and the CoS_2 FMs showed the proper transition temperature at $T_c \approx 122\,\text{K}$. However, no clear spin-valve signal was observed.

Hysteresis loops measuring the AMR of the FMs show a broad reversal mechanism, leading to the inability to achieve a clear anti-parallel state. This explanation is reinforced by M vs H loops of CoS_2 thin films, which have rounded hysteresis loops. Interfacial I-V measurements also indicate that there may be problems with the transport contributing to the inability to demonstrate spin-injection. There are a few possible solutions to this problem. One possibility is to deposit a soft FM layer to couple to the CoS_2 and improve the squareness of the loop. Another option is to use reactively sputtered CoS_2, which has shown improvements in the squareness of the hysteresis loop. Although

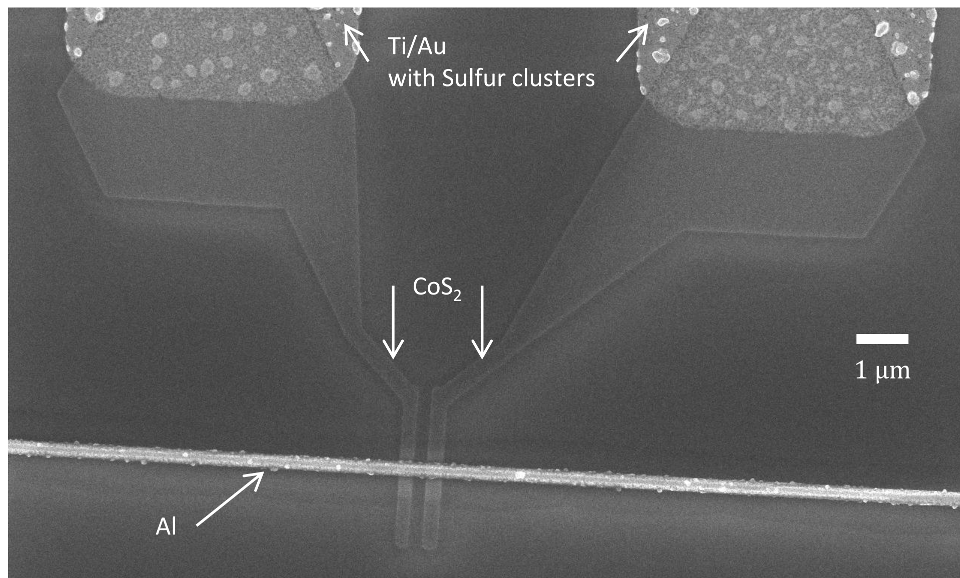

Figure 6.5: SEM micrograph of a CoS_2/Al NLSV. The horizontal Al channel, vertical CoS_2 FM contacts, and the Ti/Al bonding pad vias, with clusters of sulfur on the surface, are labeled.

experimental challenges remain, spin valves with $Co_{1-x}Fe_xS_2$ FMs have the potential to be a fruitful area of research. Measurements of ΔR_{NL} may allow P_{FM} or α_{FM} to be determined, along with $\lambda_{s,FM}$, which would be instrumental for understanding the spin-injection properties of $Co_{1-x}Fe_xS_2$ itself. Electrical injection and detection has not yet been measured in $Co_{1-x}Fe_xS_2$.

6.3 Further Increasing Spin Relaxation at Surfaces

Throughout the work presented in this thesis the influence of spin-relaxation at surfaces on the spin-accumulation in lateral devices has been demonstrated. The enhancement of spin-relaxation at surfaces in as-deposited nanostructures was observed and simulated, as discussed in Chapters 4 and 5. An interesting and useful experiment is to increase the strength of the spin-flip scattering at the boundaries intentionally.

High atomic number Z metals relax spins very quickly. $\lambda_{s,N}$ has been reported in the range of 10 to 63 nm for Au [134, 135], 25 nm for Pd [136], 14 nm for Pt [136], and 5 nm for W [137]. These high-Z materials have the potential to modify the spin relaxation of N metals such as Cu or Al with $\lambda_{s,N}$ of several hundred nm.

Ferromagnetic metals provide another material which can be used to modify the spin-accumulation in N channels. Similar to high-Z materials, FM materials have a short spin diffusion length. $\lambda_{s,FM}$ has been measured both in this work and in a variety of other experiments, some of which were tabulated and shown in Table 1.2. $\lambda_{s,FM}$ is typically ~ 5 nm to 10 nm for transition metal FMs.

Depositing varying amounts of either high-Z or FM materials on the surfaces of the N may lead to much larger spin-flip scattering at surfaces and increase the spin-relaxation rate. It may be possible to completely suppress the slope of $\lambda_{s,N}(T)$ if the surface relaxation is strong enough. This lack of temperature dependence of $\lambda_{s,N}$ has been confirmed by the numerical simulations for large surface relaxation, for probabilities of spin-flip per scattering event that is more than a factor of 100 larger than in the bulk ($p_{\uparrow\downarrow,Sur}/p_{\uparrow\downarrow,Bulk} > 100$). However, this large spin-flip scattering may result in a spin-accumulation too small to measure. Bergmann deposited submonolayers of high-Z metals onto relatively low-Z metal films, such as Al or Mg, to investigate the effect of these high-Z surface layers on spin-orbit scattering [138]. Bergman found that in the case of a Mg thin film, the spin-orbit field increased from 0.0054 T to 0.6 T with the deposition of an Au layer covering 16% of the Mg film [139]. The increase of spin-orbit coupling due to the high-Z or FM metals on the surfaces will likely lead to a similar effect in lateral spin-transport structures.

6.4 Changing the Ferromagnetic - Non-magnetic Interfaces

The insertion of a tunnel barrier between the FM and N will allow the spin-transport properties of the N to be largely separated from those of the FM. Namely, the inclusion of tunnel barriers allows $P_{FM}(T)$ to be determined as described in §6.1. Beyond measuring $P_{FM}(T)$, barriers may be used in additional experiments that can be undertaken to try to understand the temperature dependence of ΔR_{NL} for Py/Cu devices, and in particular the unexplained peak at $T \approx 50\,\mathrm{K}$ for Py/Cu, shown in Figures 4.1 and 4.4. Several efforts have been started to investigate some of the hypothesized origins of this peak, predominantly directed towards investigation of inter-diffusion of the N and FM materials at the interfaces. Annealing of FM/N samples at temperatures up to 400 °C to enhance inter-diffusion of the materials is discussed in §6.4.1. Further, sample films with structures similar to the Py/Cu and Co/Cu devices were measured using polarized neutron reflectivity, the preliminary results are given in §6.4.2.

6.4.1 Experimental Tests of Interdiffusion by Sample Annealing

The spin-transport properties of Py/Cu based NLSVs produced unexpected phenomena, with the behavior of $\Delta R_{NL}(T)$ remaining unexplained. In particular, we hypothesize that the peak near $T = 50\,\mathrm{K}$ is due to a layer forming at the Py/Cu interface with properties of neither Py or Cu. An inter-diffused interfacial layer could take several different forms, with the capability for different magnetic alloys forming at the interfaces to have different effects on the spin transport. These alloys have the potential for low-transition or freezing temperatures that may be capable of leading to a feature near 50 K.

A simple test was conducted by annealing samples at elevated temperature to increase the interdiffusion of Ni, Fe, and Cu. The four-terminal resistivity of Cu devices annealed at $T = 250\,^{\circ}\mathrm{C}$ shows a distinct change compared to that of unannealed devices. The low-temperature $\rho_N(T)$ has an upturn as $T \rightarrow 0\,\mathrm{K}$, shown in Figure 6.6, which could be caused by the interdiffusion of magnetic and non-magnetic materials. The annealed films show a different low-temperature trend compared to the unannealed samples which simply saturate to the impurity-limited resistivity at low temperature,

shown in Figure 6.6

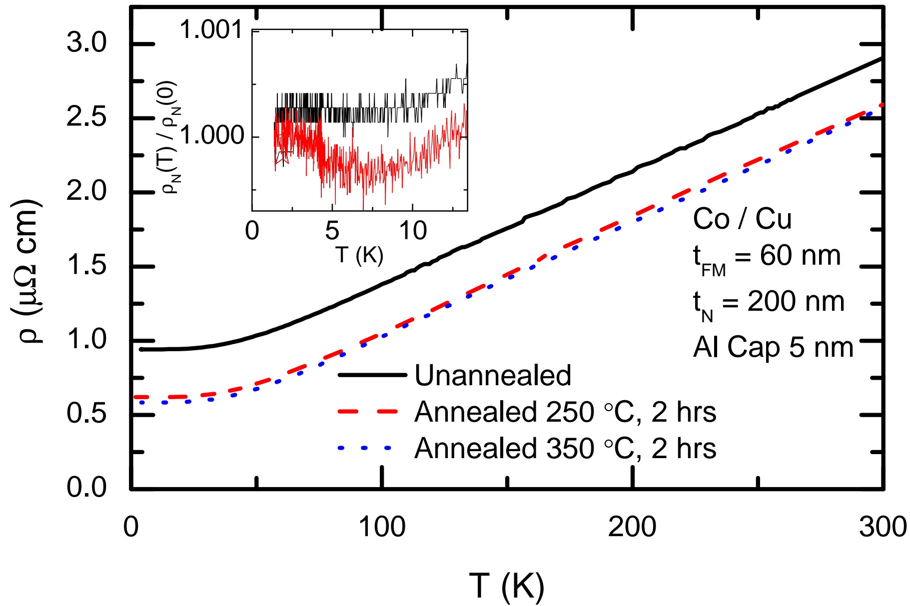

Figure 6.6: Four-terminal measurements of a Cu channel using Co electrodes. Curves are shown for an unannealed device and annealed at $T = 250\,°\mathrm{C}$ and $T = 350\,°\mathrm{C}$ for 2 hour.

The magnitude of ΔR_{NL} was also measured before and after annealing, shown in Figure 6.7. The magnitude before annealing is very similar to the Co/Cu data shown previously in Figure 4.1. The standard interpretation of the reduced resistivity with annealing would be that $\lambda_{s,N}$ will increase and ΔR_{NL} would also increase. Holwever, ΔR_{NL} in fact decreased with the decrease of the resistivity. These observations seem inconsistent, unless the spin-flip scattering was increased by annealing and interdiffusing the FM magerials.

6.4.2 Preliminary Polarized Neutron Reflectivity

Polarized neutron reflectometry (PNR) is one experimental method available to probe the magnetic structure of thin films. In collaboration and as part of this work Liam O'Brien conducted PNR measurements employed to investigate the interfacial magnetic

Anneal Conditions	ρ_{Cu}	RRR
Unannealed	0.94 – 2.91 µΩ cm	3.1
250 °C for 2 h	0.62 – 2.60 µΩ cm	4.2
350 °C for 2 h	0.58 – 2.57 µΩ cm	4.4

Table 6.1: Experimentally determined range of $\rho_{Cu}(T)$ and RRR for Co/Cu samples before and after vacuum annealing at $T = 250\,°\mathrm{C}$ and $350\,°\mathrm{C}$ for 2 h.

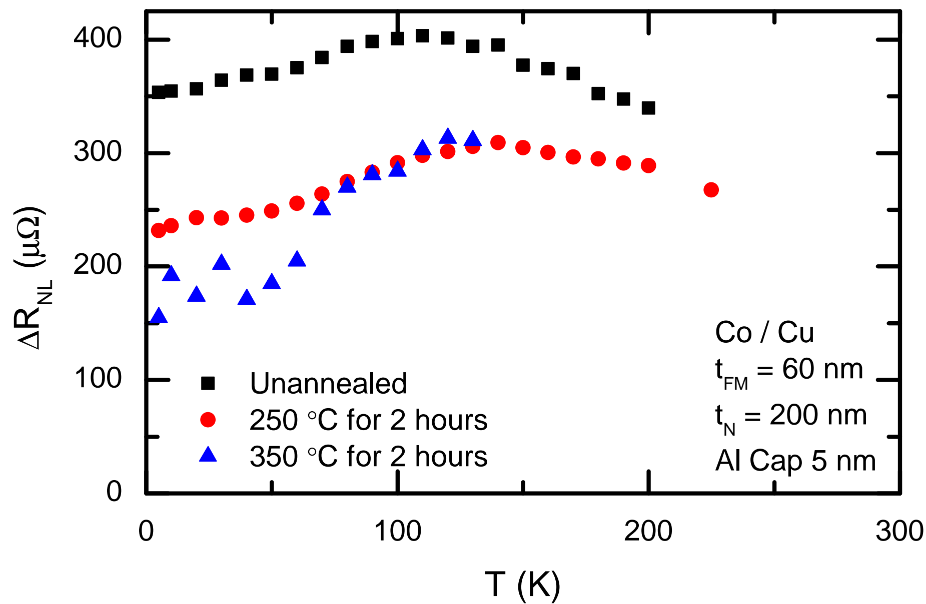

Figure 6.7: The measured ΔR_{NL} vs. T for a Co/Cu device with $d = 220\,\mathrm{nm}$, $t_N = 200\,\mathrm{nm}$, and $t_{FM} = 60\,\mathrm{nm}$. Curves are shown for an unannealed device and after annealing at $T = 250\,°\mathrm{C}$ and $T = 350\,°\mathrm{C}$ for 2 hours.

and chemical properties of FM/N heterostructures. These measurements were done on samples, consisting of either Py or Co FMs with a Cu N layer, that we deposited and characterized with GIXR and SQUID magnetometry.

PNR cannot be used to directly measure a lateral NLSV structure, so comparable films were prepared for this experiment. A FM thin film with nominal thickness $t_{FM} = 16\,\text{nm}$ followed by a Cu layer with thickness $t_N = 100\,\text{nm}$ and an Al cap with thickness $t_{Cap} = 3\,\text{nm}$ were deposited on the same Si/SiN substrates used for the NLSV fabrication. The as-deposited films were then measured along with a Py/Cu sample annealed at $T = 400\,^\circ\text{C}$. PNR was done at the Spallation Neutron Source at $T = 5,\ 50,\ 300\,\text{K}$ under an applied magnetic field of 1 T grazing incidence x-ray measurements were conducted on the same films at ambient temperature, $T = 295\,\text{K}$.

Fitting PNR and GIXR data, such as the example data shown in §2.4.3, using the COREFINE software package has allowed the detailed layer structure to be determined. X-ray reflectivity data were first fit to determine the thickness of each layer. The nominal growth thicknesses are within a factor of 1.06 of the GIXR measured thicknesses. These values, typically determined to a precision of $\pm 2\,\text{Å}$, were used as the chemical depth profile that was used to begin fitting the PNR data. The sample magnetization was determined using SQUID magnetometry. The PNR data in turn yields information about the magnetic depth profile.

The PNR data was fit to extract the magnetic layer profile of these samples. In each case attempts were made to fit the data with the inclusion of an interfacial layer. In the case of Co/Cu and annealed Py/Cu an interfacial layer was found to fit the data. The results of the fitting are shown in Table 6.2. For each of the interlayers, a thickness and roughness were found. For Co/Cu this layer was found to be 0.9 nm and 3.1 nm was found for the annealed Py/Cu sample.

A magnetic interlayer was found for Co/Cu. This was found to have $M_s = 260\,\text{emu/cm}^3$. This value of M_s is consistent with a layer composition of $Co_{0.3}Cu_{0.7}$. The scattering density of the interlayer for the annealed Py/Cu is consistent with a 50/50 mix of Py and Cu.

Layer	ρ_{PNR}	ρ_{PNR} (Bulk)	t	σ_{PNR}	M_s	Bulk $M_s(T = 5\,\mathrm{K})$
			nm	nm	emu/cm^3	emu/cm^3
As-deposited Py/Cu						
Py	8.69	8.69	15	0.6	749	880
Cu	8.21	8.96	94.3	1.6	0	0
Al_2O_3	3.97	3.97	3	2.9	0	0
As-deposited Co/Cu						
Co	8.9	8.9	15.1	0.5	1374	1440
Co (30%) Cu(70%)	8.9	8.9	0.9	0.7	260	260
Cu	8.96	8.96	94.2	1.6	0	0
Al2O3	3.27	3.97	3	2.4	0	0
Annealed Py/Cu						
Py	8.69	8.69	14	0.8	588	880
Py(50%) Cu(50%)	8.82	8.82	4.2	3.1	0	0
Cu	8.96	8.96	97.9	1	0	0
Al_2O_3	3.13	3.97	1.3	0.9	0	0

Table 6.2: Grazing-incidence x-ray and polarized neutron reflectometry fitting parameters.

Chapter 7

Conclusion

Non-local spin valves were used to to measure spin-transport properties of ferromagnetic/normal metal heterostructures patterned on 100 nm length scales. Devices were fabricated from Py ($Ni_{.80}Fe_{.20}$) and Co ferromagnets with normal metal channels of Cu and Al. Literature reports of the spin transport in similar devices has led to a wide variety of reported values for the change of non-local resistances ΔR_{NL} due to the spin-valve effect and spin diffusion lengths $\lambda_{s,N}$ in each of the materials. Due to the variety of values reported in the literature for the same materials, as discussed in §1.3, details of the fabrication or materials contribute to determining the device behavior. Despite some measurements of these materials by others, the measurement of devices fabricated using the same method for each combination is unique to this work. This approach allows comparison of devices that have been prepared as identically as possible which is invaluable for distinguishing the contributions from each material.

The measured $\Delta R_{NL}(T)$ and $\lambda_{s,N}(T)$ for Py/Cu, Co/Cu, Py/Al, and Co/Al were reported in Chapter 4 and are summarized in Table 7.1. ρ_N is reported in the table at $T = 5\,\mathrm{K}$ and $275\,\mathrm{K}$ for each material combination. The change of the non-local resistance between the parallel and antiparallel states ΔR_{NL} is included in the table for devices with the smallest contact separation $d \approx 220\,\mathrm{nm}$ and thickness $t_N = 200\,\mathrm{nm}$. Since the spin transport in devices with diffusive transport across FM/N interfaces depends on the properties of both the FM and N materials, there is no straightforward comparison of the RRR to the ratio of ΔR_{NL} at the same temperatures. In Chapter 4 it was shown that $\Delta R_{NL}(T)$ can be understood qualitatively and quantitatively

with a temperature dependent spin diffusion length of the ferromagnet $\lambda_{s,FM}(T)$ or a temperature-dependent spin-transport asymmetry of the ferromagnet α_{FM} that has a Block $T^{3/2}$ temperature dependence. The experiments here are not capable of distinguishing the temperature dependence of $\lambda_{s,FM}$ and α_{FM} simultaneously.

Fits of ΔR_{NL} as a function of d, using a model that includes diffusive transport across FM/N interfaces, allowed $\lambda_{s,N}(T)$ to be determined. The RRR, which characterizes the temperature dependence of ρ_N, is compared with the ratio of $\lambda_{s,N}$ at the same temperatures to show that bulk spin relaxation alone cannot explain the experimental results. The ratio of each of these quantities is included in the table for comparison.

Material	$\rho_N(5\,\text{K}, 275\,\text{K})$	$\frac{\rho_N(275\,\text{K})}{\rho_N(5\,\text{K})}$
Py/Cu	1.0, 3.1 µΩ cm	3.1
Co/Cu	1.1, 3.2 µΩ cm	2.9
Py/Al	4.2, 7.9 µΩ cm	1.9
Co/Al	4.3, 8.1 µΩ cm	1.9
	$\Delta R_{NL}(5\,\text{K},\ 275\,\text{K})$	$\frac{\Delta R_{NL}(5\,\text{K})}{\Delta R_{NL}(275\,\text{K})}$
Py/Cu	800, 220 nm	3.6
Co/Cu	350, 260 nm	1.3
Py/Al	780, 220 nm	3.5
Co/Al	310, 250 nm	1.2
	$\lambda_{s,N}(275\,\text{K}, 5\,\text{K})$	$\frac{\lambda_{s,N}(5\,\text{K})}{\lambda_{s,N}(275\,\text{K})}$
Py/Cu	290, 390 nm	1.2 (1.3†)
Co/Cu	260, 333 nm	1.3
Py/Al	330, 540 nm	1.6
Co/Al	290, 465 nm	1.5

Table 7.1: The measured ρ_N, ΔR_{NL} for $d = 220\,\text{nm}$, and the fitted $\lambda_{s,N}$ for lateral NLSV devices with transparent interfaces as well as the ratio of each at $T = 5\,\text{K}$ and 275 K.

I have explained these results quantitatively using a numerical model of spin diffusion and relaxation. The simulations include spin relaxation at surfaces which has larger probability of spin-flip for scattering at surfaces than in the interior of the N channel.

The spin lifetime $\tau_{s,N}$ is proportional to the momentum-relaxation time $\tau_{p,N}$, for the Elliot-Yafet mechanism. The constant of proportionality between the two lifetimes is different at the surfaces, which is 30 times larger than it is in the bulk, where the bulk values are obtained from conduction electron spin resonance experiments reported in the literature. The $\Delta R_{NL}(T)$ and $\lambda_{s,N}(T)$ were calculated numerically and reproduce the overall temperature dependence of the experimental data.

The cross sections of the N channels are $250\,\mathrm{nm} \times 200\,\mathrm{nm}$ which is less than the expected $\lambda_{s,N}$ for bulk N materials used in this work. The temperature dependence of $\lambda_{s,N}$ calculated numerically has shown that the enhanced relaxation at surfaces is capable of producing the observed $\lambda_{s,N}(T)$. Further, measurements and simulations showed increased spin diffusion with growing channel thickness t_N. The thickness of the N was varied from 200 nm to 400 nm, and an increase in $\lambda_{s,N}$ for Py/Cu devices was observed to increase from 340 nm to 530 nm at $T = 5\,\mathrm{K}$. $\lambda_{s,N}$ is listed in Table 7.2 for Py/Cu with $t_N = 200\,\mathrm{nm}$, 300 nm, and 400 nm at $T = 5\,\mathrm{K}$, 50 K, and 275 K. The

Py/Cu	$\lambda_{s,N}$		
t_N	5 K	50 K	275 K
200 nm	340 nm	390 nm	290 nm
300 nm	410 nm	440 nm	290 nm
400 nm	530 nm	600 nm	320 nm

Table 7.2: $\lambda_{s,N}$ as determined from fits of ΔR_{NL} vs. d for Py/Cu devices at $T = 5\,\mathrm{K}$, 50 K, and 275 K.

aforementioned numerical calculations where used to show that the overall thickness dependence can be reproduced by including enhanced relaxation at surfaces.

The experimental observations, Valet-Fert modeling, and numerical calculations form a consistent description of the transport in these devices. Throughout this work, a peak at $T \approx 50\,\mathrm{K}$ of ΔR_{NL} was observed for the case of Py contacts with Cu N channels that has not been observed for other materials. Remarkably, this was not observed for any other material combination, despite the properties of the FM and N materials being similar (i.e. Co/Cu or Py/Al). Due to the emergence of this peak for only Py/Cu, we have pursued several possible causes.

The unusual temperature dependence of the Py/Cu devices could be due to an interfacial effect. We have shown, as well as examples in the literature, that dilute alloys of ferromagnetic and normal metals can create materials with magnetic properties that exhibit transition temperatures at low temperatures, on the scale of tens of Kelvin. To further study the temperature dependence of spin injection and relaxation experiments with several relevant alloys, which include Ni with Cu, exhibit ferromagnetism with a tunable Curie temperature. For Ni concentrations above $50\,\% T_c$ is between $0\,\mathrm{K}$ and $600\,\mathrm{K}$. $\mathrm{Ni}_{1-x}\mathrm{Cu}_x$ provides an excellent system to further study the temperature dependence of spin injection. Another possibility is the creation of a thin interfacial layer with a low T_c, and short λ_s that would increase spin relaxation and decrease the effective spin injection as the temperature is lowered below T_c. Fe may also form a diffused interfacial layer with Cu that leads to the $T \approx 50\,\mathrm{K}$ peak. Due to the rapid oxidation of Fe it is even possible for iron oxide to form which would influence spin transport. The groundwork to begin studying each of these effects has been done, as discussed in Chapter 6.

Overall we have systematically studied the temperature dependences of ΔR_{NL} as well as $\lambda_{s,N}$ and $\lambda_{s,FM}$. We have shown that the materials resistivities are central to determining spin transport for devices with diffusive transport across interfaces. We have also shown that the asymmetry of spin transport or $\lambda_{s,FM}$ changes with temperature more rapidly for Py than Co. Most importantly we have shown that each N examined has a weak temperature dependence of the spin diffusion length, which we attribute to enhanced spin relaxation at surfaces. Numerical modeling of the bi-layers shows that surface relaxation can lead to the experimental observations. This provides a unifying picture of the observations made, leaving only the observed peak in the Py/Cu spin valve data unexplained. We have, however, been able to show that this peak is not a property of either Py or Cu alone.

References

[1] G. Binasch, P. Grünberg, F. Saurenbach, and W. Zinn, Physical Review B **39**, 4828 (1989).

[2] M. N. Baibich, J. M. Broto, and A. Fert, Physical Review **61**, 2472 (1988).

[3] M. Julliere, Physics Letters A **54**, 225 (1975).

[4] M. Johnson and R. H. Silsbee, Physical Review B **37**, 5326 (1988).

[5] X. Lou, C. Adelmann, S. Crooker, E. S. Garlid, J. Zhang, K. S. M. Reddy, S. D. Flexner, C. J. Palmstrø m, and P. A. Crowell, Nature Physics **3**, 197 (2007).

[6] G. E. W. Bauer, A. H. MacDonald, and S. Maekawa, Solid State Communications **150**, 459 (2010).

[7] K. Uchida, S. Takahashi, K. Harii, J. Ieda, W. Koshibae, K. Ando, S. Maekawa, and E. Saitoh, Nature **455**, 778 (2008).

[8] C. Chappert, A. Fert, and F. N. Van Dau, Nature materials **6**, 813 (2007).

[9] P. P. Freitas, R. Ferreira, S. Cardoso, and F. Cardoso, Journal of Physics: Condensed Matter **19**, 165221 (2007).

[10] E. Grochowski and R. D. Halem, IBM SYSTEMS JOURNAL **42**, 338 (2003).

[11] N. F. Mott, Proceedings of the Royal Society A: Mathematical, Physical and Engineering Sciences **156**, 368 (1936).

[12] N. F. Mott, Proceedings of the Royal Society A: Mathematical, Physical and Engineering Sciences **153**, 699 (1936).

[13] A. Fert and I. A. Campbell, Physical Review Letters **21**, 1190 (1968).

[14] T. Valet and A. Fert, Physical Review B **48**, 7099 (1993).

[15] P. M. Tedrow, Physical Review B **7** (1973).

[16] J. Parker, S. Watts, P. Ivanov, and P. Xiong, Physical Review Letters **88**, 3 (2002).

[17] I. Galanakis, P. Dederichs, and N. Papanikolaou, Physical Review B **66**, 1 (2002).

[18] R. A. de Groot, F. M. Mueller, P. G. van Engen, and K. H. J. Buschow, Physical Review **50** (1983).

[19] C. Leighton, M. Manno, A. Cady, J. W. Freeland, L. Wang, K. Umemoto, R. M. Wentzcovitch, T. Y. Chen, C. L. Chien, P. L. Kuhns, M. J. R. Hoch, A. P. Reyes, W. G. Moulton, E. D. Dahlberg, J. Checkelsky, and J. Eckert, Journal of physics. Condensed matter : an Institute of Physics journal **19**, 315219 (2007).

[20] A. G. Aronov, Sov. Phys. JETP Lett. **24** (1976).

[21] R. H. Silsbee, Bul. Mag. Res **2** (1980).

[22] M. Johnson and R. H. Silsbee, Physical Review Letters **55**, 1790 (1985).

[23] F. J. Jedema, A. T. Filip, and B. J. van Wees, Nature **410**, 345 (2001).

[24] G. Schmidt, D. Ferrand, L. Molenkamp, A. Filip, and B. van Wees, Physical Review B **62**, R4790 (2000).

[25] A. Fert and H. Jaffrès, Physical Review B **64**, 1 (2001).

[26] P. Drude, Annalen der Physik **1**, 566 (1900).

[27] P. Drude, Annalen der Physik **3**, 369 (1900).

[28] R. E. Hummel, *Electronic Properties of Materials* (Springer, 2001), third edit ed.

[29] J. M. Ziman, *Electrons and Phonons: The Theory of Transport Phenomena in Solids*, Oxford Classic Texts in the Physical Sciences (Oxford University Press, USA, 2001).

[30] S. Datta, *Electronic Transport in Mesoscopic Systems*, Cambridge Studies in Semiconductor Physics and Microelectronic Engineering (Cambridge University Press, 1997).

[31] J. M. Ziman, *Principles of the Theory of Solids* (Cambridge University Press, 1979).

[32] E. Akkermans and G. Montambaux, *Mesoscopic Physics of Electrons and Photons* (Cambridge University Press, 2007).

[33] N. F. Mott, Advances in Physics **13**, 325 (1964).

[34] R. C. O'Handley, *Modern Magnetic Materials: Principles and Applications* (Wiley, 2000).

[35] D. C. Jiles, *Introduction to Magnetism and Magnetic Materials, Second Edition* (Taylor & Francis, 1998).

[36] A. Aharoni, *Introduction to the Theory of Ferromagnetism*, International Series of Monographs on Physics (Oxford University Press, USA, 2001).

[37] P. C. Van Son, H. Van Kempen, and P. Wyder, Physical Review Letters **58**, 2271 (1987).

[38] A. Fert and S. F. Lee, Phys. Rev. B **53**, 6554 (1996).

[39] S. Hershfield and H. L. Zhao, Physical Review B **56**, 3296 (1997).

[40] M. Johnson and R. H. Silsbee, Physical Review B **37**, 5312 (1988).

[41] L. Piraux, S. Dubois, A. Fert, and L. Belliard, The European Physical Journal B **4**, 413 (1998).

[42] T. Kimura, J. Hamrle, and Y. Otani, Physical Review B **72**, 1 (2005).

[43] T. Kimura, T. Sato, and Y. Otani, Physical review letters **100**, 66602 (2008).

[44] F. Casanova, A. Sharoni, M. Erekhinsky, and I. Schuller, Physical Review B **79**, 1 (2009).

[45] M. Erekhinsky, A. Sharoni, F. Casanova, and I. K. Schuller, Applied Physics Letters **96**, 022513 (2010).

[46] R. J. Elliott, Physical Review **96**, 266 (1954).

[47] Y. Yafet, *Solid State Physics*, vol. 14 (Academic, New York, 1963).

[48] J. Fabian and S. D. Sarma, Journal of Vacuum Science & Technology B: Microelectronics and Nanometer Structures **17**, 1708 (1999).

[49] N. W. Ashcroft and N. D. Mermin, *Solid State Physics* (Thomson Learning, Inc., 1976), 2nd ed.

[50] F. Beuneu and P. Monod, Physical Review B **18**, 2422 (1978).

[51] P. Monod and F. Beuneu, Physical Review B **19**, 911 (1979).

[52] D. Lubzens, M. R. Shanabarger, and S. Schultz, Physical Review Letters **29** (1972).

[53] F. Beuneu and P. Monod, Physical Review B **13** (1976).

[54] S. LaShell, B. McDougall, and E. Jensen, Physical review letters **77**, 3419 (1996).

[55] E. Rotenberg, J. Chung, and S. Kevan, Physical Review Letters **82**, 4066 (1999).

[56] Y. Koroteev, G. Bihlmayer, J. Gayone, E. Chulkov, S. Blügel, P. Echenique, and P. Hofmann, Physical Review Letters **93**, 1 (2004).

[57] T. Hirahara, T. Nagao, I. Matsuda, G. Bihlmayer, E. Chulkov, Y. Koroteev, P. Echenique, M. Saito, and S. Hasegawa, Physical Review Letters **97**, 10 (2006).

[58] K. P. McKenna and G. J. Morgan, The European Physical Journal B-Condensed **456**, 451 (2007).

[59] G. Mihajlović, J. E. Pearson, S. D. Bader, and A. Hoffmann, Physical Review Letters **104**, 1 (2010).

[60] P. M. Tedrow and R. Meservey, Physical Review B **7**, 318 (1973).

[61] D. Paraskevopoulos and R. Meservey, Physica B+ C pp. 1201–1202 (1977).

[62] R. J. J. Soulen, J. M. Byers, M. S. Osofsky, B. Nadgorny, T. Ambrose, S. F. Cheng, P. R. Broussard, C. T. Tanaka, J. Nowak, J. S. Moodera, A. Barry, and J. M. D. Coey, Science **282**, 85 (1998).

[63] D. J. Monsma and S. S. P. Parkin, Applied Physics Letters **77**, 720 (2000).

[64] C. Shang, J. Nowak, R. Jansen, and J. Moodera, Physical Review B **58**, R2917 (1998).

[65] D. Scholl, M. Donath, D. Mauri, and E. Kay, Physical Review B **43**, 309 (1991).

[66] J. Bass and W. P. Pratt, Journal of Physics: Condensed Matter **19**, 183201 (2007).

[67] S. Dubois, L. Piraux, J. M. George, K. Ounadjela, J. L. Duvail, and A. Fert, Physical Review B **60**, 477 (1999).

[68] A. C. Reilly, W. Park, R. Slater, B. Ouaglal, R. Loloee, W. P. Pratt Jr., and J. Bass, Journal of Magnetism and Magnetic Materials **195**, L269 (1999).

[69] C. E. Moreau, I. C. Moraru, N. O. Birge, and W. P. Pratt, Applied Physics Letters **90**, 012101 (2007).

[70] A. C. Reilly, W.-C. Chiang, and W. Park, Magnetics, IEEE **34**, 939 (1998).

[71] R. Godfrey and M. Johnson, Physical Review Letters **96**, 1 (2006).

[72] D. Bozec, Ph.d. thesis, University of Leeds (2000).

[73] C. E. Moreau, I. C. Moraru, N. O. Birge, and W. P. Pratt, Applied Physics Letters **90**, 012101 (2007).

[74] L. Piraux, S. Dubois, and A. Fert, Journal of magnetism and magnetic materials **159**, L287 (1996).

[75] B. Doudin, A. Blondel, and J. P. Ansermet, Journal of Applied Physics **79**, 6090 (1996).

[76] F. Jedema, M. Nijboer, A. Filip, and B. J. van Wees, Physical Review B **67**, 085319 (2003).

[77] F. Albert, N. Emley, E. Myers, D. Ralph, and R. Buhrman, Physical Review Letters **89**, 1 (2002).

[78] T. Kimura, J. Hamrle, Y. Otani, K. Tsukagoshi, and Y. Aoyagi, Applied Physics Letters **85**, 3795 (2004).

[79] S. Takahashi, H. Imamura, and S. Maekawa, *Concepts in Spin Electronics* (Oxford University Press, Oxford, 2006).

[80] S. Garzon, I. Žutić, and R. Webb, Physical Review Letters **94**, 1 (2005).

[81] Y. Ji, A. Hoffmann, J. E. Pearson, and S. D. Bader, Applied Physics Letters **88**, 052509 (2006).

[82] Y. Ji, A. Hoffmann, J. S. Jiang, J. E. Pearson, and S. D. Bader, Journal of Physics D: Applied Physics **40**, 1280 (2007).

[83] MicroChem, *NANO PMMA and Copolymer Datasheet* (2001).

[84] Electronic Materials, *CD-26 Material Safety Data Sheet* (2004).

[85] G. West, *Resist O_2 Ash Rates* (2007).

[86] D. Lide, *CRC Handbook of Chemistry and Physics* (CRC Press, 2004), 85th ed.

[87] A. Aharoni, Journal of Applied Physics **83**, 3432 (1998).

[88] B. Hausmanns, T. Krome, G. Dumpich, E. Wassermann, D. Hinzke, U. Nowak, and K. Usadel, Journal of Magnetism and Magnetic Materials **240**, 297 (2002).

[89] M. S. Lund and C. Leighton, Journal of Vacuum Science Technology A: Vacuum, Surfaces, and Films **22**, 2027 (2004).

[90] MicroChem, *NANO PMGI Resists Datasheet* (2002).

[91] B. D. Cullity, *Elements of X-ray Diffraction* (Prentice Hall, 2001), 3rd ed.

[92] V. K. Pecharsky and P. Y. Zavalij, *Fundamentals of Powder Diffraction and Structural Characterization of Materials* (Kluwer Academic, 2003).

[93] M. Bikholz, *Thin Film Analysis by X-ray Scattering* (Wiley, 2006).

[94] G. Hölzer, M. Fritsch, M. Deutsch, J. Härtwig, and E. Förster, Physical Review A **56**, 4554 (1997).

[95] H. Kiessig, Annalen der Physik **402**, 769 (1931).

[96] L. G. Parratt, Physical Review **95** (1954).

[97] K. Stoev and K. Sakurai, The Rigaku Journal **14** (1997).

[98] PANalytical B.V., *X-Ray Reflectivity Software* (2012).

[99] G. P. Felcher, Journal of Applied Physics **87** (2000).

[100] H. Zabel and K. Theis-Brohl, Journal of Physics: Condensed Matter **15** (2003).

[101] M. Fitzsimmons, P. Yashar, C. Leighton, I. K. Schuller, J. Nogués, C. Majkrzak, and J. Dura, Physical Review Letters **84**, 3986 (2000).

[102] J. Goldstein, *Scanning Electron Microscopy and X-Ray Microanalysis* (Kluwer Academic/Plenum Publishers, 2003).

[103] M. S. Lund, Ph.d thesis, University of Minnesota (2006).

[104] G. Binnig, C. F. Quate, and C. Gerber, Physical review letters **56** (1986).

[105] M. Abrecht, A. Adare, and J. W. Ekin, The Review of Scientific Instruments **78**, 046104 (2007).

[106] J. W. Ekin, *Experimental Techniques for Low-Temperature Measurements: Cryostat Design, Material Properties, And Superconductor Critical-Current Testing* (Oxford University Press, 2006).

[107] P. Horowitz and W. Hill, *The Art of Electronics* (Cambridge University Press, Cambridge, 1989), 2nd ed.

[108] T. Sun, B. Yao, A. Warren, K. Barmak, M. Toney, R. Peale, and K. Coffey, Physical Review B **79**, 1 (2009).

[109] J. W. C. De Vries, Thin Solid Films **167**, 25 (1988).

[110] W. Steinhogl, G. Schindler, G. Steinlesberger, M. Traving, and M. Engelhardt, Journal of Applied Physics **97**, 023706 (2005).

[111] M. Johnson, Journal of Physics: Condensed Matter **19**, 165215 (2007).

[112] M. Viret, I. Auneau, and J. M. D. Coey, Journal of Magnetism and Magnetic Materials **140-144**, 683 (1995).

[113] R. M. Bozorth, Physical Review **70** (1946).

[114] F. Bakker, A. Slachter, J. P. Adam, and B. van Wees, Physical Review Letters **105**, 1 (2010).

[115] A. Slachter, F. L. Bakker, and B. J. van Wees, Physical Review B **84**, 1 (2011).

[116] F. J. Jedema, H. B. Heersche, A. T. Filip, J. J. A. Baselmans, and B. J. van Wees, Nature **416**, 713 (2002).

[117] S. O. Valenzuela and M. Tinkham, Nature **442**, 176 (2006).

[118] Y. Fukuma, L. Wang, H. Idzuchi, S. Takahashi, S. Maekawa, and Y. Otani, Nature materials **10**, 527 (2011).

[119] L. Bocklage, J. M. Scholtyssek, U. Merkt, and G. Meier, Journal of Applied Physics **101**, 09J512 (2007).

[120] A. T. McCallum and M. Johnson, Nano letters **9**, 2350 (2009).

[121] S. Maekawa, *Concepts in Spin Electronics* (Oxford University Press, 2006).

[122] Y. Ji, A. Hoffmann, J. E. Pearson, and S. D. Bader, Applied Physics Letters **88**, 052509 (2006).

[123] D. Mauri, D. Scholl, H. Siegmann, and E. Kay, Phys. Rev. Lett. **6**, 758 (1988).

[124] D. Pierce, R. Celotta, J. Unguris, and H. Siegmann, Physical Review B **26** (1982).

[125] J. Mathon and S. Ahmad, Physical Review B (1988).

[126] D. Mills and A. Maradudin, Journal of Physics and Chemistry of Solids **28**, 1855 (1967).

[127] G. Mihajlović, S. I. Erlingsson, K. Výborný, J. E. Pearson, S. D. Bader, and A. Hoffmann, Physical Review B **84**, 2 (2011).

[128] J. Sousa, M. Chaves, M. Pinheiro, and R. Pinto, Journal of Low Temperature Physics **18**, 125 (1975).

[129] C. Robbins, H. Claus, and P. Beck, Physical Review Letters **22**, 1307 (1969).

[130] M. Manno, R. Frakie, B. Bolon, and C. Leighton, Applied Physics Letters **95**, 182510 (2009).

[131] L. Wang, K. Umemoto, R. M. Wentzcovitch, T. Y. Chen, C. L. Chien, J. G. Checkelsky, J. C. Eckert, E. D. Dahlberg, and C. Leighton, Physical Review Letters **94**, 1 (2005).

[132] C. Leighton, M. Manno, A. Cady, J. W. Freeland, L. Wang, K. Umemoto, R. M. Wentzcovitch, T. Y. Chen, C. L. Chien, P. L. Kuhns, M. J. R. Hoch, a. P. Reyes, W. G. Moulton, E. D. Dahlberg, J. Checkelsky, and J. Eckert, Journal of Physics: Condensed Matter **19**, 315219 (2007).

[133] M. Manno, R. Frakie, and C. Leighton, Journal of Applied Physics **105**, 093912 (2009).

[134] G. Bergmann, Zeitschrift für Physik B Condensed Matter **48**, 5 (1982).

[135] Y. Ji, A. Hoffmann, J. S. Jiang, and S. D. Bader, Applied Physics Letters **85**, 6218 (2004).

[136] H. Kurt, R. Loloee, K. Eid, W. P. Pratt, and J. Bass, Applied Physics Letters **81**, 4787 (2002).

[137] W. Park, D. V. Baxter, S. Steenwyk, I. Moraru, W. P. Pratt, and J. Bass, Physical Review B **62**, 1178 (2000).

[138] G. Bergmann, Physics Reports **107**, 1 (1984).

[139] G. Bergmann, Physical Review Letters **48**, 1046 (1982).

[140] MicroChem, *T Thinner Material Safety Data Sheet* (2001).

[141] Karl Suss, *MA6 Contact Aligner Specifications* (2007).

[142] MicroChem, *Nano Remover PG Datasheet* (2001).

[143] M. Ohring, *Materials Science of Thin Films* (Academic Press, San Diego, 2002), 2nd ed.

[144] Luxel Corporation, *Radak Furnace Product Datasheet* (2011).

[145] C. S. Lu and O. Lewis, Journal of Applied Physics **43**, 4385 (1972).

[146] C. S. Lu, Journal of Vacuum Science and Technology (1975).

[147] LakeShore, *Sensor Characteristics* (2008).

Appendix A

Glossary and Acronyms

Some commonly used terms, abbreviations, and symbol definitions are included for reference in this appendix.

A.1 Glossary

- **Coulomb** ($\vec{F} = k_e \frac{q_1 q_2}{r^2} \hat{r}$) – Electrostatic interaction between point charges which is proportional to the product of the electric charges, q_1 and q_2, and inversely proportional to the square of the separation between them $\vec{r}$.

- **Cryostat** – An apparatus for maintaining low (cryogenic) temperature of samples or devices.

- **Density of States** (**DOS**) – This describes the number of states per unit energy that may be occupied by electrons.

- **Ferromagnet** (**FM**) – Ferromagnetic material that, due to the exchange splitting of the spin-resolved density of states, is spin polarized at the Fermi level.

- **Lithography** – In micro- and nano-electronic fabrication, the process comprises exposing and developing a polymer resist to pattern features to create structures.

- **Lorentz Force** ($\vec{F} = q(\vec{v} \times \vec{b})$) – Lorentz force is the force on a point charge moving through an electric and magnetic field. A particle with charge q moving with velocity v in an electric field $\vec{E}$ and a magnetic field $\vec{B}$ a force $\vec{F}$ will result.

- **Normal Metal (N)** – Normal metal that has the same density of states for spin-up and spin-down bands which is non-ferromagnetic.

- **Ohm's Law** ($\vec{j}_e = \sigma\vec{E}$) – Expression for the charge current density $\vec{j}_e$ that is directly proportional to the electric field $\vec{E}$ by the conductivity σ. Can be written in terms of the voltage drop V, charge current J_e, and resistance R as $V = J_e R$.

- **Permalloy (Py)** – Ferromagnetic alloy of nickel and iron with a typical composition of around $Ni_{0.80}Fe_{0.20}$ with high magnetic permeability and low coercivity and low magnetostriction.

- **Transparent Interface** – Low resistance interface between two materials for which the transport is diffusive. In the context of spin transport, the case where the spin resistance of the materials R_s is larger than the interfacial resistance R_I ($R_{s,N} > R_I$, $R_{s,FM} > R_I$).

- **Zeeman Energy** ($-\vec{\mu} \cdot \vec{B}$) – Energy due to the interaction of a dipole with an applied field. Typically this is a magnetic interaction that takes the form of the inner product of the dipole moment $\vec{\mu}$ with the applied field $\vec{B}$.

A.2 Symbols

Table A.1: Symbols

Symbol	Definition
$\hbar$	Reduced Planck constant or Dirac constant, $h/2\pi$
α_{EY}	Ratio of momentum to spin-flip scattering times, τ_p/τ_s
α_{FM}	Polarization of the spin current or the spin asymmetry of the spin-up and -down electrons in a ferromagnet
β_x	Attenuation coefficient for grazing-incidence x-ray reflectivity
χ_m^{SI}	Magnetic suceptability
χ_r^2	Reduced chi-squared
ΔE_B	Average energy separation to the adjacent band

Continued on next page

Table A.1 – continued from previous page

Symbol	Definition
γ	Gyromagnetic ratio
ϵ	Energy
ϵ_0	Permittivity of vacuum
ϵ_F	Fermi energy
κ_{therm}	Thermal conductivity
λ_e	Wavelength of exposing light or electrons
λ_g	Mean free path for a gas
λ_i	Wavelength of probe beam, such as neutrons or x-rays
λ_{SO}	Spin-orbit coupling constant
$\lambda_{s,FM}$	Spin diffusion length of ferromagnet
$\lambda_{s,N}$	Spin diffusion length of non-magnetic metal
μ	Electro-chemical potential
$\mu_{\uparrow(\downarrow)}$	Spin-up(-down) electro-chemical potential
μ_f	Shear modulus of deposited film
μ_n	Neutron magnetic moment
μ_q	Shear modulus of quartz
η_{BSE}	Probability of electron backscatter
ρ_{FM}	Electrical resistivity of the ferromagnet
ρ_N	Electrical resistivity of the non-magnetic metal
ρ_f	Mass density of deposited film
ρ_q	Mass density of quartz crystal
θ_c	Critical angle of grazing-incidence x-ray reflectivity measurements
θ_d	Angle of deposition source relative to the substrate normal
θ_f	Angle of reflected beam to the sample plane in reflectivity experiments
θ_i	Angle of incident beam to the sample plane in reflectivity experiments
θ_L	Spin precession angle
τ_{Bake}	Resist bake time

Continued on next page

Table A.1 – continued from previous page

Symbol	Definition
τ_p	Momentum scattering time
τ_s	Spin-lifetime
σ	Carrier conductivity, the conductivity in the spin-up $\sigma_\uparrow$ and spin-down $\sigma_\downarrow$ bands separately
ω_L	Larmor precession frequency
$\vec{B}$	Magnetic induction or magnetic flux density (magnetic field in vacuum)
$\vec{B}_{\parallel(\perp)}$	Magnetic induction in(out of) the sample plane
$\vec{B}_j$	Magnetic induction in the j$^{\text{th}}$ layer, used in polarized neutron reflectivity analysis
b_j^{mag}	Magnetic nuclear scattering length density of the j$^{\text{th}}$ layer
b_j^{nuc}	Nuclear scattering length density of the j$^{\text{th}}$ layer
c	Speed of light
D	Diffusion constant
d	Separation between the injector and detector electrodes on a transport device
d_g	Diameter of gas particles
d_{ss}	Distance between the deposition source and substrate
E	Electric field
e	Electron charge
$f(\vec{r},\vec{k},t)$	Distribution function describing the probability of finding an electron at a position $\vec{r}$, momentum $\hbar\vec{k}$, and at time t
f_q	Resonant frequency of a quartz crystal slab
f_T	Resonant frequency of the crystal and deposited film
g	Electron g-factor
$g(\epsilon)$	Density of states, often used at the Fermi energy $g(\epsilon_F)$. Can be separated into the density of states for spin-up $g_\uparrow(\epsilon)$ and -down $g_\downarrow(\epsilon)$ electrons.
H_{SOC}	Hamiltonian for the spin-orbit interaction

Continued on next page

Table A.1 – continued from previous page

Symbol	Definition
h	Plank's constant
H_c	Coercive magnetic field
I_{Emis}	Ion gauge cathode emission current
I_{Ion}	Ion current flowing to collector of an ion gauge
J_e	Charge current
J_s	Spin current, the spin-up $J_\uparrow$ and spin-down $J_\downarrow$ can be written separately
j_e	Charge current density
j_s	Spin current density, can be separated in the spin-up $\uparrow$ and spin-down $\downarrow$ components
k_B	Boltzmann constant
$\vec{k_i}$	Wavevector of incident probe beam
$\vec{k_f}$	Wavevector of reflected beam
K_{VG}	Sensitivity of vacuum gauge
l_{FM}	Length of ferromagnetic contact
M	Magnetization
M_s	Saturation magnetization
m	Mass, usually describing the electron mass
m_n	Neutron mass
$N(\epsilon_F)$	Density of states at the Fermi level
N_A	Avogadro's number
N_{at}	Frequency constant of AT-cut Quartz crystal
$N_{FM,l}$	Demagnetization factor along length of ferromagnet
$N_{FM,w}$	Demagnetization factor along width of ferromagnet
N_j	Atomic density of the j$^{\text{th}}$ layer
NA	Numerical aperture
n	number density, typically referring to the number density of carriers
p_e	Electron momentum

Continued on next page

Table A.1 – continued from previous page

Symbol	Definition
P_{FM}	Polarization of ferromagnet
P_g	Pressure of a gas
P_W	Joule heating power
$\vec{q}$	Difference between incident and reflected wavevectors, $\vec{k_f} - \vec{k_i}$
R	Electrical resistance
$R_{\uparrow\uparrow(\uparrow\downarrow)}$	Electrical resistance with the ferromagnetic layers parallel(antiparallel)
R_{Dev}	Resist develop rate
R_I	Interfacial resistance
R_{NL}	Non-local transresistance which is the detector voltage divided by injector current (V_{NL}/I_e)
R_s	Spin resistance ($\rho\lambda_s/A$)
$\vec{r}$	Spatial position
$\vec{S}$	Magnitude and orientation of the electron spin polarization
T	Temperature
T_{Bake}	Resist bake temperature
TF	Tooling factor, subscripts i and f denote values before and after calibration, respectively
T_g	Glass-transition temperature
t	Time
t_B	Bottom layer thickness of a resist bi-layer
t_{FM}	Thickness of ferromagnetic contact
t_N	Thickness of normal metal layer or channel
t_T	Top layer thickness of a resist bi-layer
U_j	Effective potential for neutron scattering
V_a	Anode voltage applied to accelerate electrons
V_e	Anode voltage used to accelerate electrons for electron beam evaporation
v	Velocity

Continued on next page

Table A.1 – continued from previous page

Symbol	Definition
v_F	Fermi velocity
w_{FM}	Width of ferromagnetic contact
y_F	Maximum lithographic feature size for which features will not be deposited on a substrate from θ_d
$\hat{z}$	Out-of-plane Cartesian coordinate
Z	Atomic number
Z_q	Acoustic impedance ratio of Quartz crystal and deposited film

A.3 Acronyms

Table A.2: Acronyms

Acronym	Meaning
AC	Alternating Current
AFM	Atomic Force Microscopy
AMR	Anisotropic Magneto-Resistance
CIP-GMR	Current in-plane giant magneto resistance
CPP-GMR	Current perpendicular to the plane giant magneto resistance
DC	Direct Current
DI H_2O	Deionized Water, or alternatively simply DI
DOS	Density of States
EBL	Electron Beam Lithography
EBSD	Electron Back Scatter Detector
EDS	Energy Dispersive X-ray Spectroscopy (also known as EDX, XEDS)
ESR	Electron Spin Resonance
FM	Ferromagnet
GIXR	Grazing Incidence X-Ray Reflectivity

Continued on next page

Table A.2 – continued from previous page

Acronym	Meaning
GMR	Giant Magneto-Resistance
IPA	Isopropanol
LNL	Lateral non-local
LNLSV	Lateral Non-Local Spin Valve
MeOH	Methanol
MTJ	Magnetic tunnel junction
N	Normal Metal
NLSV	Non-Local Spin Valve
NMP	N-methylpyrrolidone
PCAR	Point contact Andreev reflection
PNR	Polarized Neutron Reflectivity
RF	Radio Frequency
SDD	Silicon Drift Detector
SEI	Secondary Electron Imaging
SEM	Scanning Electron Microscopy
SNS	Spallation Neutron Source
SPM	Scanning Probe Microscopy
TMAH	Tetramethylammonium hydroxide
TMR	Tunneling Magneto-Resistance
TSC	Spin tunneling into superconducting strips
UHV	Ultra-high vacuum

Appendix B

Device Fabrication Recipes and Technical Information

This appendix contains recipes and information about the technical details used for device fabrication.

B.1 Resist and Process Information

The devices discussed in this thesis were fabricated utilizing a lift-off style technique. The steps of the general patterning and deposition scheme for lift-off type processes is depicted in Figure B.1. Throughout this section, the steps of this lift-off technique are explained with some relevant background information. Figure B.1 depicts the resist that is initially spun out on a substrate to a desired thickness shown in panel (a). The resist is exposed using a beam of electrons, which is rastered over the substrate to pattern the desired features. The exposed regions are depicted by a darkening of the resist in Figure B.1(b). For most lift-off processes a bilayer resist stack is the best choice. In the case of a resist bilayer, with the appropriate combination of resists, the two layers can be developed independently. The top layer can be developed first, shown in Figure B.1(c), followed by the second layer which may be developed further to create a large undercut, depicted in panel (d). Materials may then be vacuum deposited, shown in (e), with the excess materials removed by stripping the resist leaving only the desired structure on the substrate (f).

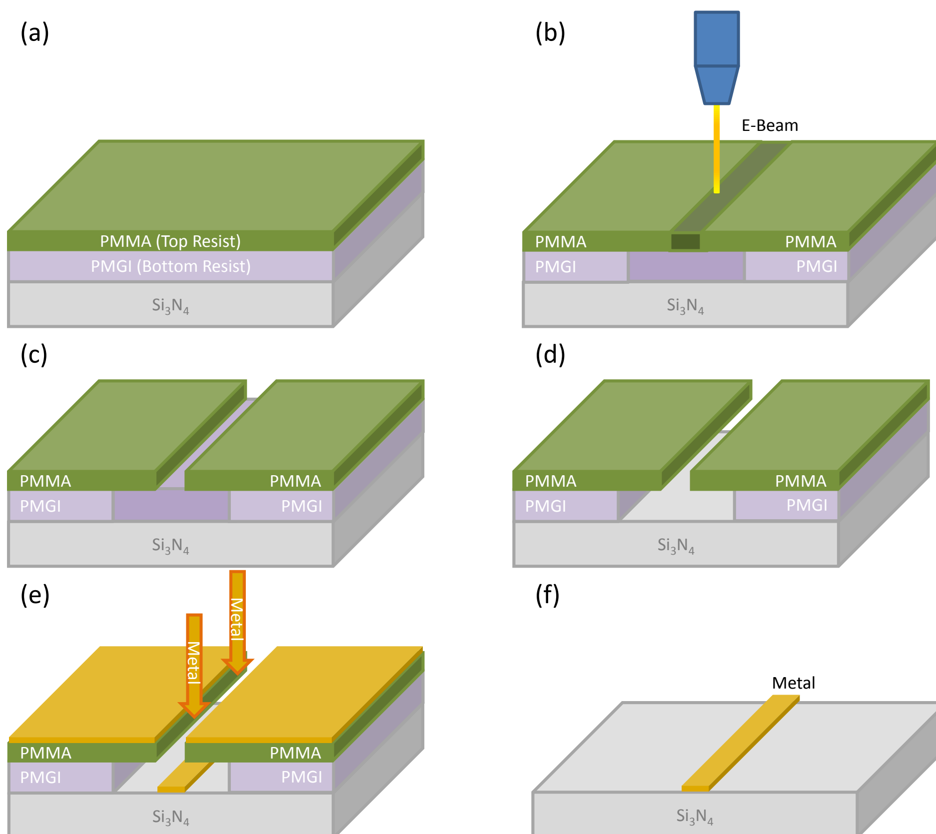

Figure B.1: Depiction of general steps of electron beam lithography liftoff process.

B.1.1 Resists

In this work many resists were explored to create lateral spin valves, some of the recipes that were developed can be found in §B.4 and §B.5. Resist bilayers composed of two different molecular weight polymethyl methacrylate (PMMA) positive resist layers were used to create and control undercut to create nanostructures that are not discussed in this work. For this double PMMA layer method a molecular weight of 495k is used as the underlayer and 950k as the overlayer which is exposed similarly to that of the recipe in §B.5. Other fabrication methods that were explored to create non-local spin valves use negative resists, such as NEB-31, to provide etch masks for top down style processing.

For the devices discussed in this thesis the resist bilayer is composed of a poly-dimethylglutarimide polymer (PMGI) underlayer with a PMMA layer on top. This combination of resists allow the undercut to be controlled due to selective development of each layer with different chemicals. Developers remove exposed positive resist; MIBK is used to develop PMMA and CD-26 is used for PMGI while minimizing the removal of the other resist. These developers are discussed in more detail in §B.1.3.

The thicknesses of each resist layer are set by the angular speed used to spin coat the substrate. The thickness also depends on the concentration of PMGI or PMMA in the solvents used with each resist, Nano™ T Thinner and Anisole, respectively. Nano™ T Thinner is a Micro-Chem proprietary solvent composed of cyclopentanone (80-90 %) and tetrahydrafurfuryl alcohol (10-20 %) [140]. In this work the concentrations used were PMGI-SF9 (9 %) and PMMA-A6 (6 %) with a molecular weight of 950000.

The substrate was loaded onto the spinner head prior to adding resist. The resist was placed on the substrate, which was at room temperature, with a clean eyedropper. To determine the spin speed required to achieve the desired thickness several 20 mm × 20 mm Si substrates were spun at various speeds and the thicknesses was measured using a Rudolph ellipsometer and/or a DekTak 3030 profilometer. The dependence of the measured resist thickness on spin speed is shown in Figure B.2. Once the required spin speed required to achieve the desired thickness was determined, this speed would be used for future substrates and checked periodically to ensure properties of the resist or spinner calibration had not changed.

For each of these polymer resists a bake is required to remove the solvent which

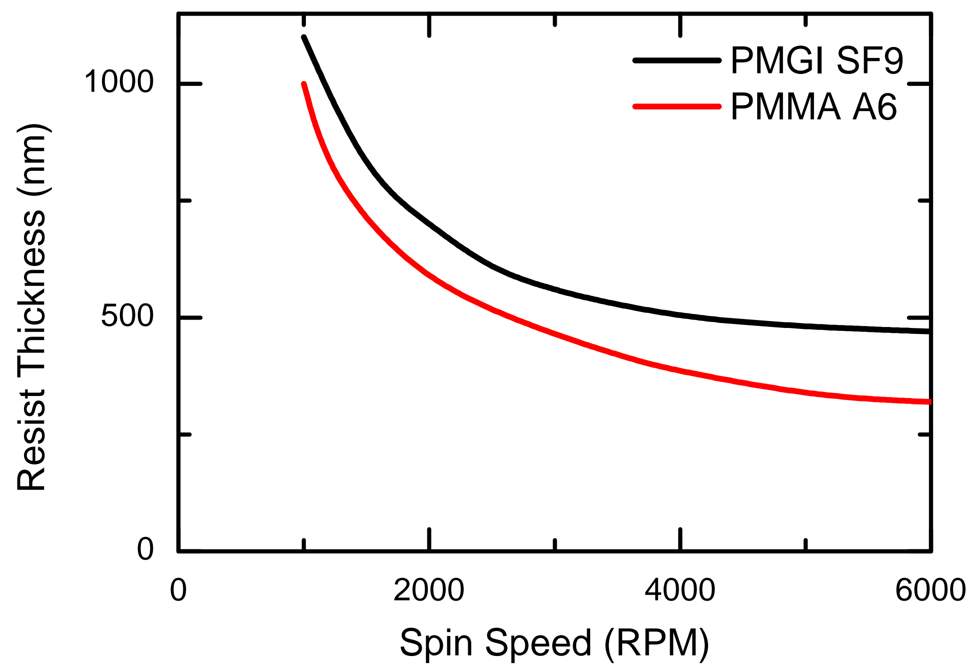

Figure B.2: Resist thickness as a function of angular spin speed for PMMA-A6 and PMGI-SF9 measured on 20 mm × 20 mm substrates by profilometry.

can have similar temperatures and durations. Typical pre-exposure bake temperatures required to remove solvent from PMGI are 150 °C – 190 °C [90] and 180 °C [83] for PMMA. The bake duration and temperature affects the develop rate post-exposure. Adjusting the bake time and/or temperature may help control the undercut of the resist underlayer in order to achieve the desired results. For PMGI the typical undercut rate R_{Dev} in nm/s quoted by the manufacturer [90] is given by:

$$R_{Dev} = -T_{Bake}\frac{\text{nm}}{\text{s}\,^{\circ}\text{C}} + \left(215.56\ \frac{\text{nm}}{\text{s}}\right), \tag{B.1}$$

$$R_{Dev} = -\left(0.0208\ \frac{\text{nm}}{\text{s}^2}\right)\tau_{Bake} + 46.25\ \frac{\text{nm}}{\text{s}}, \tag{B.2}$$

where T_{Bake} is the bake temperature in °C and τ_{Bake} is the bake time. Both T_{Bake} and τ_{Bake} can be varied to manipulate R_{Dev} and are critical to maintain consistency for sensitive develop processes such as those used in this work.

B.1.2 Exposure

The process used for optical lithography exposes regions of resist not shadowed from light by a mask plate in contact with the resist. This class of techniques has the advantage of being able to expose entire regions simultaneously, minimizing the time required to pattern features. Although optical exposures are used extensively in elaborate stepper configurations, which are able to reach feature sizes below 100 nm, in this work standard contact mode ultra-violet optical exposure lithography was used to define larger features. Patterns such as electrical interconnects that allow electrical measurement equipment to be connected to the smaller features of devices were defined using optical lithography.

The photolithography exposures were done using a Karl Suss MA 6 or MA 6/BA 6 Contact Aligner. The aligners use an x-y micrometer controlled stage to position a resist coated substrate under a glass photomask with chrome features. Visual inspection of the alignment is done using microscope optics satisfying a tolerance of 0.5 µm. Both contact aligners can be used for front-side alignment but the MA 6/BA 6 allows backside alignment as well. After alignment the sample substrate is brought into contact with the mask using one of three modes. Soft contact is used to apply slight mechanical pressure to hold the mask plate to the substrate and can achieve a line resolution ≈ 2 µm. Hard contact can be used to reduce the linewidth to ≈ 1 µm by applying mechanical and pneumatic pressure to achieve contact. Finally, a LowVac mode can be used wherein

vacuum can be used to evacuate the gap between the substrate and mask to reduce the gap to reach a line width of $\approx 0.8\,\mu m$. Both aligners use a UV400 Lamp at 350 W with a composition of spectral lines at wavelengths of 436 (g-line), 405 (h-line), 365 (i-line), 335, and 313 nm to expose resist with a total intensity of $12.0 \pm 0.1\,\mathrm{mW\,cm^{-2}}$ [141].

Optical methods are generally unable to reach the minimum feature size required for these experiments. Use of the short wavelength of electron beams employed in EBL solves this problem by allowing features with dimensions down to ≈ 10 nm to be created. The resolution of the system can be estimated from the Rayleigh criterion,

$$\ell_{Res} \approx \frac{0.61\lambda_e}{NA}, \tag{B.3}$$

where λ_e is the wavelength of the exposing light or electrons, and NA is the numerical aperture. The wavelength of electrons can be expressed by the de Broglie relation,

$$\lambda_e = \frac{h}{p_e}, \tag{B.4}$$

where h is Plank's constant and p_e is the momentum of the electrons. The non relativistic momentum $p_e = m_e v_e$ can be substituted such that $\lambda_e = \frac{h}{2mE}$. For electron energies $30 - 100$ keV Equation B.4 and the non-relativistic electron momentum yields electron wavelengths of 7.1 - 3.9 pm or 7.0 - 3.7 pm if the relativistic momentum is used. The wavelength of these electrons is very short compared to the UV light typically used in traditional photolithography (365 - 436 nm) and are therefore capable of much higher resolution.

Electron beam systems require the beam to be rastered across the resist, sequentially exposing the pattern to be written. This process has greater resolution than optical methods but has the drawback of being far more time consuming. In serial techniques, such as EBL, the time required to expose a pattern scales with the area exposed requiring between seconds and days for typical patterns. Parallel optical techniques typically require ≈ 5 s to completely expose an entire substrate. The exposed resist is depicted in Figure B.1(b) as a darkening of the resist. For some resists, such as PMMA, large exposed areas can be observed optically prior to developing the resist.

The bulk of the lithography work contained in this work was done using a Raith 150 EBL system. This used a LEO/Zeiss scanning electron microscope (SEM) with additional stage leveling and beam control electronics to adapt if for lithography work. The

electron beam voltages available for this system were similar to that of a typical SEM, 1 – 30 keV. Standard positive resists, such as PMMA, require dosages of approximately 300 µC cm^{-2} for electron beams in this energy range. Although the Raith 150 system is capable of the resolution required to make operational structures, this hybrid machine is much less stable and reliable than purpose built systems.

Towards the conclusion of this work a new purpose built 100 keV EBL system was made available and this fabrication process was adapted for the new system. Due to the higher energy electrons used in this case two significant differences emerge. At higher voltages the energy deposited into a fixed volume of resist by the incident electrons is reduced, effecting the sensitivity of the resist to the electrons. Increasing the electron energy from 30 keV to 100 keV requires an increase of the dosage from approximately 300 to 900 µC cm^{-2}. For a fixed beam current the exposure will take three times longer. This increase to the dosage and exposure time can be compensated for by generating larger electron beam currents. The second effect of the higher electron beam energy is that the exposure through the resist depth is confined and provides a more columnar profile. The lower voltage beams will deposit more energy near the bottom of the resist stack and as a result the exposure tends to broaden laterally. This effect makes it difficult to create small features using thick resist stacks at low beam energies.

B.1.3 Developing

Once exposed, the resist is developed using a wet chemical process. This requires immersing the resist in a developer bath for a specified duration followed by immersion in a stop bath, which is typically deionized water (DI H_2O) or isopropanol (IPA). In the case of the positive resists employed here, developing removes the exposed resist. A bilayer resist stack, with the appropriate choice of resists and developer selectivity, allows only the top resist layer to be developed by the first develop step as shown in Figure B.1(c). A second step using the bottom layer developer removes the exposed bottom layer. Due to the ability to independently develop each layer, the bottom layer can be developed beyond that of the top layer, as shown in Figure B.1(d), creating an undercut which is necessary for liftoff type processes. This undercut is crucial for processes requiring deposition at angles away from normal incidence.

PMMA/PMGI bi-layers can be developed selectively using the aforementioned process. PMMA is developed here using methyl isobutyl ketone (MIBK) in IPA at a volumetric ratio of 1:3, at room temperature, for high resolution feature development [83]. Here IPA is used to stop the develop, but DI H_2O can also be used. The sample is blow dried with N_2 gas then the PMGI underlayer is developed using Microposit® MF® CD-26 Developer in IPA. CD-26 is a propriety developer formulation based on tetramethylammonium hydroxide (TMAH), 2.4%, and water [84]. Although ratios of CD-26:IPA of 1:3 are typically used elsewhere, the process developed for this work requires strict control of the undercut rate, so a ratio of 1:30 is used.

The substrate surface needs to be descummed prior to materials deposition. This descumming process is used to increase adhesion to the substrate surfaces by removing residual resist that has not been removed during the develop process. This is accomplished by a short reactive ion etch which destroys resist using energetic oxygen ions that then create carbon oxides which can easily be pumped away by a vacuum pump. An oxygen plasma barrel etcher was used which achieves resist removal rates of ~ 120 Å/min [85]. Typically this etch is done for 10 s – 20 s at pressures up to a Torr and at applied radiofrequency power up to 200 W, removing $\lesssim 40$ Åof resist thickness. The details of the ash step can be found in §B.4 – §B.5.

B.1.4 Deposition

The substrate with the exposed and developed resist pattern can now be deposited on. Deposition is accomplished by a physical vapor deposition process such as evaporation or magnetron sputtering. In this work electron beam evaporation was used primarily and is discussed in greater detail in §C.2 as part of a discussion of the vacuum deposition system used §2.3.

The evaporation process involves heating a source material in a vacuum chamber with a beam of high-energy electrons. As the source material is heated it will begin to evaporate, or depending on material, may sublimate with the evaporated atoms condensing on the substrate placed in the path of the flux from the source. The deposition of material, metals in this case, on the patterned substrate is depicted in Figure B.1(e). Evaporation techniques are employed due to the directional deposition allowing clearly defined shadows of the top resist layer to be formed on the substrate. The use of more

omni-directional techniques, such as sputtering, can lead to diffuse edges or sidewall deposition on the resist which leads to "fencing" or "ears" on the edges of the features.

B.1.5 Liftoff

The final step in the process is to liftoff the excess metal deposited on the resist. This is accomplished by immersion of the sample in organic solvents. The solvent strips the resist and along with it the materials on the resist. For standard photoresists this is often done with acetone. However, for some liftoff resists acetone is ineffective and solvents such as N-methylpyrrolidone (NMP) or Micro-Chem Nano® PG-Remover (a proprietary NMP based stripper [142]) are used. Due to the relatively low vapor pressure of NMP based liftoff solvents, 9.5 Torr at 80 °C for NMP compared to 1520 Torr for Acetone [86], elevated temperatures up to 80 °C may be used to accelerate the liftoff process. Agitation of the liftoff solvent in a sonicator may also be used to speed up the process. The nanoscopic features patterned in EBL, however, may be damaged by the sonication process. A less aggressive technique is employed in this work for EBL, using an eyedropper to gently move the solvent past the piece to be lifted off. This can reduce the liftoff time significantly while avoiding damage to the structures. After removal from the solvent bath and rinsed with MeOH and IPA, only the desired structure remains which corresponds to the original patterning of the resist shown in Figure B.1(f).

B.2 Design Considerations

B.2.1 Pattern Design Requirements

An exposure pattern that satisfies the design requirements is shown in Figure B.3. The shaded regions are exposed to form openings in a resist mask suspended above the substrate, the deposition conducted as in §2.2.2. The N nanowire is along $\hat{\mathbf{x}}$, while the FMs are deposited through the small patterns running vertically along $\hat{\mathbf{y}}$, on either side of the N channel. These FM regions do not abut the N such that the deposition of the FM materials at an angle relative to the substrate will extend across the N channel and break the FM material making isolated rectangular regions. Alternatively, the unpatterned region adjacent to the FMs will prevent N material from being deposited

on the FM. N material deposited in this location would short the device due to current running through N, rather than FM, contacts into the N channel.

The technique discussed generates shadow masked features of the N material directly below the patterned mask, shown in Figure B.3. The FM is shifted by an amount determined by the resist thickness and the deposition angles. For the resist and angle used in this work ($\theta_d \approx 50°$) the N will be deposited in the blue shaded regions and the FM will be projected along positive $\hat{\mathbf{y}}$ and deposited in the red shaded areas as seen in Figure B.4.

Further, using the geometry described by Equation 2.1 for material deposited at $\theta_d = 50°$ and $t_T = 300\,\text{nm}$, the flux will not be make it through the mask if the feature size is less than 350 nm in the $\hat{\mathbf{y}}$ direction. Six micro-wires interconnect the spin-transport devices to the bonding pads allowing the device to be connected to measurement equipment. There are connections made at either end of the N channel, and connections to each end of the FM contacts to facilitate the measurement of FM/N interfacial resistances.

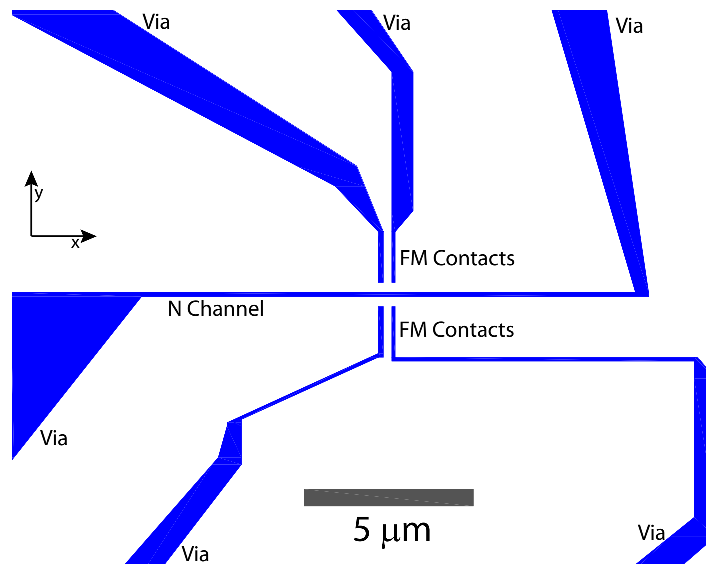

Figure B.3: Layout of a non-local spin valve pattern for shadow evaporation with the N channel horizontal along the x-axis and the FM contacts vertical along the y-axis each flaring out to larger regions interconnecting bonding pads.

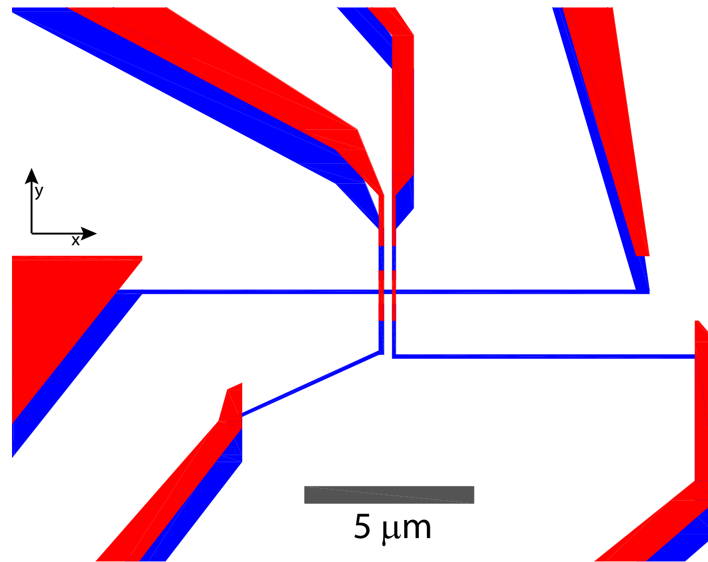

Figure B.4: Layout of a non-local spin valve for shadow evaporation including the projection of the FM deposited at an angle (red) and the area to be patterned (blue).

B.3 Electron Beam Exposure Dosage: The Proximity Effect

Due to interactions of the electron beam with the resist and substrate, electrons are scattered into the nearby resist. Regions near the pattern, therefore, receive exposure as well. There are two main effects, the first is forward scattering of electrons in the resist stack. The angle of forward scattering is typically very small and therefore the exposure of nearby areas is limited to 10 nm. Electrons that pass into the substrate can be backscattered back into the resist from collisions with the heavier substrate atoms. This can happen over a broad angular distribution and leads to exposure of neighboring resist up to 10 µm.

These radial proximity effects are typically modeled using a two-gaussian form,

$$PSF(r) = \frac{1}{\pi\left(1+\eta_e\right)}\left[\frac{1}{\alpha_e^2}e^{-\frac{r^2}{\alpha_e^2}} + \frac{\eta_e}{\beta_e^2}e^{-\frac{r^2}{\beta_e^2}}\right] \tag{B.5}$$

where r is the in-plane distance from the incident electron beam, α_e and β_e are the gaussian widths due to the contributions of forward- and back-scattered electrons respectively, and η_e is a scaling factor for the electron backscattering which is close to 1.

The resist density and thickness will be the predominant factors determining α_e. β_e is determined mainly by the density and atomic number of the substrate materials, where heavier elements scatter more strongly. These scattering mechanisms depend on beam energy as well as affect the parameters in Equation B.5. Analytic calculations of these numbers exist, but in this case Monte Carlo simulations of electrons scattering in the resist and substrate were used to estimate these values, which are given in §B.5.

The dosages calculated after proximity correction are represented using a color plot with warm and cool tones for higher and lower dosages, respectively. An example plot is shown in Figure B.5 with increasing magnification for panels B.5(a)-(c).

B.4 Photolithography Recipes

The following is the recipe for doing the photolithography required to make structures such as interconnects and bonding pads. The recipe has been used to create patterns but some parameters may need to be tweaked for particular patterns or depositions.

B.4.1 Spin Resist

1. Clean substrate. Rinse with Acetone, MeOH, IPA, and blow dry clean dry nitrogen gas.

   Bake at 115 °C for at least60 s

2. Spin HMDS at 4000 RPM for 45 s

3. Spin LOR3A at 2000 RPM for 45 s

   Bake 160 °C for 5 min

4. Spin 1813 at 4000 RPM for 45 s

   Bake at 105 °C for 60 s

Edge Bead Removal

Necessary for highest resolution $< 3\,\mu m$. The bead removal can be accomplished by exposing and developing only the substrate edges.

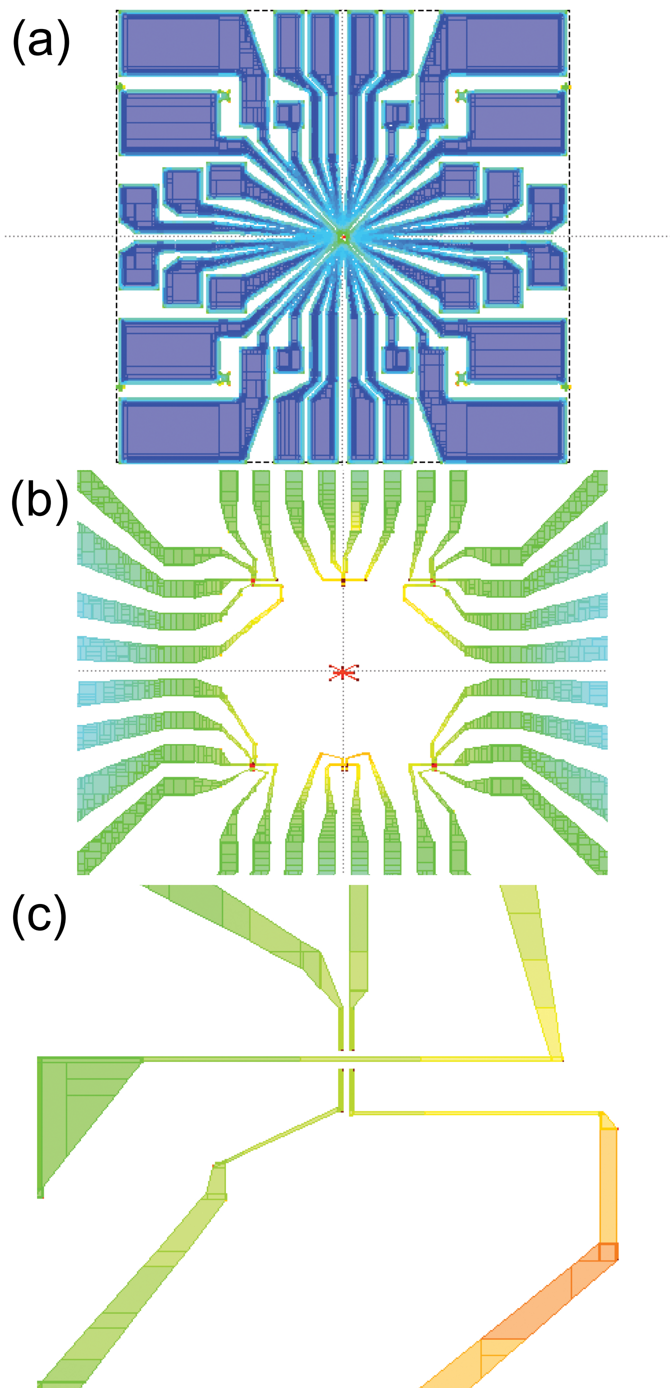

Figure B.5: Electron exposure dose for lateral non-local spin valve structures with higher dosages shown as warm colors, lower dose as colder.

B.4.2 Expose

- Use blank dummy wafer and a drop of of DI-H_2O between sample piece and dummy wafer to hold pieces in the contact aligner (prefer to use the MABA-6).
- Use Hard Contact with an alignment gap of 35 µm.
- Expose 5.3 s (may vary with mask type, feature size, source intensity, and poor mask contact)

B.4.3 Develop and Ash

1. 351:DI H_2O (1:5) for 15 – 18 s *

   Stop develop in DI H_2O for 60 s

   Dry with N_2 gun

   Hotplate bake 6 min on blank Si wafer at 140 °C.

2. Develop in CD-26 for 53-55 s (time may vary with mask type, feature size, source intensity, and poor mask contact)

   Stop develop in DI $H-2O$ for 180 s

   Dry with N_2 gun.

   Bake on bare Si at 120 °C on substrate for 150 s

3. Kapton tape pieces on glass slides and put in cleaned O_2 Asher

4. Ash for 30 s with 200 sccm at 200 W for 30 s

5. Remove and place in evaporator for metalization.

B.4.4 Metalization

Deposit in high vacuum evaporation system. Currently either Temescal or CHA systems in the Nano Fabrication Center.

Deposit 50 Åof Ti at 1.0 Å/s $P_{Base} \approx 5.0 \times 10^{-6}$ Torr		
	Start	End
Pressure	1.6×10^{-6} Torr	1.4×10^{-6} Torr
Power	13%	13.1%

Deposit 185 Åof Au at 1.0 Å/s $P_{Base} \approx 2.5 \times 10^{-6}$ Torr		
	Start	End
Pressure	4×10^{-6} Torr	6×10^{-6} Torr
Power	12%	12%

Table B.1: Deposition conditions and evaporation rates for photolithographic Ti/Au contacts.

B.5 e-Beam Lithography Recipes

Shadow Deposition Liftoff Bilayer

Make sure sample has all previous resist removed and has been cleaned prior to spinning new resist. May even require a short O_2 ashing step.

B.5.1 Spin Resist

Using Headway spinner and hotplates:

1. Spin PMGI-SF9 at 3200 RPM for 60 s

    Bake on hotplate for 20 min at 150 °C

    Bake on hotplate for 5 min at 180 °C

2. Spin PMMA-A6 at 5100 RPM for 60 s

    Bake on hotplate for 20 min at 180 °C

B.5.2 Expose

Exposure dosages will vary, typically 950 µC cm^{-2} is required for the patterns described in 2.2.3. Typical parameters for the proximity exposure correction for Equation B.5

used here are: $\beta_{Prox} = 33.3003\,\mu\text{m}$, $\alpha_{Prox} = 0.0118\,\mu\text{m}$, $\eta_{Prox} = 0.6137$.

B.5.3 Develop

1. MIBK:IPA (1:3) for 25 s

   Stop develop in IPA for 60 s

2. CD26:IPA (1:30) for 35 s (with the Vistec we have had to go up to 70 s for a large undercut).

   Stop develop in IPA for 60 s

B.5.4 DeScum

- Run barrel etcher for 2 to 5 min at 150 W to clean out previous users residue.
- Descum sample on glass dish at 100 W, 225 sccms for 20 s.
- Remove for deposition.

B.5.5 Deposit

Deposit FM material at $\approx 50°$ tilt angle relative to source. Tilt to 0° and deposit N material.

B.5.6 Liftoff

Liftoff in NMP (or PG Remover) at 80 °C for 20 – 60 min. Rinse with Acetone, MeOH, IPA then blow dry with N_2.

Appendix C

Vacuum Systems and Evaporation Equipment

This appendix contains information regarding the vacuum equipment used for deposition of samples as well as relevant background information about the basic operation of the apparatus used.

C.1 Ultra-High Vacuum Deposition System

The apparatus used to reach ultra-high vacuum (UHV) is a deposition system capable of molecular beam epitaxy (MBE) and is referred to as such. This homemade system is capable of achieving pressures less than 10×10^{-11} Torr and has been described in a previous configuration by Lund and Leighton in Reference [89]. These extremely low pressures are possible due to a metal sealed, extremely clean vacuum system made from electropolished stainless steel. Rather than using rubber gaskets, Viton or Buna-N are typically used in high vacuum applications, to make the seals between stainless steel parts metal gaskets are used instead. ConFlat® flanges are a good example of a system that uses metal gaskets. These seals employ knife edges that cut into both sides of a metal gasket, typically Cu but other soft metals such as Al are used, as the components are tightened together, forming a seal which is composed entirely of metals. Care must be taken to keep even minute levels of contamination from entering the system. Avoiding contamination from organics, such as oils and greases, is critical to maintaining UHV

within the system.

The main chamber of the system is composed of a custom 12” diameter UHV vacuum vessel manufactured by MDC. A Thermionics Ion Pump is attached via 12” Wheeler flanges with an isolation poppet valve between the main vessel and the ion pump. A load lock is attached to the side of the system which facilitates the loading of substrates up to 1” in diameter onto a manipulation stage, with XYZ and rotational positioning, inside the main vacuum chamber. Transfers from the load lock to the main chamber are done via a magnetically coupled transfer arm through a gate valve so that loading samples does not require breaking vacuum of the main chamber. The manipulator that the sample is loaded onto is capable of heating samples to 1000 °C. The load lock is isolated from the main system using an MDC 3500 gate valve. The load lock is separated from atmosphere by a Viton sealed circular door through which the samples can be loaded into the system.

The previous configuration of the load lock system, Reference [89], was altered to enhance the functionality of this deposition system. An add on to the 80/20® support system was made to stiffen the load lock support and prevent torque on the vacuum seals from the addition of equipment. The load lock ion pump was moved from below the load lock to above the load lock along with the addition of a four-way 3³/₈” CF cross. A gate valve was placed between the load lock and load lock ion pump. On the four-way cross a convectron, hot-filament ion gage, and capacatance monometer vacuum gages were installed and isolated via a right angle bonnet valve. The final port of the four-way cross is used to connect a turbo-molecular pump via a conical reducer. The turbo is backed by a rotary vane pump; this combination of pumps is used to rough the system down to pressures less than 1×10^{-6} Torr. At the bottom of the load lock, where the ion pump was located formerly, an ISO flange was installed to allow for an inductive RF plasma source to be installed. A photograph of the loadlock attached to the system is shown in Figure C.1.

The system is equipped by a variety of vacuum pumps, pressure gauges, evaporation sources, quartz crystal thickness monitors, deposition shutters, and reflection high energy electron diffraction (RHEED) system. Discussion and background information regarding the systems utilized in this work are described below.

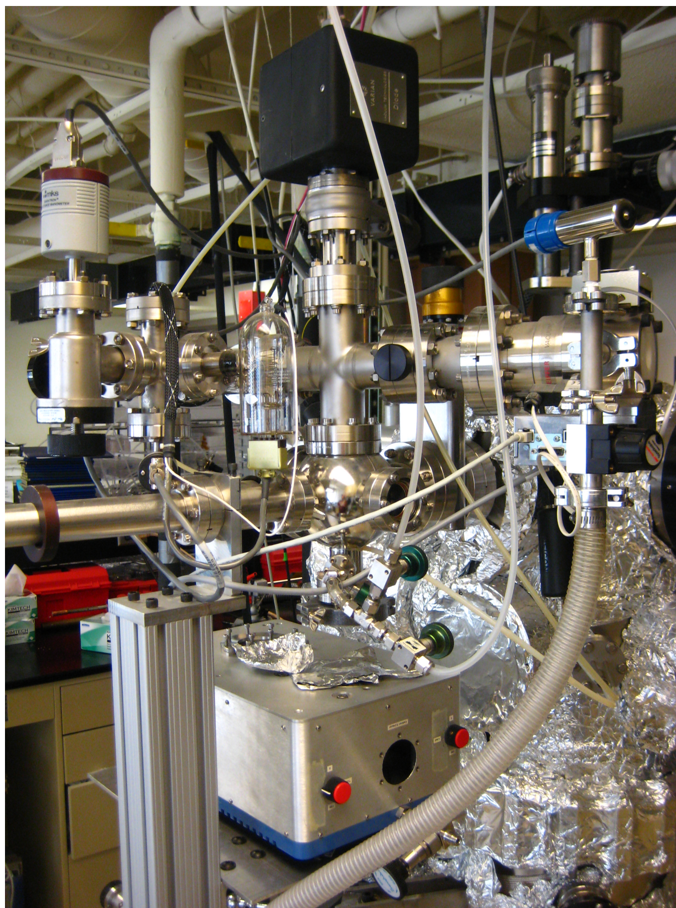

Figure C.1: Photograph of the load lock attached to the system.

C.1.1 Pumping

A pump capable of UHV is necessary to reach the desired pressure for materials deposition. In this work a large sputter-ion pump, or simply referred to as an ion pump, is used in conjunction with a titanium sublimation pump to remove gases from the system. The ion pump is composed of an anode, cathode, and permanent magnets. Although ion pump geometries vary, the anode is typically made of stainless steel with cathode plates made of titanium on either side which serve as gettering material. Under high voltage bias, typically 7 kV supplied by a Thermionics PS-1000 power supply, electrons are emitted from the cathode and take helical paths to the anode due to the applied magnetic field. The increase of path length due to the helical motion improves the chances of collision and ionization of gas in the pump. The ionized gas is accelerated toward the cathode where it will either sputter titanium away depositing a film on nearby surfaces or penetrate many atomic layers deep into the cathode itself and become trapped. Reactive or getterable gas particles will react with the titanium films deposited nearby, trapping them. Discussion of more elaborate ion-pumping designs and operation can be found in Reference [143].

In addition to the Thermionics noble diode ion pump used to pump the main chamber, capable of pumping at a rate of $240\,\mathrm{L\,s^{-1}}$, is a four filament titanium sublimation pump. The sublimation pump uses an electric current of approximately 40 A, sourced from a Thermionics Sublimator Power Supply PS-500, passed through one of the titanium filaments to heat the metal until it sublimates. The sublimated titanium coats the neighboring walls which serves to pump the system by trapping gas molecules. Some of these getterable gases include H_2, N_2, O_2, CO, and CO_2.

The chamber pressure can be reduced through the use of liquid nitrogen cooled surfaces inside the vacuum vessel and the ion pump. These cryo-cooled surfaces consist of stainless steel tubing that extends into the interior of the system which are cooled by flowing liquid nitrogen. Gas molecules condense on the surfaces, effectively removing them from the system. This additional pumping can be very useful in helping to lower the pressure from 1×10^{-9} Torr to less than 1×10^{-10} Torr, especially when outgassing source material which may produce large amounts of residual gas rapidly.

Rough pumping of the chamber down from atmospheric pressure is done by a mechanical diaphragm pump and two cryosorption pumps connected to the vacuum vessel

by an UHV metal sealed in-line valve. The diaphragm pump is capable of pumping the chamber down to 10 Torr. Cryosorption pumps are used to lower the pressure further. Crysorption pumps loaded with zeolite, which is porus and has large surface area, are cooled to 77 K by immersion in liquid nitrogen. Gases will be cooled and condensed as it interacts with the cryogenically cooled zeolite, removing it from the system. This type of pumping can be used to reach intermediate vacuum pressure, $\lesssim 10 \times 10^{-4}$ Torr. Once this level of vacuum has been achieved the main ion pump can begin to be used.

To achieve the lowest possible system pressure, a bake-out is performed at elevated temperature. The system is baked by heating the chamber walls with external heating tapes, controlled by Variacs set to a maximum of 90 V to 95 V, reaching $\approx 110\,^{\circ}$C to aid desorption of gases from the walls. The sample stage is held at a greater temperature, in excess of $200\,^{\circ}$C, for the duration of the bake out. The bake-out is maintained for 5 to 10 days at the maximum allowed temperature. After the bake is finished and the chamber returns to room temperature, then further cooling the cryo panels to 77 K, the system pressure will reach $< 5 \times 10^{-10}$ Torr and continue to fall after the source materials are degassed.

C.1.2 Vacuum Gauges

A hot-filament ionization gauge is used to measure the chamber pressure once the system has been pumped below 10×10^{-5} Torr. Although other vacuum gauges are often used at higher pressures (e.g. a convectron gauge is used during pump down of the vacuum chamber) the hot-cathode ion gauge is best suited for the operational pressures of a UHV chamber down to 1×10^{-11} Torr. This ion gauge is in the hot-cathode Bayard-Alpert configuration inserted directly into the vacuum system; this configuration is referred to as a nude gage. The electrical connections are fed through a vacuum flange, in this case a 2 3/4 inch ConFlat. These gauges are composed of three electrodes configured as a triode with a collector wire, a helical grid, and a loop filament serving as the cathode. A constant electron current is emitted from the heated filament and attracted to the grid which is held at an increased potential of $\approx$ 150 V. The electrons moving from filament to grid collide with local gas molecules ionizing a fraction of them. The ionized molecules move to the collector held at negative potential. The collected ion current is

proportional to the pressure given by

$$P_{gas} = \frac{I_{Ion}}{I_{Emis} K_{VG}}, \tag{C.1}$$

where I_{Ion} is the ion current, I_{Emis} is the emission current, and K_{VG} is the sensitivity of the vacuum gauge which is typically 25 Torr. The vacuum system used in this work utilizes a Granville-Phillips 307 vacuum gauge controller which supplies the filament current, grid, and collector biases along with displaying the collector current measured by an internal electrometer converted to a pressure using Equation C.1. To further increase the reliability of the ion-gauge pressure measurement, a degassing procedure is used. The grid is heated by electron bombardment or resistive Joule heating to high temperatures ($\sim 900\,°C$). This heat treatment serves to desorb gas molecules adsorbed onto the gauge elements to minimize outgassing and electron-stimulated desorption during operation which could lead to erroneous pressure readings.

A Convectron gauge is used to monitor the chamber pressure during pump down. The Convectron gauge is capable of measuring pressures down to 1×10^{-4} Torr. This gauge operates by measuring the thermal conduction of heat by the residual gas from a tungsten filament kept at a fixed temperature of 105 °C. As the pressure decreases, the number of gas molecules in the active region of the gauge decreases and the thermal conduction away from the filament decreases. This reduction of the filament cooling decreases the voltage required to maintain the filament temperature. The filament voltage is a non-linear function of the pressure and allows the pressure to be measured.

Finally, an Inficon Quadrex 100 Residual Gas Analyzer (RGA) is installed. The RGA consists of a quadrupole mass spectrometer head to measure the partial pressures of ionized species of residual gases in the chamber. The mass spectrum contains information useful for diagnosing the source of leaks or contamination from the mass species present and their relative partial pressures. The RGA can further be used as a leak detector by measuring a particular mass species as a function of time. Leak checking is done using ^{4}He sprayed around components and seals while monitoring the ^{4}He peak to localize leaks.

C.2 Electron Beam Evaporation

In order to vacuum deposit materials a source of material vapor must be created. Among other techniques, this can be done via evaporation or sputtering of a source. In the case of shadow mask deposition, evaporation is desirable due to the capability for highly directional deposition. If the mean free path of the material vapor is larger than the source-substrate distance the deposition will be highly directional. In the other limit, if the source-substrate distance is much longer than the mean free path, the material vapor will scatter before arriving at the substrate. The material will now arrive from a broad distribution of angles. The mean free path can be written in the kinetic theory of gases as,

$$\lambda_g = \frac{k_B T}{\sqrt{2}\pi d_g^2 P_g} \tag{C.2}$$

where k_B is the Boltzmann constant, T is the temperature of the gas, d_g is the diameter of the scattering gas, and P_g is the pressure.

In the case of evaporation in a UHV environment, the mean free path is larger than any deposition system reaching 3×10^6 m for Nitrogen (diameter 1.42 Å) at 1×10^{-10} Torr. Alternately, for Ar sputtering processes with typical pressures of 2×10^{-3} Torr has a mean free path of 8 cm which is comparable or shorter than the source-substrate separation in many systems. The UHV system used in this work has a source-substrate separation of $\approx$ 69 cm, much shorter than λ_g. Additionally, by having such a large source-substrate separation the distribution of arrival angles of the evaporated flux is less than 2°.

Since evaporative deposition is the method of choice for these experiments other physical vapor deposition techniques, such as sputtering and pulsed laser ablation, are not discussed in detail. Electron beam evaporation is used for the deposition of the spin valves discussed in this thesis. The capability to use thermal evaporation to create devices has been added to the vacuum deposition system and is discussed in Appendix D.

An electron beam evaporator, shown in Figure C.2, operates by heating a source ingot with an intense beam of high-energy electrons until it evaporates. The evaporator uses electrons sourced by Thermionic emission from a filament. The emitted electrons are accelerated by an anode held at $V_e = 7\,\text{kV}$. The filament is mounted below the

source material to be heated; the electron beam is turned by a magnetic field created by permanent magnets so that they are incident on the source material. The energy of the incident electrons is dissipated in the source, heating the material. The precise positioning of the beam is determined by a pair of electromagnetic coil sets. These steering coils are able to fine tune the beam position on the source in both in-plane directions with the application of orthogonal fields. Continuously sweeping the beam over the source material provides improved heating uniformity over a larger area. Heating over a larger area is especially useful for materials with low thermal conductivities as a stationary beam may only evaporate materially locally, drilling a hole through the source and making ineffective use of the source material. Source material is placed in a copper hearth with brazed inserts, as shown in Figure 2.4, and for materials with high thermal conductivity they are placed in a thermally insulating crucible liners to isolate the material from the cooling of the hearth as well as keeping the source from intermixing with the hearth.

To control the evaporation rate the power imparted to the source via the electron beam can be adjusted. This can be expressed as $P_e = I_e V_e$, where V_e is held fixed by the controller while the beam current I_e is adjusted to change the source temperature and thereby change the evaporation rate. A quartz crystal microbalance (QCM) is used to monitor the thickness of the deposited material to determine the deposition rate. The measured deposition rate is used to provide feedback for setting I_e. Evaporation rates from 0.01 Å s^{-1} to 10.0 Å s^{-1} can be achieved, although the chamber configuration makes rates above 3 Å s^{-1} difficult to maintain due to the large source-substrate distance.

In practice the electron beam evaporator may have several source ingots contained in multi-pocket source. Using a single high-energy beam multiple materials can be sequentially evaporated without breaking vacuum by shifting the desired material to lie in the path of the electron beam. Traditional configurations include a rotary system with a wheel of pockets rotating among the materials or the Telemark evaporator used here has a linear shift between four pockets each able to hold 15 cm^3 of source material. Photographs of the multi-pocket source are shown in Figure C.3 from the side and an overhead view.

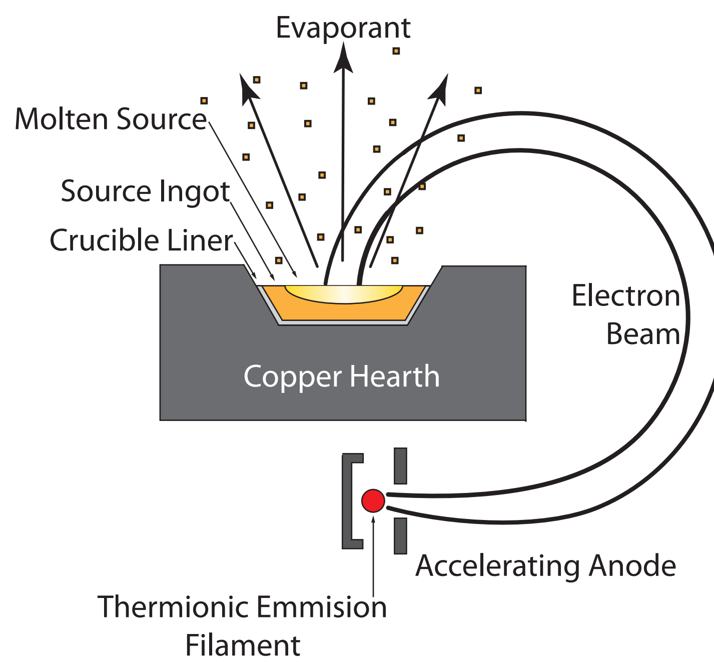

Figure C.2: General layout of the main components of an electron beam evaporation source.

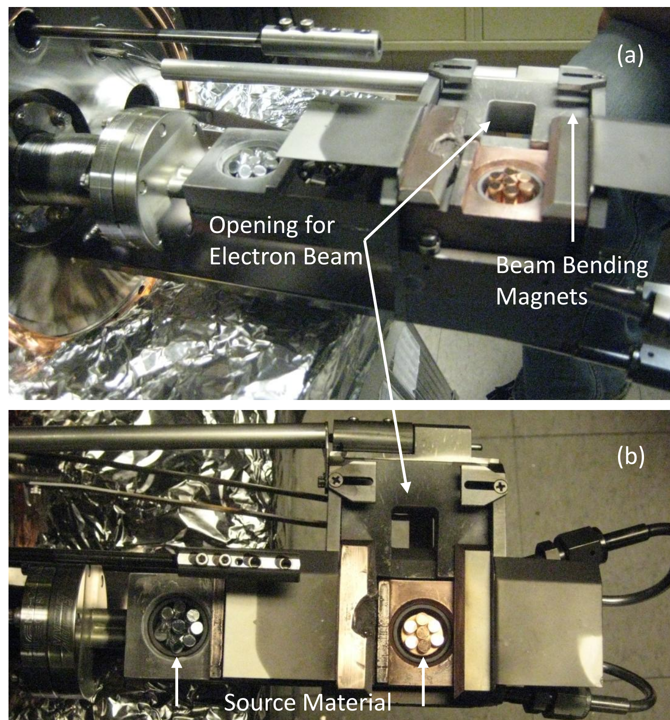

Figure C.3: Photographs of the electron beam evaporator used in this thesis (a) from the side and (b) from above. Two of the four in-line source pockets in the copper hearth are indicated with arrows along with the opening allowing the high-energy electron beam originating from below the hearth to be bent by a magnetic field to be incident on the source material.

C.2.1 Depositing onto Resist Patterned Substrates

The metals evaporated to create devices for this work require a molten source to be held at temperatures near 1500 °C. This leads to radiative heating of the resist. For most resists, temperatures below 100 °C will not damage the patterning. If heated above the glass transition temperature T_g, which is 105 °C for PMMA [83] and 180 °C to 190 °C for PMGI [90], the resist will begin to reflow and distort the pattern. This distortion can be in the form of in-plane changes to the features or, equally troublesome, the undercut regions can collapse. To avoid this damage, depositions must be finished before the substrate temperature exceeds T_g of either resist layer. To do so the deposition rate is adjusted, to change the total deposition time. Due to the non-linear dependence of deposition rate on source temperature, the increased heating of the substrate due to increased source temperature is small compared to the reduction in deposition time. As a result the maximum temperature reached during deposition is reduced. For lateral spin valves the FM materials were deposited at 0.5 $\text{Å}\,\text{s}^{-1}$ and the N materials at 1.0 $\text{Å}\,\text{s}^{-1}$ keeping the final sample temperature below 65 °C as measured by a thermocouple on the sample manipulator.

One unfortunate consequence of using electron beam evaporation for depositing material in a EBL patterned resist mask is the effect of stray electrons on the mask itself. The high-energy electron beam incident on the metallic source material serves as a source of secondary and back-scattered electrons that may reach the sample and cause damage to the resist. Damage due to electrons emanating from the source interacting with the resist is shown in Figure C.4(a), which appear as blisters under the deposited metal film. A simple solution to this problem is to add a magnetic field placed along, and oriented perpendicular to, the line between the source and substrate. However, the Earth's magnetic field is insufficient to deflect the stray electrons. A magnetic field of a several gauss, depending on geometry, which is orthogonal to the stray electron flux will deflect or trap those electrons transiting from the source to substrate. The Lorentz force due to a magnetic field of 10 G applied over a 10 cm path of the stray electron flux is sufficient to deflect the electrons and prevent them from damaging the resist. This field is generated using a large electromagnetic solenoid external to the vacuum system. A marked improvement has been observed in the ability for resist to withstand prolonged evaporation due to the removal of these excess electrons incident on the EBL

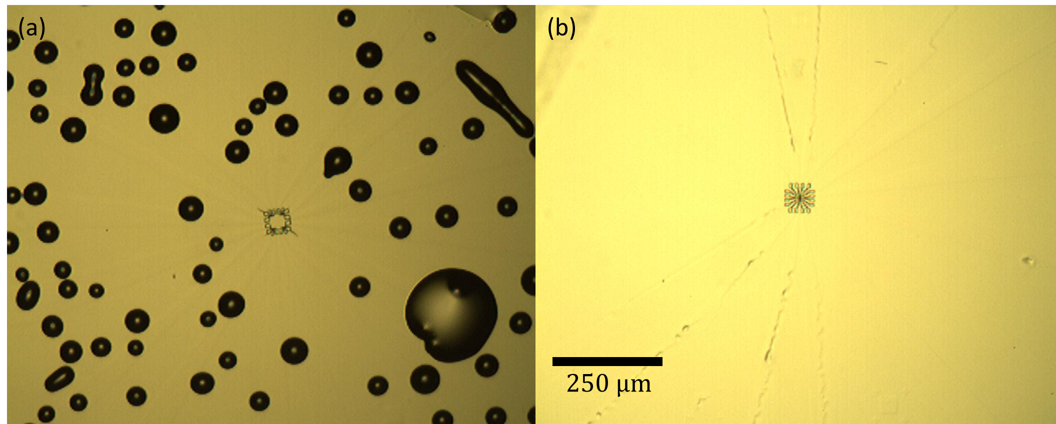

Figure C.4: Optical micrographs of metal films on resist. (a) Blistering of resist due to secondary electrons. (b) Application of a magnetic field removes the secondary electron flux.

resist, shown in Figure C.4(b).

C.3 Thermal Evaporation

A second evaporative technique may be employed, where source material is heated by Joule heating. Some materials can be evaporated or sublimated from refractory metal boats, baskets, or canoes where a large current is passed through the metal to heat the source and create source vapor for deposition. By controlling the total power dissipated in the heating element the source temperature, and therefore the deposition rate, can be controlled. Many materials are incompatible with evaporation directly from a metal boat, in this case the source material is placed in an Alumina or Boron Nitride crucible. This is wrapped with a wire heating element to heat the crucible and source for deposition. An example of silver source material loaded in this manner is shown in Figure C.6(a). Although this technique allows for deposition of a large range of materials it is incapable of depositing from source material requiring higher temperatures, such as those required for transition metals.

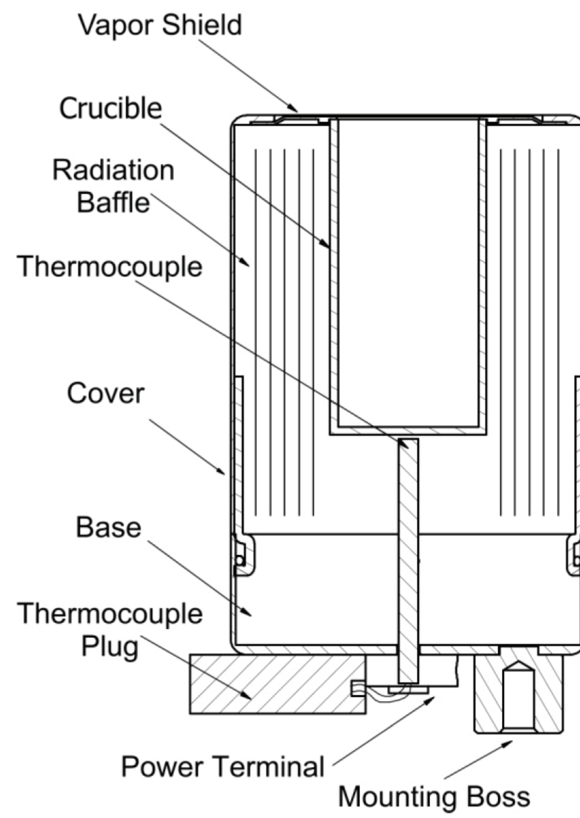

Figure C.5: Cross sectional schematic of a resistively heated thermal deposition cell taken from the product manual [144].

The resistive heating deposition technique can be made more functional by engineering an enhanced version of the simple wire wound crucible. To do so several improvements are made. The wire is wrapped around the crucible so that there are more turns near the top of the crucible. Current flowing through the wire delivers more thermal energy near the orifice at the top of the crucible and gradually drops towards the bottom of the crucible. This is referred to as a hot-lip evaporator, which prevents material from accumulating at the opening of the crucible and altering the evaporant flux during operation.

A cell of this design was installed in the vacuum system described in §2.3.1 and is shown in Figure C.6(b). To further increase the stability of the deposition cell a themocouple is in thermal contact with the base of the crucible to measure the temperature, as shown in Figure C.5. The ability to measure the temperature allows the power to be regulated to keep the cell temperature constant, thereby keeping the deposition rate stable. Finally, these parts are placed within a series of Molybdemum coaxial radiation shields, or baffles, to minimize radiative thermal loss, source temperature non-uniformity, and temperature fluctuations of the source. These design components allow for measured flux stability of 1% and a maximum temperature above 1500 °C, even reaching 2000 °C. In this case the cell is mounted on a stainless steel mount using a thermally and electrically insulating ceramic boss, as shown in Figure C.6(d). Details of the mounting system that I designed for this work are given in Appendix D.

Several photographs of thermal evaporators are shown in Figure C.6. (a) Photograph of a tantalum wire wound evaporation source shown loaded with a ceramic crucible and silver source shot prior to being heated. (b) A “hot-lip” vacuum furnace evaporator heating coil wound around an Alumina crucible which sits atop a thermocouple. (c) Ni source material is shown filling the alumina crucible to be loaded into the vacuum furnace shown in (b). (d) The fully assembled vacuum furnace with radiation baffles, top vapor shield, and external molybdenum enclosure.

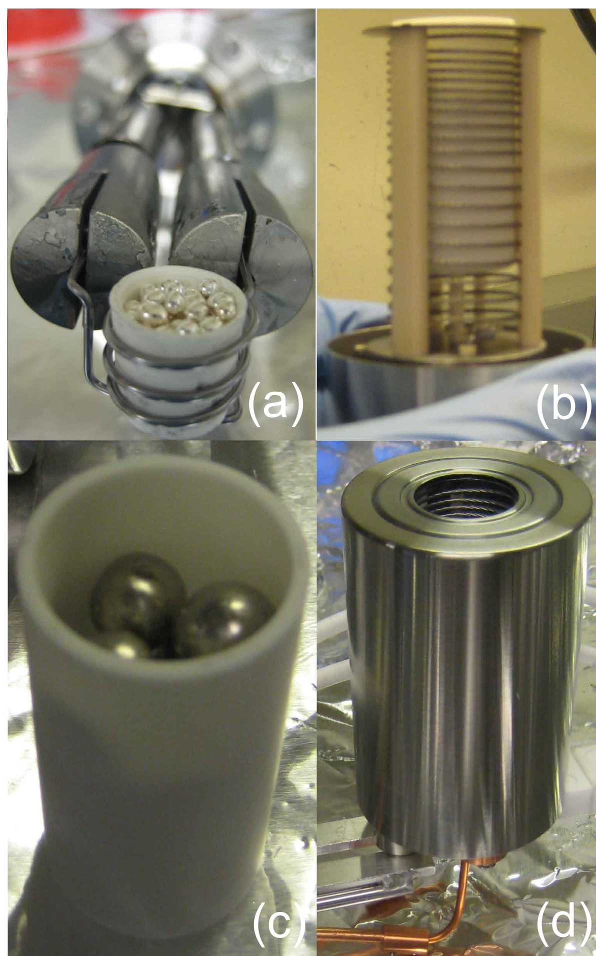

Figure C.6: Photos of resistive heating thermal evaporators.

C.4 Quartz Crystal Thickness Monitors

To measure and control the flux of material Quartz crystal microbalances, or monitors, (QCM) are employed. These devices measure the mass within a defined area by measuring changes in the resonance frequency of a Quartz crystal driven via the Piezo electric effect. For a material of known density the thickness can be calculated. The addition of material to the crystal will load down the oscillations and decrease the resonant frequency. A model can be developed for the case of an oscillating quartz crystal and uniform thin film rigidly coupled to the crystal. The Sauerbrey equation can be used to describe the change in resonance frequency with the addition of mass to the surface,

$$\Delta f_q = -\frac{2f_{q0}^2}{\sqrt{\rho_q \mu_q}} \frac{\Delta m}{A}, \tag{C.3}$$

where f_{q0} is the resonance frequency, ρ_q is the quartz density, μ_q is the shear modulus of quartz, Δm is the change in mass, and A is the area of the crystal that mass is added to. For typical QCM crystals the resonance is near 6 MHz, measuring $\Delta f_q = 1$ Hz is straightforward and for corresponds to a change in thickness of a partial atomic layer, 0.14 Å from Equation C.3 for Cu. The INFICON® IC/5 thin film deposition controller used for these experiments is capable of measuring a frequency of 0.005 Hz which corresponds to 0.0006 Å, again for Cu. Equation C.3 is adequate to describe changes in frequency only for $\Delta f_q / f_{q0} < 0.02$. If this inequality is not satisfied, a more complicated expression must be used that takes into account the properties of the deposited film as well.

Further work by Lu and Lewis developed a more elaborate model that additionally accounts for the acoustic properties of the quartz crystal and deposited film system. The film thickness can then be written,

$$t_f = \frac{N_{at} \rho_q}{\pi \rho_f f_T Z_q} \arctan\left(Z_q \tan\left(\frac{\pi (f_q - f_T)}{f_q} \right) \right) \tag{C.4}$$

where $Z_q = \sqrt{\rho_q \mu_q / \rho_f \mu_f}$ is the acoustic impedance ratio of the quartz crystal and film, ρ_f is the density of the film, N_{at} is the frequency constant of the AT cut quartz crystal, f_q is the resonant frequency of the quartz crystal and f_T is the frequency of the crystal and deposited film. Modern thickness monitoring systems solve Equation C.4 to measure accurately the deposited film thickness [145] [146]. For most depositions a

QCM provides feedback for controlling the rate of deposition and total film thickness deposited.

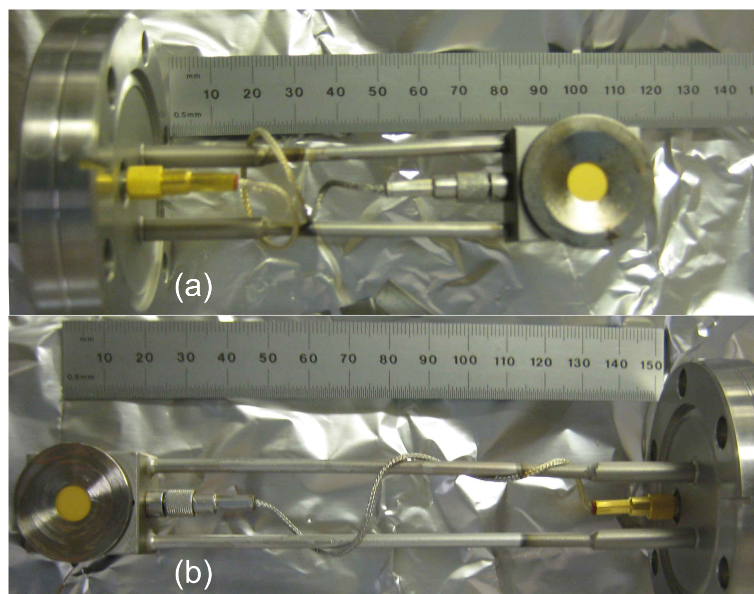

Figure C.7: Photographs of two Quartz crystal thickness monitoring micro-balances, located (a) above the main thermal source and (b) near the sample stage.

Two Quartz crystal monitors micro-balances are shown in Figure C.7. Each crystal monitor is mounted on a $2^{3}/_{4}$ inch ConFlat flange via the water cooling input and output lines. An RF coax cable connection is wrapped around the lines to connect the QCM to the feedthrough. The gold coated quartz crystals have a circular shadow mask to define the area of to be coated by source material. Each monitor extends into the chamber by different lengths. One monitor, shown in Figure C.7(a), reaches in approximately 10 cm to measure only flux from the thermal evaporator while the other monitor, Figure C.7(b), reaches in 15 cm and is positioned close to the growth stage to monitor the total flux at the sample.

C.4.1 Quartz Crystal Monitor Calibration

The precision of the Quartz Crystal Microbalances, discussed in §C.4, are capable of measuring less than a monolayer of deposited material. The spatial position of the

QCMs relative to the source require calibration of the thickness measured on the QCM to the thickness deposited on the sample substrate. A tooling factor TF corrects the thickness measured with the QCM to give the actual deposited thickness. A corrected tooling factor TF_F can be found by depositing a film on a substrate while recording the QCM measured thickness t_x and deposited thickness t_f through other means such as ellipsometry, profilometry, or grazing incidence x-ray reflectivity (GIXR). In this work GIXR is used to determine the calibration film thicknesses, which is discussed in §2.4.2. Given the tooling factor used for the initial deposition TF_i the corrected tooling factor can be computed using,

$$TF_F = TF_i \frac{t_f}{t_x} \,. \tag{C.5}$$

If the tooling factor is off by a large amount, this calibration may not provide the desired accuracy and the process to correct TF_F should be repeated. The tooling factor is checked periodically, for example when source material is refilled or changed, to verify that it has not changed and correct it if so. The tooling factor for the main crystal monitor is 100.3 %.

C.5 Multiple Source Evaporation

The addition of a second evaporative source allows for a variety of materials to be deposited that are otherwise impossible. Alloys may be co-deposited with the composition being tuned by varying the relative deposition rates of the constituent materials. This added functionality has a broad range of possibilities, one of which is the deposition of ferromagnetic alloys with tunable Curie Temperature T_c such as $Ni_{1-x}Cu_x$ alloys, which are discussed in §6.2.1 or for the creation of $Co_{1-x}Ni_xS_2$ discussed in §6.2.2. Co-deposition can be accomplished in a controlled way by having two QCMs to allow for the rates from each source to be decoupled. The particular deployment used here is to have one QCM near the substrate to measure the total rate of material deposition on the sample. A second QCM measures only the rate from the thermal cell and is shielded from the electron-beam source by a metal plate to block the flux. As a result the rates due to each source can be decoupled and careful control of both sources can be made. In practice, due to the stability of the thermal cell, the flux from the cell can be fixed and the electron beam flux can be adjusted to maintain the desired concentration.

C.5.1 Growth Control Shutters

To control the evaporate emanating from the evaporation sources the system is installed with a variety of growth shutters. These shutters are constructed to block the line of sight between the source and the substrate. The system is equipped with three shutters, one 2 inches above the electron beam evaporator, another 2 inches above the thermal cell, and a third a few inches below the sample stage. The source shutters are pneumatically operated by compressed air and electrically activated using solenoid valves. These valves are activated by the Inficon® IC/5 depositon controller which is described in §C.4. The shutters can be automatically opened and closed to create films of predefined thickness.

Since there is a shutter for each source the system can be programmed to deposit superlattices, repeating alternating depositions from each source. Using shutters over each source one material may be deposited followed by another, then this multilayer is repeated several times. This can be used to create a variety of multilayers, including ferromagnetic films such as Co/Ni multilayers. Perpendicular media has been successfully deposited such as [Co (2 Å/s)/Ni (8 Å/s)] superlattices with the magnetization oriented out of the plane rather than in plane as is the case for most thin film ferromagnets, due to shape anisotropy.

The third shutter, placed just below the sample, is operated manually using a rotational vacuum feedthrough. This shutter is most often used to keep source material from reaching the sample while one, or multiple, sources are stabilized with the source shutters open at the desired rates using the crystal monitors. Once the desired deposition conditions have been dialed in, the sample shutter can be opened to begin deposition on the sample itself. Since this shutter is capable of operation beyond strictly open or closed, it can be used to shadow regions of the sample platen from the source material. This ability to partially close the shutter allows multiple samples to be deposited while varying a parameter, such as one of the layer thicknesses, while keeping everything else constant. This feedthrough includes an angular position indicator which allows the position of the sample shutter to be repeatably set.

To use the shutter for these purposes the position relative to the sample platen was first calibrated. Alignment was accomplished by covering the platen with a substrate and stepping the shutter position while depositing material. By stepping the shutter position every 10 nm of deposited material results in a series of contours that can be

optically measured on the platen corresponding to the shutter positions. A photograph of the substrate and platen are shown in Figure C.8 along with the corresponding calibration contour plot. Using this plot samples can be placed on the platen so that for given shutter positions part or all of a layer can be blocked for some of the samples.

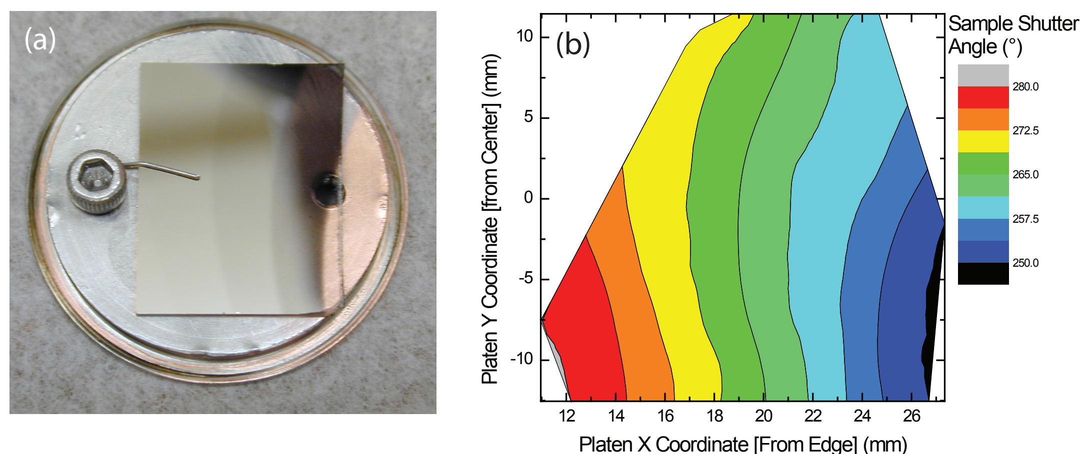

Figure C.8: Growth contours due to intermediate positioning of the sample shutter with an xy-plot of the contours.

One example is of two samples placed at either edge of the platen. By depositing films on both samples simultaneously they should be as identical as possible. Partway through a deposition the shutter could be closed to shadow the first sample (265° in this case) such that you would get two identical films up to the thickness the shutter was partially closed and the second sample could be grown thicker with the same base material. This technique is extremely useful in many situations to deposit nearly identical structures with only a single layer thickness varied. This incremental closure of the shutter is used for non-local spin valves where we want to vary the channel thickness but minimize any other differences in material.

Appendix D

Radak Design and Installation

This appendix contains information about the design and installation of the Radak thermal-evaporation source. The thermal evaporation of materials can be done from various source designs. The vacuum deposition system has been equipped with two simple thermal evaporators consisting of electrical feedthrough and heating element. The electrical feedthoughs have two terminals rated to carry more than 100 A. Various configurations of refractory metals, such as baskets, boats, or canoes, are used to hold the evaporation source materials. A ceramic crucible, such as Alumina or Boron Nitride, which is wrapped with a W or Ta wire can also be used.

Simple thermal evaporators, as just described, can be used to deposit a variety of materials. These evaporators allow additional materials to be deposited without breaking vacuum. The addition of thermal evaporators allow the simultaneous deposition of materials from the thermal and e-gun sources. These simple sources are very good for depositing materials such as Mn or Ag; however, these simple sources do not have the capability to evaporate other materials that require higher temperatures for deposition. A source with improved radiative shielding, larger capacity, and temperature sensing allows materials to be heated to greater temperature with better stability than simple thermal sources.

D.1 Radak Mount Design

The ability to deposit a larger range of materials with a greater stability than the simple evaporators requires several enhancements. Knudsen type evaporators are often mounted so that the evaporated flux is perpendicular to the feed-through flange. Although these cells can also be configured parallel to the plane of the vacuum flange, the space available in the vacuum system discussed here that can be utilized without disturbing the other functions is limited.

The geometry of the vacuum system used in this work requires an evaporation source which is parallel to the plane of the flange. Due to the vacuum system geometry the only available port is a 2³/4" ConFlat flange. A Radak II vacuum furnace was used as the thermal source, which could not be installed through the 2³/4" ConFlat flange. As a result the installation was done in two parts. First, the 2³/4" ConFlat vacuum feed-through and attached mount for the Radak II was installed into the vacuum system followed by the installation of the Radak II evaporator onto the mount inside the vacuum chamber.

The system needed to be designed to satisfy the various requirements. A three-dimensional rendering of the design that I arrived at is shown in Figure D.1. The ISI™ 9392023-0193902-C vacuum feedthrough, shaded gray, is a 2³/4" ConFlat power feedthrough flange. The feedthrough is equipped with three Cu power connections which are sealed using ceramics. The Cu connections, shaded yellow, are capable of sustaining 60 A of charge current and 5000 V DC. The feedthrough is also equipped with a pair of C-type thermocouple connections (Tungsten 5% Rhenium / Tungsten 26% Rhenium).

A 304 stainless steel support mount was welded to the interior of the vacuum flange, shaded blue. This mount consists of two parallel bars welded to the flange and a bridge between them opposite the flange, which serves as the mount for the Radak II source. This bridge is slotted so that the vacuum furnace may be affixed with a stainless steel 1/4-20 bolt. The ceramic mounting boss on the vacuum furnace is shown in Figure D.2 which is a schematic of the Radak II vacuum furnace. The vacuum furnace is then connected to the power and thermocouple feedthrough wires with Cu wire and C-type

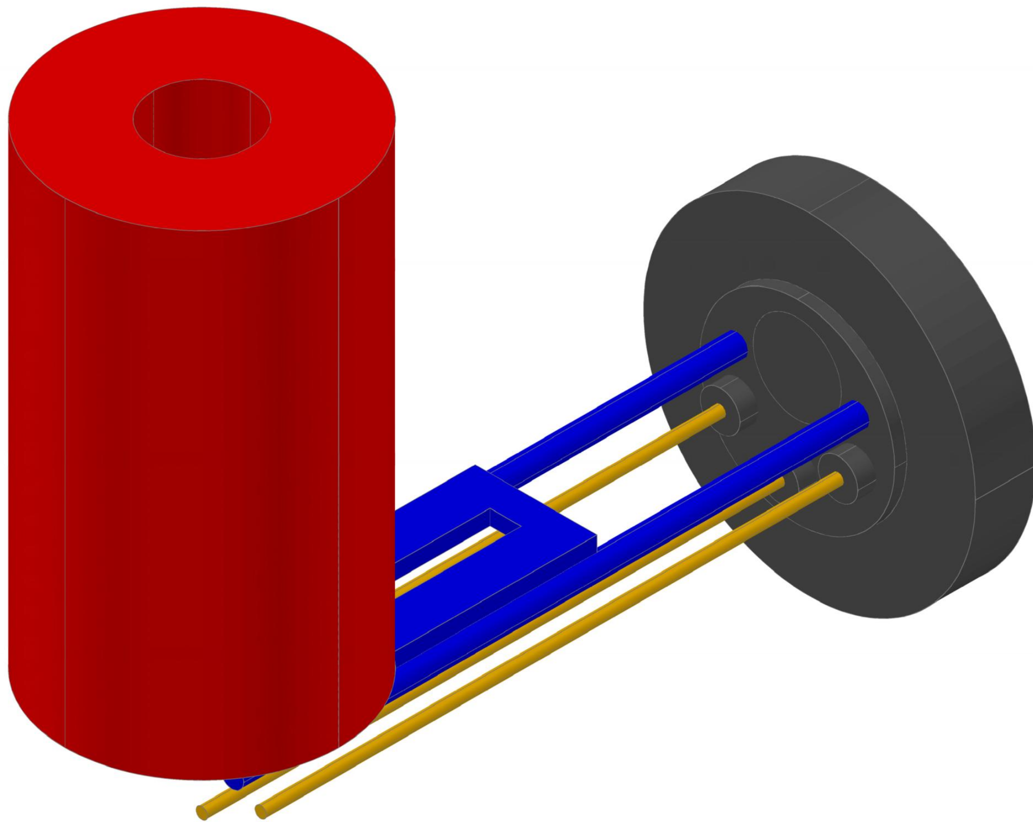

Figure D.1: Three-dimensional rendering of the design for the thermal source, mount, and feedthrough. The 2³/4" ConFlat flange (grey), stainless supports (blue), power connectors (yellow), and the Radak evaporator (red) are shown.

interconnecting wires, respectively. The joints for each of these connections is made using tube interconnects with set screws to hold the wires together. The connecting wires are threaded through insulating ceramic beads to help prevent shorts from occurring.

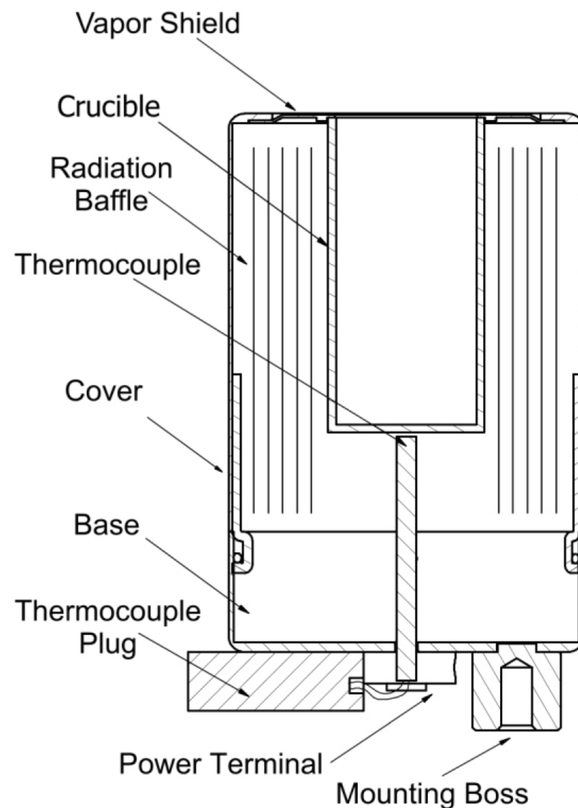

Figure D.2: Cross sectional schematic of a resistively heated thermal deposition Radak II source taken from the product manual [144].

Finally, the extra power feedthrough wire, shown at the bottom in Figures D.1, D.4, D.5 is used to affix a refractory metal shield to protect the evaporator and associated wiring from accumulating materials evaporated from the e-beam evaporator. The shield also prevents flux from the e-beam evaporator from reaching the quartz crystal monitor located above the thermal source, such that the two sources and the two monitors can be decoupled, while not blocking the flux from the e-gun evaporator from reaching the sample position.

Schematics are shown for three different views in Figures D.3, D.4, D.5. These schematics were used for the fabrication of the vacuum support structure and are available here in the event modification are necessary. For normal maintenance, this is straight forward as the top of the evaporator may be removed *in-situ* so that the evaporation source and crucible may be changed as needed.

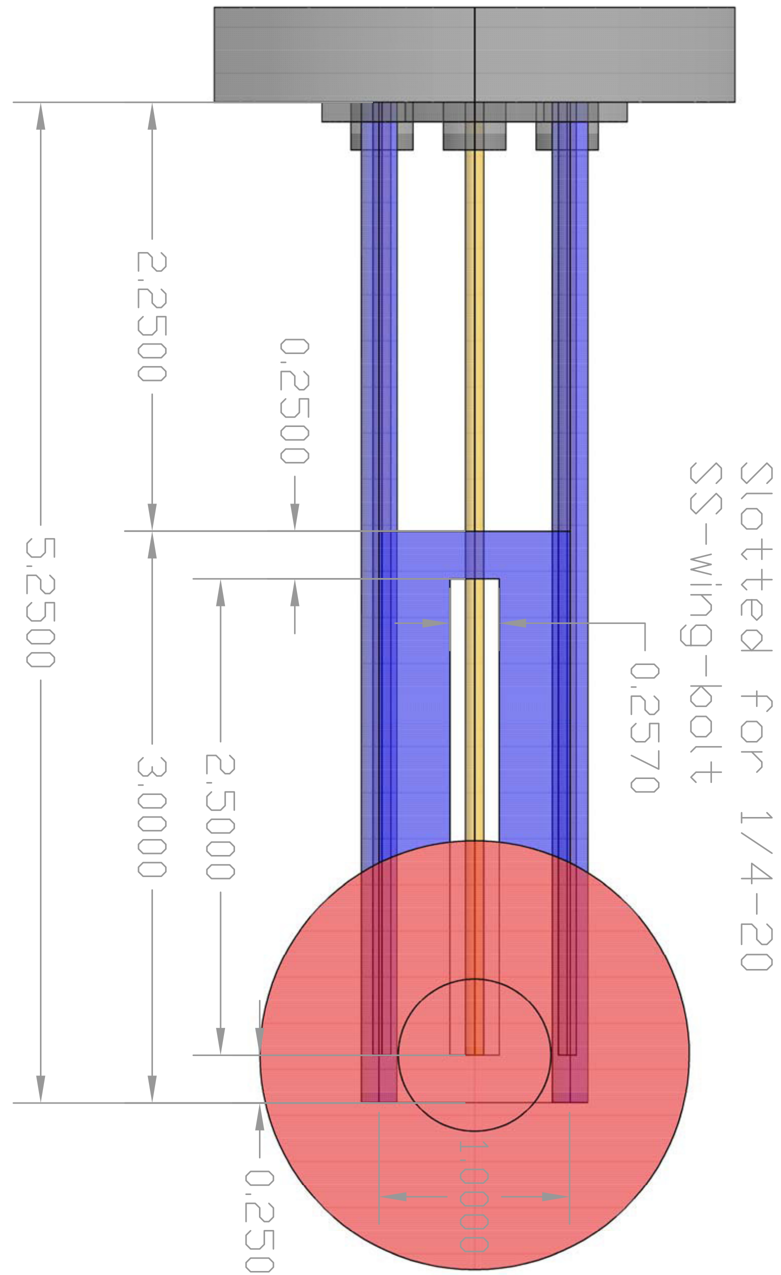

Figure D.3: A top-view schematic of the design for the thermal source, mount, and feedthrough. The stainless supports (blue) are shown with various dimensions labeled in inches.

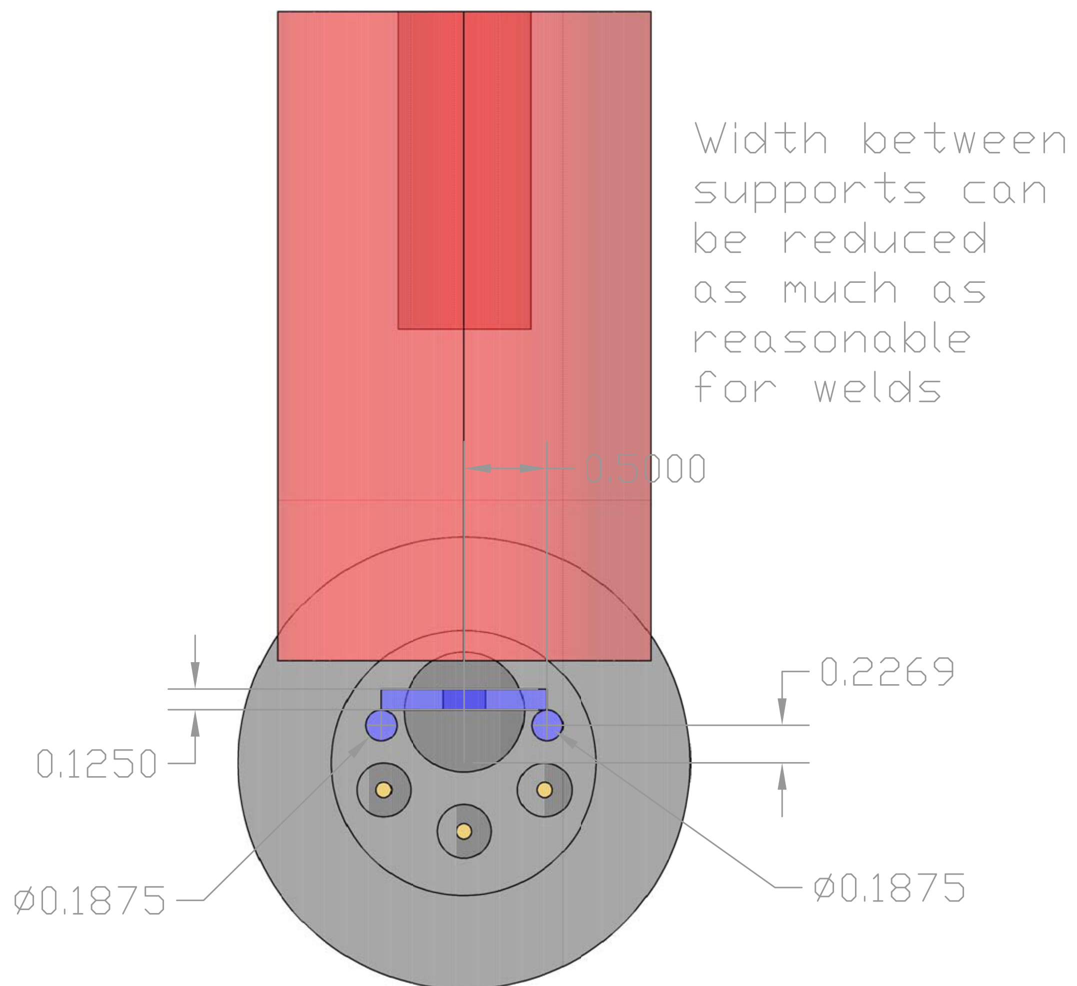

Figure D.4: A side-view schematic of the design for the thermal source, mount, and feedthrough. The stainless supports (blue) are shown with the thicknesses of the bridge support and rods labeled as well as the offsets from the center of the flange.

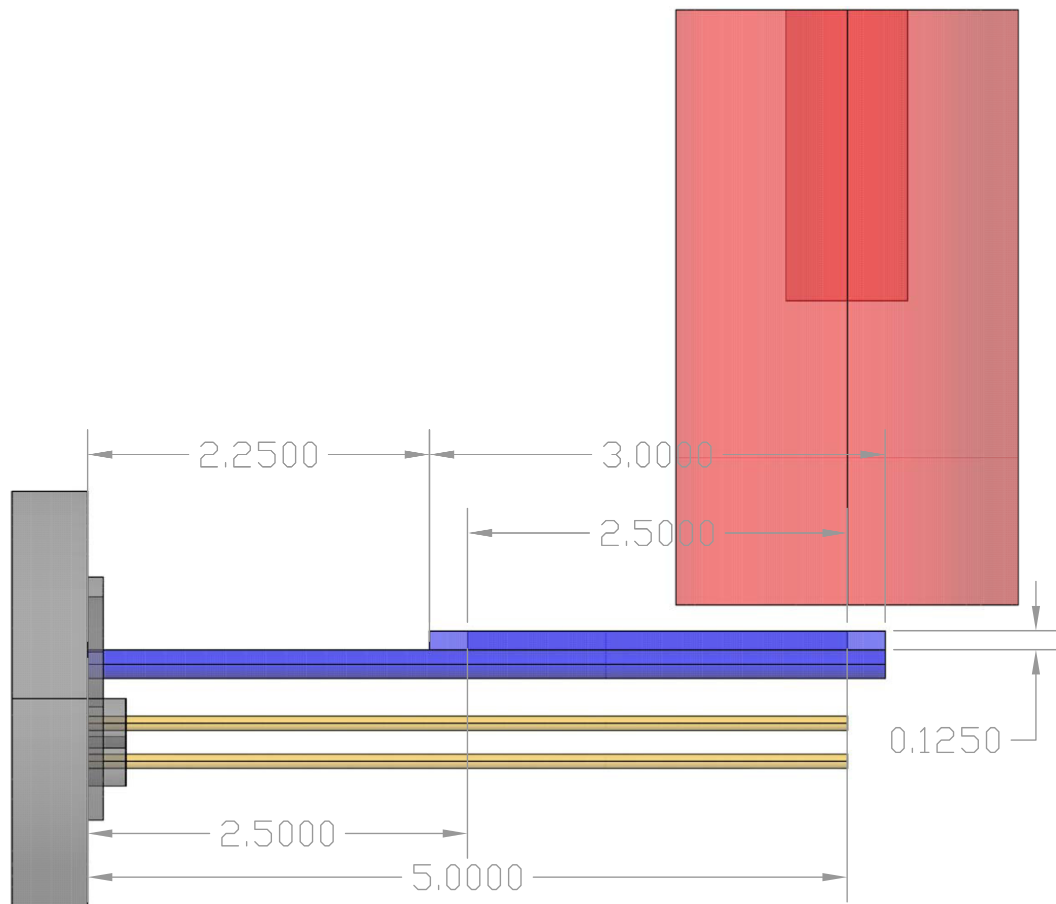

Figure D.5: A side-view schematic (perpendicular to the view shown in Figure D.4) of the design for the thermal source, mount, and feedthrough. The stainless supports (blue) are shown with the lengths of each section extending from the flange face into the interior of the vacuum system.

Appendix E

Probe Design and Schematics

This appendix contains information about the design, fabrication, and operation of the rotator probe that was custom built for the transport experiments conducted as part of this work. The probe was created to be used in a He vapor magneto-transport cryostat manufactured by Janis Research Company. Samples are mounted on the probe to be placed into a low-temperature and high-magnetic field environment. To satisfy these needs the probe was constructed from a low conductivity stainless steel vertical tube to connect copper components. A schematic of the probe is shown in Figure E.1. The four panels show the probe from different spatial directions. The probe is oriented vertically on the page as inserted into the cryostat.

E.1 Probe Schematics

In Figure E.1(a) a three-dimensional rendering of the probe is shown. Figure panels E.1(b)-(c) show side and front views of the probe as it is oriented when loaded into the cryostat. The final panel in E.1(d) shows a transparent rendering of the probe similar to panel (a) in order to see the internal structure of the fabricated parts.

The vertical stick, shaded blue in Figure E.1, is constructed from 304 stainless steel to minimize low-temperature thermal conductivity and magnetic interactions while retaining physical strength. Due to the increased mass of the sample mount and rotation system over the standard probe an increased wall thickness and outer diameter of the stainless tube is used. This tube is welded to the interior of a stainless steel NW-40

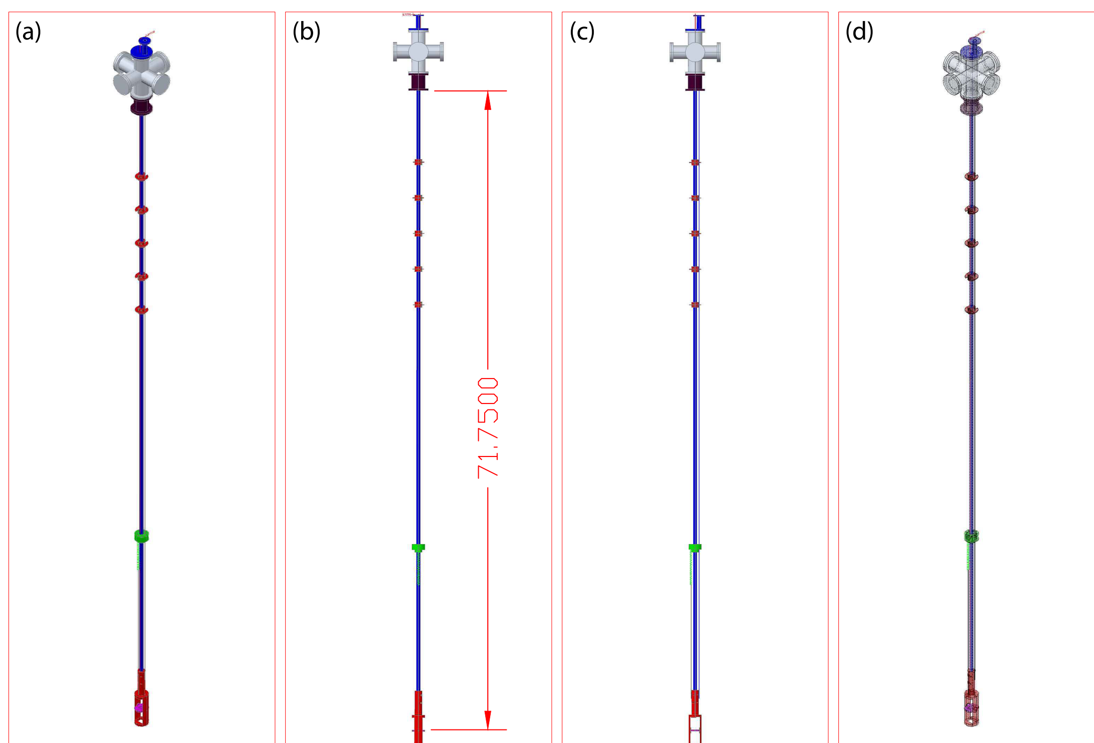

Figure E.1: Schematics of complete multi sample electrical transport probe with sample rotation stage. Three-dimensional schematics of the rotator probe shown from different viewing angles, (b) from the side and (c) front as loaded into the cryostat. The rendering in panel (d) is the same as panel (a) except that it is transparent to see internal structure of the parts.

(QF-40) blank at the center. Also connected to the top NW-40 flange is a reducing connection to a NW-16 flange welded off center, facing out allowing a linear positioner vacuum feedthrough to be attached. The linear positioner is used to activate the rotation of the sample mount at the bottom of the stick. The NW-40 blank, with the components welded on is shown schematically in Figure E.2, is connected to a six-way NW-40 cross at the top of the probe with a viton o-ring, centering ring, and an Edwards clamp.

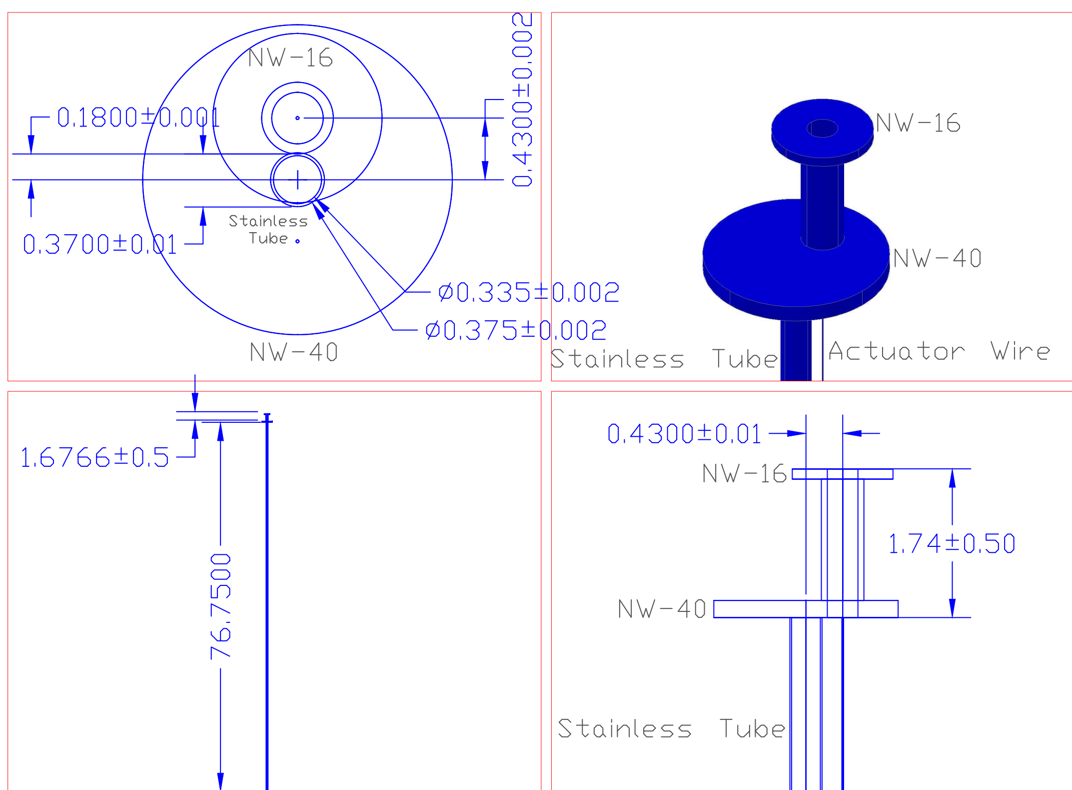

Figure E.2: Schematics of the main stainless rod and NW-16 feedthrough attached to the top NW-40 flange which form the backbone of the rotator probe.

The six-way cross has four ports orthogonal to the vertical axis that the probe stick runs along. The flanges covering two of these ports are installed with hermetic 19-pin panel mount electrical feedthoughs sealed with o-rings. The o-ring compression is provided by four screws threaded into bottom tapped holes on the NW-40 blank. The 19-pin military connectors provide connections to thermometery and heaters on one

side and sample measurement wiring on the other. The other two ports are blanked off but are available for adding further feedthroughs into the sample space. The bottom port on the NW-40 cross is occupied by a homemade NW-40 to Laddish flange, also known as Tri-Clover, adapter for making a vacuum tight connection to the cryostat. The stainless tube extends down through the cross into the cryostat allowing the wiring to run along it to reach the sample area at the end of the stick in the cryostat magnet.

Along the middle of the stainless tube lies five radiation baffles, blocking line of sight access between room temperature at the top and low temperature at the bottom. These circular baffles have cutouts azimuthaly rotated down the length of the probe allowing the wiring to run past but blocking direct line of sight. A small hole passes though each of them, which are vertically aligned, so that a tungsten wire can reach from the linear feedthough down to a pulley on the sample rotation stage to change the sample angle. Each stainless steel baffle is held in place by a pair of split clamps. The baffle assembly is shown in Figure E.3.

E.2 Sample Rotation Stage Schematic

At the bottom of the sample probe is the rotation stage where the sample is mounted. The stage itself is designed to be equipped with a thermometer, polyimide (Kapton®) foil heater, cryogenic Hall generator, and connections for sample measurement leads. Two stainless steel pivot points extend from the sample block, along the rotation axis, which are held by sapphire seats to allow the stage to rotate freely. A pair of pulleys are mounted along the rotation axis so that a wire can be wrapped around each pulley. The wire wrapped around one pulley is attached to the linear feedthough at the top of the probe to rotate the stage when tension is put on the wire. The other wire is attached to a coil spring rotating the stage back when the tension on the first wire is relaxed.

Schematics of the rotation stage are shown in Figure E.4 with the various part dimensions labeled in inches. The sample block, pulleys, and pivot points are depicted. In the sample block there are two slots which are occupied by spring socket connections installed using Stycast® 1266 Epoxy. Seven socket connections are installed in each slot, forming a standard 14-pin dip socket. Samples mounted to dip packages can be installed in this socket with the bottom of the dip package resting in thermal contact with the

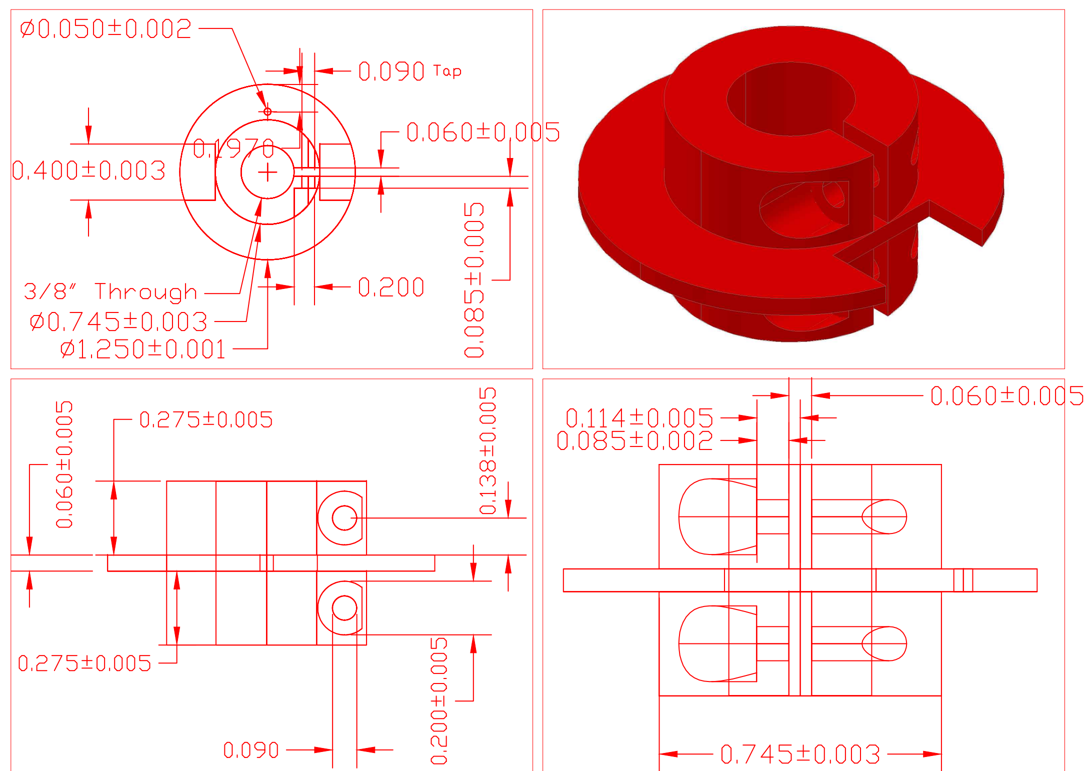

Figure E.3: Design schematic of the five radiation baffles that are along the probe. Dimensions are given in inches.

copper piece between the slots for the socket connections. A resistive Kapton foil heater (Minco HK5566R15.0L12A) is epoxied to the copper piece running between the two dip socket slots. A hole is counterbored into the side of the copper block extending into the region between the dip socket slots where the sample is mounted. A LakeShore Cernox™ thermometer in an AA-cannister package, described in §2.5.2, fits closely into the hole and is installed so that it is in good thermal contact with the sample enabling accurate measurement of the sample temperature.

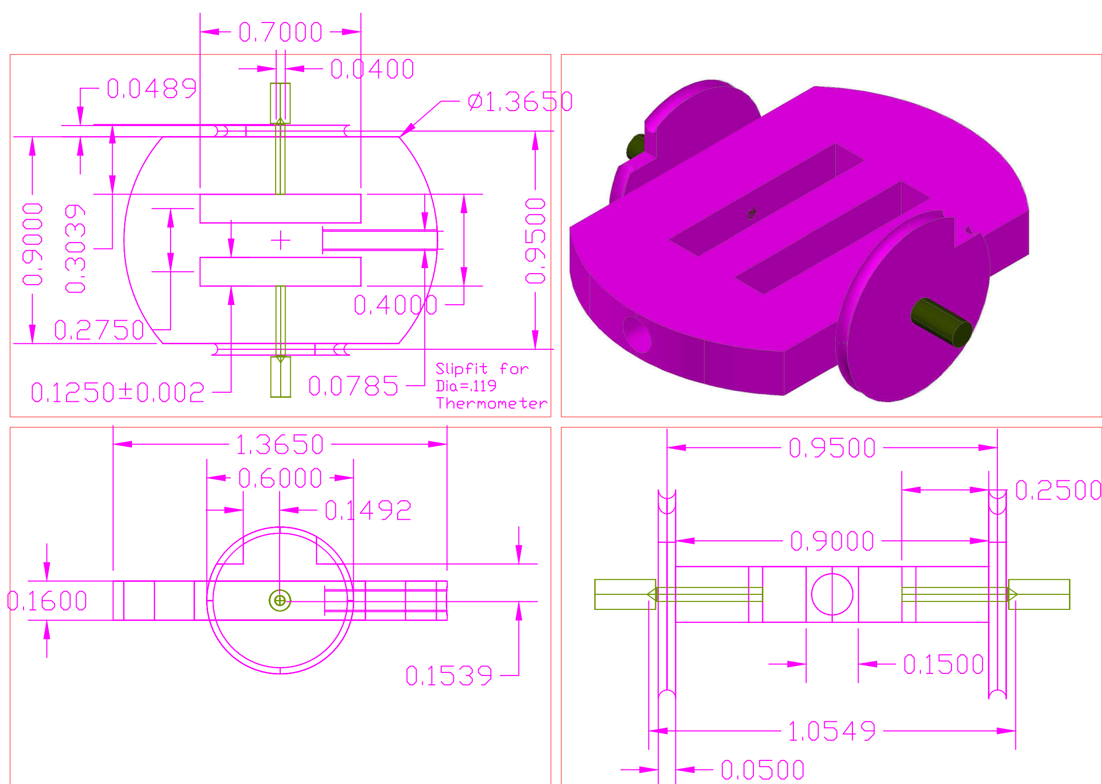

Figure E.4: Schematics of sample rotation stage.

E.2.1 Sample Rotation Stage in Retaining Block

The sample rotation stage described previously must be affixed to the end the stainless steel tube that forms the backbone of the probe. A cylindrical copper cage is affixed to the end of the probe using a single copper split clamp bolted to the top of the cage.

Threaded into either side of the cage is a pair of spring loaded sapphire pivot seats which constrain the rotation stage. The sample rotation stage being retained by the copper cage is shown schematically in Figure E.5.

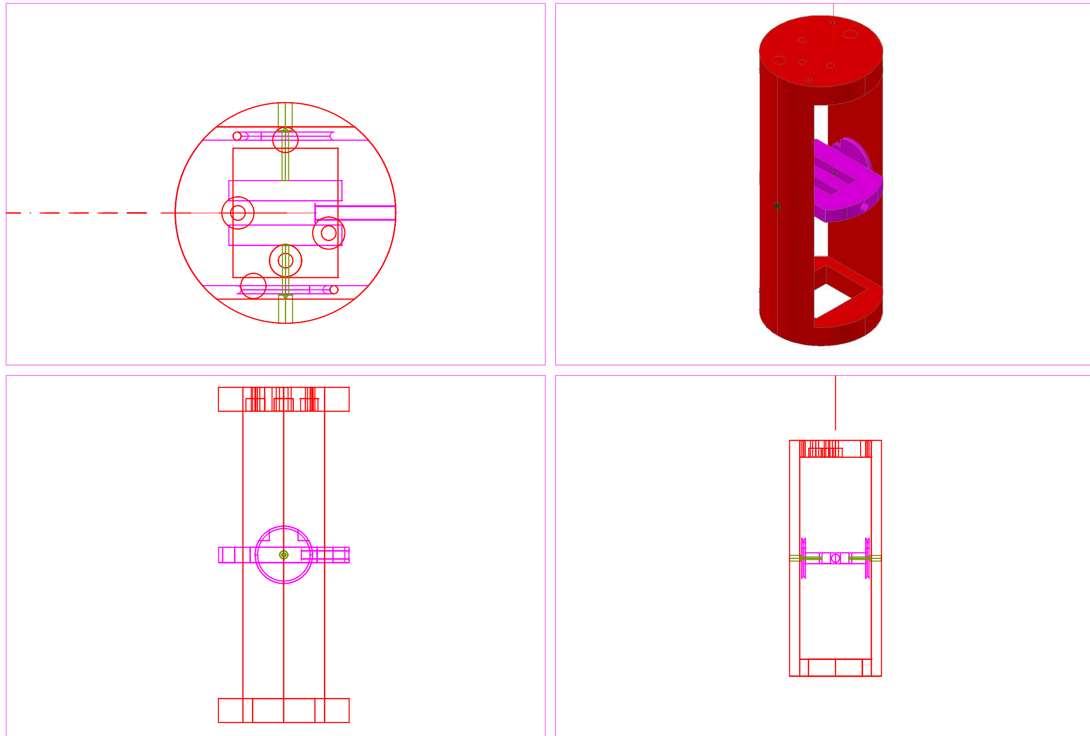

Figure E.5: Schematics of sample rotation stage retained by support block.

The top of the cage has several holes drilled through in various diameters. There are three holes for bolting on the split clamp, two to pass the electrical wiring to the sample stage, and two aligned along the vertical tangent of the pulleys for passing the wires to rotate the sample. The electrical wiring runs from the sample block up to a thermal sink with soldering posts mounted on the stainless steel tube eight inches above the sample. The thermal sink wiring is connected on the other side to the top of the probe to the electrical feedthroughs. The heat sink is used to prevent thermal loading of the sample from the electrical wiring that is connected to room temperature.

Photographs of the completed and wired stage are shown in Figure E.6. Figure E.6(a) shows a front view of the sample rotation mount with wiring up to the thermal

sink and beryllium-copper centering spring. Panel (b) shows a closer view of the rotation stage where the sample is mounted. The socket pins for the sample carrier package, shown in Figure E.7, are clearly visible in the center of the rotation stage. The foil heater and cryogenic Hall generator mounted to the back of the sample stage is shown in Figure E.6(c).

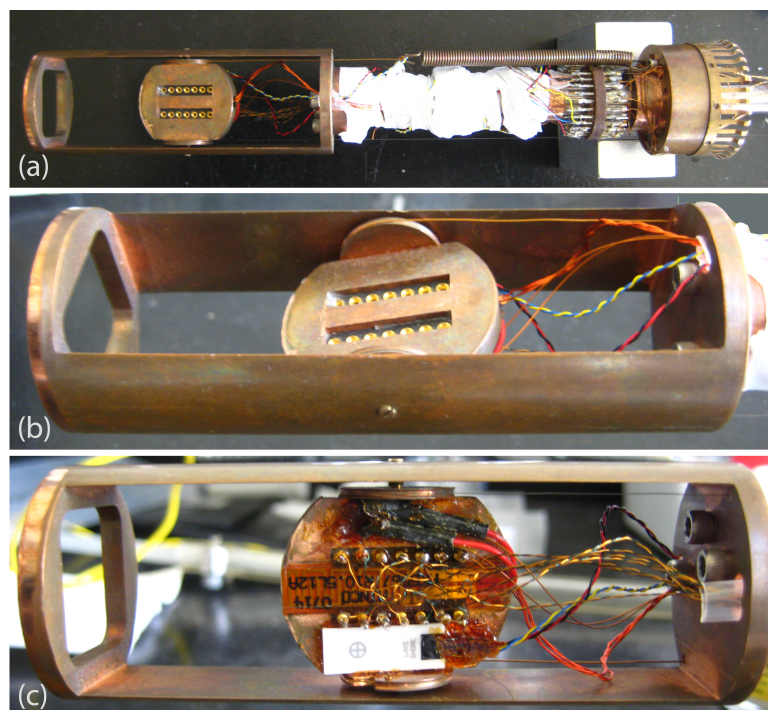

Figure E.6: Photographs of (a) the sample rotation stage retained by the support block, the (b) front side of the rotator probe sample package mount, and (c) back views of the rotation stage foil heater and Hall sensor.

E.3 Design of the Sample Holder

In order to provide thermal measurement and control of the sample, the rotator stage is constructed from a piece of copper which has high thermal conductivity. Helium vapor flows over the sample and copper stage to provide cooling. A foil heater attached to the opposite side of the copper mounting stage provides thermal energy to control

temperature. The heater consists of a serpentine resistive heating element encased in Kapton® film. This film heater is mounted across the back surface of the copper stage using STYCAST® 1266 A/B cryogenic epoxy although STYCAST® 2850 FT would be more desirable for it's thermal properties but the low viscosity of 1266 makes it easier to put in place and remove the excess epoxy between the heater and the copper making it more effective. A machined piece of Al is used to apply force to the foil heater while the Stycast is curing and maintain the smallest possible gap between the heater and Cu block and prevent bubbles from forming in the Stycast. Again, the thermal conductivity of the epoxy is crucial to effectively keeping the heater and the stage in good thermal equilibrium. If this thermal link is broken the foil heater will quickly fail and require replacement.

The final component mounted on the stage to provide thermal regulation is the thermometry. Here a LakeShore Cernox™ CX-AA thermometer is used to provide accurate temperature measurements, especially at low temperature. Cernox™ thermometers operate using a four-terminal resistance measurement of a sputter-deposited zirconium oxy-nitride thin film [147]. Advantages of this type of thermometer is the negative temperature coefficient making it accurate to very low temperatures, the monotonic response from below 325 K, and it's low sensitivity to large magnetic fields which reduce systematic field-dependent errors. Typical resistance values for such a thermometer are quite high at low temperature $R_{Thermo}\,(1.2\mathrm{K}) = 43.2\mathrm{k}\Omega$ decreasing as the temperature increases to $R_{Thermo}\,(300\ \mathrm{K}) = 66.5\Omega$. These thermometers also have low magnetic field induced error [147]. The typical magnetic field induced error $\Delta T/T$ under an applied field of 8 Tesla is 0.004 at 300 K, 0.022 at 77 K, and changes sign to -0.15 at 4.2 K. Further, for applications where the magnetic field may be applied in different orientations to the thermometer the Cernox performs well, changing by less than any other LakeShore thermometer over this temperature range. The design of these thermometers does not impact the magnetic environment and minimizes changes to the temperature, adding less than 1 µW of heating power while in operation, reaching down to 10 nW at 4.2 K, which does not change the base temperature that can be reached appreciably.

The thermometer is mounted in a gold plated cylindrical copper cannister which is inserted into the center of the copper sample block to keep it in thermal equilibrium with the stage, heater, and sample. However, the mounting the sample on a standard stage

can provide a challenge. Often insulating varnish, such as General Electric varnish, or rubber cement is used to mount samples to cryogenic probes for transport measurements. The samples can be contacted electrically using indium to join leads to the sample. However, due to the sensitivity of metallic nanostructures to electrostatic discharge (ESD) another method must be employed. Rather than adhering the sample to the stage itself, it is mounted on a package that includes pads for making wirebonds to the sample that are connected to pins that can then be connected for measurement. With the package grounded, a wirebonding machine is used to make electrical connections between the sample and the package bonding pads. The cryogenic sample stage is configured with a set of spring loaded pin sockets in a standard 14-pin DIP socket configuration that allows the package to be mounted without difficulty. The DIP mounting system allows the electrical connections to be made simultaneously and while allowing the package to be in thermal contact with the probe.

Photographs of packages for mounting and wirebonding samples are shown in Figure E.7. Each package is capable of being mounted on the rotation stage using a dip style socket. Oblique (a) and overhead (b) photographs of a commercial dip package made by Spectrum Semiconductor for mounting and wirebonding samples to be loaded onto the sample probe for rotating the magnetic field into the out-of-plane direction. Oblique (c) and end on (d) photographs of a homemade package for rotation of the magnetic field in-plane. The commercial dip package or custom copper sample mount is placed in direct thermal contact with the rotation block.

E.3.1 Probe Wiring

The measurement probe must have wiring to connect the low temperature sample environment to the laboratory environment to make transport measurements. Such a probe must provide electrical measurement leads, thermometry, heating, field sensing, and in this case physical rotation as well. The measurement wires provide electrical connections between laboratory test equipment and the sample environment via a Deteronix hermetically sealed 19-pin military connector attached to a NW-40 flange. These wires must provide low-noise, low-resistance connections while minimizing additional thermal loading due to thermal conduction in the wires between the sample and room temperature.

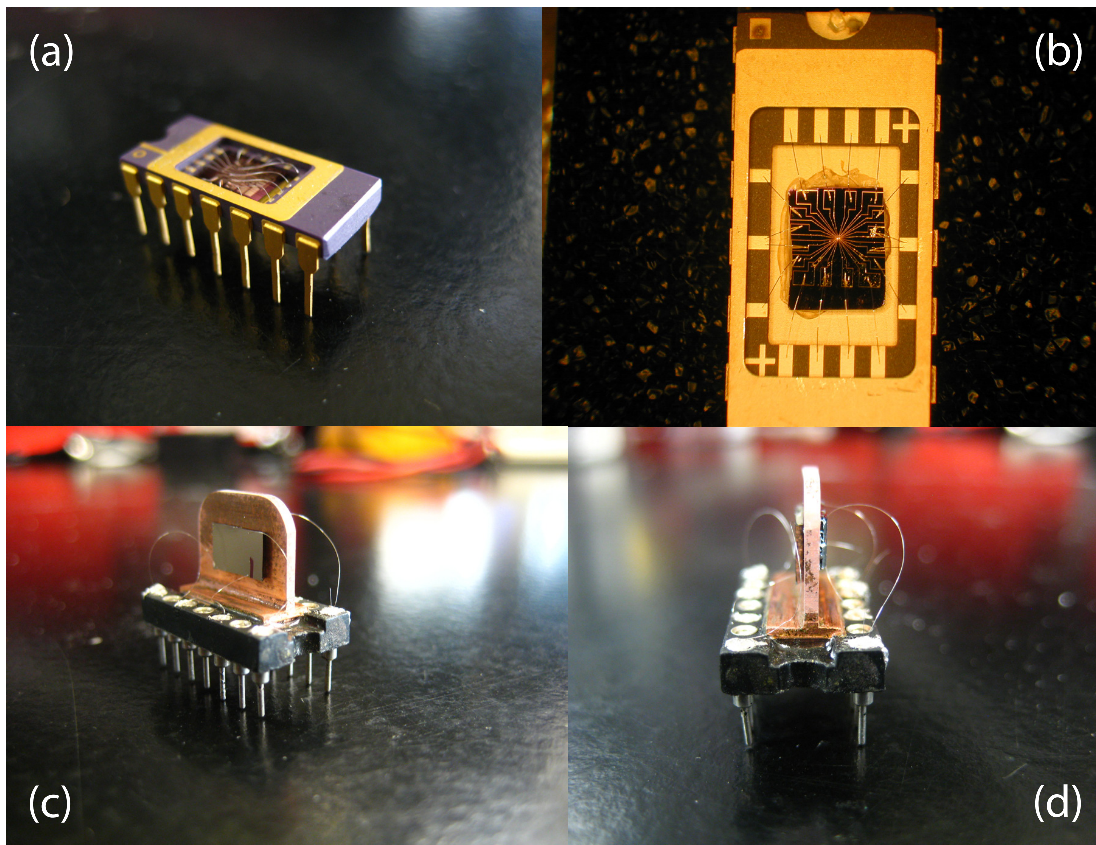

Figure E.7: Photographs of packages for mounting and wirebonding samples to be loaded into the cryostat for transport measurements.

The WiedemannFranz Law relates the thermal κ_{therm} and electrical σ conductivities,

$$\frac{\kappa_{therm}}{\sigma} = LT, \tag{E.1}$$

where the product of the Lorenz number $L \sim 3 \times 10^{-8}\ W\,\Omega\,K^{-2}$ and temperature T is the constant of proportionality between the thermal and electrical conductivities. Copper and alloys such as phosphor bronze (copper with tin and phosphorus), Nichrome (nickel with chromium), and Manganin (copper with manganese and nickel) are often used for cryostat wiring. Manganin and Phosphor Bronze are used here to balance the trade-offs of effects of κ_{therm} and σ.

As an additional constraint, the choice of materials should also have low magneto-resistance for magnetic field dependent measurements such as these. The susceptibilities χ_m^{SI} and magneto-resistances MR for each wire are shown in Table E.1 from References [105, 106]. The magneto resistance is defined elsewhere but is reiterated here,

$$MR = \frac{R(H) - R(0)}{R(0)}, \tag{E.2}$$

where $R(H)$ and $R(0)$ are the wire resistances at a finite applied field H and zero field respectively at $T = 5$ K. Using values from the table ideal wire choices can be made for various applications. Due to the low-electrical resistivity, residual resistivity ratio (RRR), and magneto-resistance compared to many elemental metals, phosphor bronze is chosen for wiring sample leads. Although at $T = 5$ K the MR is larger for phosphor bronze than some other metals, it is reduced to a fraction of other materials as the temperature increases to 77 K. The wires employed are also twisted to aid in the rejection of unwanted coupling in the lines along the length of the probe. These twisted pairs are heat sunk at low temperature near the bottom of the probe to minimize thermal loading of the sample itself. Manganin is also a good choice for the last connection between the thermal sink and the sample as the lower thermal conductivity of the Manganin will further minimize thermal loading of the sample, allow for a lower base temperature, and limit thermal fluctuations. If used only for the last step in limits thermal load while keeping the overall lead resistance lower. One major drawback is that Manganin is more difficult to solder than phosphor bronze, which is also more difficult that pure copper.

Additional wires must be strung for the thermometer, heater, and magnetic field sensor. The thermometer and magnetic field are both served by a pair of twisted-pair phosphor bronze wires as they both require a four terminal measurement. One

Wire Material	ρ(295 K) $\mu\Omega\ cm$ ρ(5 K) $\mu\Omega\ cm$	RRR	MR ($\Delta R/R$) at $T = 5$ K	$\chi_m^{SI}(T = 5\text{ K})$ $\chi_m^{SI}(T = 295\text{ K})$
Copper	1.68 ~ 0.02	76	188	
Manganin	48.2 42.9	1.25	-2.83	1.25×10^-2 2.7×10^-3
Nichrome	109 106	1.09	0.69	5.6×10^-3 5.2×10^-4
Phosphor Bronze	12.8 10.7	1.67	4.5 0.08 at 77 K	-3.3×10^-5 -5.2×10^-5

Table E.1: Transport properties of commonly used materials for low temperature cryostat wiring. For each material the Residual Resistivity Ratio $\rho(T = 295\text{ K})/\rho(T = 5\text{ K})$, $T = 5$ K magnetoresistance $(R(H = 10\text{ T}) - R(H = 0\text{ T}))/R(H = 0\text{ T})$, and magnetic suceptabilities are shown.

pair carries current while the other is for the voltage. The sensitivity of each of these measurements requires equal consideration as the wires used for the sample wiring itself. The only component that is wired differently is the two charge current leads for the heater. In this case a slightly larger diameter is used to minimize Ohmic heating in the wires supplying current to the resistive heating element.

E.4 Probe Rotation Block Calibration

The Hall generator attached to the sample rotator can be used to measure the angle made with the applied magnetic field. The Hall generator is attached to the back of the rotation stage offset to the side using GE varnish rather than epoxy so that it can be removed. To calibrate the angle a constant magnetic field is applied and the Hall voltage is recorded while adjusting the linear positioner that controls rotation. The resulting data can be fit by a sinusoid to find the sample angle in the field and must compensate for changes in environmental factors such as temperature and He flow rate. This procedure must be repeated if the sample is rotated too far and the rotation activation wire is damaged or broken as the field parallel and perpendicular positions

may have changed during repairs. An example curve is shown in Figure E.8.

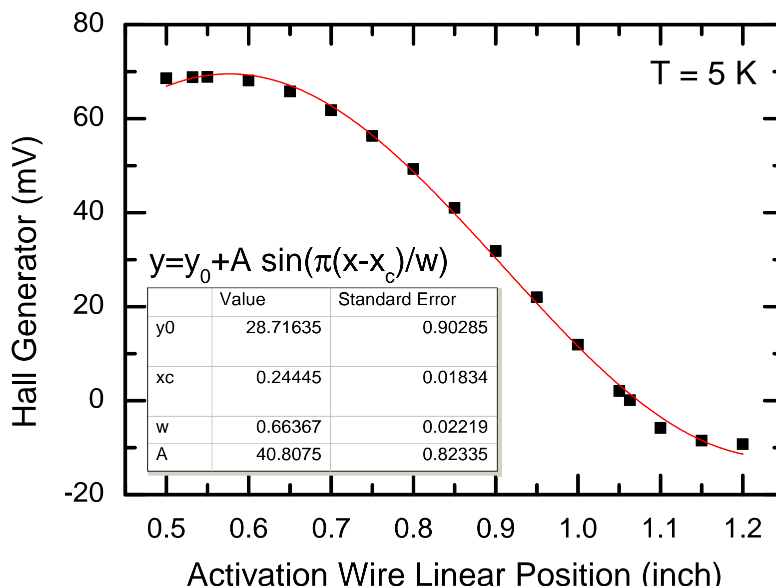

Figure E.8: Sample Hall voltage from sensor on rotation probe plotted as a function of the linear feedthrough position in order to align the sample angle under various conditions.

E.5 Helium Vapor Cryostat Operation

Low-temperature transport measurements are conducted using a custom sample mount constructed to load samples into a low temperature He vapor magneto cryostat, a SuperVariMag manufactured by Janis Research Company. The cryostat vaporizes liquid He that then flows over a sample to regulate the temperature between 1.1 K and 300 K. Although, at temperatures < 4.2 K the sample can also be immersed in liquid He rather than vapor.

At the most fundamental level the cryostat is composed of concentric spaces for the sample at the center, a vacuum isolation space, a liquid helium bath, a vacuum isolation space, a liquid nitrogen bath, and an outer vacuum jacket. These spaces are vacuum tight and are joined at the top flange of the cryostat. The center region is a variable temperature region into which helium flows from the liquid helium bath via

a pickup tube and needle valve. The needle valve controls the flow rate, and thus the cooling power, of the helium that is then pumped through a vacuum pump attached to the top of the sample tube. Typical helium vapor flow rates in this configuration are between 50 - 1000 cm^3/min. A heater is attached to the base of the sample tube and heats the helium flowing in. A Cernox thermometer is also attached to the base of the sample tube allowing the temperature of the gas to be controlled and is typically set 10 mK to 2 K below the desired sample temperature. Temperature control of the sample space gas is achieved via a Proportional-Integral-Derivative (PID) control loop with a LakeShore 340 two channel temperature controller with the second channel being used to control the sample mount itself. The surrounding isolation space prevents thermal loading the liquid helium space from a warm sample tube and the outer vacuum and nitrogen jackets are design to minimize radiative loading of the helium bath from the room temperature laboratory environment. The sample is top-loaded into the central sample space on the end of a probe stick. The series of spaces are depicted in Figure E.9. The vacuum isolation spaces are complemented with baffles and super insulation to reduce radiative losses. Due to the isolation features of this cryostat it should consume about 4-5 L of liquid helium per day.

The magnetic field is applied by current flowing through a superconducting solenoid immersed in the liquid He bath. Although the application of large magnetic fields is unnecessary for some measurements in this work, others require the application of larger fields up to several Tesla. The niobium titanium wire wound superconducting magnet used here is capable of applying fields up to ± 9 Tesla. The solenoid provides a uniform magnetic field varying by $\pm 0.5 - \pm 0.01\%$ over a 1 cm region. The superconducting solenoid, however, it is only capable of generating magnetic fields in a fixed direction (oriented vertically as the cryostat sits). Since the magnet cannot be rotated, experiments requiring fields applied in other directions require the sample to be rotated *in-situ* instead. This requires the probe described previously in this appendix to load samples.

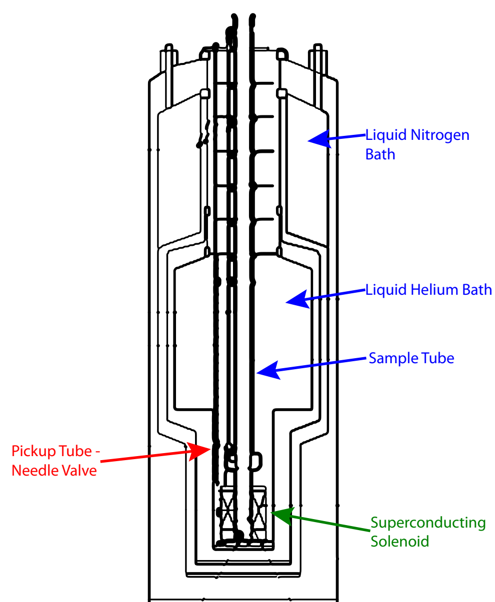

Figure E.9: Schematic diagram of cryostat.